

N-164, 239

P+I

AD-A286 700



ASD TR 61-191 (I)

000000

Reproduced From
Best Available Copy

**THEORETICAL FORMABILITY
VOLUME I
DEVELOPMENT**

W. W. Wood
R. E. Goforth
R. A. Ford
et al

1000000000

*Manufacturing Research and Development
Vought Aeronautics
a division of
Chance Vought Corporation*

000000

AUGUST 1961

LIBRARY COPY

OV 24 1961

3632X

94-24339



[REDACTED]

AERONAUTICAL SYSTEMS DIVISION

DTIC QUALITY ASSURED 1

94 8 02 006

**Best
Available
Copy**

NOTICES

When Government drawings, specifications, or other data are used for any purpose other than in connection with a definitely related Government procurement operation, the United States Government thereby incurs no responsibility nor any obligation whatsoever; and the fact that the Government may have formulated, furnished, or in any way supplied the said drawings, specifications, or other data, is not to be regarded by implication or otherwise as in any manner licensing the holder or any other person or corporation, or conveying any rights or permission to manufacture, use, or sell any patented invention that may in any way be related hereto.

Qualified requesters may obtain copies of this report from the Armed Services Technical Information Agency, (ASTIA), Arlington Hall Station, Arlington 12, Virginia.

This report has been released to the Office of Technical Services, U. S. Department of Commerce, Washington 25, D. C., for sale to the general public.

Copies of ASD Technical Reports and Technical Notes should not be returned to the Aeronautical Systems Division unless return is required by security considerations, contractual obligations, or notice on a specific document.

**THEORETICAL FORMABILITY
VOLUME I
DEVELOPMENT**

*W. W. Wood
R. E. Goforth
R. A. Ford
et al*

*Manufacturing Research and Development
Vought Aeronautics
a division of
Chance Vought Corporation*

AUGUST 1961

Directorate of Materials and Processes
Contract No. AF 33(616)-6951
Project No. 7381

**AERONAUTICAL SYSTEMS DIVISION
AIR FORCE SYSTEMS COMMAND
UNITED STATES AIR FORCE
WRIGHT-PATTERSON AIR FORCE BASE, OHIO**

FOREWORD

This report was prepared by the Manufacturing Research and Development Section, Vought Aeronautics, a division of Chance Vought Corporation, under Contract AF 33(616)-6951. The contract period covered from March 1960 to July 1961 and was administered by the Directorate of Materials and Processes, Deputy for Technology, Aeronautical Systems Division, under the direction of Messrs: C. W. Douglass, G. L. Campbell, and J. M. Bryars. Mr. C. W. Kniffen, Air Force Systems Command, is to be commended for invaluable assistance and guidance in the program.

This report is presented in two volumes. The first volume on development gives the basic theory and the procedure used to accomplish the objective. The second volume on application gives results in handbook form for ready reference.

Mr. W. W. Wood was the project engineer in charge of the program. The research described in this report was conducted under the direction of Mr. G. Gasper, Manufacturing Engineering Manager, and Mr. J. A. Millsap, Chief, Manufacturing Research and Development. Others from the Manufacturing R and D Section who cooperated in the research and in the preparation of the report are: W. W. Akins, R. E. Goforth, R. A. Ford, B. L. Scott, J. N. Lesikar, G. R. DiGiacomo, F. Camden, J. R. Russell, D. L. Norwood, W. D. Moore, and C. R. Clifton.

For their assistance in the program, acknowledgement is due to personnel of the Manufacturing R and D Laboratory, Production Sheet Metal Fabrication, Structures Test Laboratory, and Technical Publications sections who participated in the research work throughout the program.

The Fort Worth Division of Convair performed all the experimental work for the Androform process.

Accession For	
NTIS GRA&I	<input checked="checked" type="checkbox"/>
DTIC TAB	<input type="checkbox"/>
Unannounced	<input type="checkbox"/>
Justification	
By _____	
Distribution/ _____	
Availability Codes	
Dist	Avail and/or Special
A-1	

ABSTRACT

The "cut-and-try" method of determining sheet metal formability has long been the standard practice in the aircraft industry. This two-volume report presents methods of determining formability analytically for the twelve most common processes of forming sheet metal. This method is based on utilization of a material's mechanical properties to predict formability.

The first volume on development gives the procedure used to arrive at the objective of predicting formability. First, basic limit equations are developed relating geometry of the parts to the material properties. These equations are used to determine the shape of the limit graphs and to give indices relating formability to the material. Then, experimental parts are formed to position the theoretically shaped curves with the aid of the formability indices.

The second volume on application is presented in handbook form giving design and manufacturing information for the nineteen materials in the program. These materials covered some of the most currently used alloys in the following categories: (1) magnesium, (2) aluminum, (3) titanium, (4) stainless steel, (5) tool steel, (6) nickel and cobalt base, and (7) the refractory metals. Graphs, equations, and design tables are presented for each process, statistically proven with experimental work comprising a total of approximately twenty-one-thousand formed parts.

PUBLICATION REVIEW

This report has been reviewed and is approved.

FOR THE COMMANDER:

J. Teres
Technical Director
Applications Lab
Directorate of Materials
and Processes

TABLE OF CONTENTS

<u>Chapter</u>		<u>Page</u>
	INTRODUCTION	
I.	DESCRIPTION OF PROCESSES AND FAILURE ANALYSIS OF PARTS	I-1
	Brake Forming	I-1
	Joggling	I-9
	Dimpling	I-17
	Rubber Shrink and Stretch Flanging	I-26
	Linear Stretch Forming	I-41
	Linear Roll Forming	I-60
	Sheet Stretch Forming	I-72
	Androforming	I-81
	Deep Drawing with Mechanical Dies	I-90
	Spinning	I-100
	Rubber Press Beading.....	I-112
	Drop Hammer Beading	I-120
	Effective Strain	I-128
II.	DEVELOPMENT OF BASIC EQUATIONS	II-1
	Splitting Theory	II-1
	Buckling Theory	II-2
	Brake Forming	II-16
	Joggling	II-20
	Dimpling	II-23
	Rubber Flanging.....	II-26

TABLE OF CONTENTS (contd.)

<u>Chapter</u>	<u>Page</u>
DEVELOPMENT OF BASIC EQUATIONS (contd.)	
Linear Stretch and Roll Forming	II-29
Sheet Stretch	II-32
Androforming	II-35
Deep Drawing with Mechanical Dies and Manual Spinning	II-38
Rubber Press Beading	II-43
Drop Hammer Beading	II-44
III. FORMABILITY INDICES	III-1
Brake Forming	III-3
Dimpling	III-4
Drop Hammer Beading	III-4
Rubber Press Beading	III-5
Sheet Stretch	III-6
Androforming	III-7
Joggling	III-8
Linear Stretch	III-9
Rubber Press Stretch Flanges	III-10
Rubber Press Shrink Flanges	III-11
Roll Forming	III-12
Manual Spinning	III-13
Deep Drawing with Mechanical Dies	III-14
Summary	III-15

TABLE OF CONTENTS (contd.)

<u>Chapter</u>		<u>Page</u>
IV.	FORMABILITY TESTS	IV-1
	Standard Tensile Specimens	IV-1
	Standard Compression Specimens	IV-17
	Special Tests	IV-19
	Gridded Parts	IV-22
V.	COMPOSITE GRAPHS, PREDICTABILITY EQUATIONS AND DESIGN TABLES	V-1
	Brake Forming	V-1
	Design Tables	V-5
	Joggling	V-8
	Design Tables	V-14
	Dimpling	V-16
	Design Tables	V-21
	Rubber Stretch Flanges	V-22
	Design Tables	V-31
	Rubber Formed Shrink Flanges	V-33
	Design Tables	V-35
	Linear Stretch Forming	V-37
	Design Tables	V-45
	Linear Roll Forming	V-47
	Design Tables	V-49
	Sheet Stretch Forming	V-51
	Design Tables	V-54

TABLE OF CONTENTS (contd.)

<u>Chapter</u>		<u>Page</u>
	COMPOSITE GRAPHS, PREDICTABILITY EQUATIONS AND DESIGN TABLES (contd.)	
	Androforming	V-56
	Design Tables	V-60
	Deep Drawing with Mechanical Dies	V-61
	Design Tables	V-65
	Manual Spinning	V-67
	Design Tables	V-74
	Beading on the Rubber Press	V-76
	Design Tables	V-78
	Drop Hammer Beading	V-81
	Design Tables	V-83
VI.	SURVEY OF INDUSTRY AND INSTITUTIONS	VI-1
VII.	SUMMARY OF PROGRAM AND DISCUSSION OF PROBLEM AREAS	VII-1
	Formability Tests	VII-4
	Bending	VII-5
	Flanging	VII-9
	Linear Contouring of Sections	VII-10
	Plane Contouring of Sheet	VII-11
	Deep Recessing	VII-12
	Shallow Recessing	VII-14

TABLE OF CONTENTS (contd.)

<u>Chapter</u>		<u>Page</u>
VIII	RECOMMENDATIONS FOR FUTURE WORK	VIII-1
	Additional Part Shapes	VIII-2
	Extension of Forming Limits	VIII-4
	Results of Forming	VIII-10
	Additional Conventional Forming Processes	VIII-11
	Advanced Forming Processes	VIII-14
	Primary Forming Processes	VIII-16
	Basic Mechanisms in Metal Forming	VIII-17
IX.	BIBLIOGRAPHY	IX-1

LIST OF PHOTOGRAPHS

<u>Figure</u>		<u>Page</u>
I-1	60 Ton Verson Brake Press	I-1
I-2	Adjustable Brake Press Die	I-2
I-11	Hamilton Press for Joggling.....	I-5
I-13	Universal Joggle Tool.....	I-11
I-19	Shear Buckling and Splitting Failures for Joggling	I-16
I-20	CP450EA Zephyr Triple Action Coin Ram Dimpling Machine	I-17
I-22	Dimpling Dies	I-18
I-23	Triple Action Coin Ram Dimpling Die	I-19
I-29	Circumferential and Radial Splitting Failures for Dimpling	I-25
I-30	5,000 Ton Lake Erie Rubber Press	I-26
I-32	Tooling for Rubber Formed Flanges	I-28
I-44	Progressive Sine Wave Buckling for Rubber Formed Stretch Flanges	I-38
I-44(a)	Splitting for Rubber Formed Stretch Flanges	I-39
I-44(b)	Plastic Buckling for Rubber Formed Shrink Flanges	I-40
I-45	17 1/2 Ton A-10 Hufford Stretch Press	I-41
I-46	Tooling for Linear Stretch Forming	I-42
I-48	Heel-Out Sections - Stretched to Yield Before Wrapping	I-44
I-49	Heel-Out Sections - In Process of Wrapping	I-44
I-50	Heel-Out Sections - Completely Wrapped	I-45
I-59	Buckling of Linear Stretch Formed Heel-Out Angle Sections	I-54

LIST OF PHOTOGRAPHS (Contd)

<u>Figure</u>		<u>Page</u>
I-59(a)	Splitting of Linear Stretch Formed Heel-Out Angle Sections	I-55
I-59(b)	Buckling of Linear Stretch Formed Heel-In Angle Sections	I-56
I-59(c)	Splitting of Linear Stretch Formed Heel-In Angle Sections	I-57
I-59(d)	Buckling of Linear Stretch Formed Heel-Out Channel Sections	I-58
I-59(e)	Twist Buckling of Linear Stretch Formed Heel-In Hat Sections	I-59
I-60	Kane-Roach (3 Roll) Rolling Machine	I-60
I-61	Dies for Roll Forming	I-61
I-70	Sine Wave Buckling of Linear Roll Formed Heel-In Channel Sections	I-70
I-70(a)	Splitting in the Web Radius of Linear Roll Formed Heel-In Channel Sections	I-71
I-71	300 Ton Sheridan Stretch Press	I-72
I-74	Double Contour Sheet Stretch Dies	I-75
I-75	Splitting Failure in Free Area for Sheet Stretch Forming	I-76
I-79	Double Contoured Sheet Stretch Parts	I-80
I-82	Androform Die (20 Inch Radius).....	I-83
I-84	Splitting of Androform Parts	I-85
I-86	Buckling of Androform Parts	I-87
I-88	Androforming - Double Contouring with the 20 Inch Die	I-88
I-89	Androforming - Double Contour Area Between the Forming and Hold-Back Stages	I-89
I-90	600 Ton Lake Erie Hydraulic Press	I-90
I-92	Deep Draw Tooling	I-92

LIST OF PHOTOGRAPHS (Contd.)

<u>Figure</u>		<u>Page</u>
I-99	Buckling and Splitting of Deep Draw Parts	I-99
I-100	Model 1006 Haag Spin Master.....	I-100
I-101	Spinning Dies	I-101
I-114	Shear Splitting and Circumferential Splitting of Spun Parts	I-111
I-115	3,000 PSI. HPM Die Press	I-112
I-116	Rubber Bead Tooling	I-113
I-123	Splitting for Rubber Formed Beaded Panels	I-119
I-124	Cecostamp Drop Hammer	I-120
I-125	Drop Hammer Beading Dies	I-121
I-131	Splitting for Drop Hammer Beaded Panels	I-127
IV-1	Model FGT-SR4 T/M Baldwin Tensile Test Machine	IV-1
IV-4	TSMD Extensometer	IV-4
IV-12	Tensile Specimen Fracture on the Scope of the Optical Comparator	IV-14
IV-16	Baldwin Tensile and Compression Machine	IV-17

LIST OF ILLUSTRATIONS AND TABLES

<u>Figure</u>		<u>Page</u>
I-3	Criteria for Brake Form Dies	I-3
I-4	Bending Strain Vs. Width to Thickness Ratio	I-4
I-5	Brake Forming Procedure	I-4
I-6	Major Failure in Brake Forming	I-5
I-7	Minor Distortions in Brake Forming	I-5
I-8	Brake Forming Parameters and Limit Curve	I-6
I-9	Punch and Die Effect in Brake Forming	I-7
I-10	Applied Stress and Strain Diagrams for Brake Forming	I-8
I-12	Basic Methods of Forming Joggles	I-10
I-14	Joggling Parameters	I-12
I-15	Joggling Procedure	I-12
I-16	Major Joggling Failures	I-13
I-17	Joggling Limit Curve	I-14
I-18	Applied Stress and Strain Diagrams for Joggling	I-15
I-21	Dimpling Parameters	I-18
I-24	Dimpling Procedure	I-20
I-25	Major Failures in Dimpling	I-21
I-26	Limit Curve for Circumferential Failures	I-22
I-27	Limit Curve for Radial Failures	I-23
I-28	Applied Stress and Strain Diagrams for Dimpling	I-24
I-31	Rubber Flanging Dies	I-27
I-33	Rubber Formed Stretch and Shrink Flange Blanks and Resulting Good Parts	I-29

LIST OF ILLUSTRATIONS AND TABLES (Contd.)

<u>Figure</u>		<u>Page</u>
I-34	Parameters for Rubber Flanging	I-30
I-35	Sine Wave Buckling of Rubber Formed Stretch Flange	I-30
I-36	Flange Splitting of Rubber Formed Stretch Flange ...	I-31
I-37	Insufficient Pressure Failure	I-31
I-38	Wrinkling in Rubber Formed Shrink Flange	I-32
I-39	Formation of Wrinkles in Rubber Formed Shrink Flange	I-32
I-40	Minor Failures for Rubber Formed Stretch and Shrink Flanges	I-34
I-41	Rubber Formed Stretch Flange Curve	I-35
I-42	Rubber Formed Shrink Flange Curve	I-36
I-43	Applied Stress and Strain Diagrams for Rubber Formed Stretch Flanging	I-37
I-47	Parameters for Linear Stretch Forming	I-43
I-51	Failures for Heel-In Angle Sections	I-46
I-52	Failures for Heel-Out Angle Sections	I-47
I-53	Failures for Heel-In Channel Sections	I-48
I-54	Failures for Heel-Out Channel Sections	I-49
I-55	Failures for Heel-In Hat Sections	I-50
I-56	Splitting Criteria for Linear Stretch Forming	I-51
I-57	Linear Stretch Limit Curve	I-52
I-58	Applied Stress and Strain Diagrams for Linear Stretch and Linear Roll Forming.....	I-53
I-62	Part Types and Set-Up for Roll Forming	I-62
I-63	Parameters for Linear Roll Forming	I-63

LIST OF ILLUSTRATIONS AND TABLES (Contd.)

<u>Figure</u>		<u>Page</u>
I-64	Major Failure for Heel-Out Channel Sections	I-64
I-65	Major Failure for Heel-In Channel Sections	I-65
I-66	Set-Up for Heel-In Channel Sections	I-66
I-67	Minor Distortions for Heel-In Channel Sections.....	I-67
I-68	Minor Distortions for Heel-Out Channel Sections	I-68
I-69	Linear Roll Limit Curve	I-69
I-72	Schematic of Sheet Stretch Set-Up	I-73
I-73	Parameters for Sheet Stretch Forming	I-74
I-76	Splitting Failures for Sheet Stretch Forming	I-77
I-77	Sheet Stretch Limit Curve	I-78
I-78	Applied Stress and Strain Diagrams for Sheet Stretch Forming and Androforming	I-79
I-80	Schematic of Model J Androform Machine	I-81
I-81	Dimension "A" Between Hold-Back and Forming Stages (Androforming)	I-82
I-83	Parameters for Androforming	I-84
I-85	Androform Splitting Curve	I-86
I-87	Androform Buckling Curve	I-87
I-91	Schematic of Draw Press and Tooling	I-91
I-93	Parameters for Deep Drawing	I-93
I-94	Circumferential Compression in Deep Drawing	I-94
I-95	Free-Strain From Circumferential Compression	I-95

LIST OF ILLUSTRATIONS AND TABLES (Contd.)

<u>Figure</u>		<u>Page</u>
I-96	Failures for Deep Drawn Parts	I-96
I-97	Deep Draw Limit Curve	I-97
I-98	Applied Stress and Strain Diagrams for Deep Drawing	I-98
I-102	Spinning Procedure (Step 1)	I-102
I-103	Spinning Procedure (Step 2)	I-103
I-104	Spinning Procedure (Step 3)	I-103
I-105	Spinning Procedure (Step 4)	I-104
I-106	Parameters for Spinning	I-104
I-107	Circumferential Compression in Spinning	I-105
I-108	Free-Strain from Circumferential Compression	I-106
I-109	Elastic Buckling Failure for Spinning	I-107
I-110	Plastic Buckling and Shear Splitting Failures for Spinning	I-108
I-111	Circumferential Splitting Failures for Spinning	I-108
I-112	Spinning Limit Curve	I-109
I-113	Applied Stress and Strain Diagrams for Spinning	I-110
I-117	Parameters for Rubber Beading	I-114
I-118	Free Form Radius in Rubber Beading	I-115
I-119	Major Splitting Failure in Rubber Beading.....	I-115
I-120	Bending Failures in Rubber Beading	I-116
I-121	Rubber Beading Limit Curve	I-117
I-122	Applied Stress and Strain Diagrams for Rubber Beading	I-118

LIST OF ILLUSTRATIONS AND TABLES (Contd.)

<u>Figure</u>		<u>Page</u>
I-126	Parameters for Drop Hammer Beading	I-122
I-127	Initial and Final Stages of Drop Hammer Forming	I-123
I-128	Splitting Failures in Drop Hammer Beading	I-124
I-129	Drop Hammer Beading Limit Curve	I-125
I-130	Applied Stress and Strain Diagrams for Drop Hammer Beading	I-126
I-132	Strain Ratios for Plotting the "Effective Strain" Ellipse (Table)	I-129
I-133	"Effective Strain" Ellipse for Sheet Metal Forming	I-130
II-1	Edge Conditions of Practical Parts for Buckling ...	II-3
II-2	Four Basic Buckling Types for Sheet Material	II-4
II-3	Distribution of "k" for Basic Buckling Types.....	II-7
II-4	Buckling of Thin Sheet	II-13
II-5	Elongation of Pure Bending	II-16
II-6	Brake Forming Limits	II-18
II-7	Formability Curve for Brake Forming	II-18
II-8	Relative Brake Formability for Different Materials	II-19
II-9	Cross Section of a Joggle	II-20
II-10	Joggling Formability Curve	II-21
II-11	Relative Joggling Formability for Different Materials	II-22
II-12	Cross Section of a Dimple	II-23
II-13	Dimpling Formability Curve	II-24

LIST OF ILLUSTRATIONS AND TABLES (Contd.)

<u>Figure</u>		<u>Page</u>
II-14	Relative Dimpling Formability for Different Materials	II-24
II-15	Dimple Showing Flange Lengthening	II-25
II-16	Dimpling Formability for Different Materials.....	II-26
II-17	Stretch and Shrink Flange Parts	II-26
II-18	Rubber Press Formability	II-27
II-19	Relative Stretch Flange Formability for Different Materials.....	II-28
II-20	Linear Stretch Formed Part	II-29
II-21	Linear Stretch Formability Curve	II-30
II-22	Relative Linear Stretch Formability for Different Materials	II-31
II-23	Cross Section of Spherical Sheet	II-32
II-24	Sheet Stretch Formability Curve	II-33
II-25	Relative Sheet Stretch Formability for Different Materials	II-34
II-26	Androforming Formability Curve	II-36
II-27	Androforming Formability Curve	II-37
II-28	Cross Section of Deep Recessed Part	II-38
II-29	Thickness Strains for Deep Recessing	II-39
II-30	Overhang Flange to Cup Depth Ratio	II-41
II-31	Deep Recessing Formability	II-42
II-32	Cross Section of Rubber Formed Bead	II-43
II-33	Rubber Press Bead Formability Limits	II-44
II-34	Cross Section of Drop Hammer Formed Bead	II-44

LIST OF ILLUSTRATIONS AND TABLES (Contd.)

<u>Figure</u>		<u>Page</u>
II-35	Cross Section of Flat Area in Beading	II-45
II-36	Stress Versus Gage for Drop Hammer Beading	II-46
II-37	Drop Hammer Formability Limits	II-47
III-1	Application of Indices (Table)	III-2
III-2	Brake Forming Limit Curves	III-3
III-3	Dimpling Limit Curves	III-4
III-4	Drop Hammer Beading Curve	III-4
III-5	Rubber Press Beading Curve	III-5
III-6	Sheet Stretch Formability Curve	III-6
III-7	Androforming Splitting and Buckling Limit Curves ...	III-7
III-8	Joggling Formability Limits	III-8
III-9	Linear Stretch Forming Limits	III-9
III-10	Rubber Press Stretch Flange Limit Graph	III-10
III-11	Rubber Press Shrink Flange Limit Graph	III-11
III-12	Roll Forming Limit Graph	III-12
III-13	Formability Limit Graph for Spinning	III-13
III-14	Formability Limits for Deep Drawing	III-14
III-15	Application of Formability Indices (Table)	III-16
IV-2	CVL 1922-82A (Tensile Specimen)	IV-2
IV-3	Types of Tensile Load - Strain Curves	IV-3
IV-5	Sixteenth Infinite Plate (Tensile Specimen)	IV-5
IV-6	Instability of Tensile Specimen	IV-6
IV-7	Shear Flow in Tensile Specimens	IV-7

LIST OF ILLUSTRATIONS AND TABLES (Contd.)

<u>Figure</u>		<u>Page</u>
IV-8	Failure of Thick Tensile Specimens	IV-7
IV-9	Failure of Thin Tensile Specimens	IV-8
IV-10	Uniform Strain Distribution for Tensile Specimens...	IV-9
IV-11	"Effective Strain" Ellipse	IV-12
IV-13	Correction for Lateral Contraction	IV-15
IV-14	Correction for Lateral Contraction (.25" Gage Length)	IV-16
IV-15	Correction for Lateral Contraction (.5" Gage Length)	IV-16
IV-17	Compressive Load - Strain Curve	IV-18
IV-18	Three Types of 12 Inch Wide Tensile Specimens	IV-19
IV-19	Eccentric Tensile Test	IV-21
IV-20	Sheet Stretch Formed Part	IV-22
IV-21	"Effective Strain" Ellipse	IV-24
V-1	Composite Graph for Brake Forming	V-1
V-2	Strain in a Bend Specimen	V-2
V-3	Sine Wave Curve	V-3
V-4	Composite Graph for Brake Forming	V-4
V-5	Formability Curve for Brake Forming	V-6
V-6	Design Table Format for Brake Forming	V-6
V-7	Composite Graph for Jogging	V-8
V-8	Joggle Section Parameters	V-9
V-9	Buckling Formability Index Line	V-10
V-10	Splitting Limit Correlation Curve for Jogging	V-12
V-11	Predictability Equations for Jogging	V-13

LIST OF ILLUSTRATIONS AND TABLES (Contd.)

<u>Figure</u>		<u>Page</u>
V-12	Composite Graph for Jogging	V-14
V-13	Design Table Format for Jogging	V-15
V-14	Composite Graph for Dimpling	V-16
V-15	Geometric Parameters in Dimpling	V-17
V-16	Correlation Curve for Dimpling	V-18
V-17	Correlation Curve for Dimpling Plotted on Log-Log Graph Paper	V-19
V-18	Design Table Format for Dimpling	V-21
V-19	Composite Graph for Stretch Flanges	V-22
V-20	Geometric Parameters for Stretch Flanges	V-23
V-21	Buckling Formability Index Line for Rubber Stretch Flanges	V-24
V-22	Splitting Limits in Rubber Stretch Flanges	V-25
V-23	Correlation Curve for Rubber Stretch Flange Limits	V-26
V-24	Composite of Minimum Flange Limits in Rubber Stretch Forming	V-27
V-25	Formability Index Line for Rubber Stretch Flanges...	V-28
V-26	Minimum Flange Limit Curves for Rubber Stretch Flanges	V-29
V-27	Predictability Equations for Rubber Stretch Flanges	V-30
V-28	Composite Graph and Constant R_p/t Overlay Graphs for Rubber Stretch Flanges	V-31
V-29	Design Table Format for Rubber Stretch Flanges	V-32
V-30	Composite Graph for Rubber Shrink Flange Limits	V-33
V-31	Predictability Equations for Rubber Shrink Flanges	V-34

LIST OF ILLUSTRATIONS AND TABLES (Contd.)

<u>Figure</u>		<u>Page</u>
V-32	Composite Graph and Constant R_D/t Overlay Graphs for Rubber Shrink Flanges	V-35
V-33	Design Table Format for Rubber Formed Shrink Flanges	V-36
V-34	Linear Stretch Forming Geometric Shapes	V-37
V-35	Composite Graph for Linear Stretch Forming	V-38
V-36	Splitting Limits in Linear Stretch Forming	V-40
V-37	Correlation Curve for Splitting in Linear Stretch Forming	V-40
V-38	Composite of Splitting Limits for Linear Stretch Forming on Semi-Lcg Graph Paper	V-41
V-39	Equations for Linear Stretch Formed Heel-Out Angles and Channels	V-43
V-40	Equations for Linear Stretch Formed Heel-In Angles and Channels	V-44
V-41	Equations for Linear Stretch Formed Heel-In Hat Sections	V-44
V-42	Constant R_D/t Curves for Overlay Graphs for Linear Stretch Formed Parts	V-45
V-43	Design Table Format for Linear Stretch Forming	V-46
V-44	Geometric Parameters for Roll Forming	V-47
V-45	Composite for Roll Formed Heel-In Channels	V-47
V-46	Composite for Roll Formed Heel-Out Channels	V-48
V-47	Constant R_D/t Curves for Overlay Graphs for Linear Roll Forming	V-49
V-48	Design Table Format for Linear Roll Forming	V-50
V-49	Composite Graph for Sheet Stretch Forming	V-51
V-50	Geometric Parameters in Sheet Stretch Forming	V-52

LIST OF ILLUSTRATIONS AND TABLES (Contd.)

<u>Figure</u>		<u>Page</u>
V-51	Correlation Curve for Sheet Stretch Forming	V-53
V-52	Correlation Curve for Sheet Stretch Forming	V-53
V-53	Forming Limit Curve and Method to Determine the Forming Limits for Sheet Stretch Forming	V-54
V-54	Design Table Format for Sheet Stretch Forming	V-55
V-55	Geometric Parameters for Androforming	V-56
V-56	Androform Splitting Limit (50" Die)	V-57
V-57	Androform Buckling Limits (50" Die)	V-57
V-58	Design Table Format for Androforming	V-60
V-59	Composite Graph for Deep Drawing	V-61
V-60	Geometric Parameters for Deep Drawing	V-62
V-61	Buckling Curves and Index Lines for Deep Drawing....	V-63
V-62	Deep Drawing Limit Curve and Overlay Graph	V-65
V-63	Design Table Format for Deep Drawing	V-66
V-64	Manual Spinning Limit Composite	V-67
V-65	Geometric Parameters for Spinning	V-68
V-66	Plastic Buckling Limits for Spinning	V-69
V-67	Elastic Buckling Limits for Spinning	V-70
V-68	Machine Limit Index Lines for Spinning	V-71
V-69	Machine Limit Curve for Spinning	V-72
V-70	Spinning Predictability Equations	V-73
V-71	Spinning Limit Curve and Overlay Graph	V-74
V-72	Design Table Format for Spinning	V-75
V-73	Composite Graph for Rubber Formed Bead Limits	V-76

LIST OF ILLUSTRATIONS AND TABLES (Contd.)

<u>Figure</u>		<u>Page</u>
V-74	Geometric Parameters for Rubber Bead Forming	V-77
V-75	Composite Graph Used to Establish Design Limits for Rubber Bead Forming	V-79
V-76	Design Table for Rubber Bead Forming	V-80
V-77	Composite Graph for Drop Hammer Bead Forming	V-81
V-78	Geometric Parameters for Drop Hammer Bead Forming	V-82
VI-1	Formability Survey Results (Table).....	VI-3
VII-1	Table of Total Parts Formed on Contract	VII-1
VII-2	Table of Number of Parts per Material per Phase	VII-2
VII-3	Table of Gages Used for Types of Parts and Specimens.....	VII-3
VII-4	Gage Deviation in Brake Forming (Table)	VII-6
VII-5	Elongation Variation with Temperature	VII-7
VII-6	Joggle Bend Radius	VII-8
VII-7	View of Bottom of Cup Showing Cracking at 45° to Grain Direction for Deep Drawing	VII-13
VII-8	Premature Failure in Drop Hammer Beading	VII-14
VIII-1	Linear Contoured Section Types	VIII-4
VIII-2	Increased Formability with Pressure in Rubber Press Shrink Flanging	VIII-5
VIII-3	Increased Definition with Pressure in Rubber Press Shallow Recessing	VIII-6
VIII-4	Increased Formability for Decreased Segment Angle for Linear Stretch Forming	VIII-6
VIII-5	Increased Formability with Elevated Tempera- ture Creep Forming for Linear Contouring	VIII-7

LIST OF ILLUSTRATIONS AND TABLES (Contd.)

<u>Figure</u>		<u>Page</u>
VIII-6	Increased Formability in Deep Recessing with Multistage Tooling	VIII-8
VIII-7	Increased Limits in Compression Brake Forming	VIII-8
VIII-8	Increased Formability with Improved Forming Techniques	VIII-9
VIII-9	Expected Formability Curve for Tube Bending	VIII-12
VIII-10	Deep Drawing with a Rubber Bladder Press	VIII-12
VIII-11	Stretch - Mechanical Die Forming	VIII-13
VIII-12	Progressive Forming Double Contoured Skins	VIII-14

LIST OF SYMBOLS

Because of the large number of terms used, the following list of symbols is supplied for easy reference:

$P =$ load on tensile specimen

$l_o =$ original gage length

$l_f =$ final gage length

$A_o =$ original cross-sectional area

$A_f =$ final cross-sectional area

$A_i =$ instantaneous cross-sectional area

$E_T =$ Young's Modulus of elasticity in tension

$E_c =$ Young's Modulus of elasticity in compression

$S_u =$ tensile stress $\left(\frac{P}{A_o}\right)$ at ultimate load

$S_{Ty} =$ tensile stress $\left(\frac{P}{A_o}\right)$ at yield point

$S_{Cy} =$ compressive stress $\left(\frac{P}{A_o}\right)$ at yield point

$\sigma =$ true stress $\left(\frac{P}{A_i}\right)$; subscripts l , w and t
represent the longitudinal, width and thickness
directions

$\sigma_e =$ effective stress from Energy of Distortion Theory

ϵ = conventional strain $\left(\frac{l_f - l_o}{l_o} \right)$

$\epsilon_{2.0}$ = conventional strain for 2 inch gage length

$\epsilon_{.02}$ = conventional strain for .02 inch gage length

$\bar{\epsilon}$ = natural strain $\left(\ln \frac{l_f}{l_o} \right)$; subscripts l , w and t
represent the longitudinal, width and thickness
directions

$\bar{\epsilon}_e$ = effective strain from Energy of Distortion Theory

$[\epsilon_{.5}]_{\text{CORRECTED}}$ = 0.5 inch gage length elongation corrected to a
condition of plane strain

$[\bar{\epsilon}_{.25}]_{\text{CORRECTED}}$ = 0.25 inch gage length elongation corrected to a
condition of plane strain

NOTE: Additional symbols are described throughout the
text for continuity.

INTRODUCTION

The concept of theoretical formability was initiated at Chance Vought Corporation in 1953 with the introduction of the hard-to-form heat treated stainless steels and the titaniums. Prior to this, the accepted method of "cut-and-try" was used to determine sheet metal formability. It was determined at this time that, in order to minimize lead times, costs, and other factors affected by forming, better methods were needed for predicting formability.

A search of previous work in this field indicated that the major effort relating to analytical treatments of formability was carried on during World War II and the years immediately following. Most of this effort, however, was very narrow in scope, relating only to a few processes and materials. In addition, the projects were more of the experimental type with little regard to theoretical treatments of predicting formability based on material properties.

There have been several unique approaches to analytical formability in the past decade. These have practically all been associated with the laboratory type work such as relating tensile data to bending of straight sections. Chance Vought initiated the theoretical formability concept during this period on such basic forming processes as linear stretch forming and rubber flanging. The program covered in this two-volume report was conducted to develop the concept as applied to twelve basic forming processes and nineteen materials used in the aerospace industry.

Manuscript released by authors August 1961 for publication as an ASD Technical Report.

CHAPTER I
DESCRIPTION OF PROCESSES
AND FAILURE ANALYSIS OF PARTS

BRAKE FORMING

Brake forming is the most simple type forming operation and is widely used for forming flat sheets into sections such as angles, channels and hats. The $7\frac{1}{2}$ horsepower, 60 ton Verson Press Brake shown in Figure I-1 was used to establish the material limits in bending for this program. All parts were formed with a ram stroke of 3" at a speed of 8.77 feet per minute.

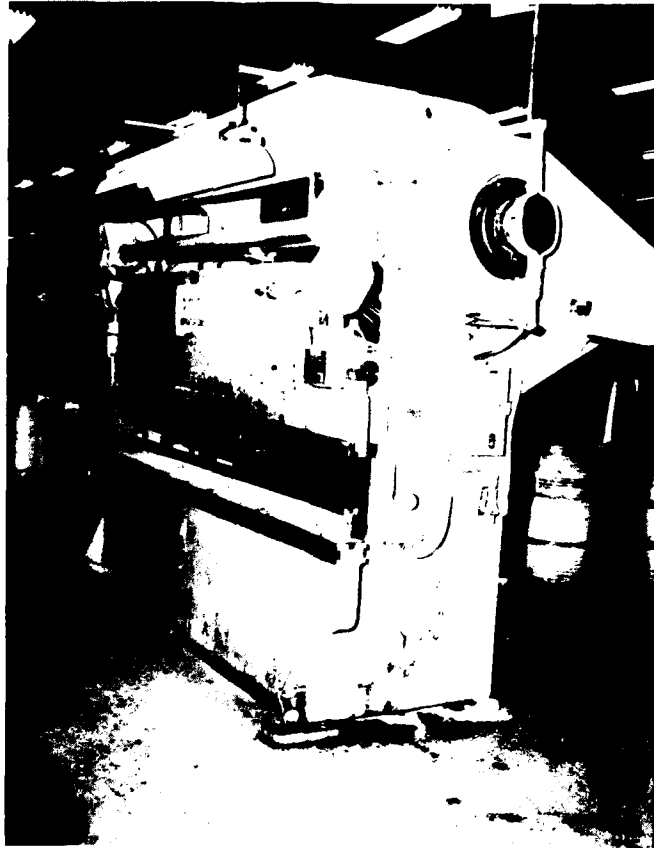


FIGURE I-1 60 TON VERNON BRAKE PRESS

The tooling used for brake forming is shown in Figure I-2. Since previous research indicated that the span width of the die affected the formability of bend specimens, an adjustable die was designed for this program. Where stationary channel dies have been used in the past, the graph in Figure I-3 shows the acceptable criteria as the area between the dotted lines. The median line was chosen for all parts formed in this program with the adjustable die. Thirty punches with radii ranging from 0.015" to 1.125" were used to allow complete coverage of the R/t failure range.



FIGURE I-2 ADJUSTABLE BRAKE PRESS DIE

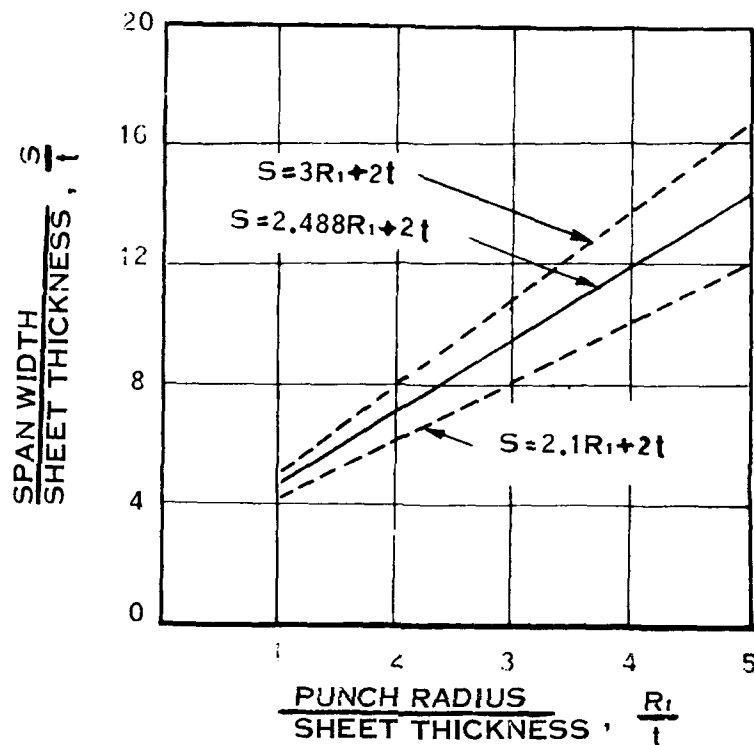


FIGURE I-3 CRITERIA FOR BRAKE FORM DIES

The length of the bend zone also affects minimum bend radius. According to Sachs⁽¹³⁾, the minimum bend radius remains nearly constant for bend specimens with a breadth which exceeds the metal thickness by approximately 8 times. Since the maximum material thickness for this program was 0.187", a specimen width of two inches was chosen to give W/t (Min.) = 10.7 and insure constant minimum bend radii. Figure I-4 graphically represents the W/t range covered in this program.

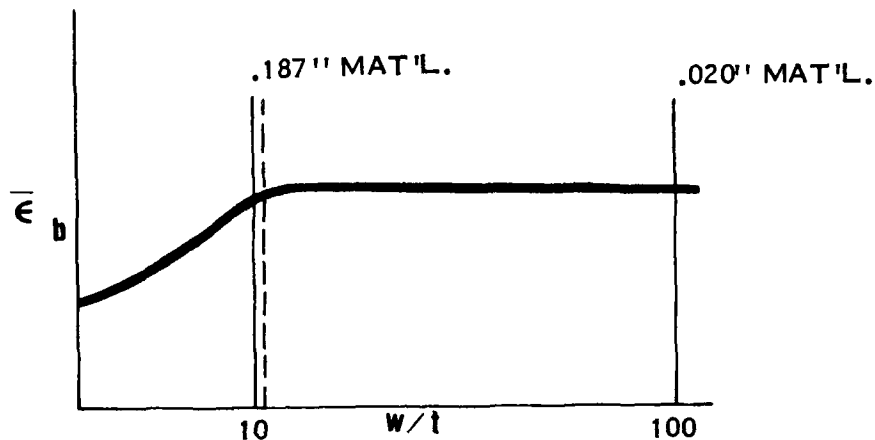


FIGURE I-4 BENDING STRAIN VS. WIDTH TO THICKNESS RATIO

Figure I-5 shows the brake form blank prepared for forming and the resulting good part.

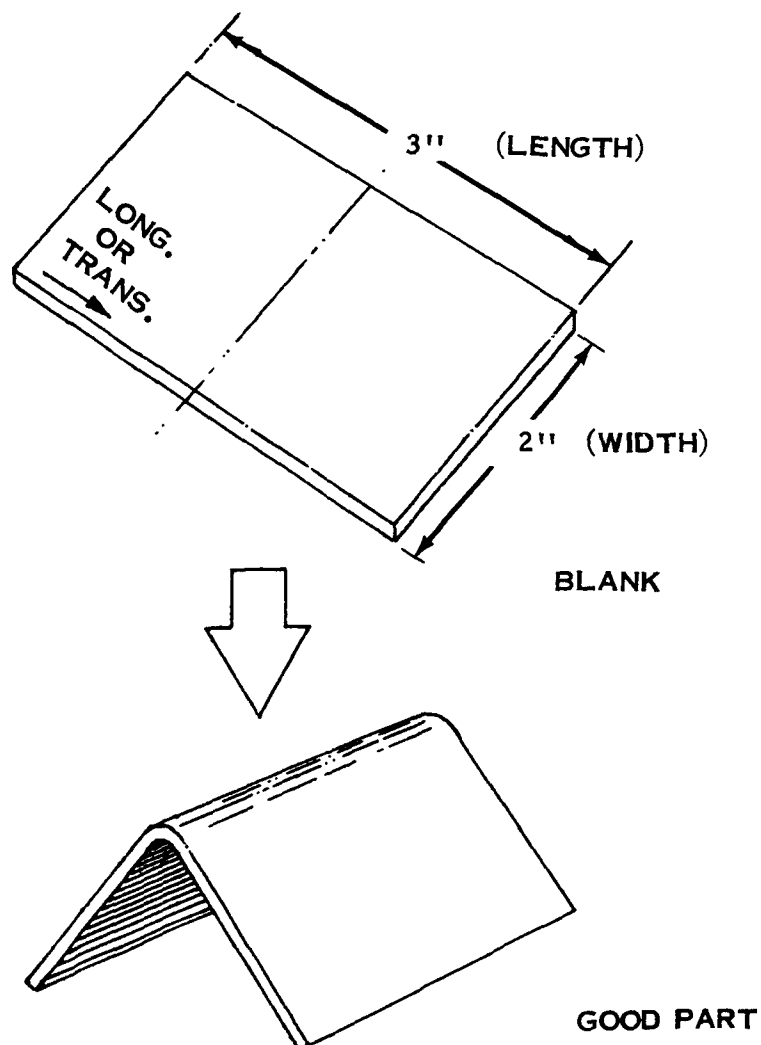


FIGURE I-5 BRAKE FORMING PROCEDURE

Only one major failure occurs along with minor distortions which are incidental to the process and can be corrected. The major failure in brake forming is longitudinal cracking in the outer fiber of the bend where the maximum bending strain occurs. This failure, shown in Figure I-6, is dependent on the punch radius and the material thickness.

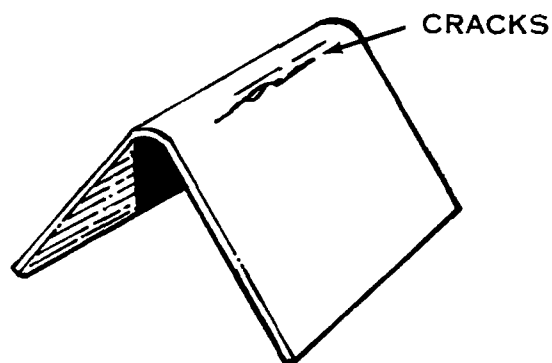


FIGURE I-6 MAJOR FAILURE IN BRAKE FORMING

Two minor distortions, end cracks and end displacement, are incidental to the process and can be corrected by sufficient deburring of the brake form blanks for notch sensitive materials. Figure I-7 illustrates the two minor distortions considered.

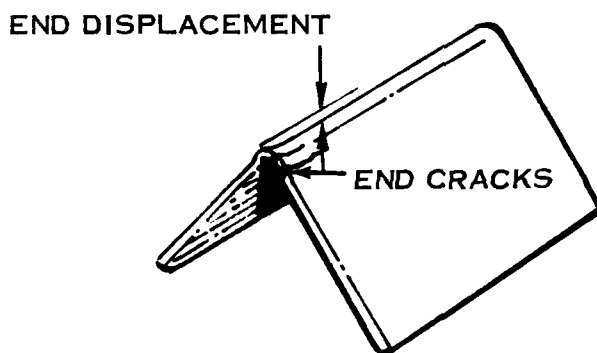


FIGURE I-7 MINOR DISTORTIONS IN BRAKE FORMING

Another minor distortion encountered in brake forming is the bowing of long parts which results from the residual stresses set up across the bend. Since brake formed parts in this contract were relatively short, bowing was not considered and did not affect the forming limits. Methods of controlling extreme cases of bowing are hot finish forming and final hand working.

The parameters for brake forming curves are R/t and α , where R is the radius of the punch, t is the material thickness and α is the part angle. A schematic curve of R/t vs. α and a sketch of parameters are shown in Figure I-8.

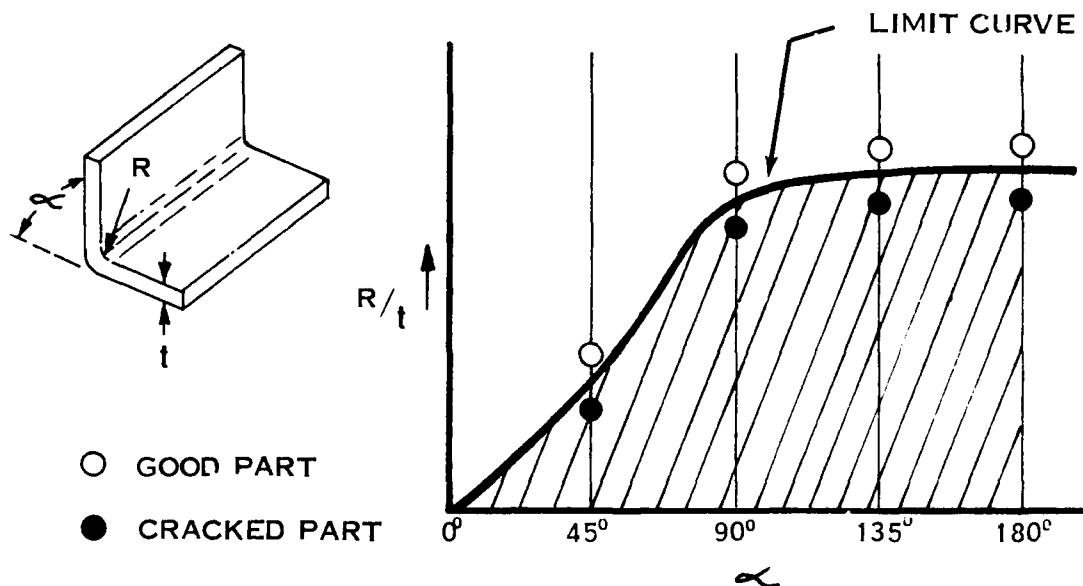


FIGURE I-8 BRAKE FORMING PARAMETERS AND LIMIT CURVE

The curve in Figure 1-8 is defined by good parts above the curve and cracked parts below the curve. As the part angle (α) is increased, the R/t value necessary to form a given material is increased to reduce the strain in the outer fiber resulting from increased part angle. The failed parts represented on the curve are of the major failure type shown in Figure 1-6. Minor distortions shown in Figure 1-7 can be corrected by sufficient deburring and do not affect the brake forming limits.

The punch and die effects illustrated in Figure 1-9 cause deviation from the theoretical curves for Rockwell hardnesses of 20 or less since "dig in" by the die superimposes tensile strain in the outer fiber of the formed part and coining by the punch results in localized tension in the inner fiber and resulting compression in the outer fiber. Bending strain is increased by the "dig in" effect since the neutral axis is shifted toward the inside fiber, but the coining effect causes a shift in the neutral axis toward the outer fiber thereby decreasing the bending strain.

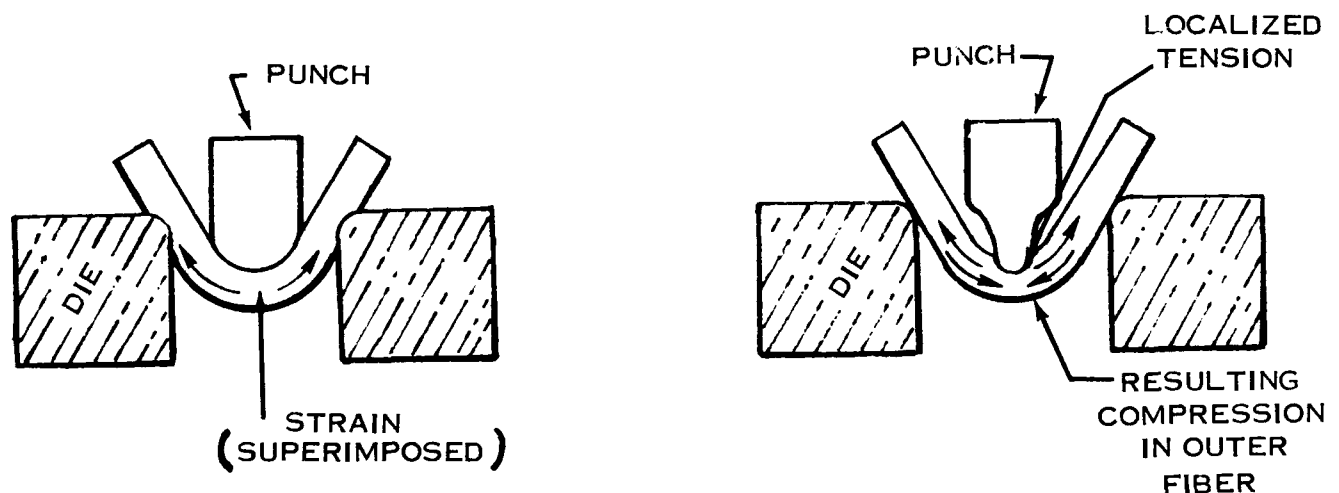


FIGURE 1-9 PUNCH AND DIE EFFECT IN BRAKE FORMING

The applied stress and the strain diagram of a brake form sample is illustrated in Figure I-10. The strain diagram shows that $\bar{\epsilon}_L = \epsilon_t$ and $\bar{\epsilon}_w = 0$; therefore, $\bar{\epsilon}_L / \bar{\epsilon}_w = \infty$. The value for $\bar{\epsilon}_L / \bar{\epsilon}_e = 0.866$ was determined by the Energy of Distortion Theory and allows the process to be plotted on the "Effective Strain" Ellipse in Figure I-133 for correlation to the standard tensile specimen.

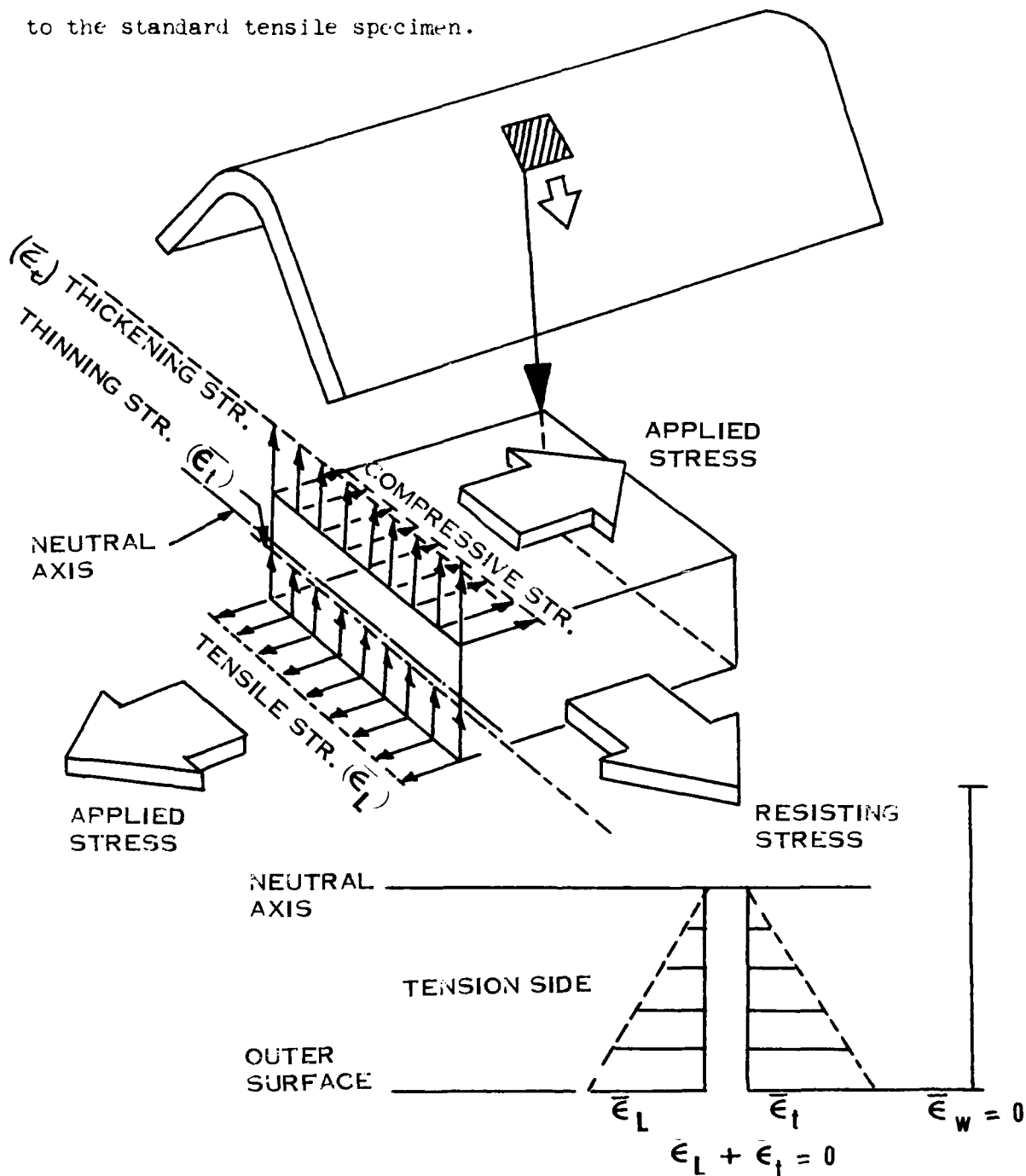


FIGURE I-10 APPLIED STRESS AND STRAIN DIAGRAMS FOR BRAKE FORMING

JOGGLING

Joggling is a process for recessing brake formed or extruded angle parts to enable flush connection with other angle parts or flat plates in assembly. The Hamilton press, shown in Figure I-11, was used to form the brake formed joggle samples for this program.

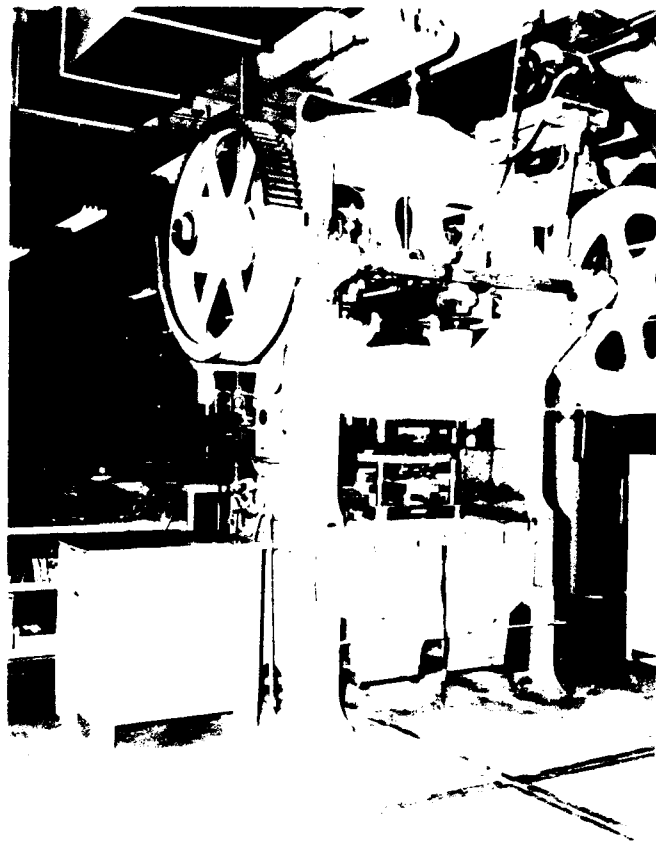


FIGURE I-11 HAMILTON PRESS FOR JOGGLING

Two basic methods of forming joggles are by a wiping action and section movement as shown in Figure I-12. The wiping action produces a joggle by straightening one mold line and forming another one, whereas the section joggling creates no new mold line but results in a shear displacement in the joggle transition region. The Universal Joggle Tool, shown in Figure I-13, is a combination of both although section movement is more predominant. This tool was selected for joggling because it was adaptable to a large number of parts.

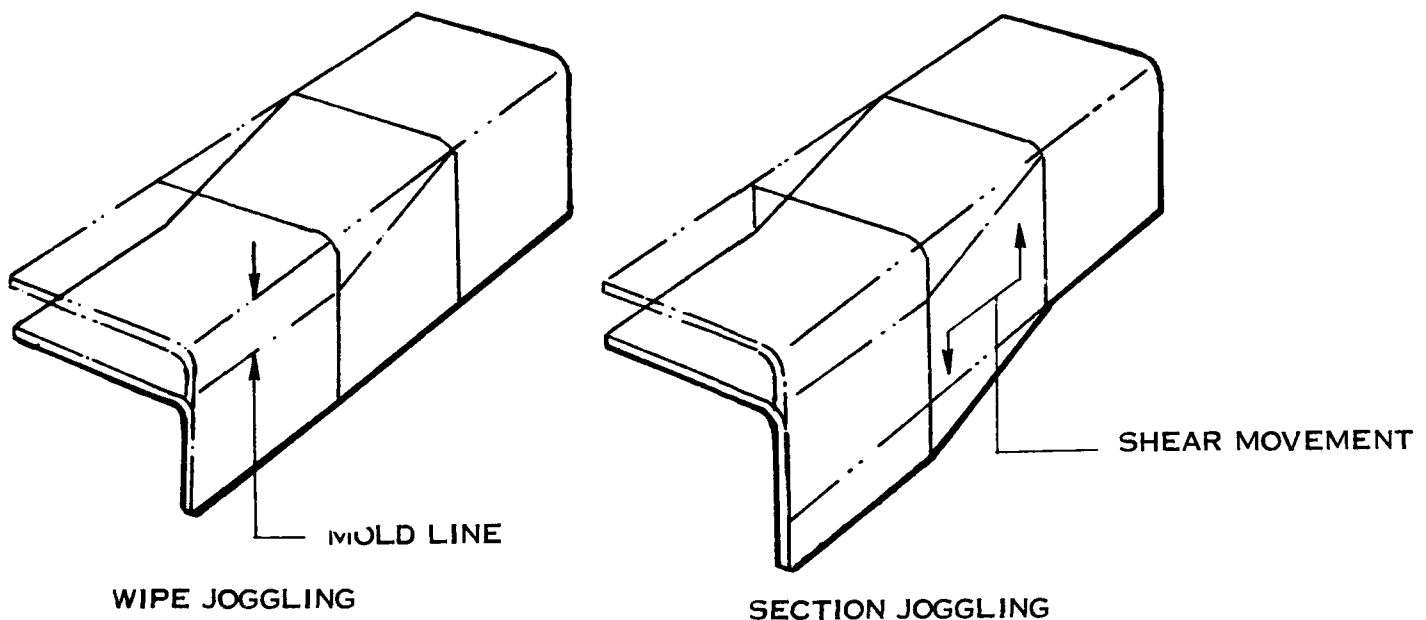


FIGURE I-12 BASIC METHODS OF FORMING JOGGLES

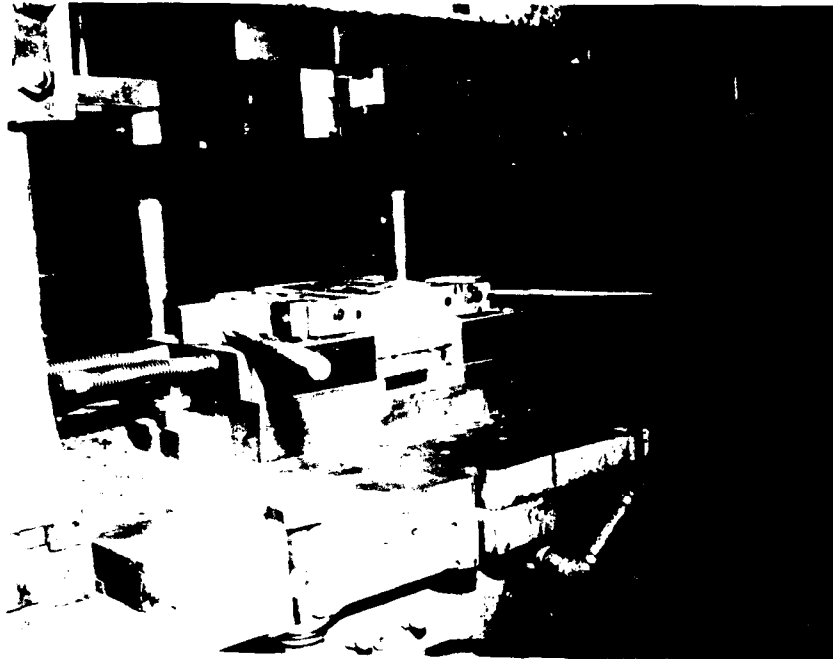


FIGURE I-13 UNIVERSAL JOGGLE TOOL

The parameters for joggling, illustrated in Figure I-14, are joggle depth (D), joggle run-out length (L) and material thickness (t). The only major limitation in joggling is the 0.4 inch maximum joggle depth but most practical parts will not exceed this limitation.

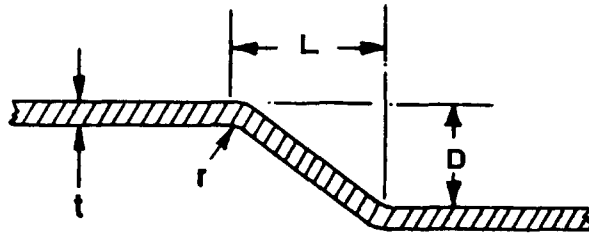


FIGURE 1-14 JOGGLING PARAMETERS

The flow diagram in Figure I-15 illustrates the jogging procedure. The joggle blanks were brake formed to a standard $6t$ radius in the intermediate forming stage to prevent bending failures in some materials.

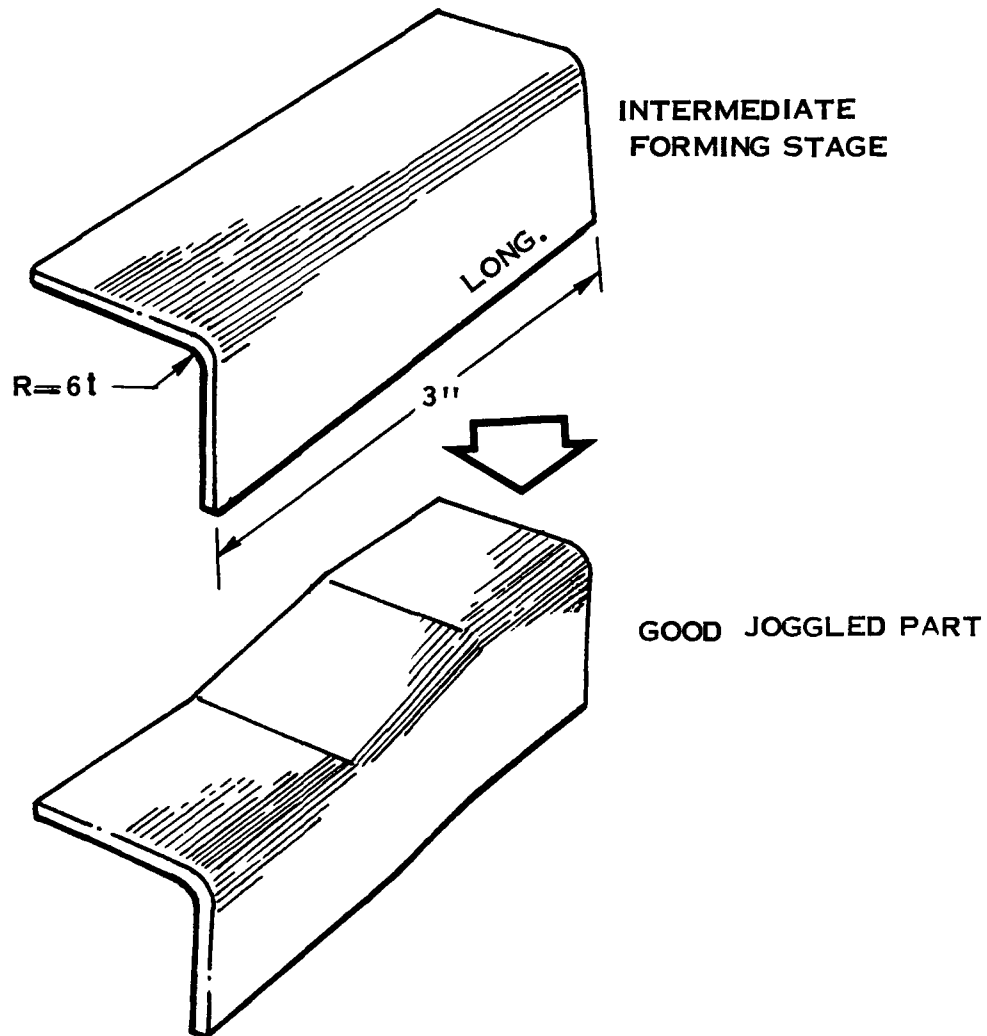


FIGURE I-15 JOGGLING PROCEDURE

The two major failures in joggling are splitting and shear buckling as shown in Figure I-16. Splitting occurs near the top of the transition region due to biaxial stresses in double bending. Some brittle materials failed prematurely in joggling since the standard radius of the joggle die, $r = 0.032''$ (see Figure I-14), was less than the radius necessary to brake form the same material. These premature failures were eliminated by forming the brittle materials on a special die block with a $0.060''$ radius. Shear buckling occurs in the web of the transition region as result of shear movement previously illustrated in Figure I-12.

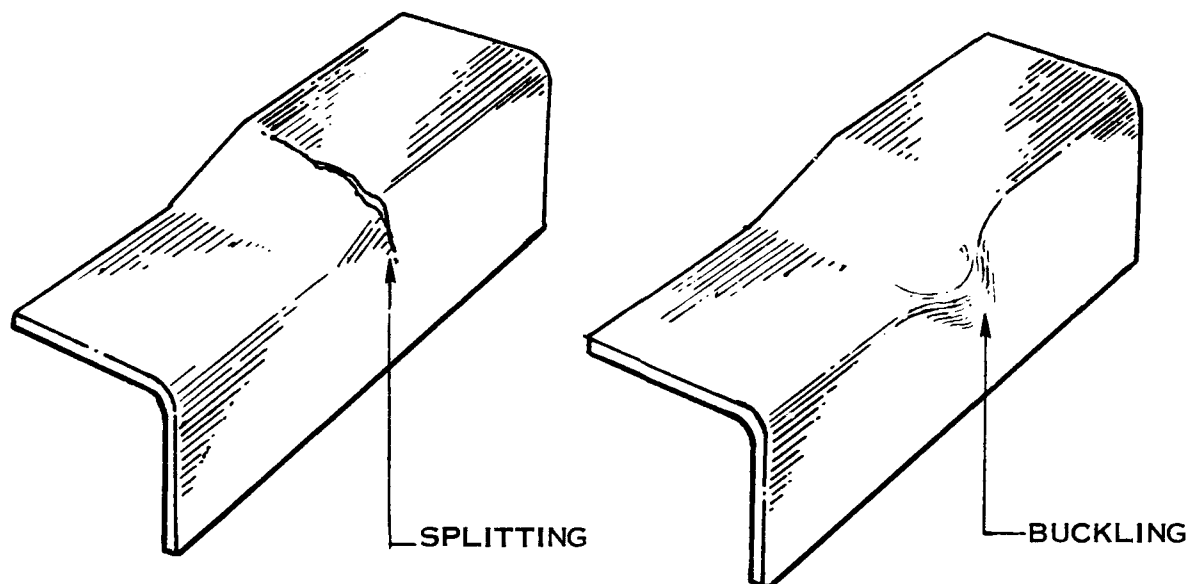


FIGURE I-16 MAJOR JOGGLING FAILURES

The joggle curve, shown in Figure I-17, is defined by good parts inside the curve and buckled or split parts outside the curve. The curve shows that splitting occurs for high values of D/L and shear buckling for high values of D/t .

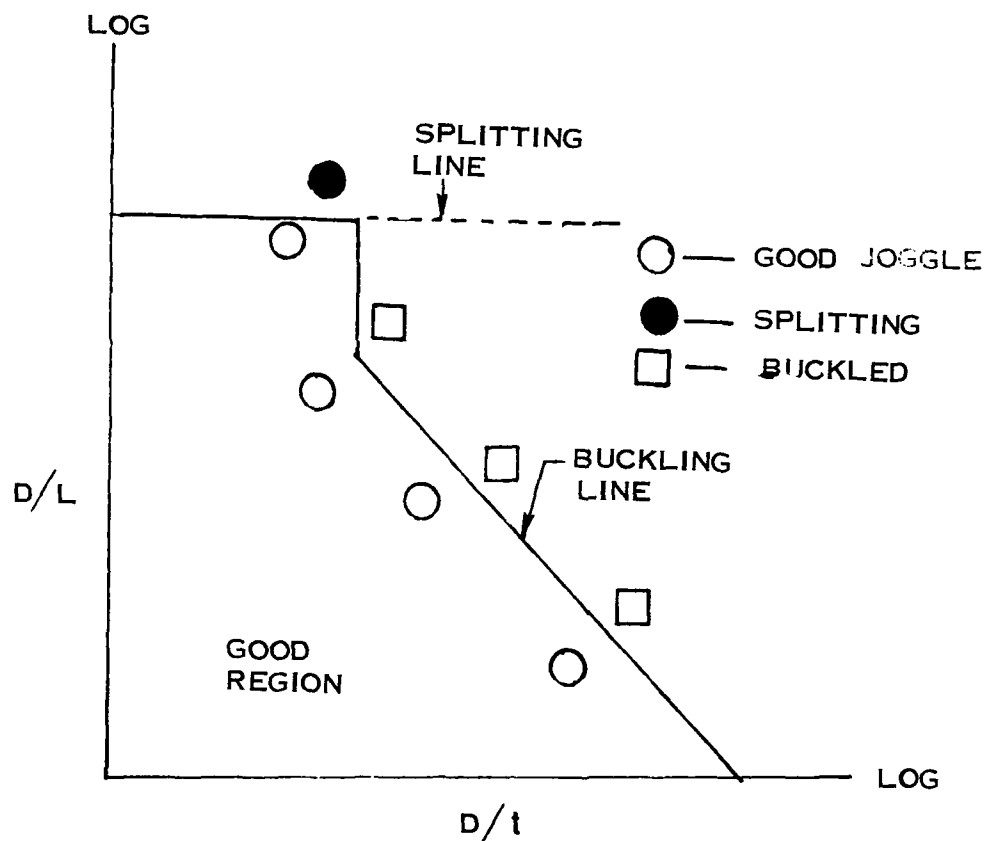


FIGURE I-17 JOGGLING LIMIT CURVE

The applied stress and the strain diagram of a joggle sample is illustrated in Figure I-18. The strain diagram shows $\bar{\epsilon}_L = \bar{\epsilon}_t$ and $\bar{\epsilon}_w = 0$; therefore, $\bar{\epsilon}_L / \bar{\epsilon}_w = \infty$. The value for $\bar{\epsilon}_L / \bar{\epsilon}_e = 0.866$

determined by the Energy of Distortion Theory and allows the process to be plotted on the "Effective Strain" Ellipse in Figure I-133 for correlation to the standard tensile specimen.

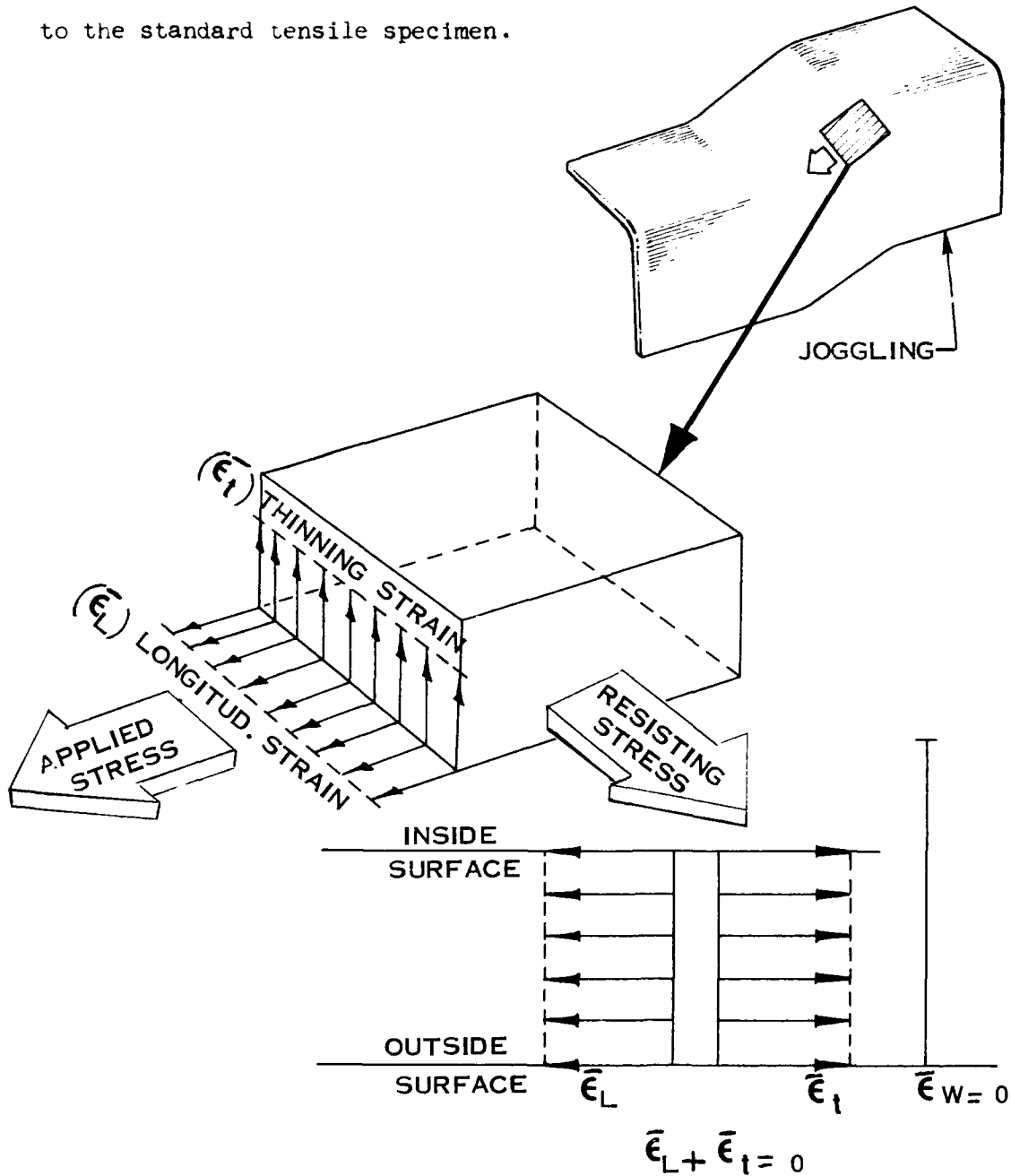


FIGURE I-18 APPLIED STRESS AND STRAIN DIAGRAMS FOR JOGGLING

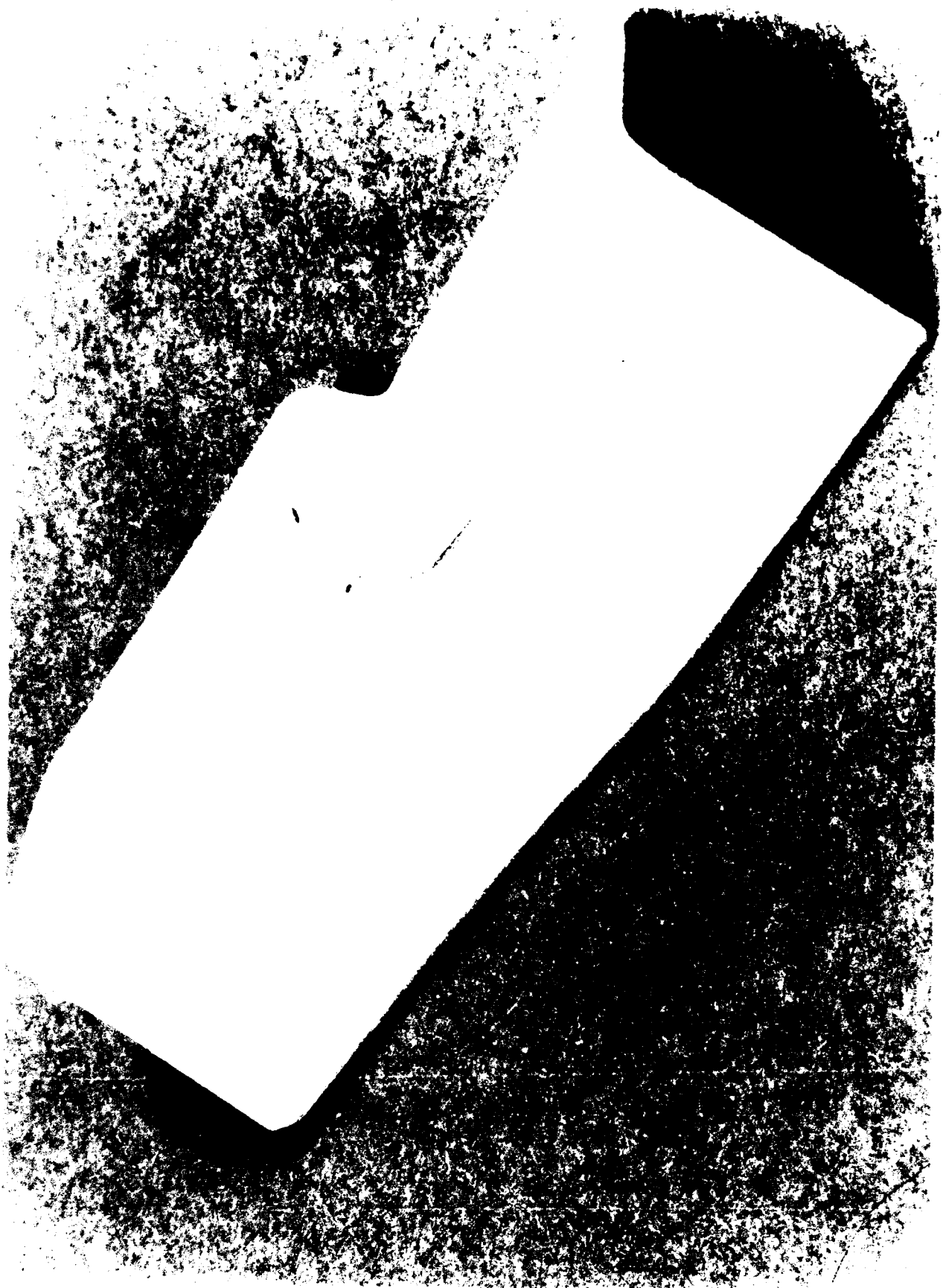


FIGURE I-19 SHEAR BUCKLING AND SPLITTING FAILURES FOR JOGGLING

DIMPLING

Dimpling is a process of forming a recessed area for a fastener in order that the fastener head can be made flush with the sheet surface. A 5,000 pound CP450EA Zephyr Triple Action Coin Ram dimpling machine, as shown in Figure I-20, was used to form all parts. Induction type heaters were used to accomplish elevated temperature forming with materials displaying failures and/or poor definition at room temperature.

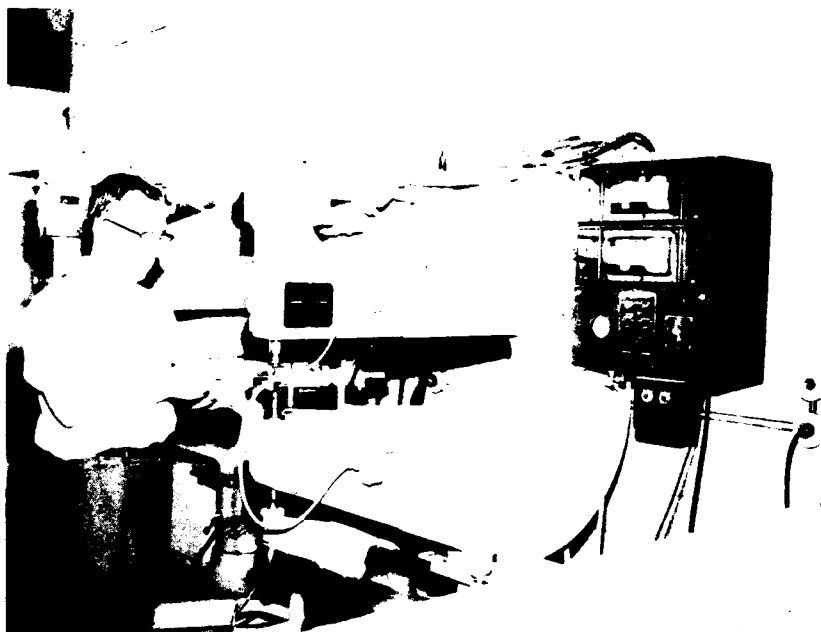


FIGURE I-20 CP450EA ZEPHYR TRIPLE ACTION COIN
RAM DIMPLING MACHINE

The parameters for dimpling are h/R vs. α for radial failures and t vs. α for circumferential failures as shown in Figure I-21.

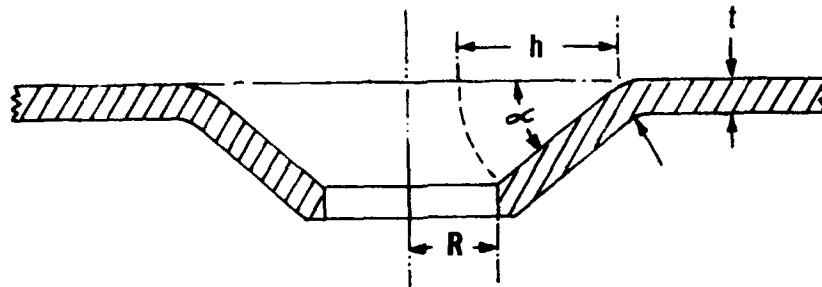


FIGURE I-21 DIMPLING PARAMETERS

One standard dimple angle ($\alpha = 40^\circ$) is generally used in aircraft, but special dies for $\alpha = 30^\circ$ and $\alpha = 50^\circ$ were made to enable full coverage of the dimpling spectrum. Figure I-22 displays the dies graphically to show the wide range of dimple angles (α) and flange heights (h/R) used in this program.

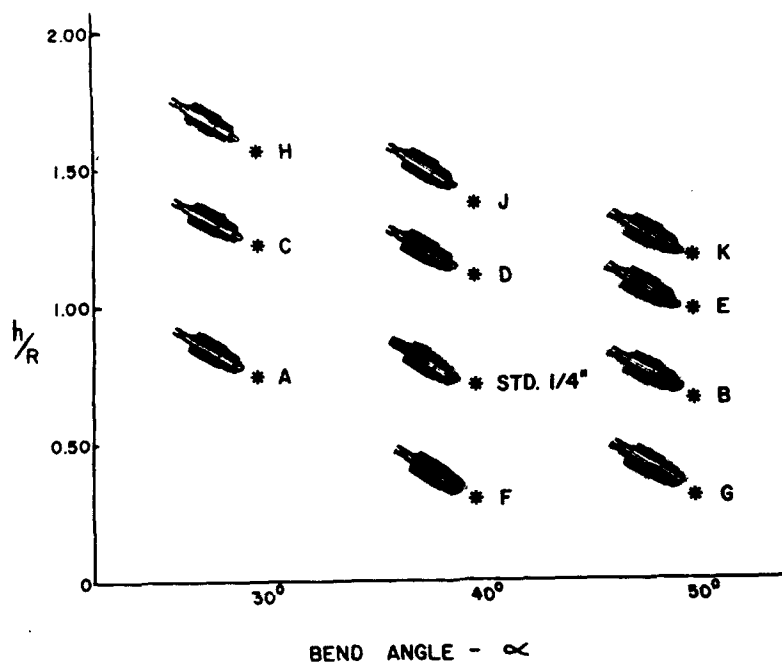


FIGURE I-22 DIMPLING DIES

Figure I-23 is a close-up view of a triple action coin ram die shown in Figure I-22.



FIGURE I-23 TRIPLE ACTION COIN RAM DIMPLING DIE

All materials having improved properties in the heat treated condition were dimpled in this condition to simulate actual part fabrication. Production parts are almost never dimpled in the annealed condition because subsequent heat treatment would cause a misalignment of holes.

The major limitations in dimpling were machine pressure and die temperature. Many of the high strength alloys displayed poor definition at room temperature due to insufficient pressure and were dimpled at elevated temperature.

The elevated temperature dimpling also displayed poor definition for some materials because the induction heated dies did not develop sufficient temperature. However, resistance heated dies are being made available by vendors to accommodate the new alloys.

Dimpling blanks usually contain a series of pilot holes to be dimpled in rapid succession. However, the sketches in Figures I-24 and I-25 show a one hole segment for illustration. Figure I-24 illustrates the preparatory pilot hole and resulting good dimple.

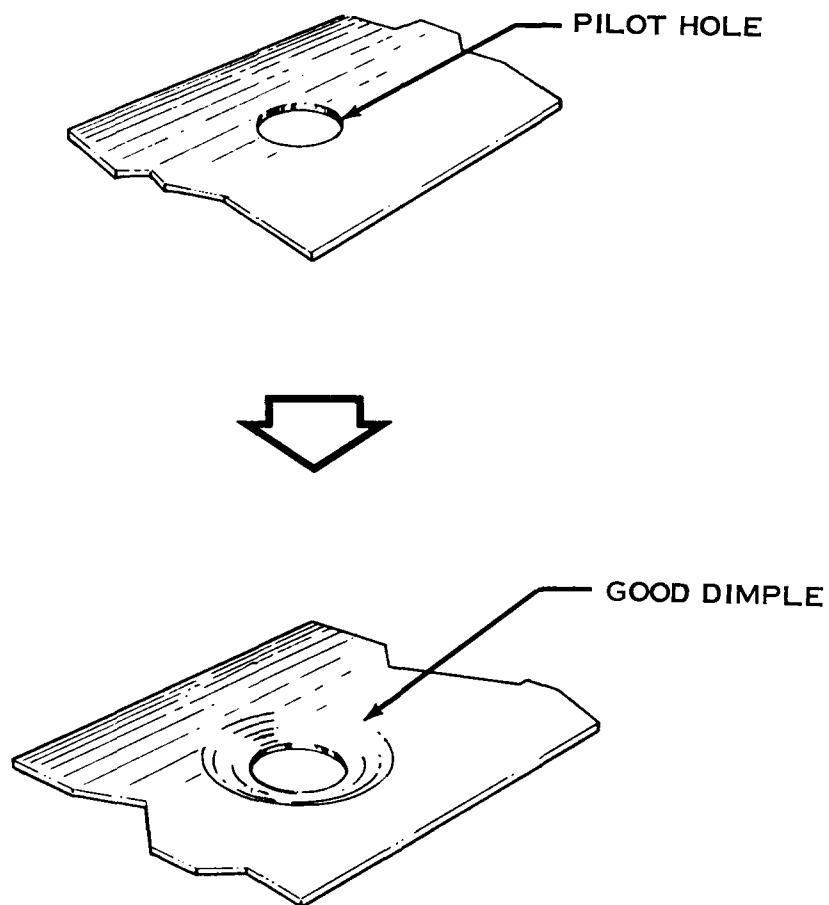
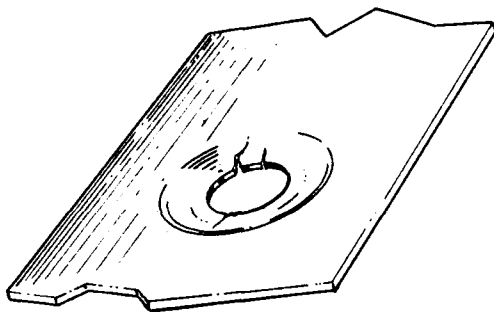
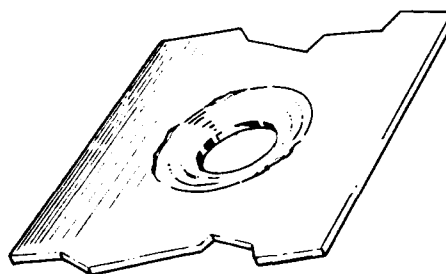


FIGURE I-24 DIMPLING PROCEDURE

The two major failures in dimpling are circumferential and radial splitting as shown in Figure I-25.



RADIAL CRACKS



CIRCUMFERENTIAL CRACKS

FIGURE I-25 MAJOR FAILURES IN DIMPLING

Minor distortions resulting from the dimpling process are web buckling and edge extrusion. These distortions are not applicable for this contract since a triple-action coin dimpler was used to eliminate both effects.

Circumferential failure is the result of bending which is strongly affected by the coining action and material thickness. The sketches and t vs. α curve in Figure I-26 show that thin gage materials will conform to the small radius (r) and fail if r/t is less than that necessary for brake forming the same material. However, the die pressure and coining force is insufficient to cause thick material gages to conform to the small radius (r) so that larger free-form radii result in increased formability.

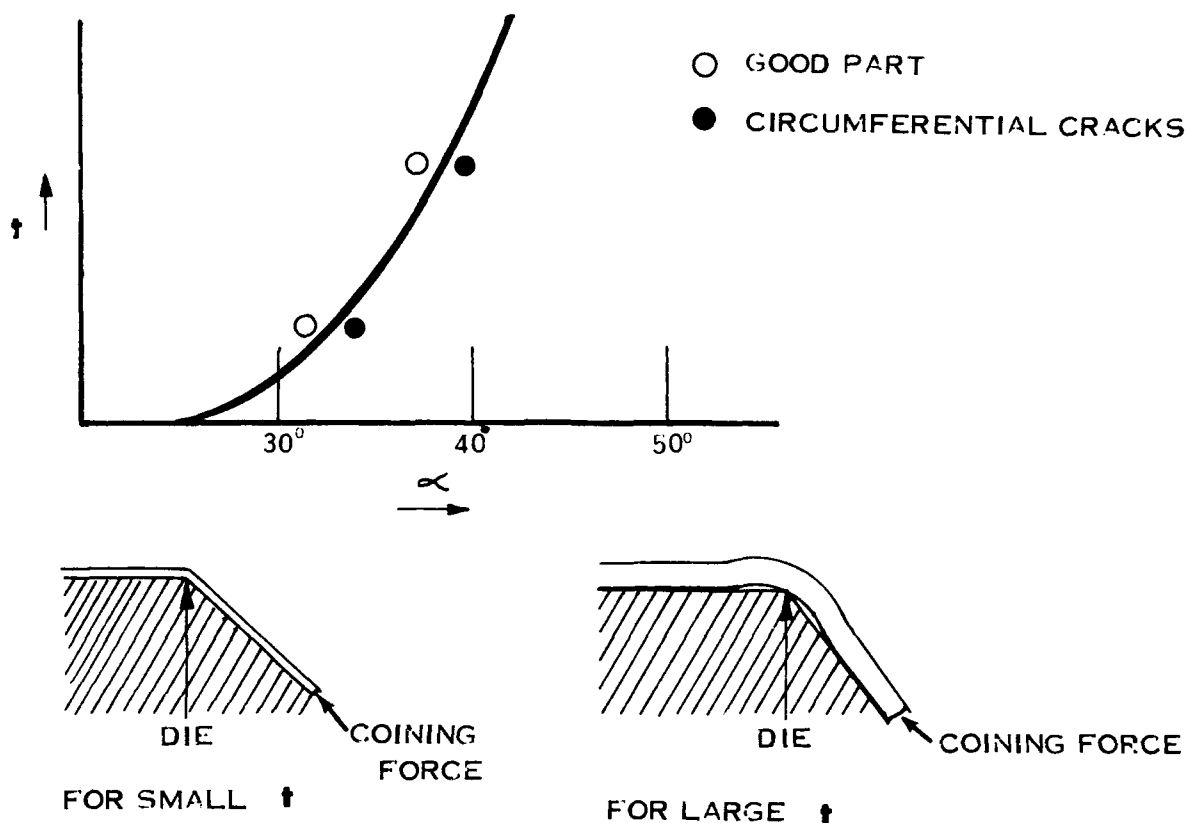


FIGURE I-26 LIMIT CURVE FOR CIRCUMFERENTIAL FAILURES

Radial failures occur when the available elongation in the outer fiber of the stretch flange is exceeded. The curve in Figure I-27 is defined by good parts below the curve and radially failed parts above the curve. The curve shows high h/R flange heights can be formed for small angles and that large angles require reduced h/R values. Thin gage material fails more readily than thick gage material since the forging action causes thinning and the thicker gage can supply more elongation than a thin gage material.

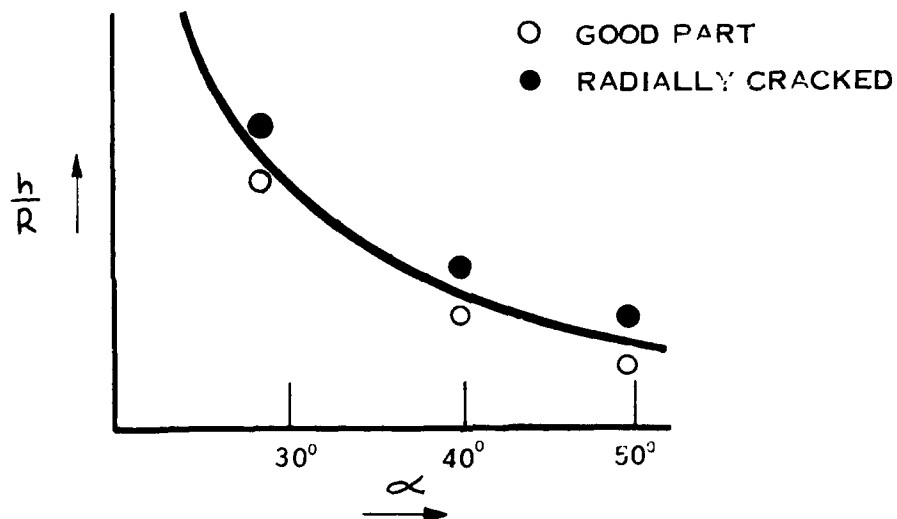


FIGURE I-27 LIMIT CURVE FOR RADIAL FAILURES

The applied stress and the strain diagram of a dimple specimen is shown in Figure I-28. The strain diagram shows that $\epsilon_L + \epsilon_f + \epsilon_w = 0$. The value for $\bar{\epsilon}_L / \bar{\epsilon}_e \approx 1$ was determined by the Energy of Distortion Theory using empirical data and allows the dimpling process to be plotted on the "Effective Strain" Ellipse in Figure I-133 for correlation to the standard tensile specimen.

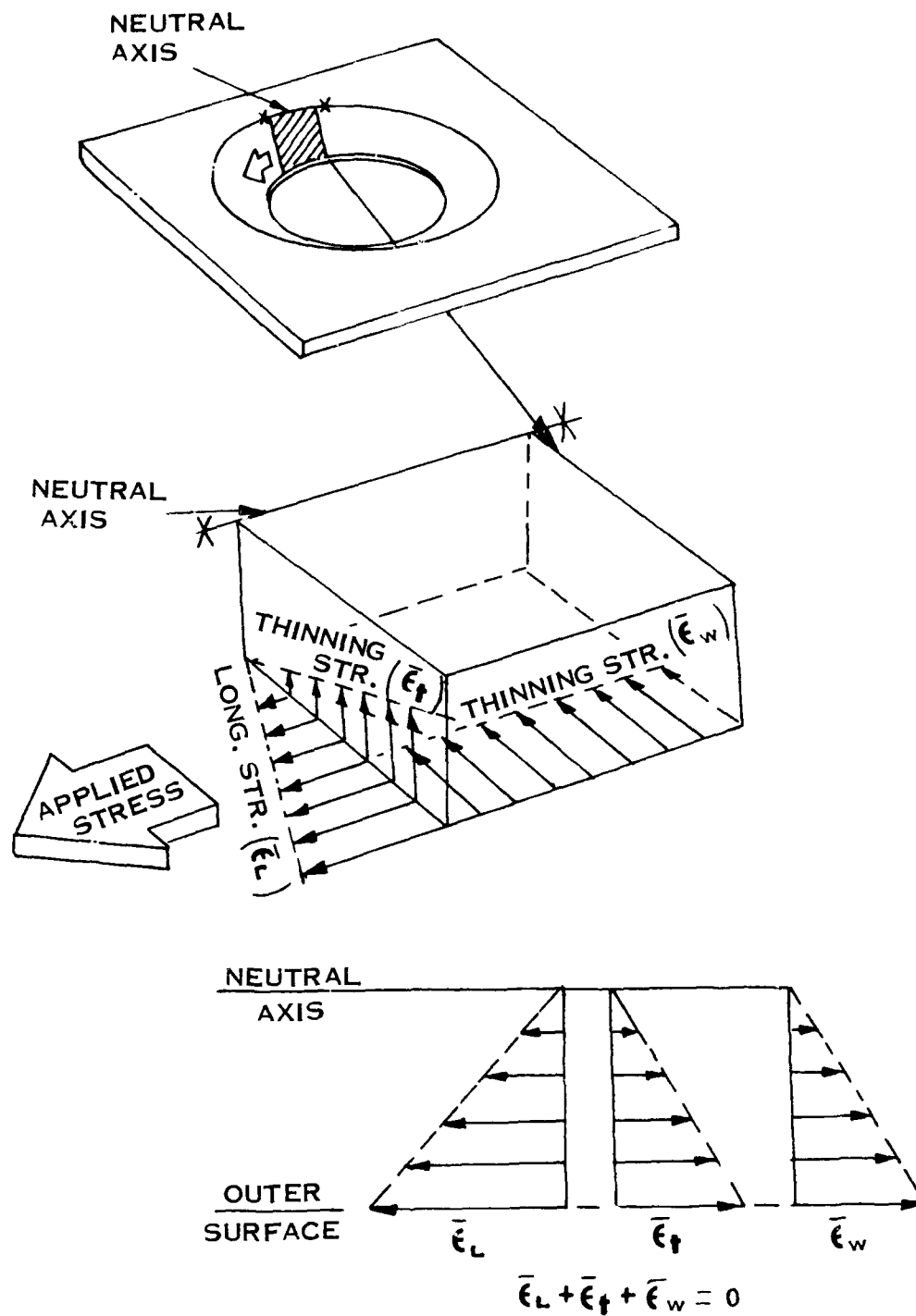


FIGURE I-28 APPLIED STRESS AND STRAIN DIAGRAM FOR DIMPLING

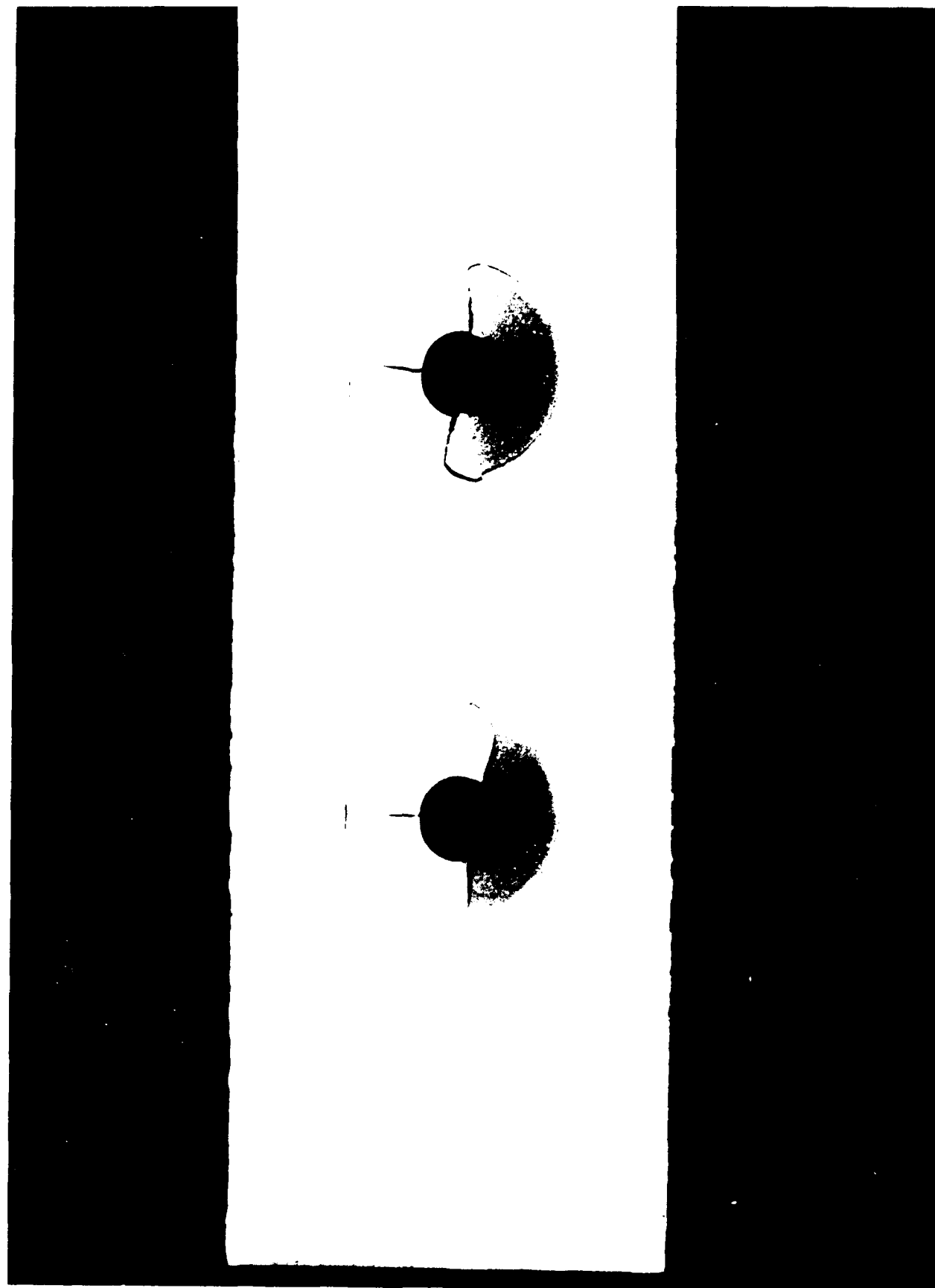


FIGURE I-29 CIRCUMFERENTIAL AND RADIAL SPLITTING FAILURES FOR DIMPLING

RUBBER STRETCH AND SHRINK FLANGING

The forming of stretch and shrink flanges on the rubber press (the Guerin Process) is one of the major methods of producing contoured flanges for aircraft parts. A 5,000 ton Lake Erie rubber press, shown in Figure I-30, was used to form both stretch and shrink flanges on this program.

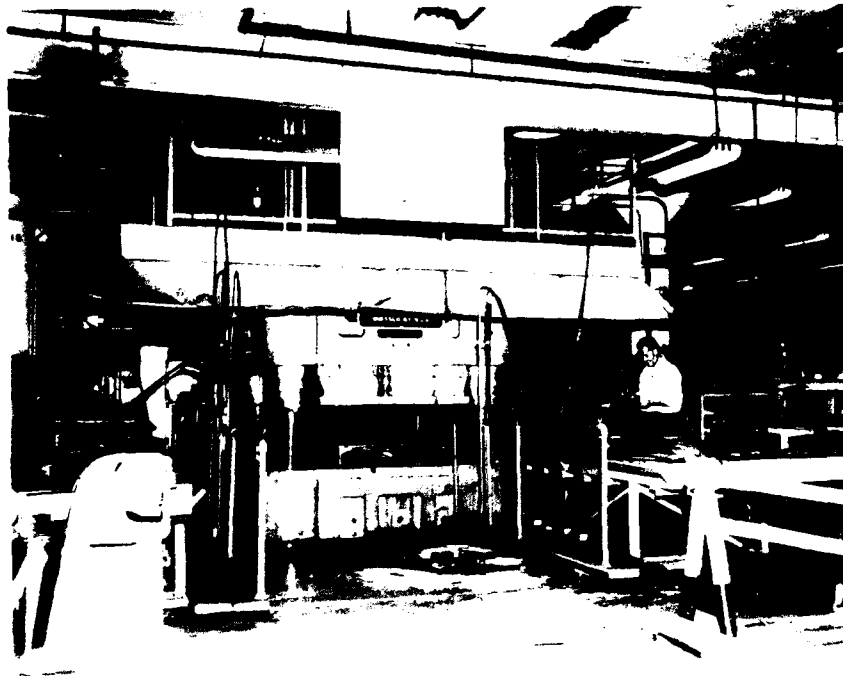


FIGURE I-30 5,000 TON LAKE ERIE RUBBER PRESS

Stretch and shrink flange dies, as illustrated in Figure I-31(a), for determining buckling limits were used to form parts ranging in radius from 10 inches to 160 inches with a 4 inch maximum flange height. The circular die illustrated in Figure I-31(b) was used to provide a 4 inch radius for stretch flange splitting and a 6 inch radius for increased shrink flange range. The photograph of tooling is shown in Figure I-32.

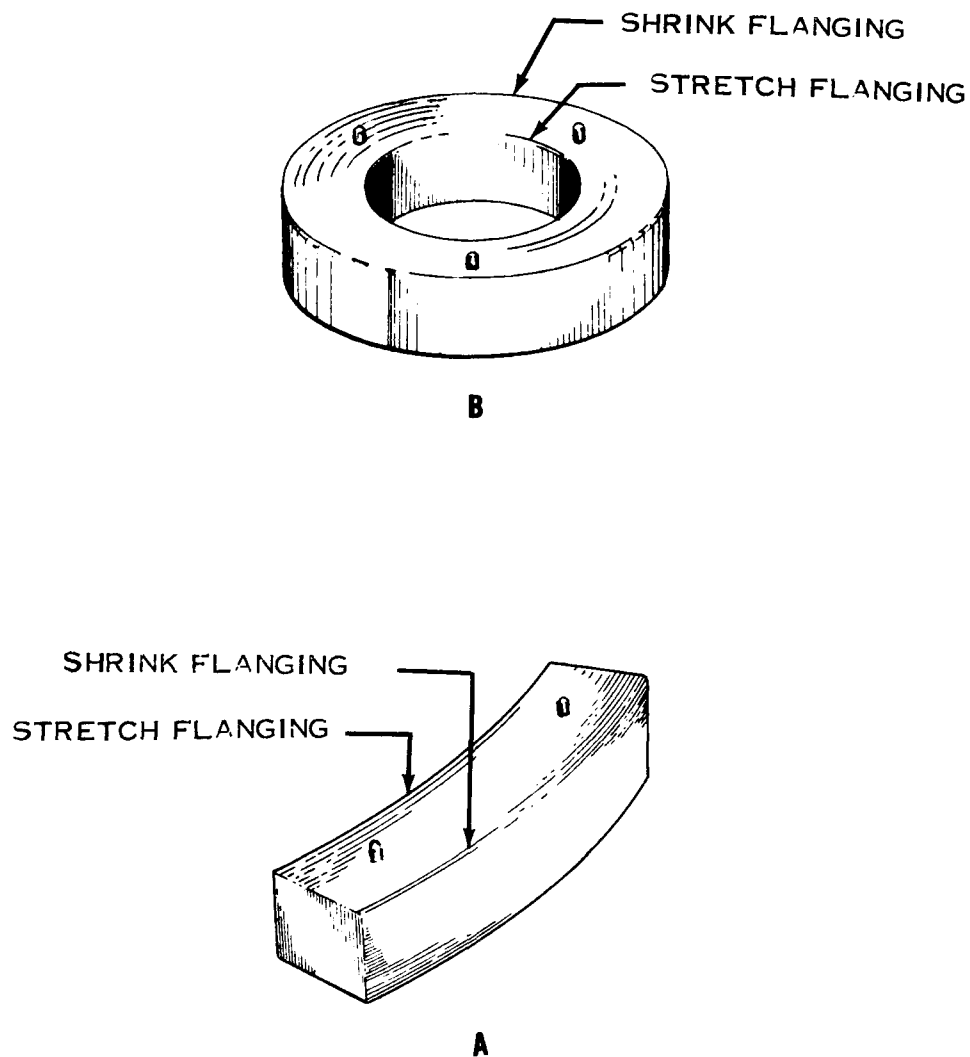


FIGURE I-31 RUBBER FLANGING DIES



FIGURE I-32 TOOLING FOR
RUBBER FORMED FLANGES

The blanks for producing rubber formed stretch and shrink flanges are generally fabricated by either sawing or blanking with a subsequent deburring operation. Figure I-33 illustrates the stretch and shrink flange blanks and resulting good parts.

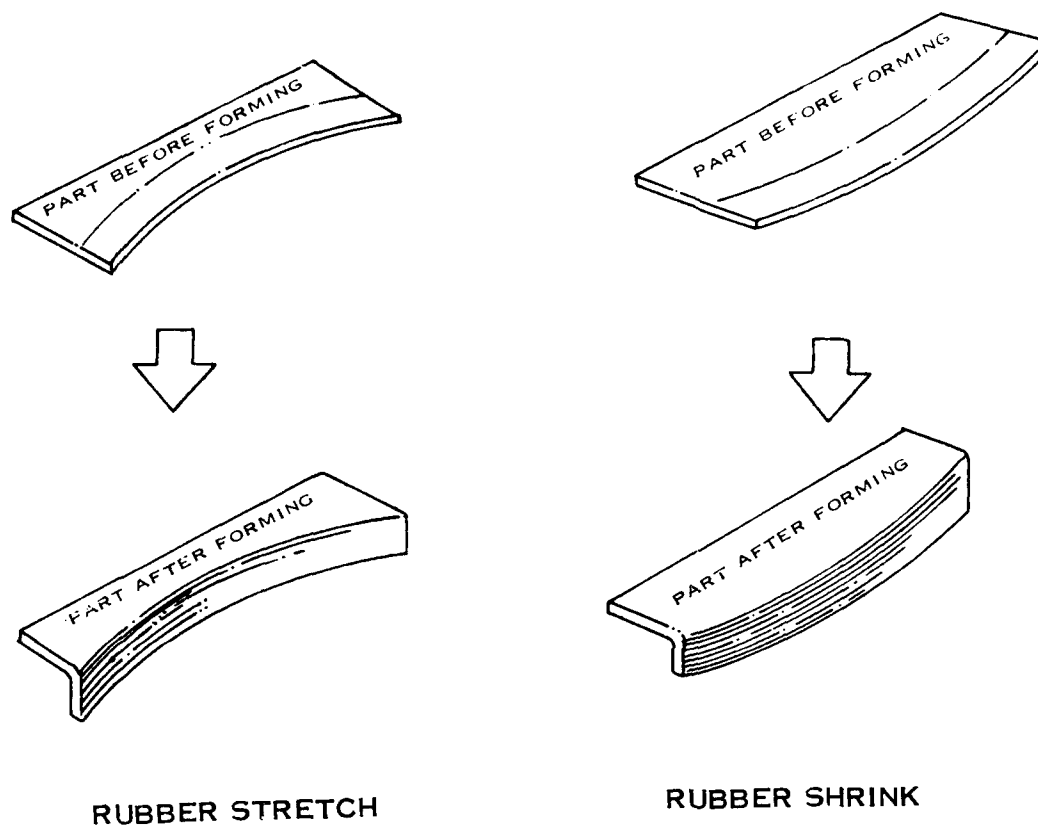


FIGURE I-33 RUBBER FORMED STRETCH AND SHRINK FLANGE BLANKS AND RESULTING GOOD PARTS

The parameters for rubber formed stretch and shrink flanges are flange height (h), contour radius (R) and material thickness (t) as shown in the sketches in Figure I-34.

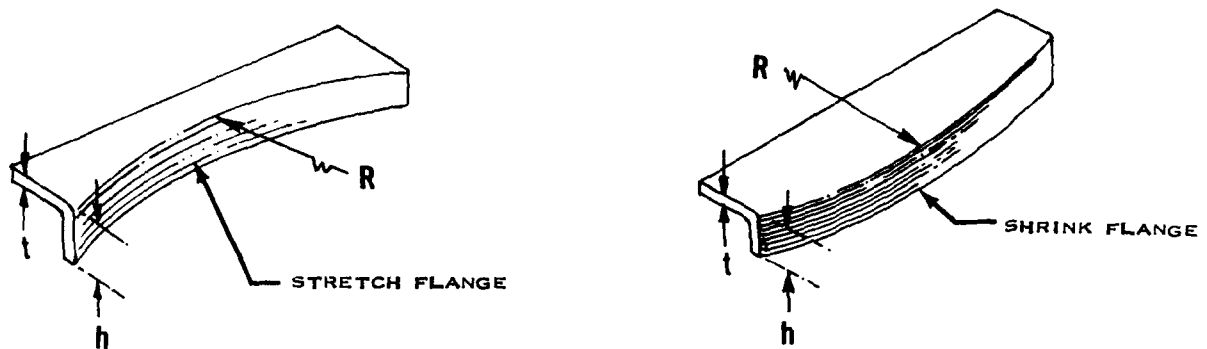


FIGURE 1-34 PARAMETERS FOR RUBBER FLANGING

Major failures for rubber formed stretch flanges are elastic sine wave buckling, splitting and insufficient pressure.

Sine wave buckling, shown in Figure I-35, occurs when the forming pressure is removed from the part due to residual stresses remaining in the flange. These buckles can generally be pressed out by subsequent hot finish forming if buckling is not too severe.

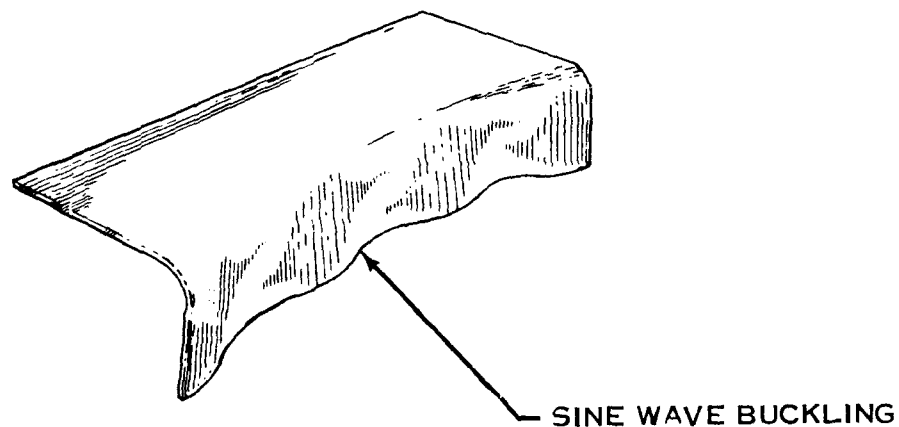


FIGURE I-35 SINE WAVE BUCKLING OF RUBBER FORMED STRETCH FLANGE

Flange splitting, shown in Figure I-36, is dependent on the available elongation for a given material and eliminated only by decreasing the h/R value to formable limits.

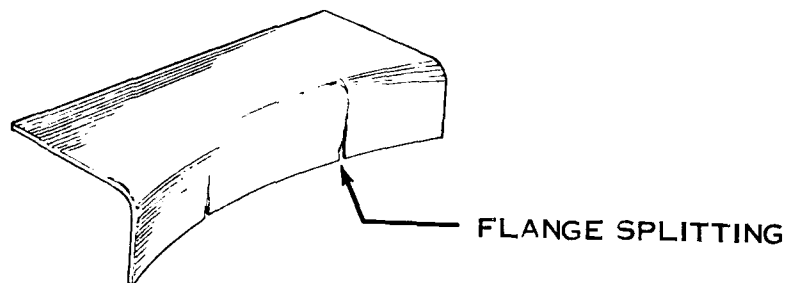


FIGURE I-36 FLANGE SPLITTING OF RUBBER FORMED STRETCH FLANGE

Insufficient pressure results in a part that is not completely pressed against the die. This failure is shown in a cross-sectional view of the flange and die in Figure I-37. Insufficient pressure failures result for low values of h/t and can be eliminated only by increasing the h/t value or the forming pressure.

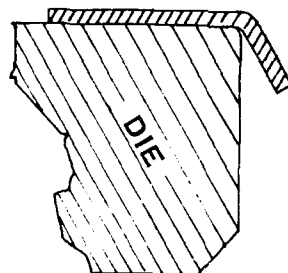


FIGURE I-37 INSUFFICIENT PRESSURE FAILURE

The major failure in rubber formed shrink flanges is the formation of wrinkles, as illustrated in Figure I-38. These wrinkles form for large h/t and small h/R values or small h/t and large h/R values.

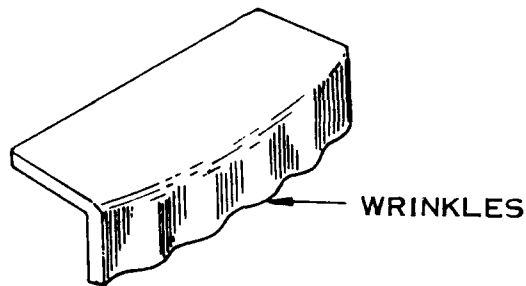


FIGURE I-38 WRINKLING IN RUBBER FORMED SHRINK FLANGE

The wrinkles first form as normal plate buckling sine waves from compressive hoop stresses and are pressed into wrinkles with continued forming as shown in Figure I-39.

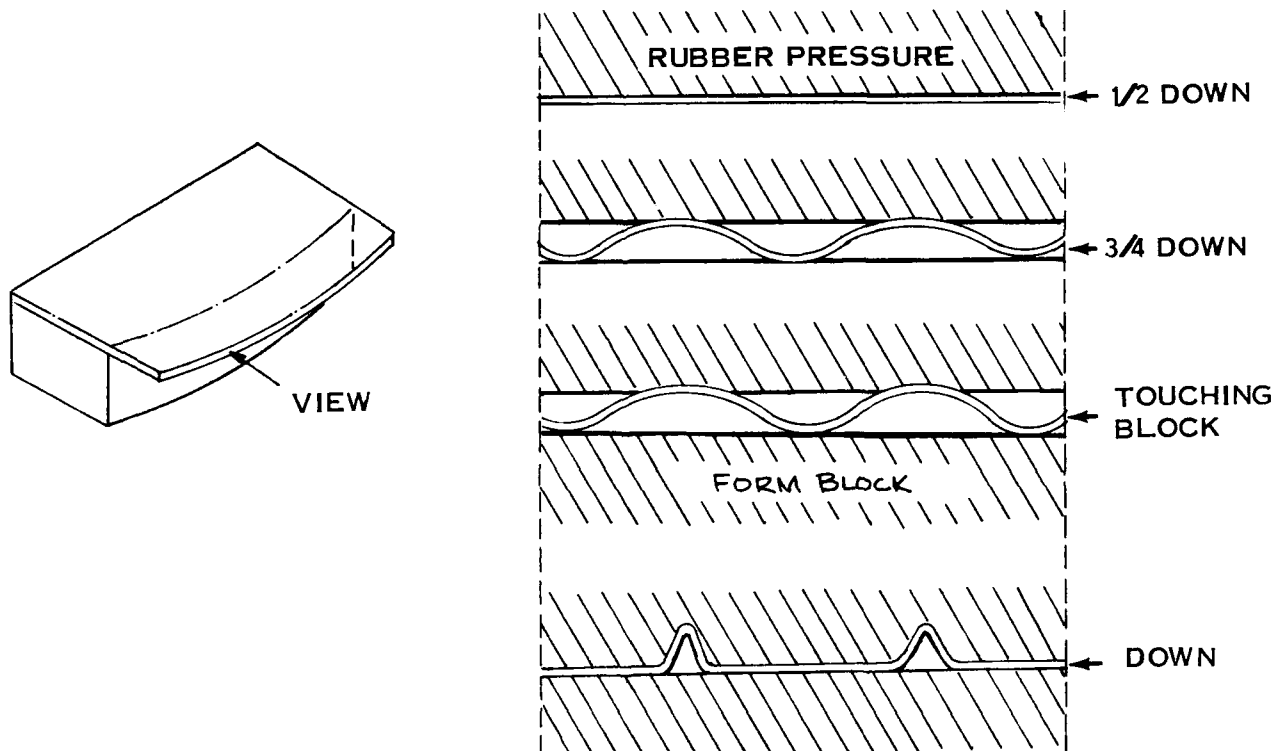


FIGURE I-39 FORMATION OF WRINKLES IN RUBBER FORMED SHRINK FLANGE

The minor distortions for rubber formed stretch and shrink flanges are hump, springback, crown and shear buckling, as shown in Figure I-40. These minor distortions are common for stretch and shrink flanges, however, it should be noted that the shear buckling and crown for stretch flanges are in opposite directions from the shrink flanges.

A hump in the bend area occurs when there is insufficient pressure to force the part to the die and is common for parts with large h/R and small h/t values. This distortion can be minimized by using higher forming pressures and smaller material thicknesses.

Springback and crown occur on all formed parts and depend on the material and the shape of the part. They can be eliminated by hot finish forming, allowance for springback and crown on the forming tool or hand working.

Shear buckling is an end condition that occurs at high h/R values for materials with a low E/S_{TY} value, where E is the modulus of elasticity and S_{TY} is the tensile yield strength. Control of this distortion can be made only by allowing excessive material so that ends can be trimmed.

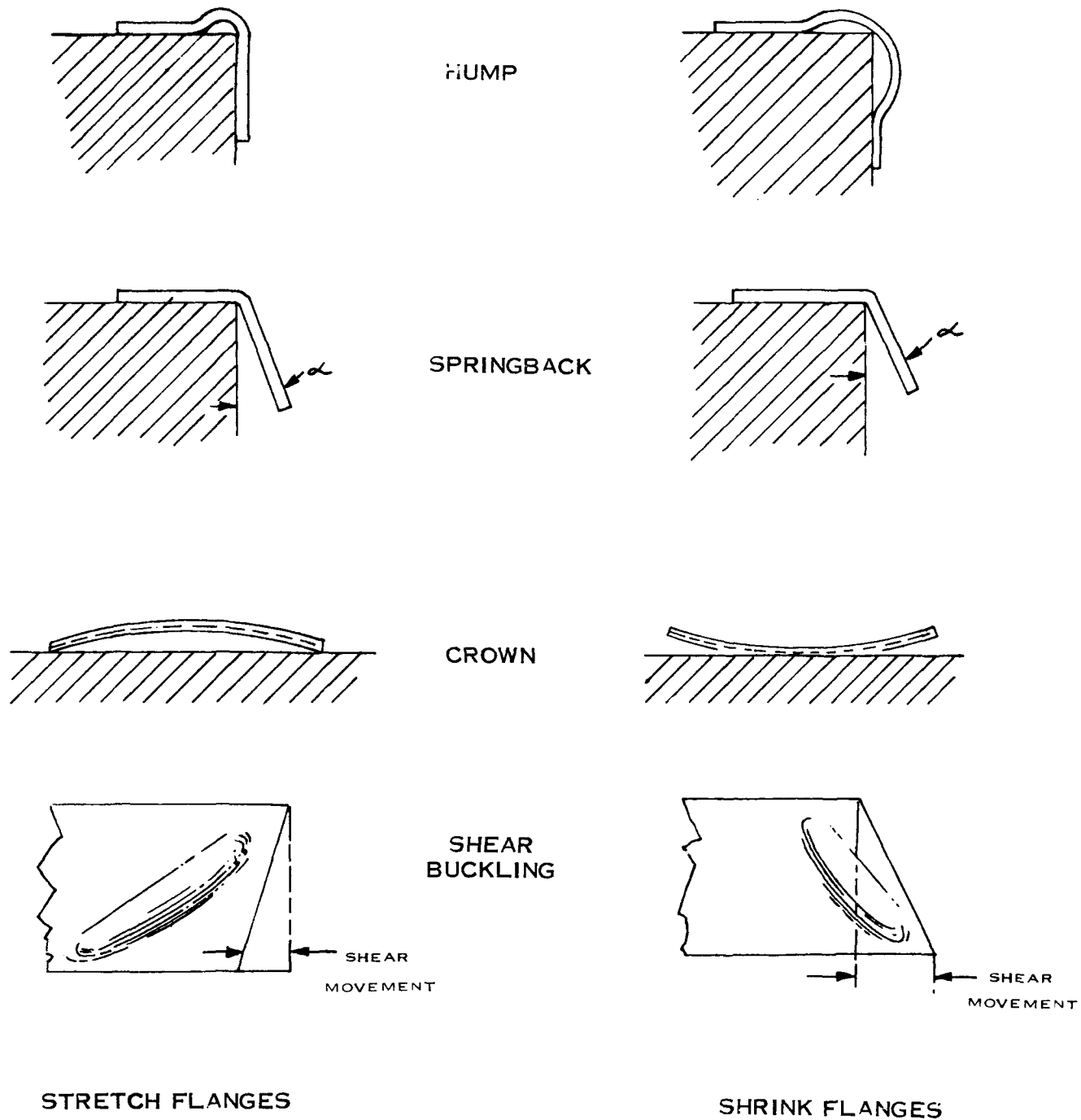


FIGURE I-40 MINOR FAILURES FOR RUBBER FORMED STRETCH AND SHRINK FLANGES

Rubber formed stretch flange curves, illustrated in Figure I-41, are defined by good parts under the curve and failed parts over the curve. Buckling occurs for large h/t values and splitting occurs for high h/R values.

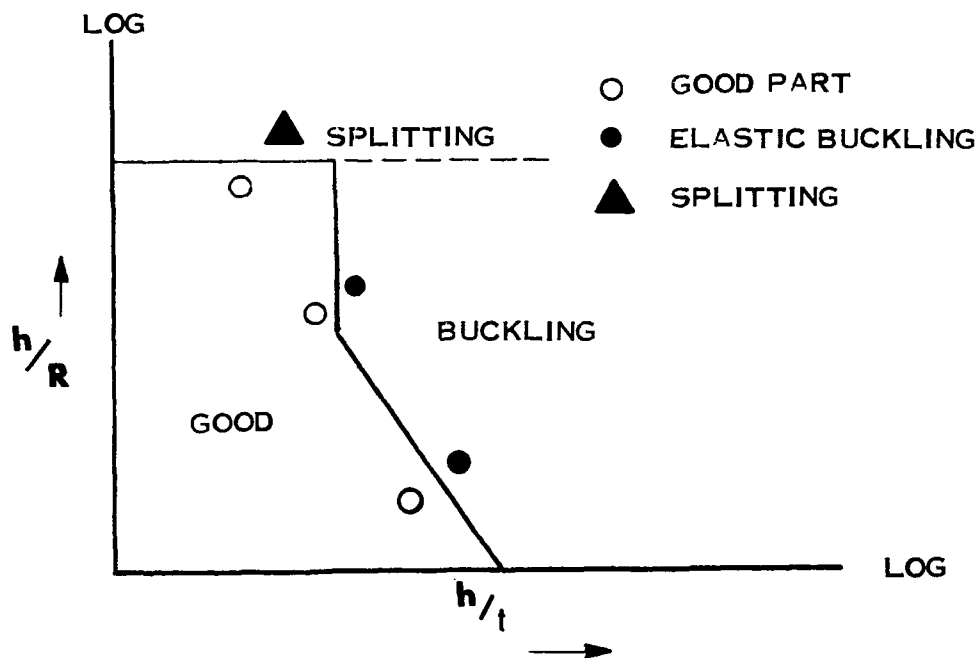


FIGURE I-41 RUBBER FORMED STRETCH FLANGE CURVE

Rubber formed shrink flange curves, illustrated in Figure I-42, are defined by good parts under the curve and failed parts over the curve. Elastic buckling occurs for large h/t and small h/R values while plastic buckling occurs for small h/t and large h/R values.

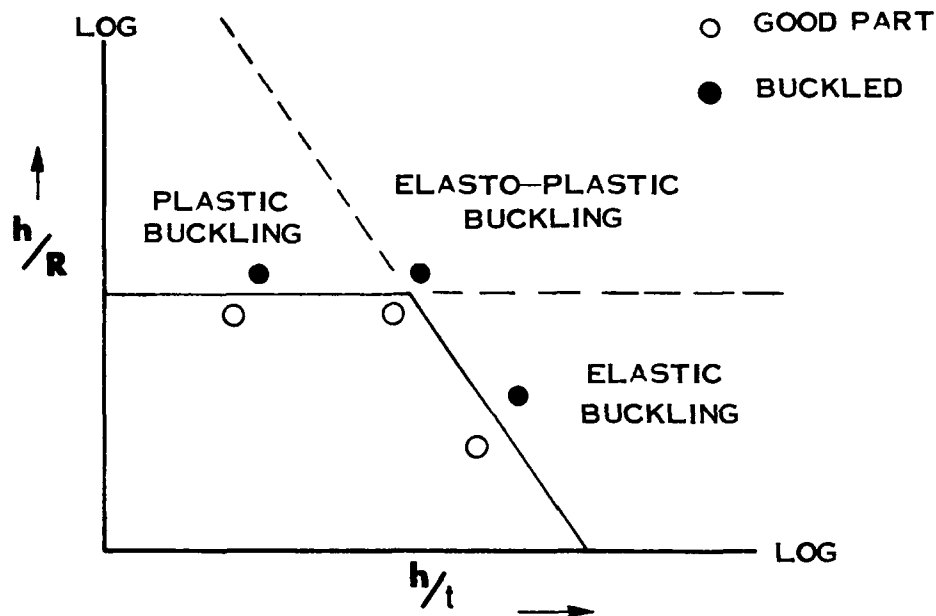


FIGURE I-42 RUBBER FORMED SHRINK FLANGE CURVE

The applied stress and the strain diagram for a rubber formed stretch flange is shown in Figure I-133. The strain diagram shows $\bar{\epsilon}_L + \bar{\epsilon}_T + \bar{\epsilon}_W = 0$. The value for $\bar{\epsilon}_L / \bar{\epsilon}_e = 0.99$ was determined by the Energy of Distortion Theory using empirical data and allows the rubber stretch flanging process to be plotted on the "Effective Strain" Ellipse in Figure I-133 for correlation to the standard tensile specimen.

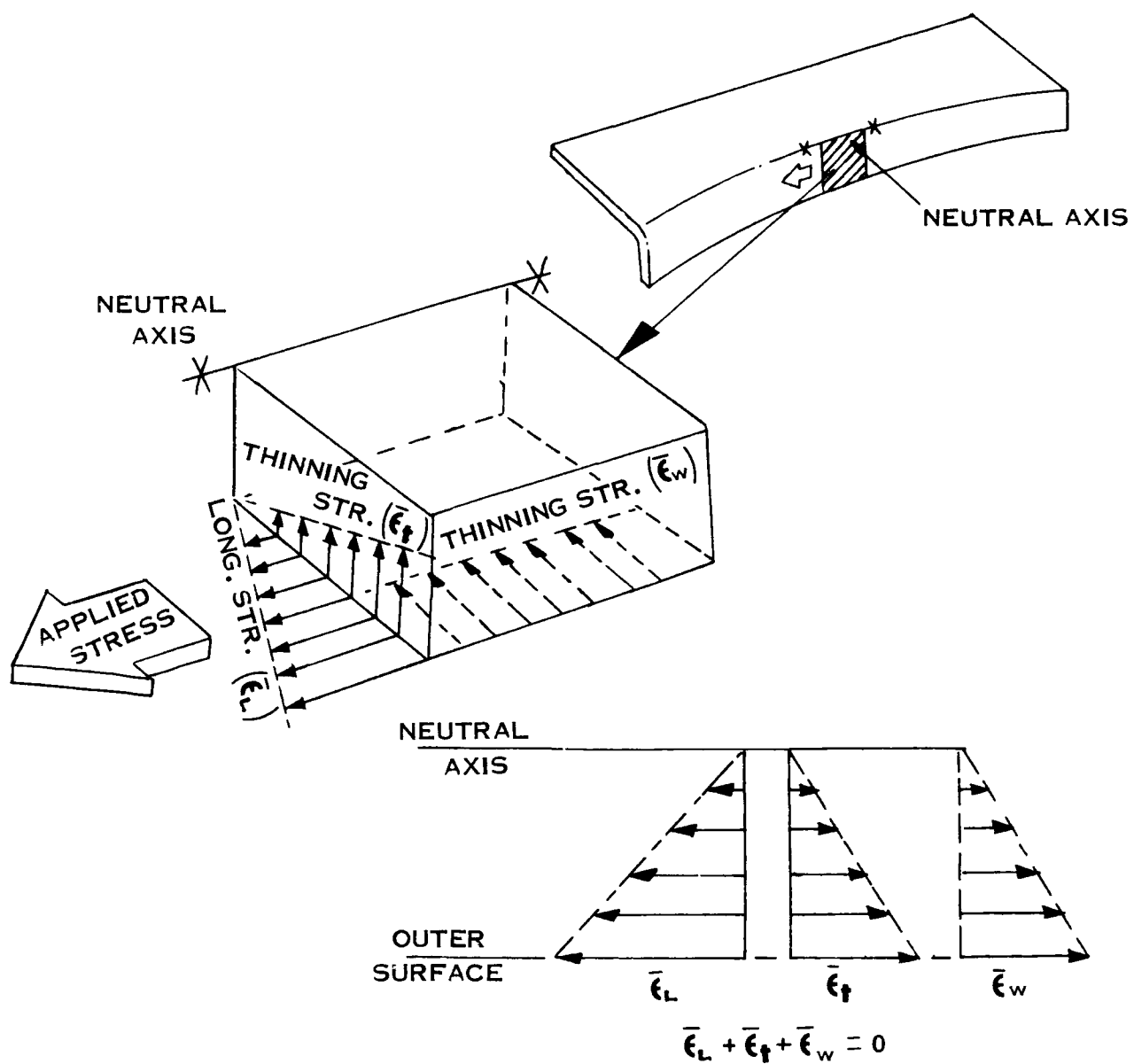


FIGURE I-43 APPLIED STRESS AND STRAIN DIAGRAM FOR RUBBER FORMED STRETCH FLANGING



FIGURE 1 44 PROGRESSIVE SINE WAVE BUCKLING FOR RUBBER FORMED STRETCH FLANGES

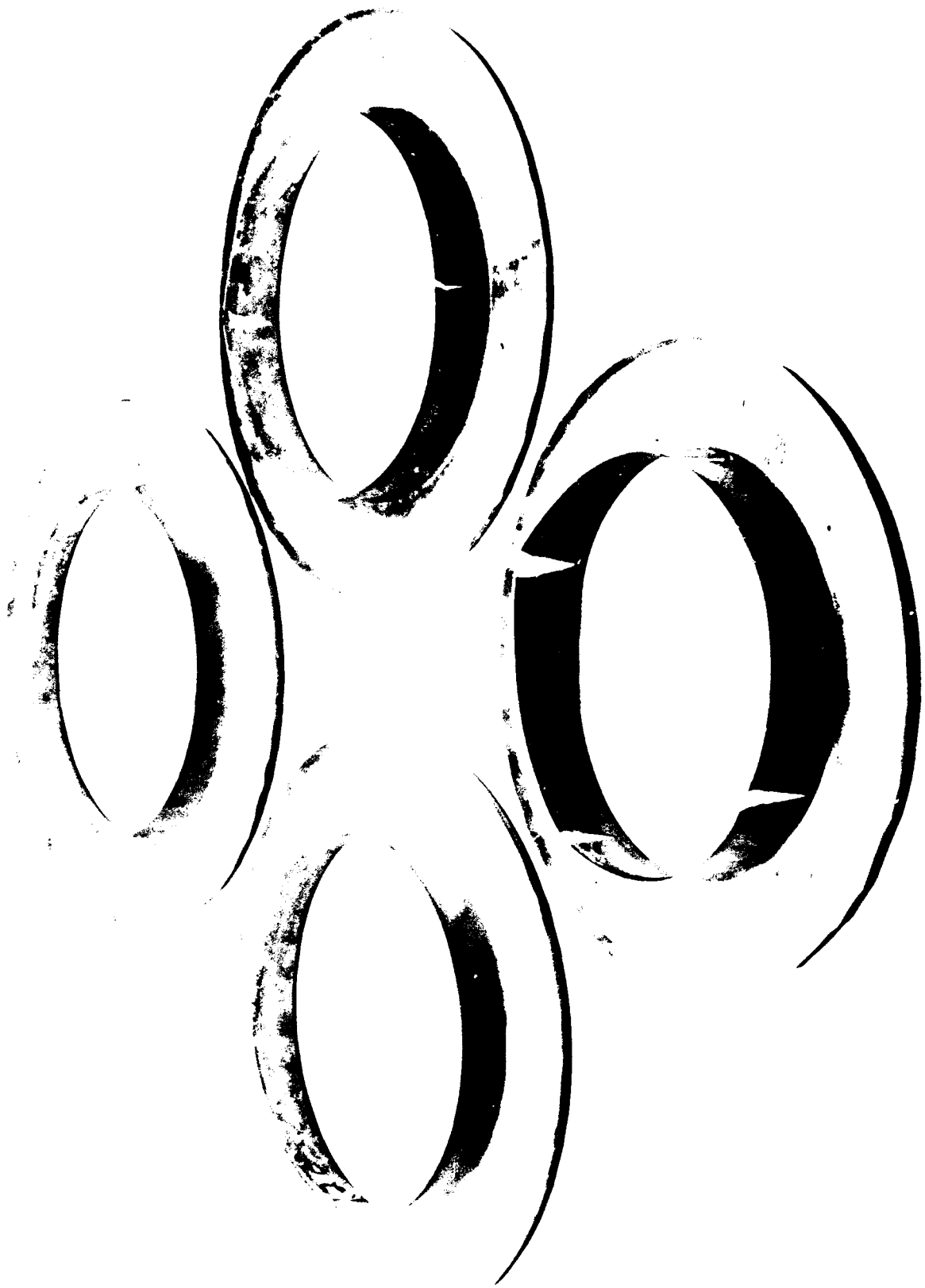


FIGURE I-44(A) SPLITTING FOR RUBBER FORMED STRETCH FLANGES



FIGURE 1 41 B PLASTIC BUCKLING FOR RUBBER FORMED SHRINK FLANGES

LINEAR STRETCH FORMING

The principle method of forming contoured angle, channel and hat sections is by stretching on the linear stretch press. The 17½ ton, A-10 Hufford Stretch Press, shown in Figure I-45, was used to form heel-in and heel-out angle and channel sections and heel-in hat sections for this program.

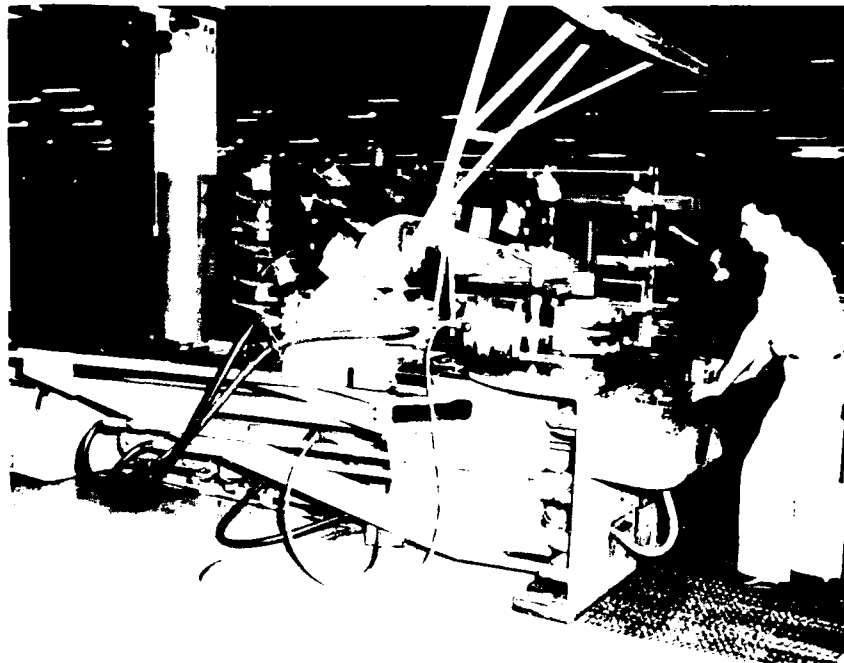


FIGURE I-45 17 1/2 TON, A-10 HUFFORD STRETCH PRESS

The linear stretch dies, shown in Figure I-46, provided a wide range of contour radii for sections which were formed with contour radii ranging 1" to 80" for angle and channel sections and 3" to 80" for hat sections.



FIGURE I-46 TOOLING FOR LINEAR STRETCH FORMING

The parameters in linear stretch forming are flange height (h), contour radius (R) and material thickness (t) as illustrated by the heel-in angle section in Figure I-47.

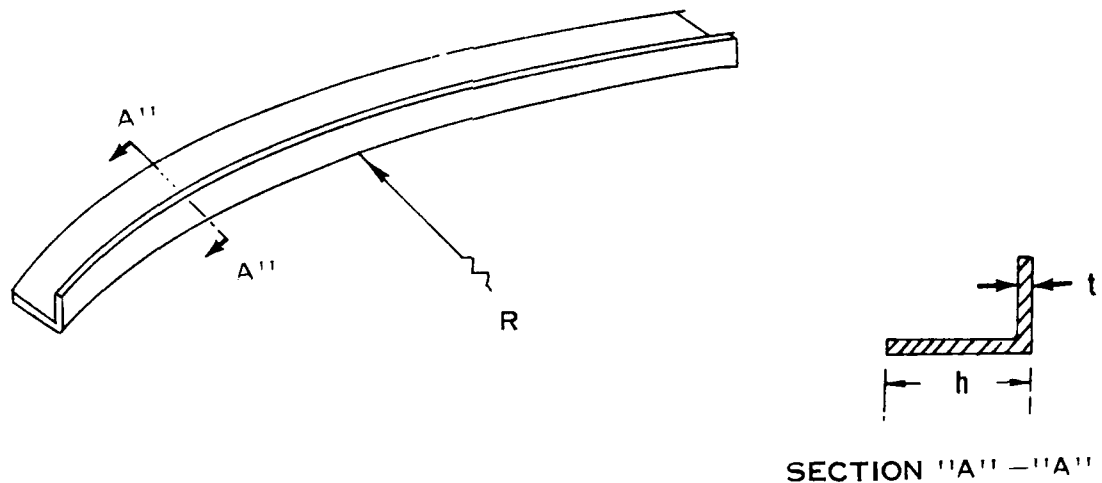


FIGURE I-47 PARAMETERS FOR LINEAR STRETCH FORMING

The photographs in Figures I-48, I-49 and I-50 show the progressive steps in linear stretch forming. Figure I-48 shows a heel-out angle section being stretched to yield before wrapping. Stretching to yield before wrapping enables the neutral axis of the heel-out angle section to shift to the inner fiber of the flange as further wrapping is accomplished in Figure I-49.



FIGURE 1-48 HEEL-OUT SECTIONS-STRETCHED TO YIELD BEFORE WRAPPING

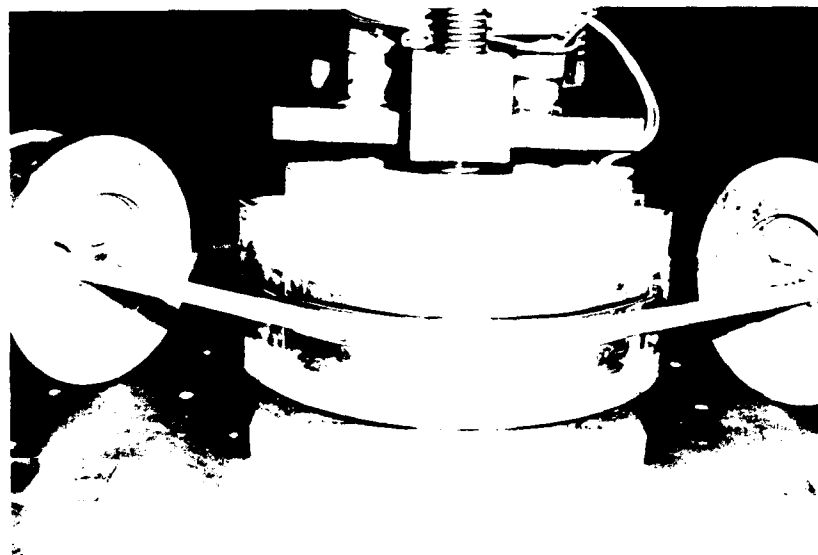


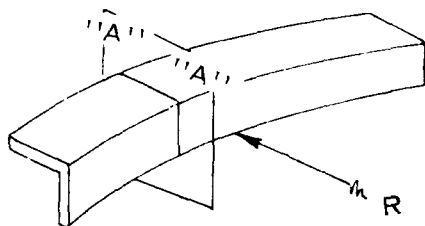
FIGURE 1-49 HEEL-OUT SECTIONS-IN PROCESS OF WRAPPING

Figure I-50 shows the heel-out angle section completely wrapped. The part is given a final setting operation by increasing the tension to reduce springback and assure part to die fit.



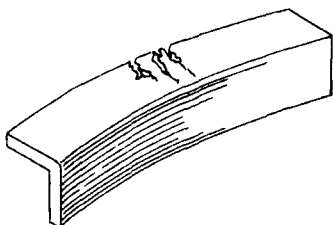
FIGURE I-50 HEEL-OUT SECTIONS — COMPLETELY WRAPPED

The major failures in linear stretch forming are splitting, plate buckling and twist buckling while the minor distortions involved are "walking", transverse buckling and wrinkling. Since five part configurations are involved in the failure analysis, failures for each configuration will be presented separately in pictorial form in Figures I- 1 thru I-55 on the following pages.

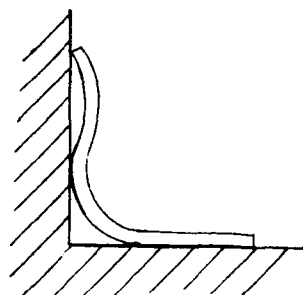


MAJOR FAILURES

MINOR DISTORTIONS



SPLITTING



SECTION "A"- "A"
TRANSVERSE BUCKLING

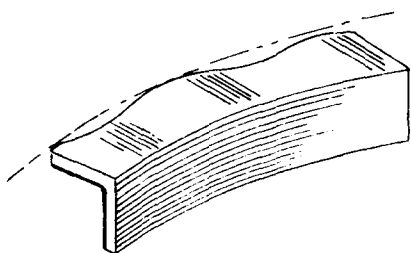
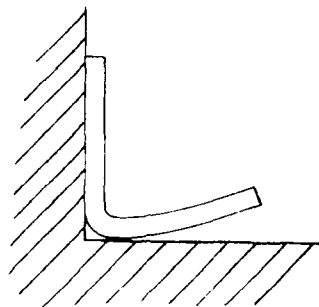


PLATE BUCKLING



SECTION "A"- "A"
WALK

FIGURE I-51 FAILURES FOR HEEL-IN ANGLE SECTIONS

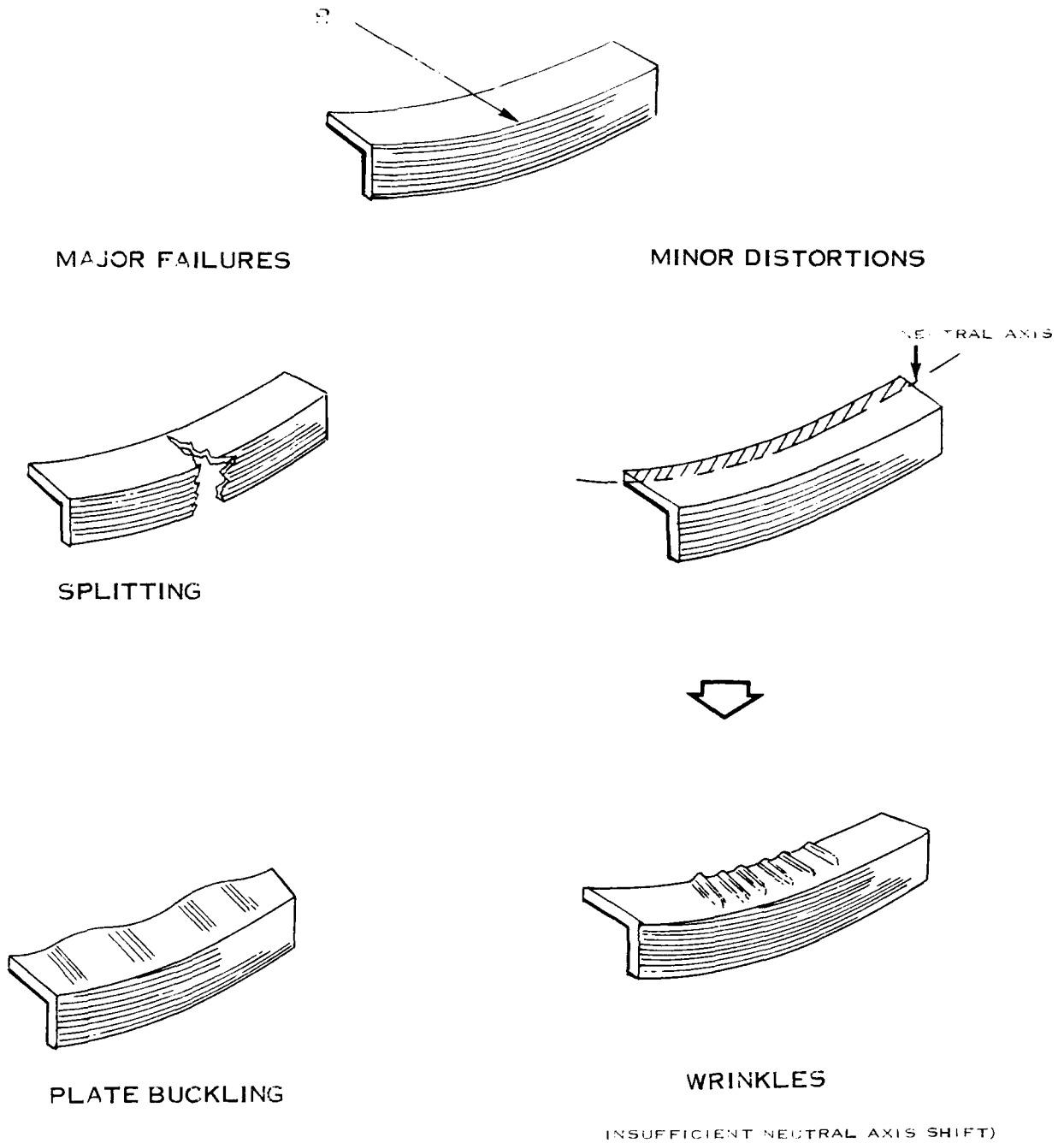
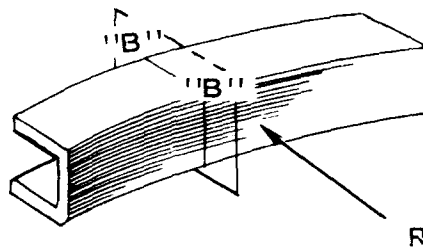
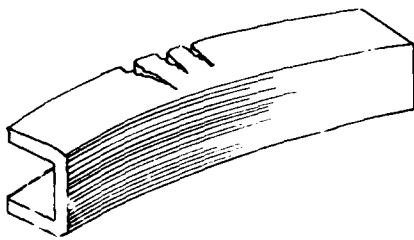


FIGURE I-52 FAILURES FOR HEEL-OUT ANGLE SECTIONS

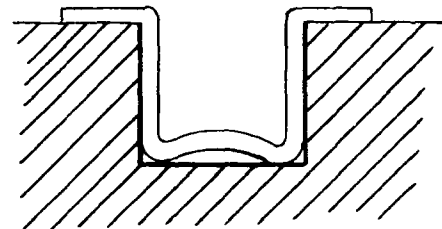


MAJOR FAILURES

MINOR DISTORTIONS



SPLITTING



SECTION "B"-"B"

WALK

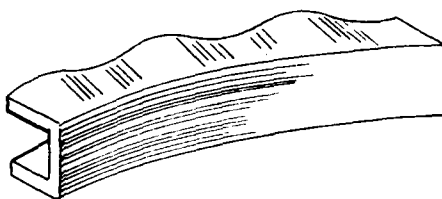
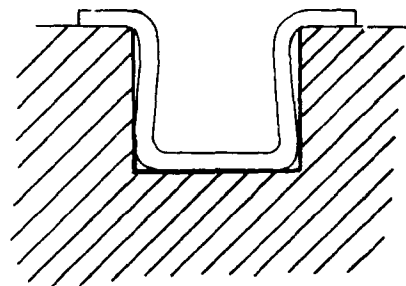


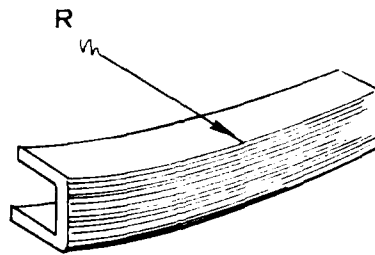
PLATE BUCKLING



SECTION "B"-"B"

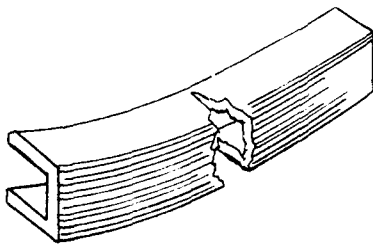
TRANSVERSE BUCKLING

FIGURE I-53 FAILURES FOR HEEL-IN CHANNEL SECTIONS



MAJOR FAILURES

MINOR DISTORTIONS



SPLITTING

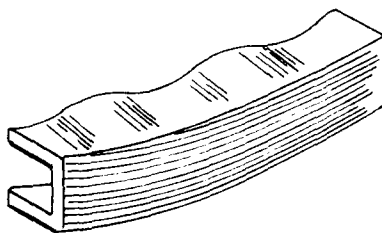
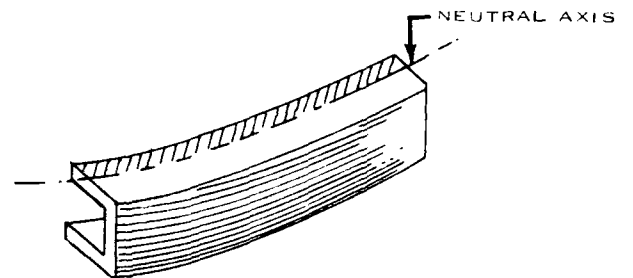
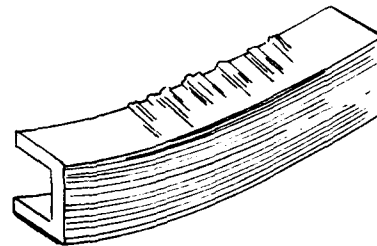


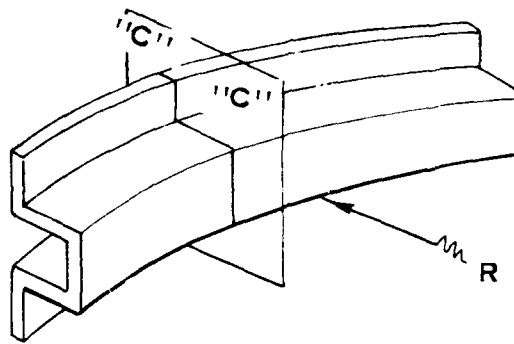
PLATE BUCKLING



WRINKLES

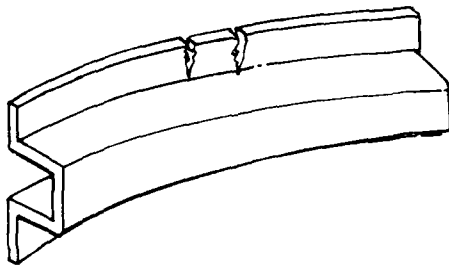
(INSUFFICIENT NEUTRAL AXIS SHIFT)

FIGURE I-54 FAILURES FOR HEEL-OUT CHANNEL SECTIONS

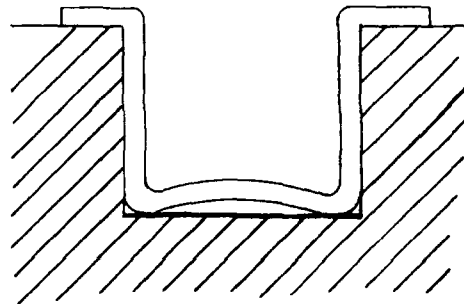


MAJOR FAILURES

MINOR FAILURES

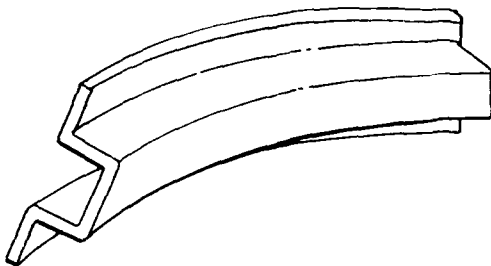


SPLITTING

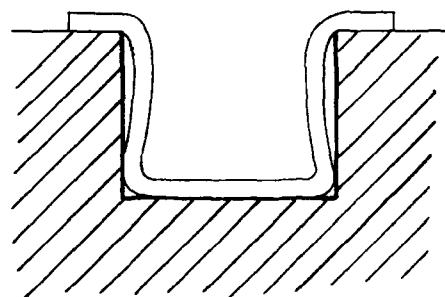


SECTION "C" - "C"

WALK



TWIST BUCKLING



SECTION "C" - "C"

TRANSVERSE BUCKLING

FIGURE I-55 FAILURES FOR HEEL-IN HAT SECTIONS

Transverse buckling is a minor distortion occurring in heel-in sections which is caused by improper die clearances. This distortion can be minimized by proper shimming of parts.

"Walk" and wrinkles are minor distortions occurring in heel-in and heel-out sections respectively. Both "walking" and wrinkling occur as the part is first wrapped around the die and can be removed by subsequent stretching of the part. The only limitation of this subsequent stretching is the ultimate strength of the material. If no "walking" or wrinkling is evident in a fractured part, the part cannot be evaluated because there is no evidence that the part has not been pulled beyond the amount necessary to eliminate the minor distortions. If "walking" or wrinkling is present but no fracture occurs, the part cannot be evaluated because it has not been pulled enough.

The above discussion defines the splitting criteria illustrated in Figure I-56. The cross hatched quadrants represent parts that cannot be evaluated.

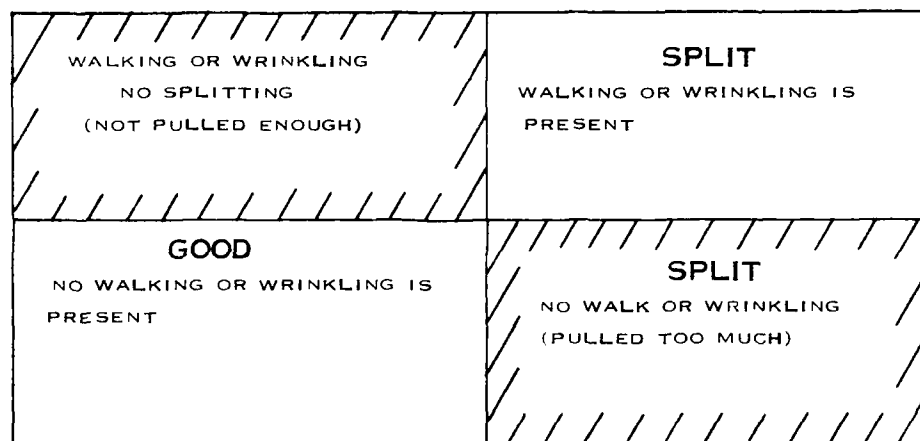


FIGURE I-56 SPLITTING CRITERIA FOR LINEAR STRETCH FORMING

Plate buckling results from residual stresses which deform the part after machine pressures are released and is evaluated in the same manner for both heel-in and heel-out parts. The buckle appears as a regular sine wave in the flange and a slight amount of "walking" in heel-in parts will assure that the part has not been pulled too much, whereas, wrinkling in heel-out parts will show that the part has not been pulled enough.

The linear stretch curve, illustrated in Figure I-57, is defined by good parts below the curve and failed parts above the curve. It will be noticed that the splitting limit line takes on increasingly negative slopes as h/t increases and is dependent on h/t as well as h/R . The reason becomes clear when it is realized that the splitting criteria involved buckling which is a function of h/t .

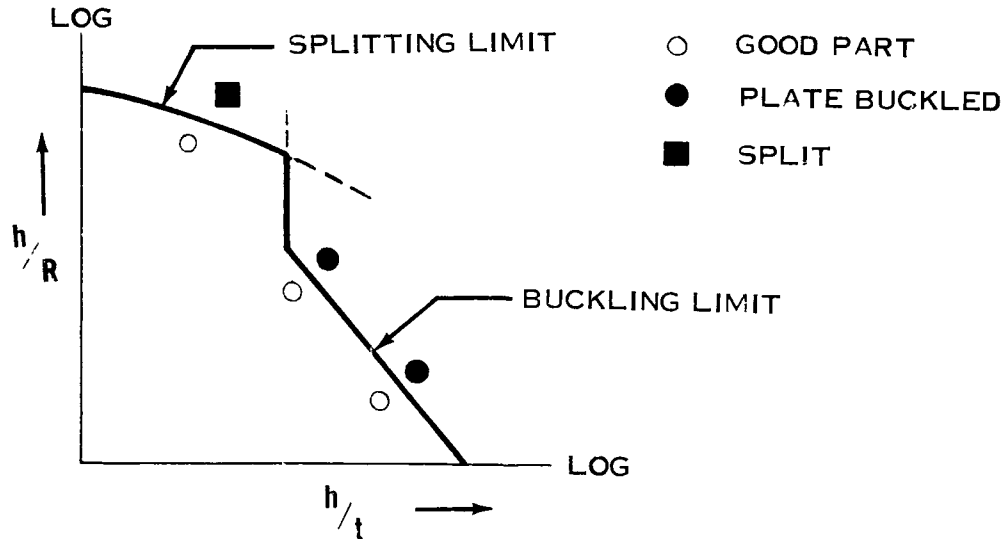


FIGURE I-57 LINEAR STRETCH LIMIT CURVE

The applied stress and the strain diagram for a linear stretch sample is illustrated in Figure I-58. The strain diagram shows $\bar{\epsilon}_L + \bar{\epsilon}_t + \bar{\epsilon}_w = 0$. The value for $\bar{\epsilon}_L / \bar{\epsilon}_e = 0.98$ was determined by the Energy of Distortion Theory using empirical data and allows the linear stretch process to be plotted on the "Effective Strain" Ellipse in Figure I-133 for correlation to the standard tensile specimen.

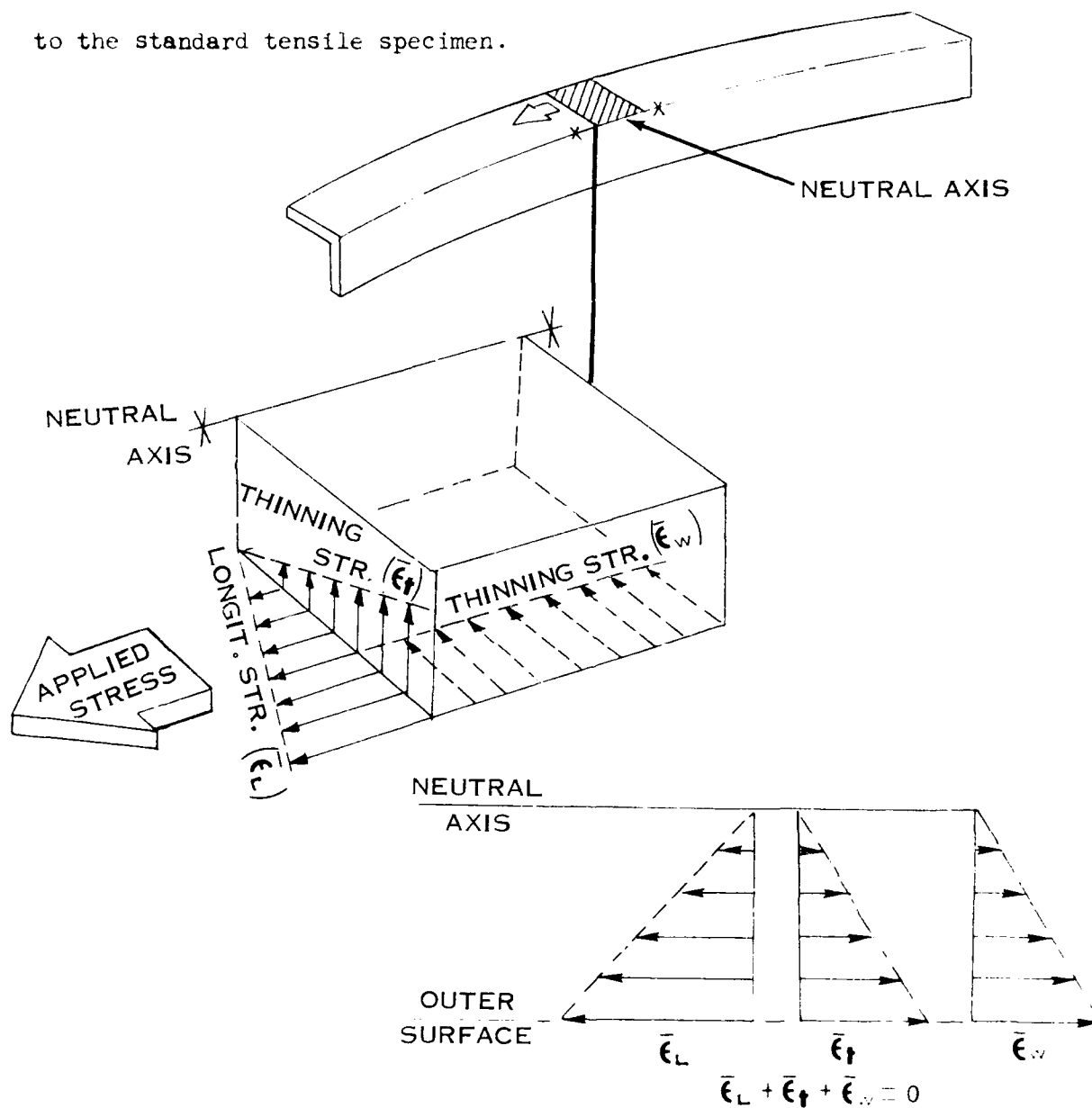


FIGURE I-58 APPLIED STRESS AND STRAIN DIAGRAMS FOR LINEAR STRETCH AND LINEAR ROLL FORMING

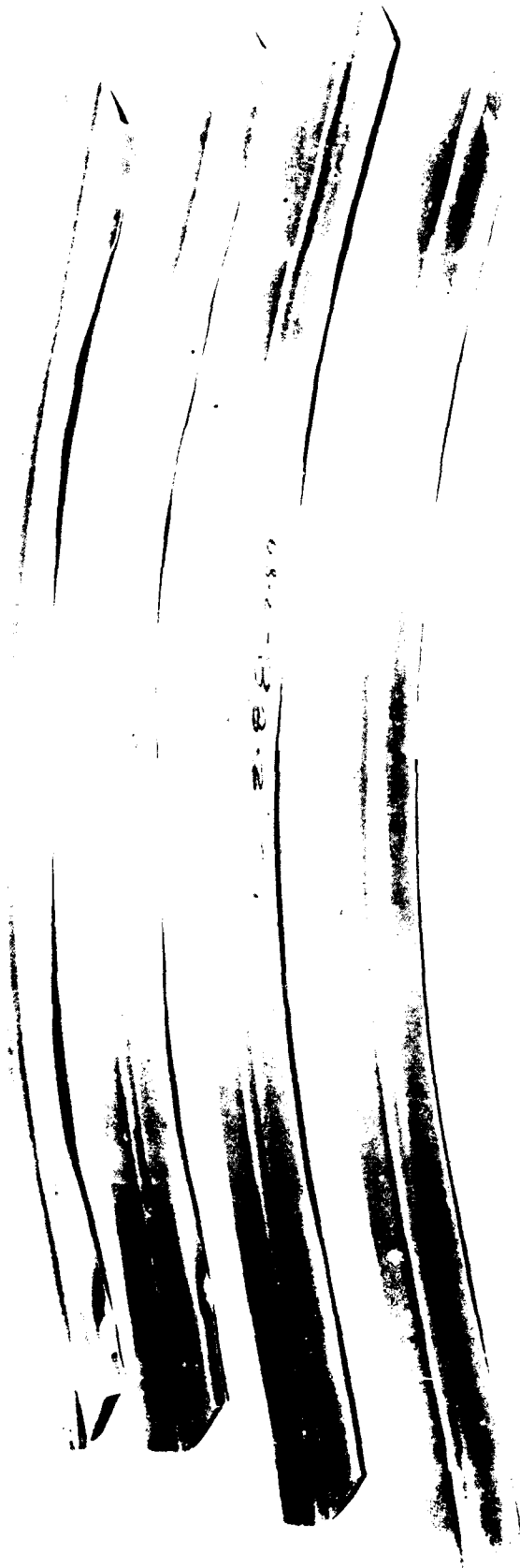


FIGURE I-59 BUCKLING OF LINEAR STRETCH FORMED HEEL-OUT ANGLE SECTIONS



FIGURE I 59(A) SPLITTING OF LINEAR STRETCH FORMED HEEL OUT ANGLE SECTIONS



FIGURE I-59(B) BUCKLING OF LINEAR STRETCH FORMED HEEL--IN ANGLE SECTIONS

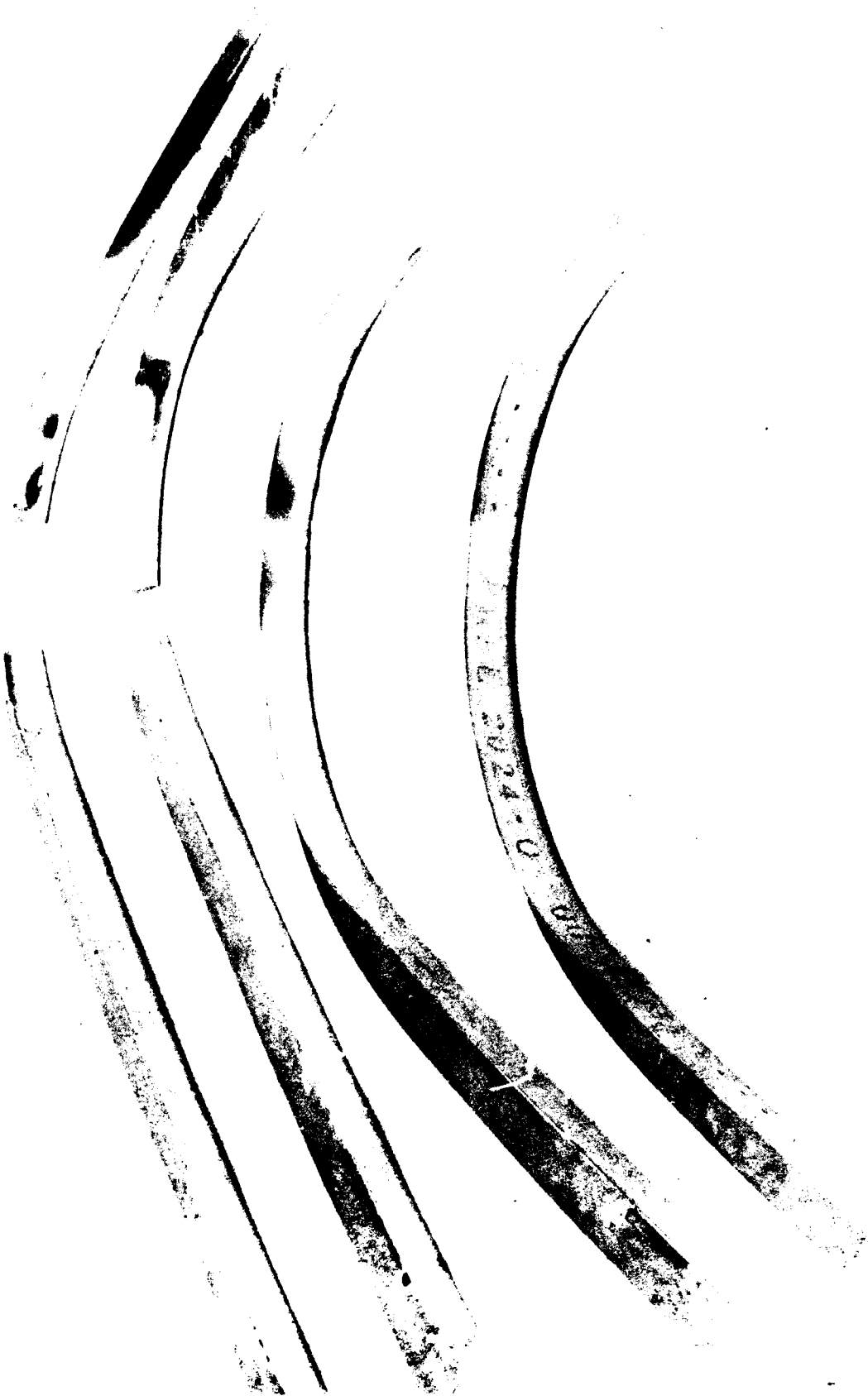


FIGURE I-59(C) SPLITTING OF LINEAR STRETCH FORMED HEEL-IN ANGLE SECTIONS



FIGURE 1 59(D) BUCKLING OF LINEAR STRETCH FORMED HEEL-OUT CHANNEL SECTIONS



FIGURE I 59(E) TWIST BUCKLING OF LINEAR STRETCH FORMED HEEL-IN HAT SECTIONS

LINEAR ROLL FORMING

The linear roll process is commonly used for forming contoured heel-in and heel-out channel sections when the maximum flange heights desired do not exceed 1.5 inches. Angle sections are obtained by forming channel sections and subsequent splitting of the channels into angle sections. The Kane-Roach (3 Roll) rolling machine, shown in Figure I-60, was used to form heel-in and heel-out channel sections for this program.

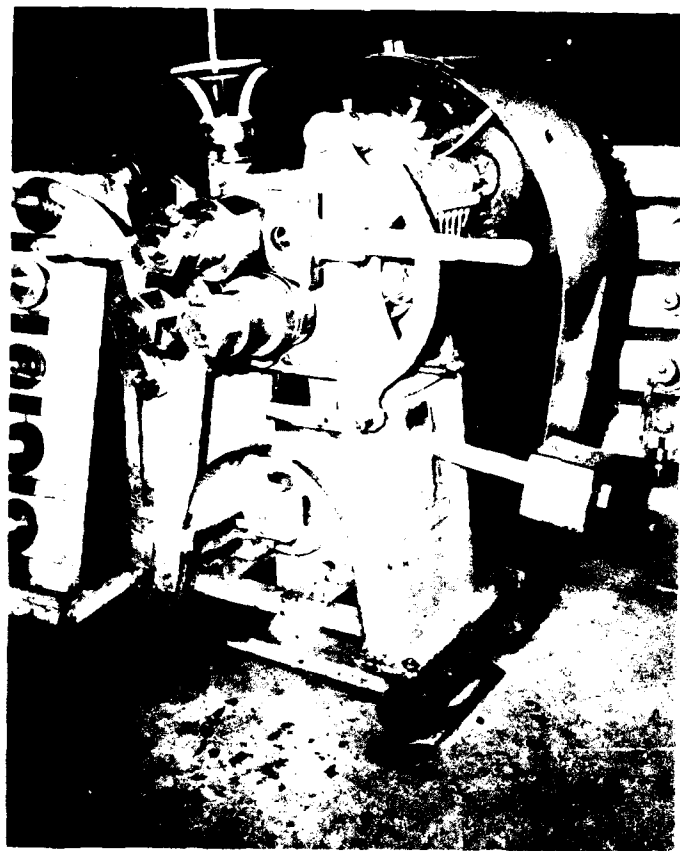


FIGURE I-60 KANE-ROACH (3 ROLL)
ROLLING MACHINE

The rolling dies shown on the Kane-Roach rolling machine in Figure I-61 are typical of the dies used to form the channel sections for this program. The dies required contour radii of 5" or greater, a minimum material thickness of 0.020" and a maximum material thickness of 0.063". The schematic of the linear roll process, shown in Figure I-62, illustrates the part types (heel-in and heel-out channels) and the set-up for a heel-in channel section.



FIGURE I-61 DIES FOR ROLL FORMING

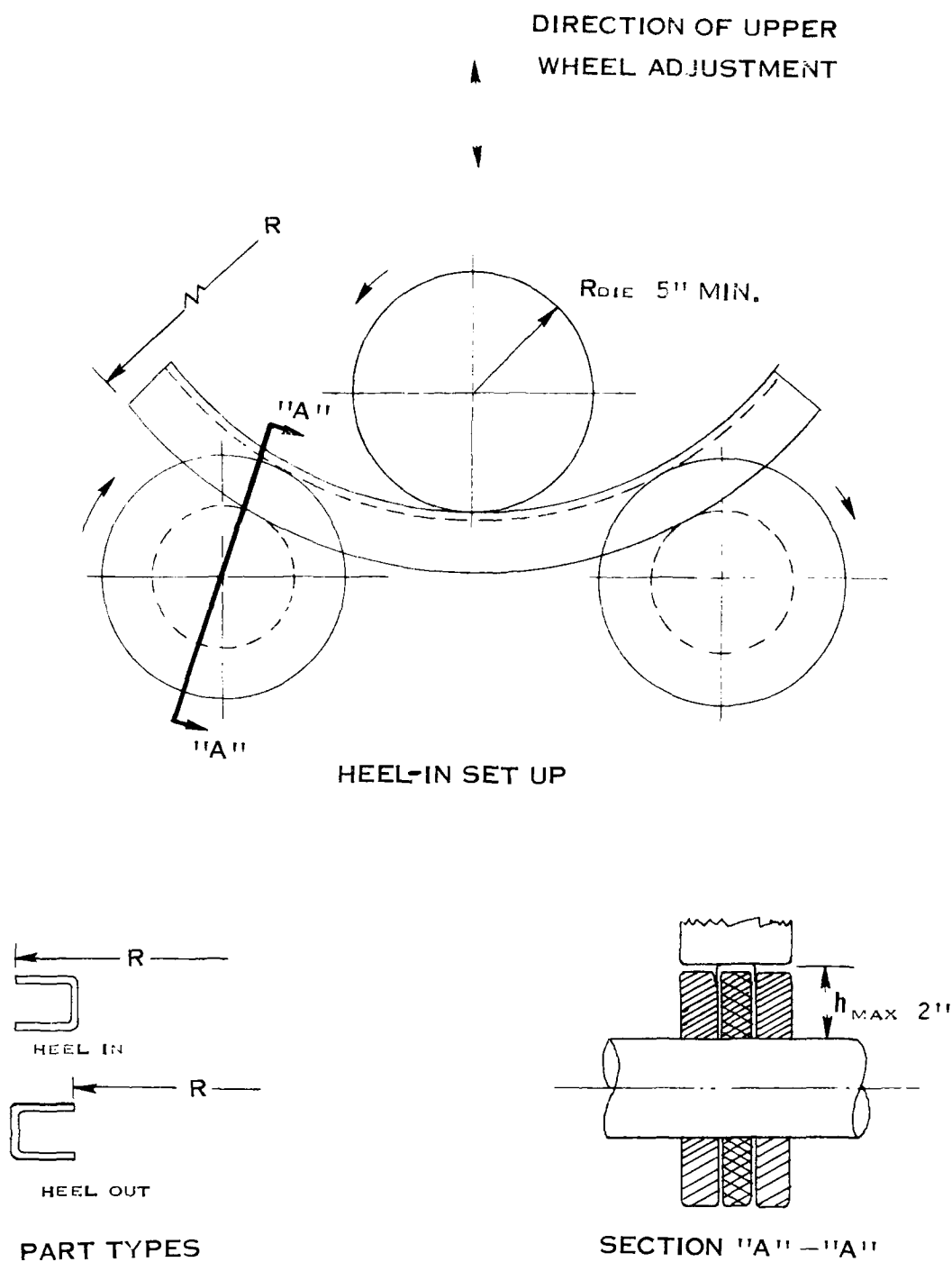


FIGURE I-62 PART TYPES AND SET-UP FOR ROLL FORMING

The parameters for linear roll forming are flange height (h), contour radius (R) and material thickness (t), as illustrated in Figure I-63.

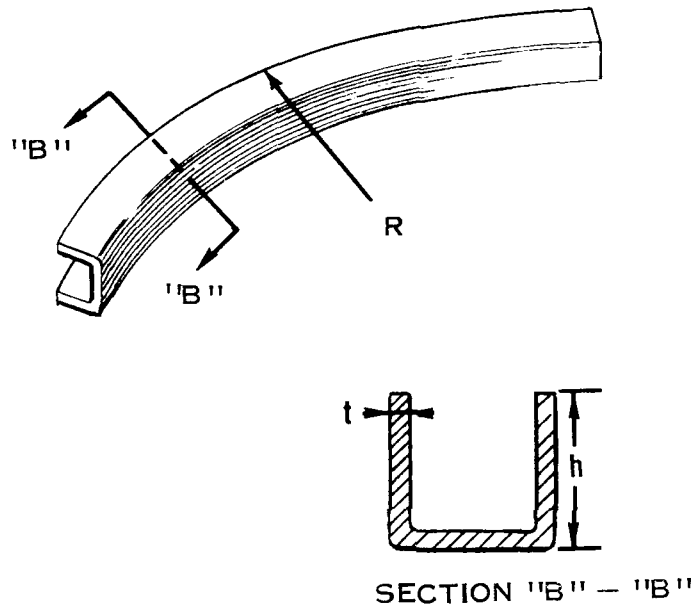


FIGURE I-63 PARAMETERS FOR LINEAR ROLL FORMING

Roll forming is a process that depends on operator technique. Premature buckling will occur if the contour radius (R) is decreased in increments that are too severe or too many passes are made causing work hardening of the material and changing its buckling characteristics. The operator usually forms several trial parts in order to get a feel for the material involved and the geometry desired.

The major failure for linear roll forming of heel-out channel sections is wrinkling. This failure occurs as a result of the neutral axis not shifting to the inner fiber of the flange as illustrated in Figure I-64.

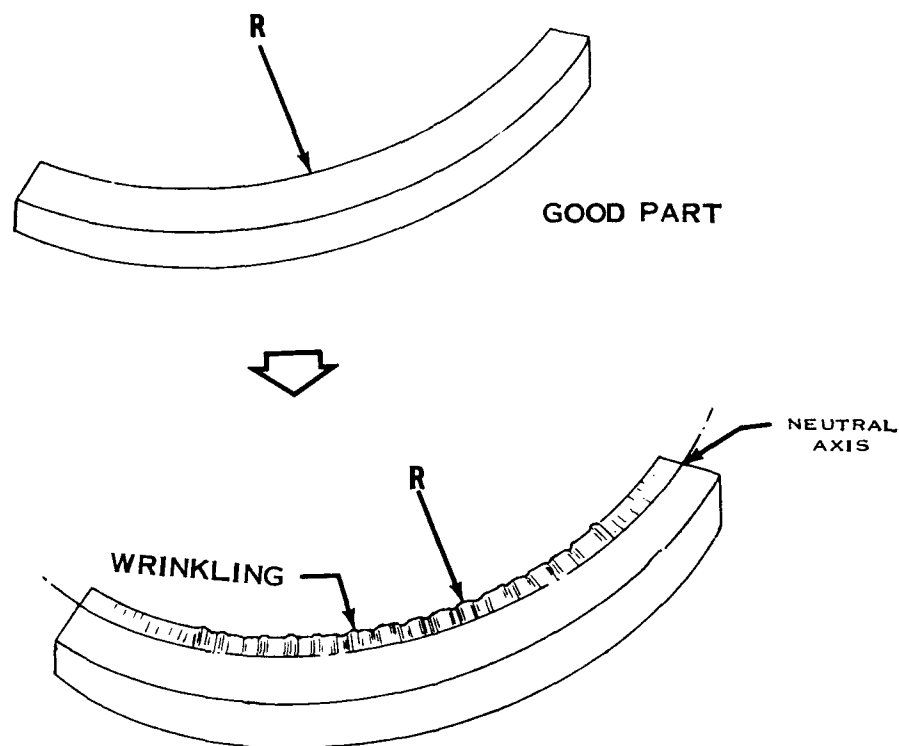
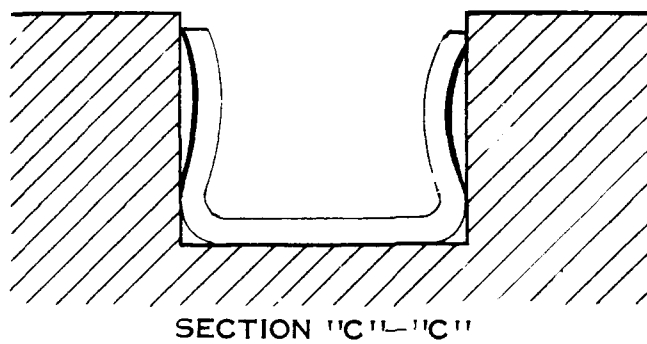
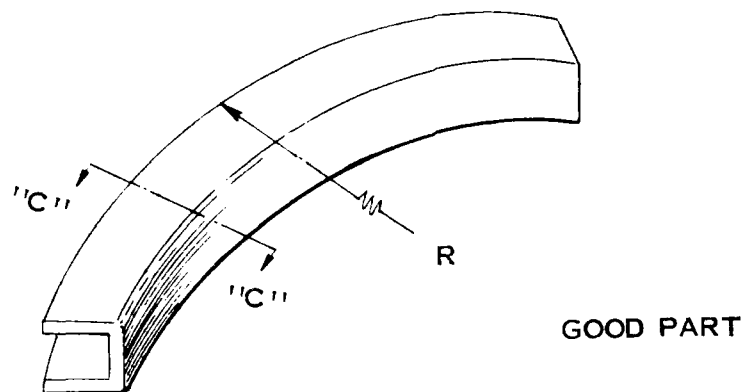


FIGURE I-64 MAJOR FAILURE FOR HEEL-OUT CHANNEL SECTIONS

The major failure occurring for linear roll forming of heel-in channel sections is transverse buckling as illustrated in Figure I-65.



TRANSVERSE BUCKLING

FIGURE I-65 MAJOR FAILURE FOR HEEL-IN CHANNEL SECTIONS

Transverse buckling of heel-in parts is the result of the flange buckling to relieve tensile stresses in the outer fiber. This buckling occurs in the area between the rolling dies where the flange is unsupported as shown in Figure I-66.

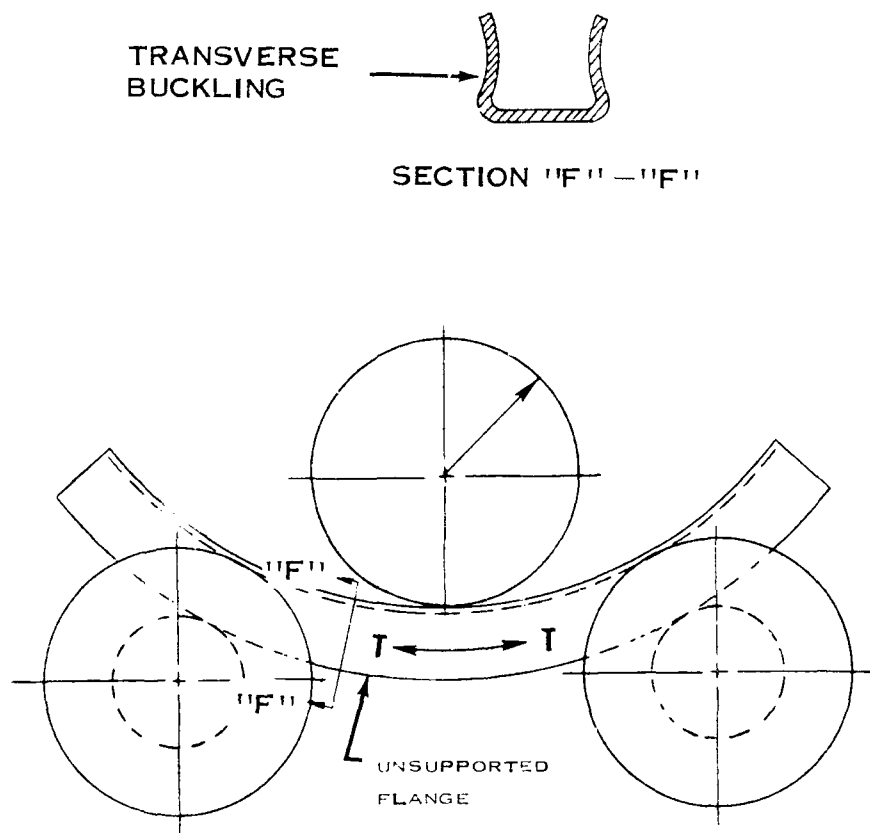


FIGURE I-66 SET-UP FOR HEEL-IN CHANNEL SECTIONS

The minor distortions in linear roll forming are "walking", plate buckling, web buckling and splitting in the web. "Walking" or crown in the web occurs for both heel-in and heel-out channel sections while plate buckling, web buckling and splitting in the web occur only in heel-in channel sections. These minor distortions are illustrated in Figures I-67 and I-68.

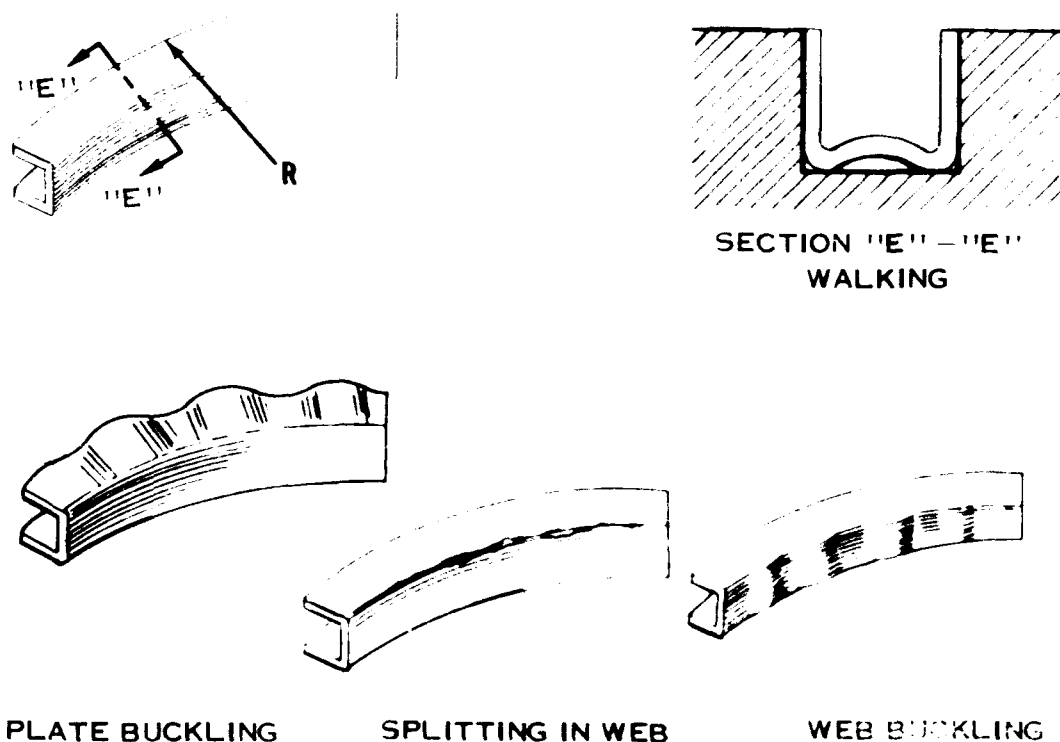


FIGURE I-67 MINOR DISTORTIONS FOR HEEL-IN CHANNEL SECTIONS

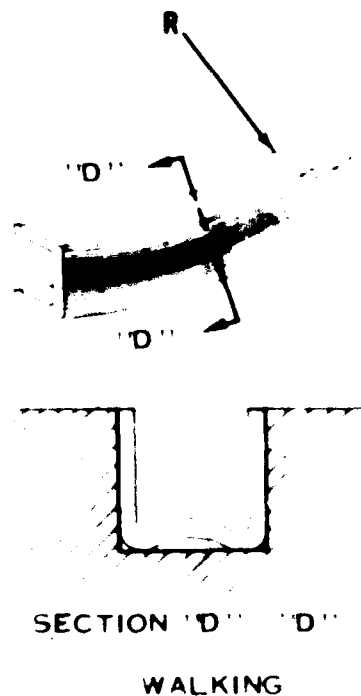


FIGURE I-68 MINOR DISTORTIONS FOR HEEL OUT CHANNEL SECTIONS

Although sine wave plate buckling is usually considered a major failure, it is considered minor for heel-in roll formed sections because transverse buckling occurs first. The exception is for materials with low E/S_T values where transverse buckling and plate buckling occur simultaneously.

Buckling in the web occurs when the web width exceeds $3/4$ " for material thicknesses of 0.020" or less and splitting in the web results from bend radius reduction as the contour radius (R) is decreased. Both web conditions are considered secondary failures since transverse buckling occurs in the earlier stages of forming.

The linear roll curve, illustrated in Figure I-69, is defined by good parts below the curve and failed parts above the curve. The curve shows that buckling occurs for high values of h/t and splitting for high values of h/R . Splitting was not encountered in this program because transverse buckling occurred to relieve the tensile stresses in the outer fibers of the flanges. However, the theoretical splitting limit curve is shown since splitting would occur for high values of h/R if flange stability were attained.

Since the part geometry for linear roll forming and linear stretch forming are identical, the applied stress and the strain diagram is not repeated. Refer to Figure I-67.

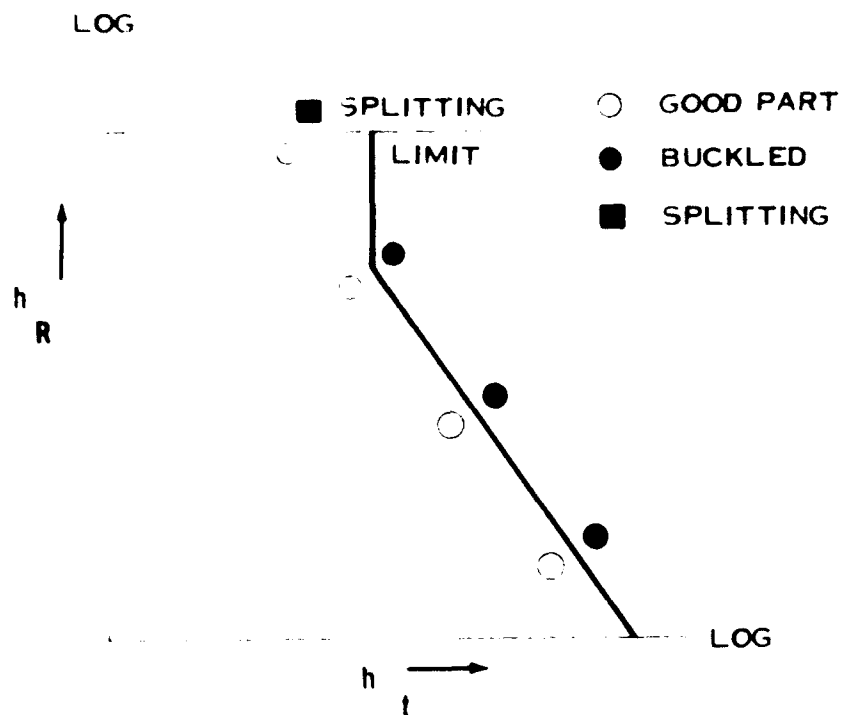


FIGURE I-69 LINEAR ROLL LIMIT CURVE



FIGURE I-70 SINE WAVE BUCKLING OF LINEAR ROLL FORMED
HEEL-IN CHANNEL SECTIONS



FIGURE 1 70(A) SPLITTING IN THE WEB RADIUS OF LINEAR ROLL FORMED
HEEL IN CHANNEL SECTIONS

SHEET STRETCH FORMING

Sheet stretch forming is a common method for double contouring relatively large sheet metal parts. The 300 ton Sheridan Stretch Press, shown in Figure I-71, was used to form sheet stretched double contour parts for this program. Although the sheet can be stretched in either one or both directions by the jaws of the stretch press while the die is displaced upward into the part, only a single set of jaws were used and the two free edges of the sheet were free to move inward while the sheet was stretched in the other direction. The sheet stretch forming set-up is illustrated in Figure I-72.



FIGURE I - 71 300 TON SHERIDAN STRETCH PRESS

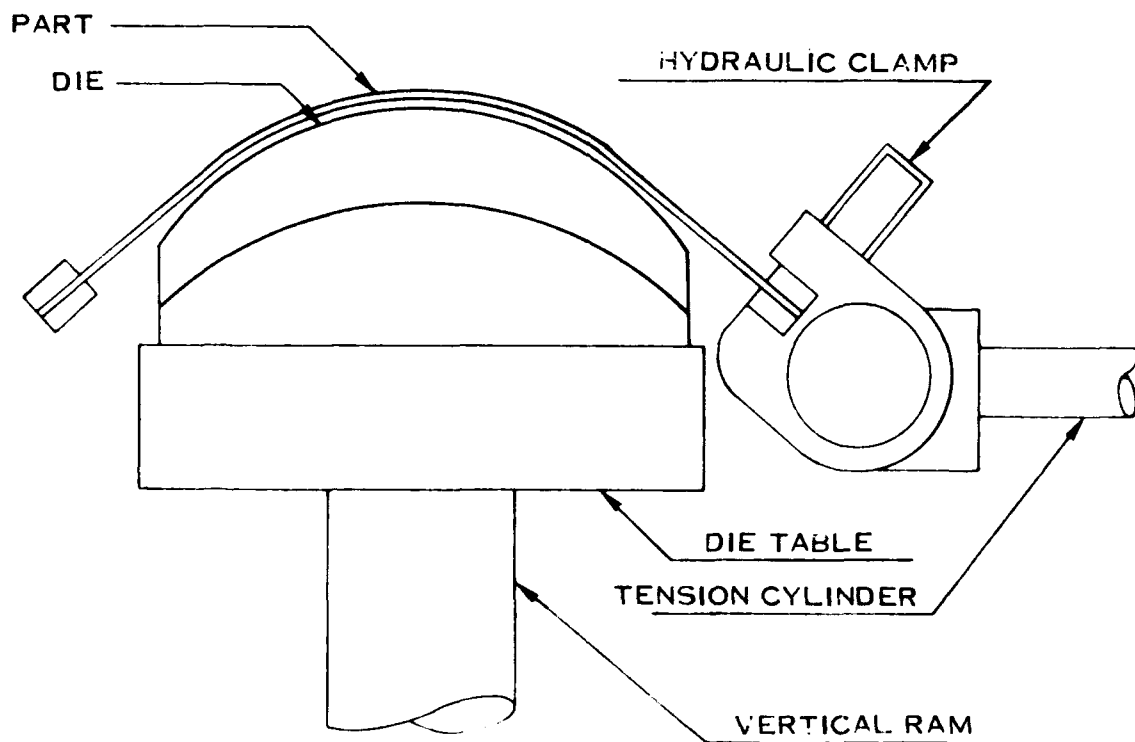


FIGURE I - 72 SCHEMATIC OF SHEET STRETCH SET-UP

The parameters for sheet stretch forming are longitudinal radius (R_L), transverse radius (R_T), longitudinal chord length (L) and transverse chord length (T), as illustrated in Figure I-73.

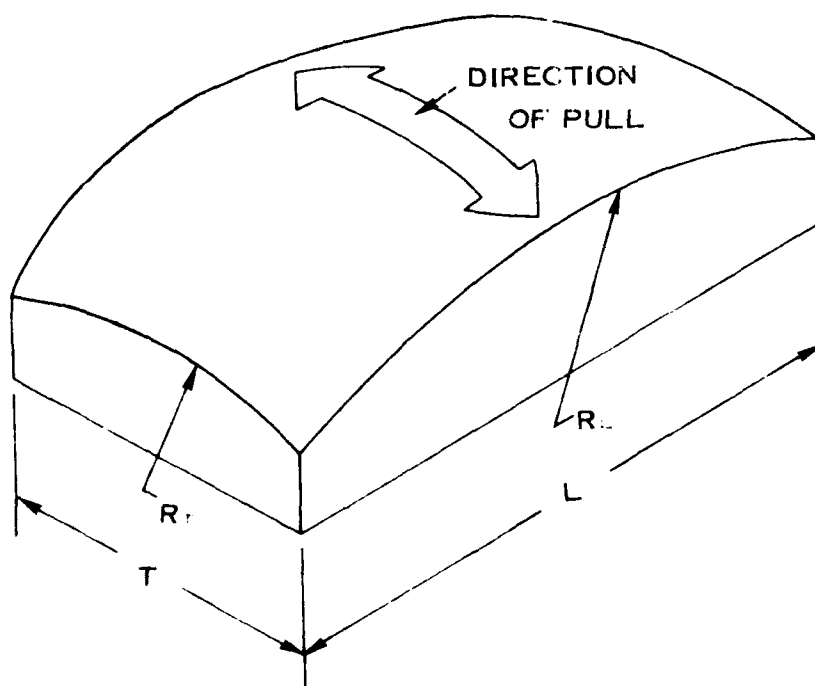


FIGURE I - 73 PARAMETERS FOR SHEET STRETCH FORMING

The double contour dies for sheet stretch forming, shown in Figure I-74, covered a wide range of contour radii and chord lengths. The combinations of contour radii and chord lengths are given in the following table.

R_L	L	R_T	T
15	17.5	15	17.5
30	24.0	15	21.5
40	24.0	15	23.5
60	24.0	15	24.5
60	25.5	60	25.5

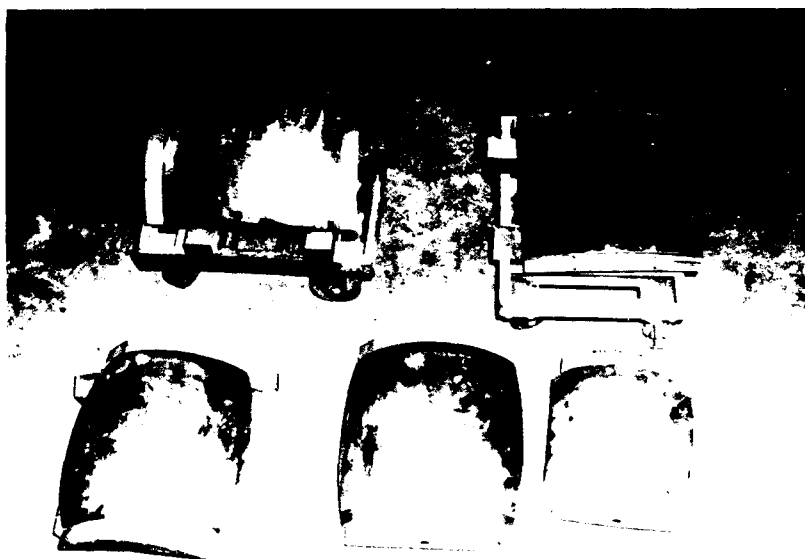


FIGURE I - 74 DOUBLE CONTOUR SHEET STRETCH DIES

The only failures in sheet stretch forming are three types of splitting. The first type of splitting, shown in Figure I-75, occurs at the stretch press jaws for ductile materials that do not thin excessively when formed over the double contour die. This type of failure occurs for almost all materials and is defined as the forming limit.

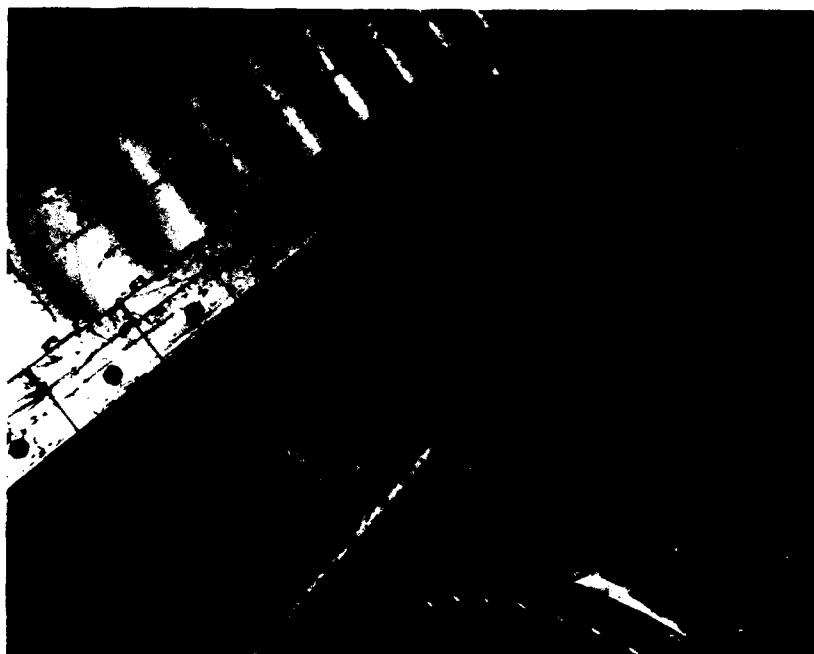
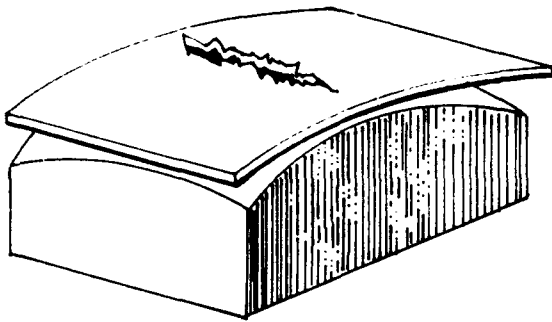
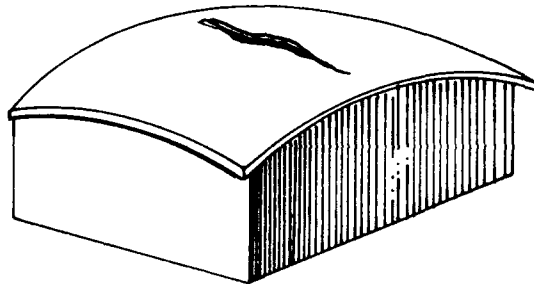


FIGURE I - 75 SPLITTING FAILURE IN FREE AREA
FOR SHEET STRETCH FORMING

The other two types of splitting, illustrated in Figure I-76, occur near the center of the contour die for materials with insufficient ductility to conform to the dies or ductile materials that thin excessively when stretched.



BRITTLE FAILURE



DUCTILE FAILURE
(MATERIAL THINNING)

FIGURE I - 76 SPLITTING FAILURES FOR SHEET STRETCH FORMING

The sheet stretch curve, illustrated in Figure I-77, is defined by good parts above the curve and failed parts below the curve. Splitting results for small values of R_T/T and R_L/L while good parts result for larger values of R_T/T and R_L/L . The theoretical limit is the point where the radius is equal to 1/2 the diameter so that the die would have to be a complete half sphere.

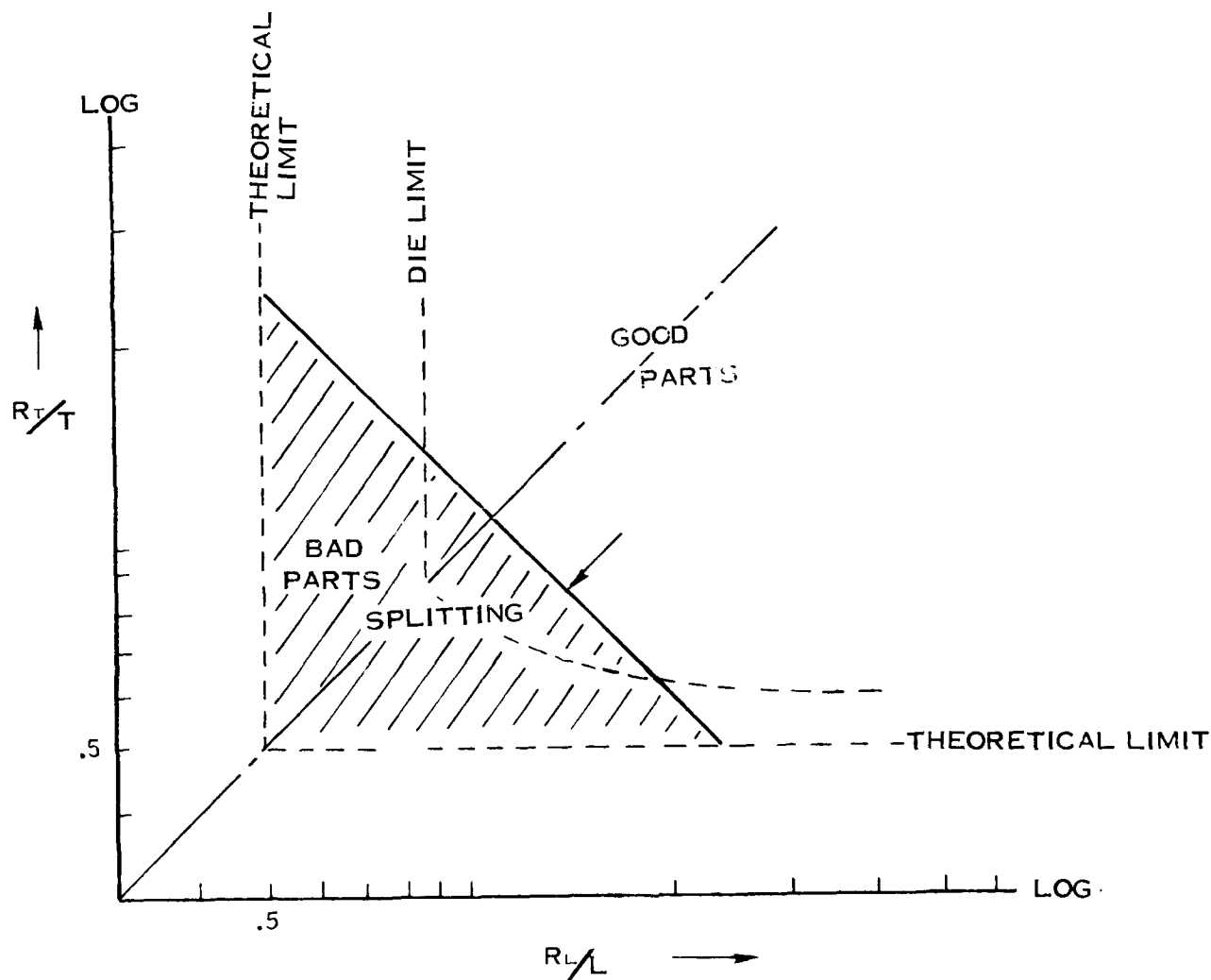
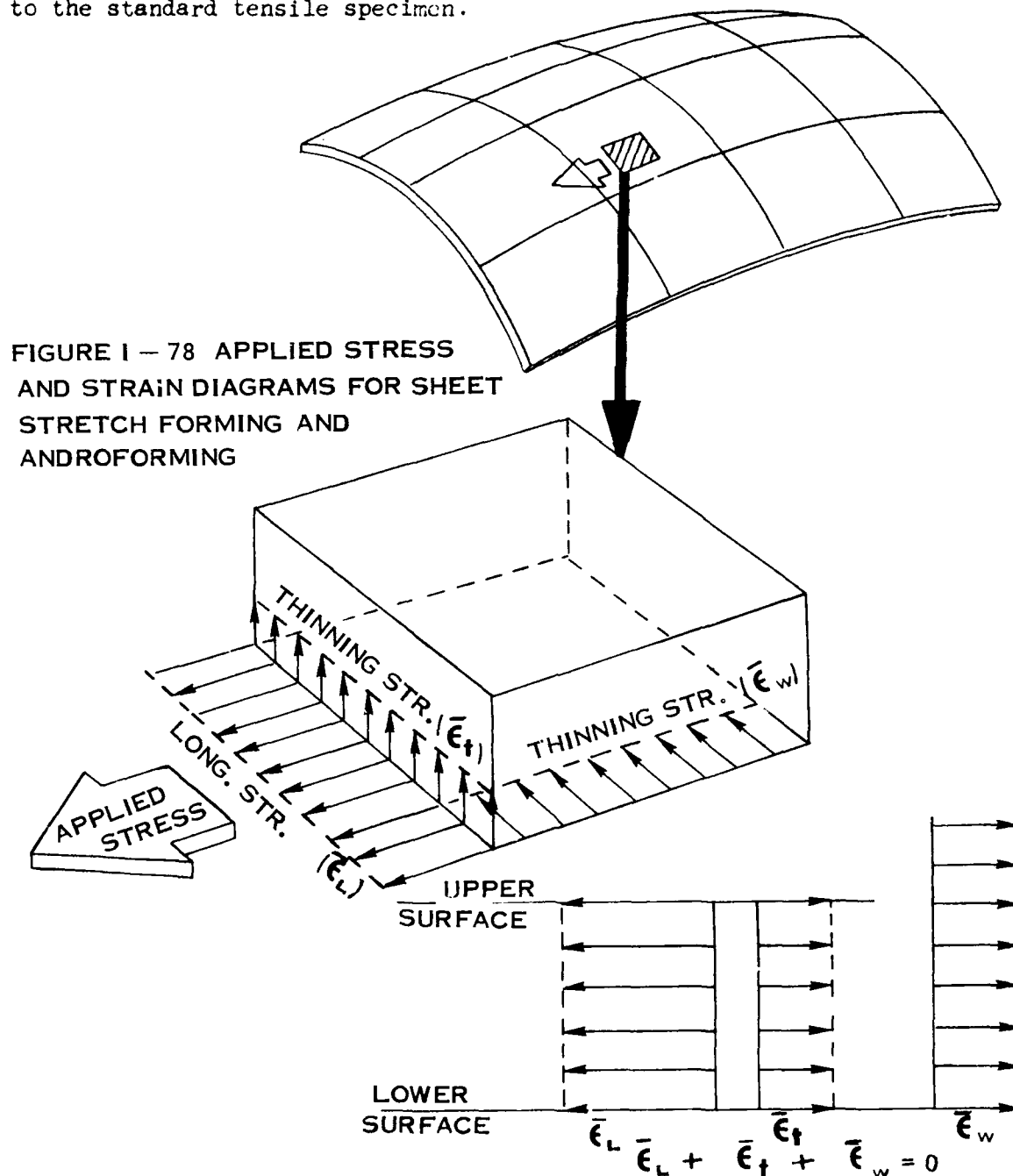


FIGURE I - 77 SHEET STRETCH LIMIT CURVE

The applied stress and the strain diagram for a double contoured sheet stretch part is shown in Figure I-78. The strain diagram shows $\bar{\epsilon}_L + \bar{\epsilon}_t + \bar{\epsilon}_w = 0$. The value for $\bar{\epsilon}_L / \bar{\epsilon}_e = 0.96$ was determined by the Energy of Distortion Theory using empirical data and allows the sheet stretch process to be plotted on the "Effective Strain" Ellipse in Figure I-133 for correlation to the standard tensile specimen.



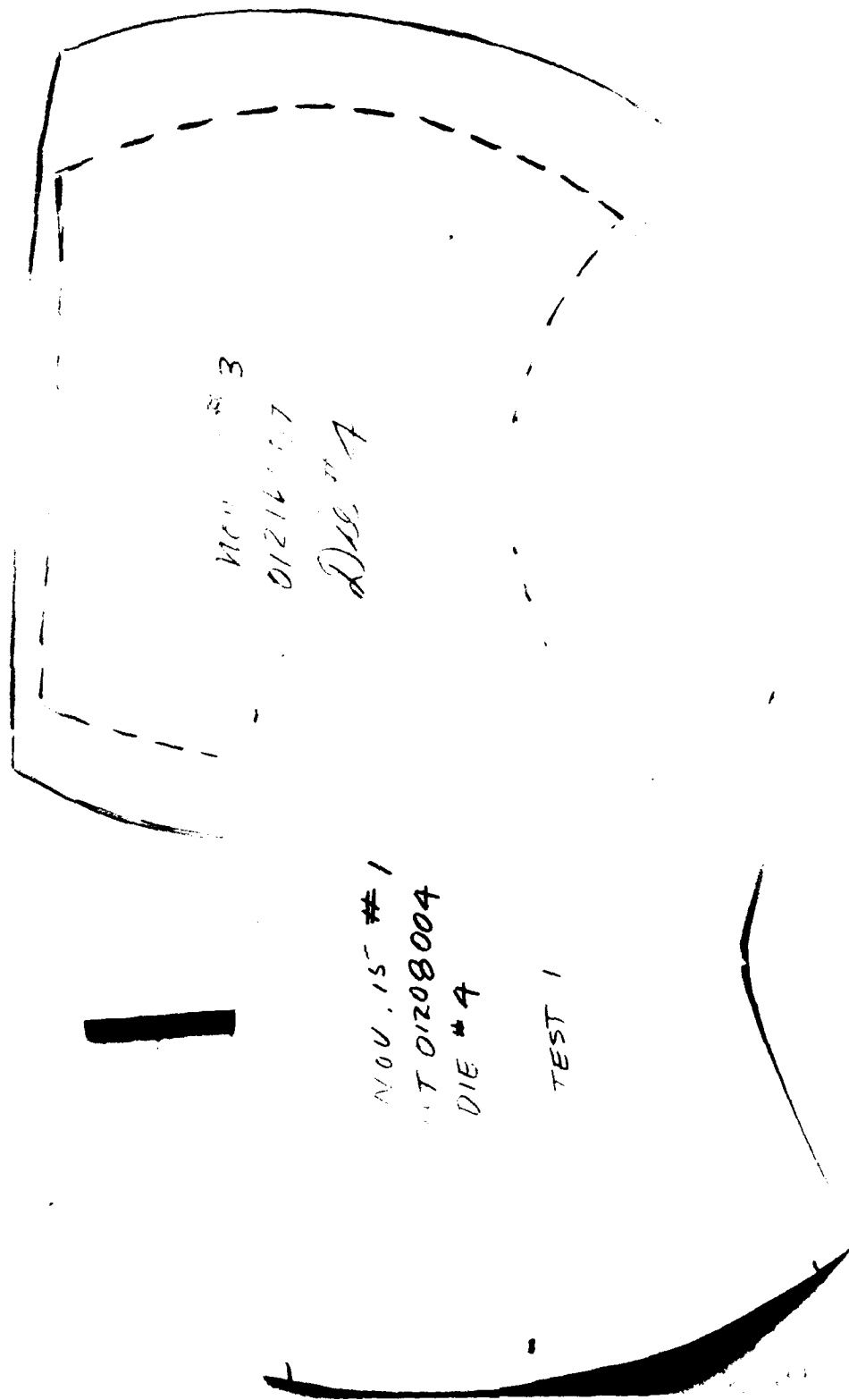


FIGURE 1-79 DOUBLE CONTOURED SHEET STRETCH PARTS

ANDROFORMING

Androforming is a double contour skin forming process. A Model J Androforming machine, illustrated in Figure 1-80, was used to form the symmetrical double contour parts for this program. The machine used was located at the Air Force Research Laboratory, Texas.

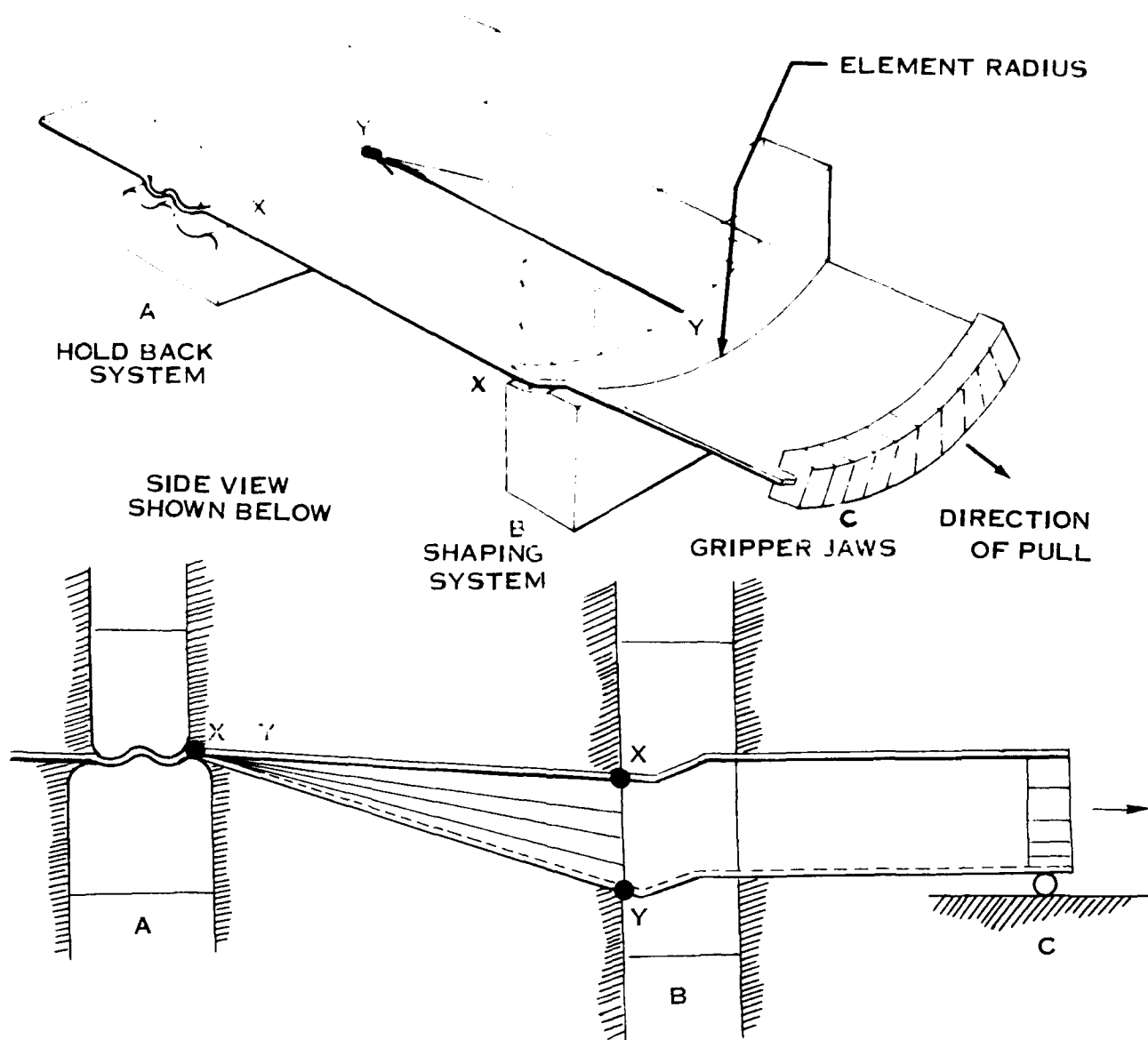


FIGURE 1-80 SCHEMATIC OF MODEL J ANDROFORM MACHINE

The machine consists of three components: (1) the hold-back system, (2) the shaping system, and (3) the gripper jaws. The leading edge of the sheet is fed between the elements in "a" and "b" and clamped in "c". The elements at "a" and "b" are closed to predetermined gaps and the sheet is pulled between them as "c" moves as shown. The elements at "a" are straight; they have no transverse curvature, while the elements at "b" and "c" are set to a given curvature before forming begins. The edges, represented by the distance "X-X", change little during forming but the center longitudinal element stretches to the length "Y-Y". It is the difference between the stretch at the center and the edge of the sheet that causes the contour in the transverse as the longitudinal direction. There is another factor which contributes to the contour. The center longitudinal element, having stretched more than the edges, has a greater amount of springback, thus adding to the double contour.

The changing of dimension "A", shown in Figure 1-81, has the greatest effect on the severity of double contouring of any of the machine adjustments. Therefore, all adjustments are set to optimum conditions of a given gage and the "A" dimension is varied.

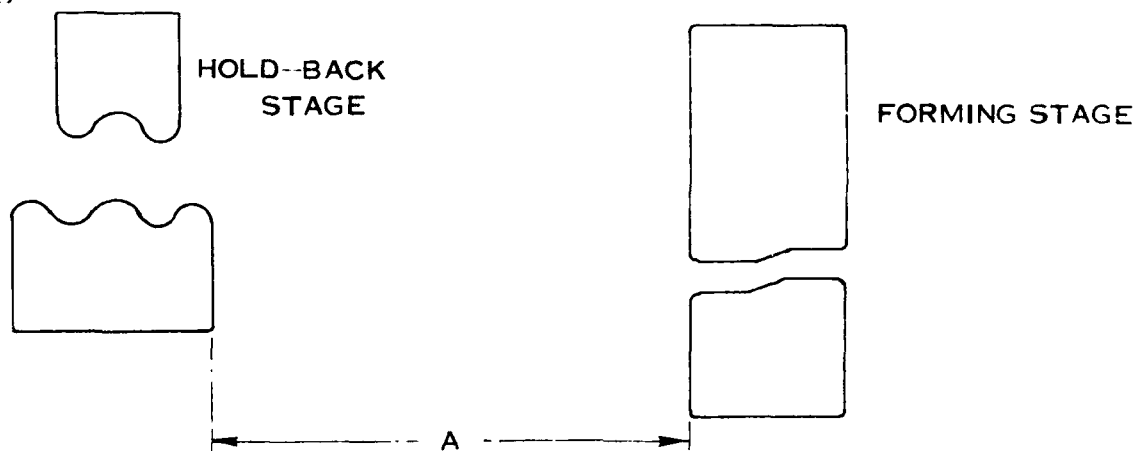


FIGURE 1-81 DIMENSION "A" BETWEEN HOLD BACK AND FORMING STAGES (ANDROFORMING)

Two sets of special forming stage dies were used to investigate the formability of the materials. The first set used was the property of Convair and had a radius of 50 inches. Since this radius was not severe enough to find the forming limits for some materials, a 20 inch radius set was fabricated and used. A photograph of the 20 inch die is shown in Figure I-82.



FIGURE I - 82 ANDROFORM DIE (20 INCH RADIUS)

The parameters for Androforming, illustrated in Figure 1-83, are longitudinal contour radius (R_L), transverse contour radius (R_T), and the material thickness (t).

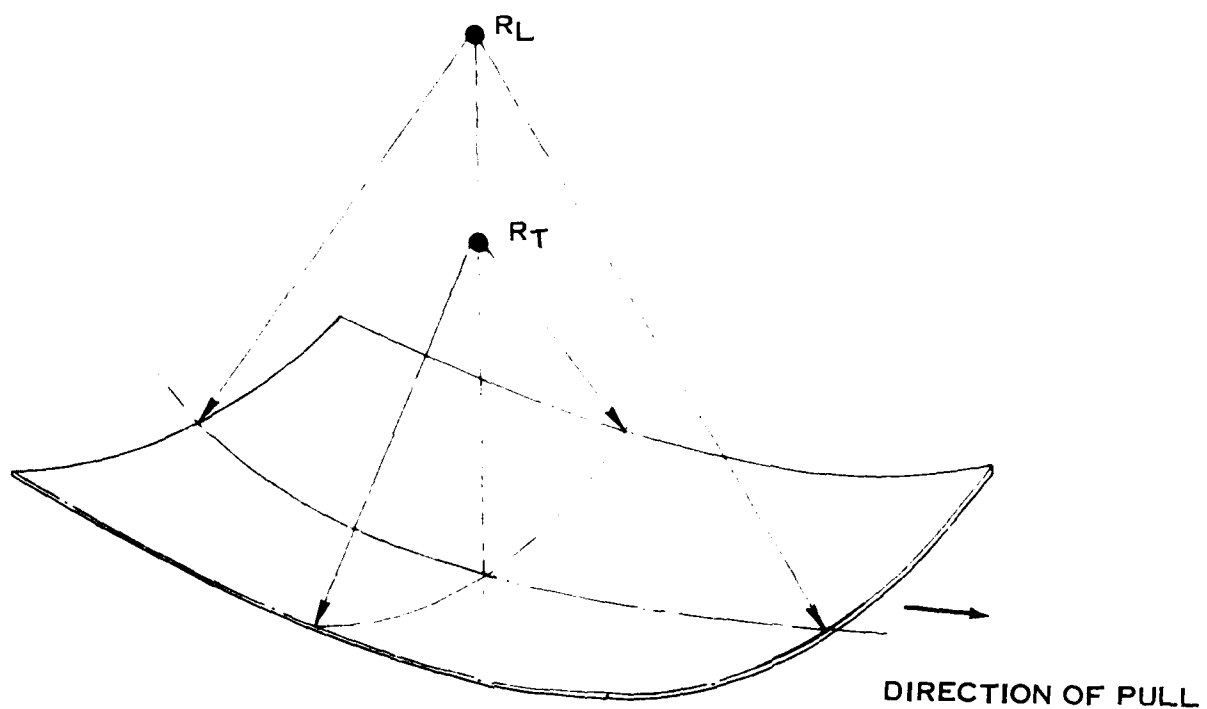


FIGURE 1 - 83 PARAMETERS FOR ANDROFORMING

The failures for Androforming are splitting, longitudinal buckling and transverse buckling.

Splitting, shown in Figure I-84, is the result of bending failure when the distance "A" (see Figure I-81) between the hold-back stage and the forming stage becomes critically small. The Androform splitting curve, illustrated in Figure I-85, is defined by good parts above the curve and split parts below the curve. Similar to bending failures which result for small values of R/t , splitting occurs for small values of R_L/\sqrt{t} and R_T/\sqrt{t} .

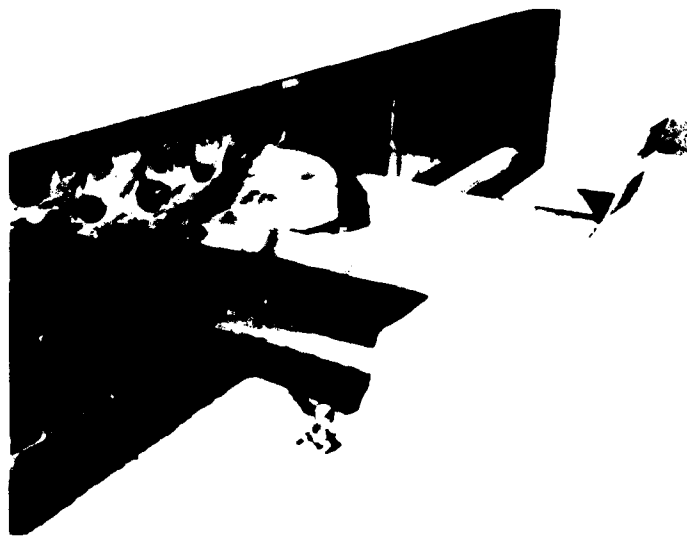


FIGURE I - 84 SPLITTING OF ANDROFORM PARTS

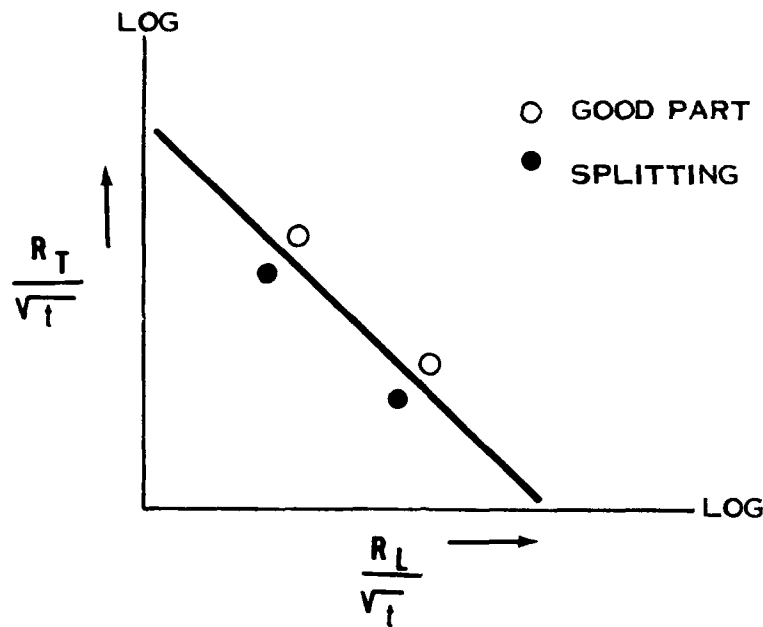


FIGURE I - 85 ANDROFORM SPLITTING CURVE

Longitudinal and transverse buckling for Androforming are shown in Figure I-86. Buckling results for small contour radii and thin material gages; thick material gages are more resistant to buckling. The Androform buckling curve, illustrated in Figure I-87, is defined by good parts above the curve and buckled parts below the curve and shows that buckling occurs for small values of R_{Tt} and R_{Lt} . Stretching after buckling occurs will result in splitting.

The Androforming process is not plotted on the "Effective Strain" Ellipse because heat treated materials were used that had elongations of only 6 to 8 percent. These small values of elongation allow considerable error in grid measurements for calculation of the effective strain.

Since the part geometry for Androforming and sheet stretch forming are identical, the applied stress and the strain diagram is not repeated. Refer to Figure I-78.

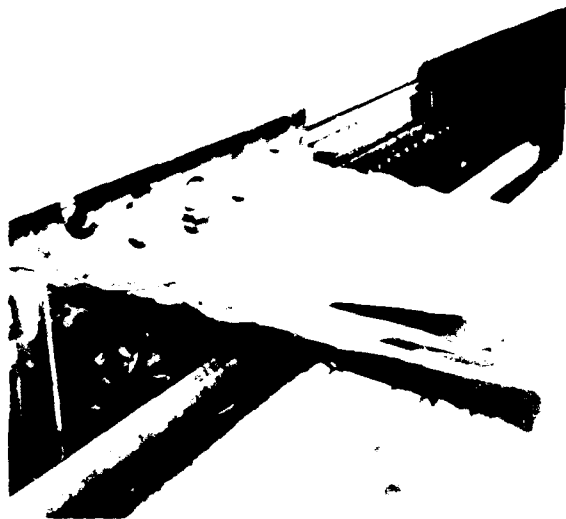


FIGURE I - 86 BUCKLING OF ANDROFORM PARTS

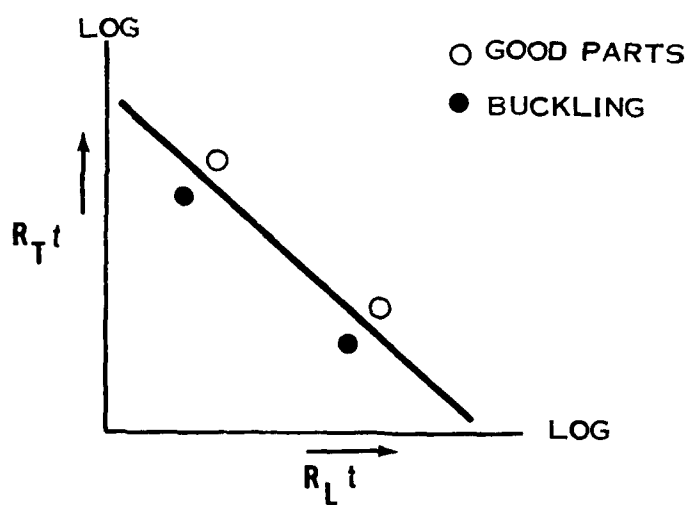


FIGURE I - 87 ANDROFORM BUCKLING CURVE



FIGURE I-88 ANDROFORMING DOUBLE CONTOURING WITH THE 20 INCH DIE



FIGURE I-89 ANDROFORMING—DOUBLE CONTOUR AREA BETWEEN THE FORMING AND HOLD-BACK STAGES

DEEP DRAWING WITH MECHANICAL DIES

Deep drawing with mechanical dies is the principle method of forming deep recessed parts. A 600 ton Lake Erie hydraulic press, shown in Figure I-90, was used to form cylindrical cups for this program.

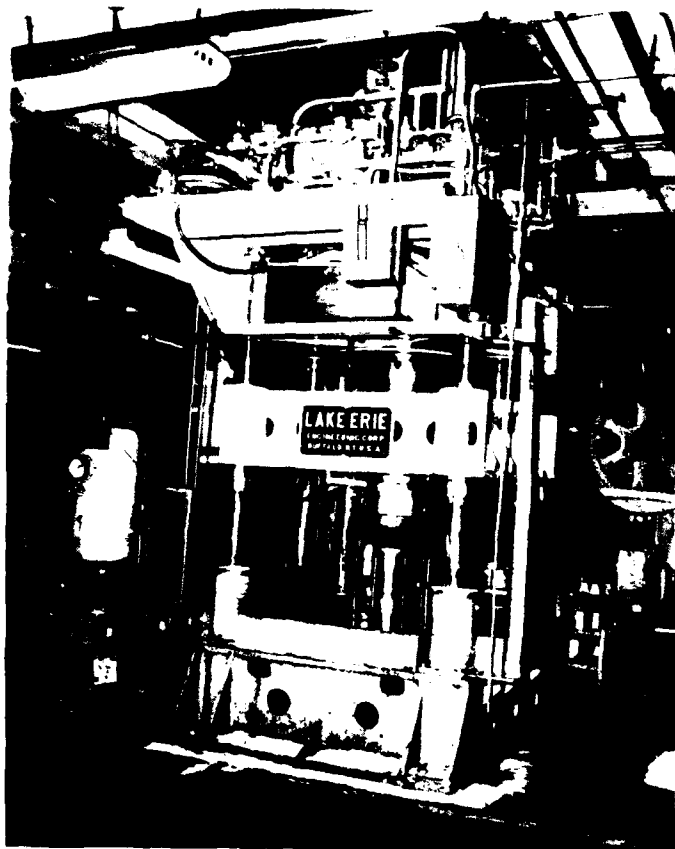


FIGURE I-90 600 TON LAKE ERIE HYDRAULIC PRESS

Figure I-91 is a schematic of the tooling used in deep drawing. The shoe and spring arrangement was used to prevent movement of the blank during forming and resulted in increased formability by eliminating uneven draw across the top of the punch.

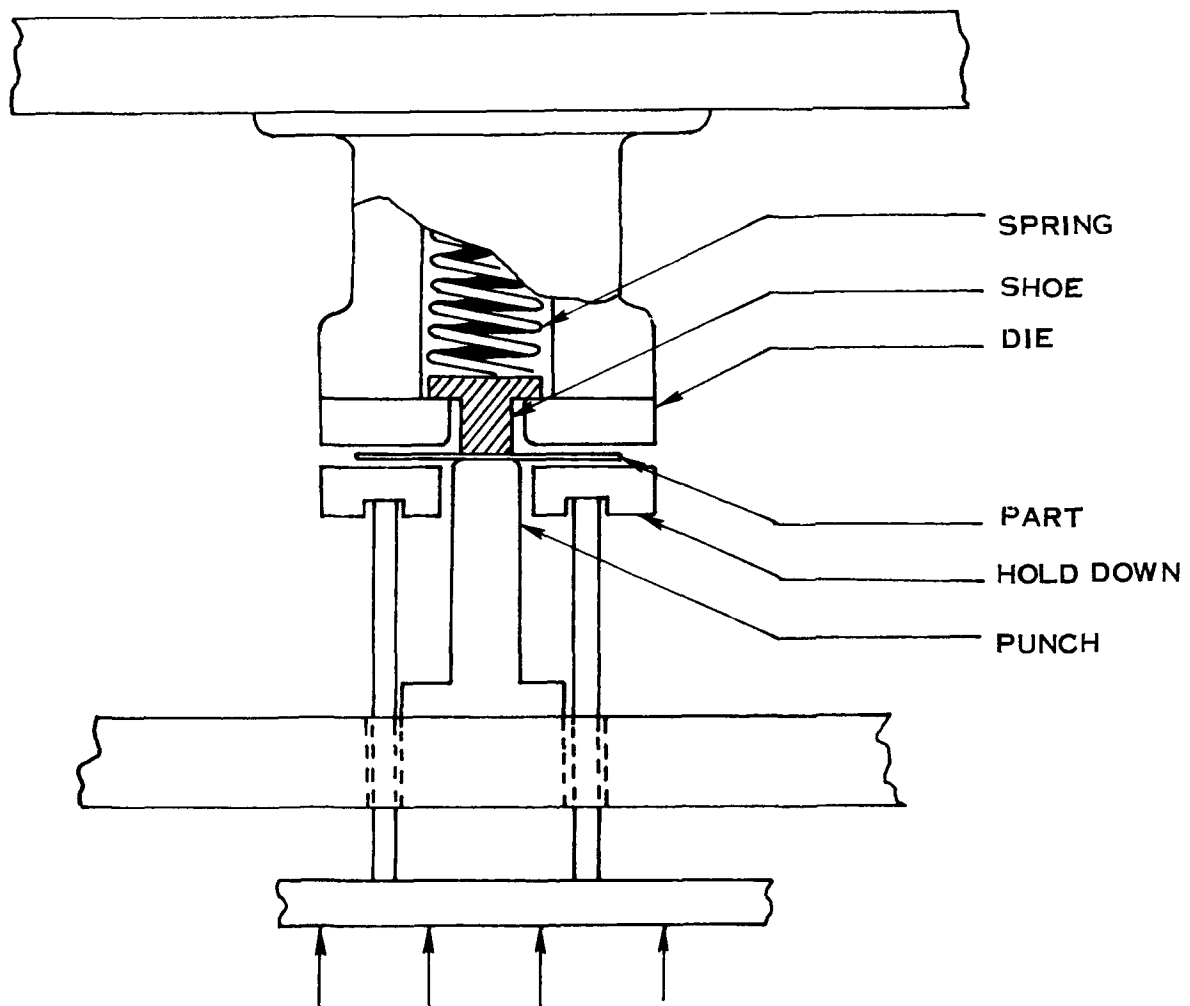


FIGURE I-91 SCHEMATIC OF DRAW PRESS AND TOOLING

The deep draw punches and die rings, shown in Figure I-92, were used to form parts ranging in diameter from $2\frac{1}{2}$ to 10 inches. The tools were fabricated from hardened steel and chrome plated to reduce friction to a minimum. Further friction reduction was accomplished with International Drawing compound - 155 DS.

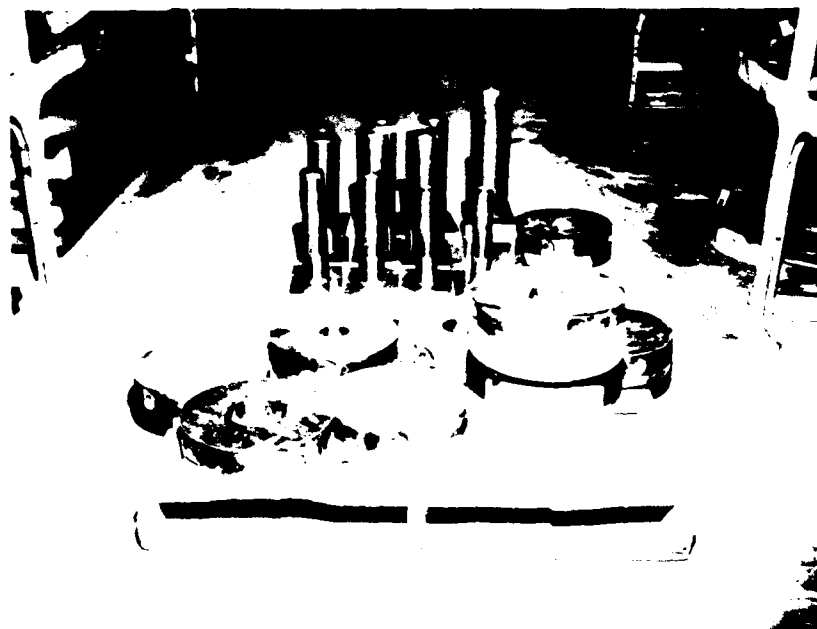
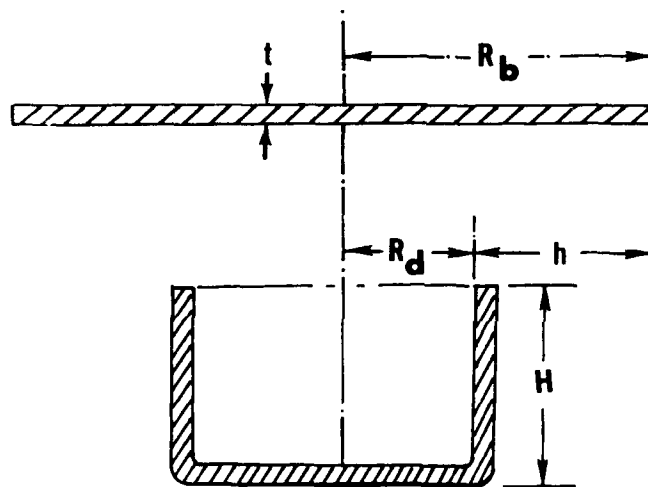


FIGURE I-92 DEEP DRAW TOOLING

The parameters for deep drawing, as shown in Figure I-93, are blank radius (R_b), flange height before forming (h), and material thickness (t). The relationship of the flange before forming (h) to the final cup depth (H) is developed in Chapter II of this report.



$$h = R_b - R_d$$

FIGURE I-93 PARAMETERS FOR DEEP DRAWING

The sketch in Figure I-94 illustrates the compression that results as a given segment of the blank conforms to the draw ring and corresponding punch. Each segment on the blank compresses a different amount as the part is drawn to the punch because each segment is at an increasingly larger distance away from the punch radius.

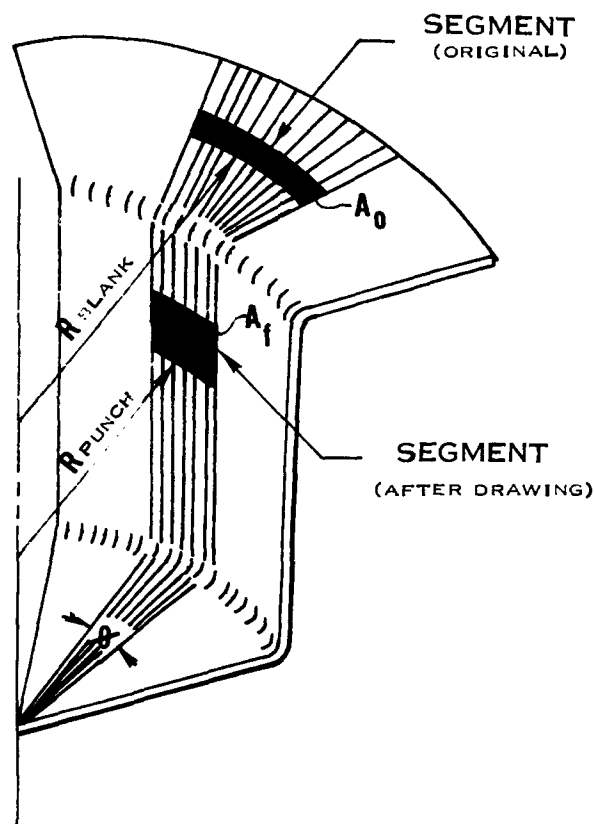


FIGURE I-94 CIRCUMFERENTIAL COMPRESSION IN DEEP DRAWING

The maximum principle strain in deep drawing is defined as the strain that occurs from actually stretching the part and not the "free" strain (Poisson's Effect) that occurs from circumferential compression. The actual compression that occurs after the part has been drawn over the punch is equal to zero. The "free" strain from circumferential compression is illustrated in Figure I-95.

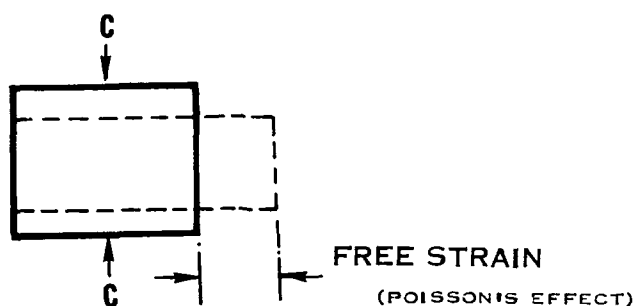


FIGURE I-95 FREE-STRAIN FROM CIRCUMFERENTIAL COMPRESSION

The failures in deep drawing are circumferential buckling (wrinkling) and splitting in the cup wall at the point of maximum stretching as illustrated in Figure I-96.

Splitting results from the punch force being transferred from the cup bottom into the cup wall which is subject to axial tensile stresses. As the drawing operation is continued, thinning occurs in the cup wall near the punch radius and results in splitting.

The axial tensile stresses in the cup wall produce reactive stresses which circumferentially compress and radially stretch the flange. The hoop stresses introduced cause wrinkling in the flange under the pressure ring. If the pressure is excessively increased to stop wrinkling, premature splitting failure may result.

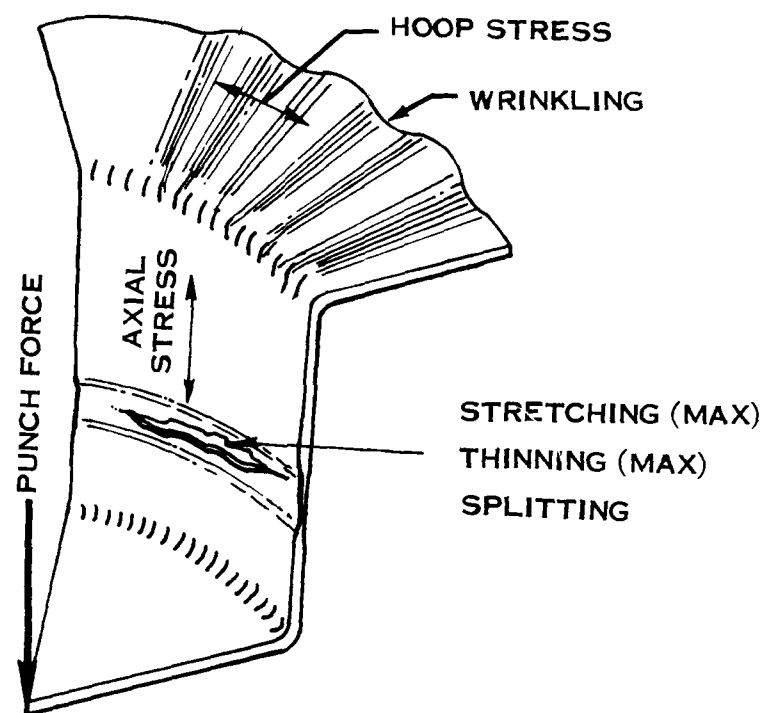


FIGURE I-96 FAILURES FOR DEEP DRAWN PARTS

The deep draw curve, illustrated in Figure I-97, is defined by good parts below the curve and failed (buckled and split) parts above the curve. Buckled parts are drawn until splitting occurs to assure that the buckling can not be removed by increased pad pressure.

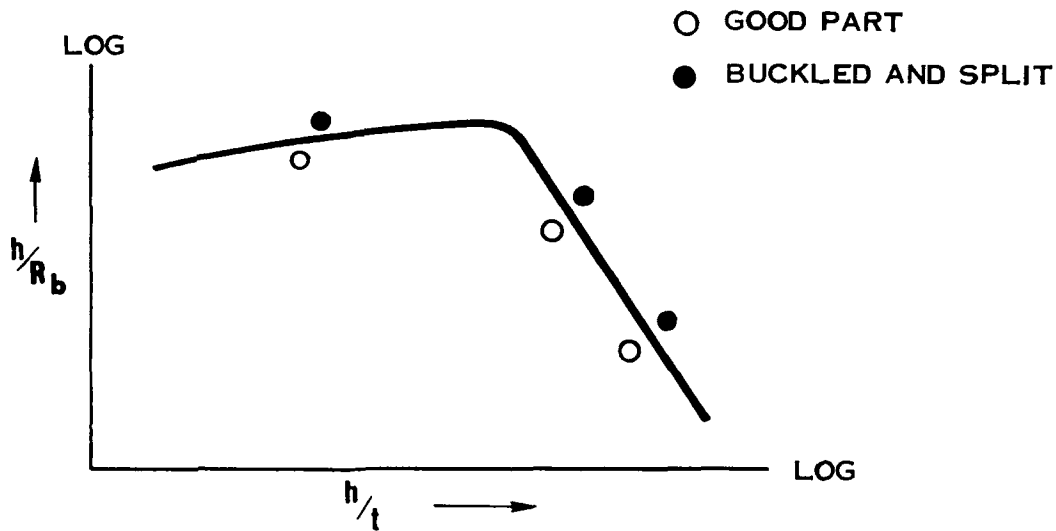


FIGURE I-97 DEEP DRAW LIMIT CURVE

The applied stress and the strain diagram of a deep draw sample is illustrated in Figure I-98. The strain diagram shows $\bar{\epsilon}_L = \bar{\epsilon}_t$ and $\bar{\epsilon}_w = 0$; therefore, $\bar{\epsilon}_L / \bar{\epsilon}_w = \infty$. The value for $\bar{\epsilon}_L / \bar{\epsilon}_e = 0.866$ was determined by the Energy of Distortion Theory and allows the process to be plotted on the "Effective Strain" Ellipse in Figure I-133 for correlation to the standard tensile specimen.

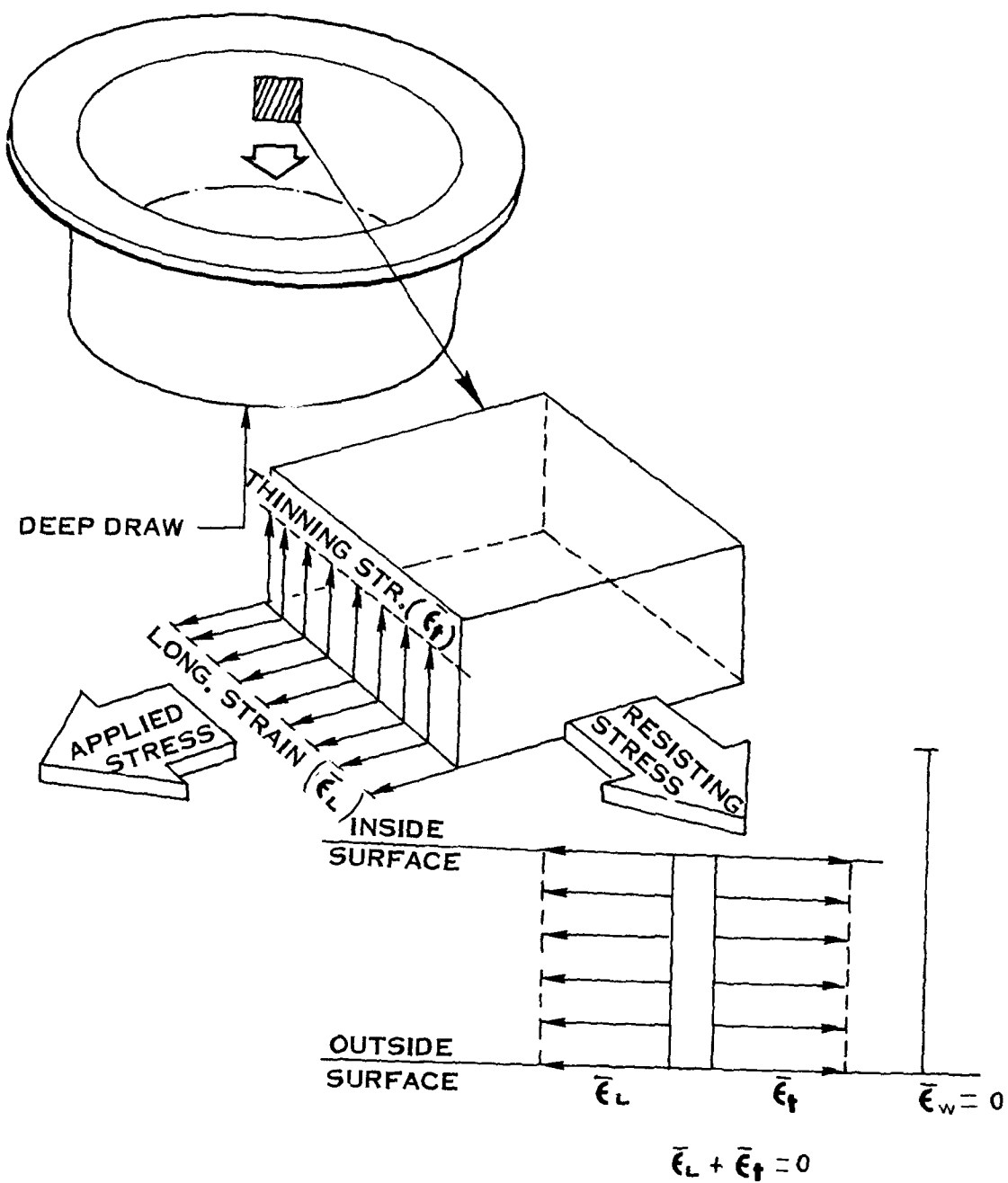


FIGURE I-98 APPLIED STRESS AND STRAIN DIAGRAM FOR DEEP DRAWING

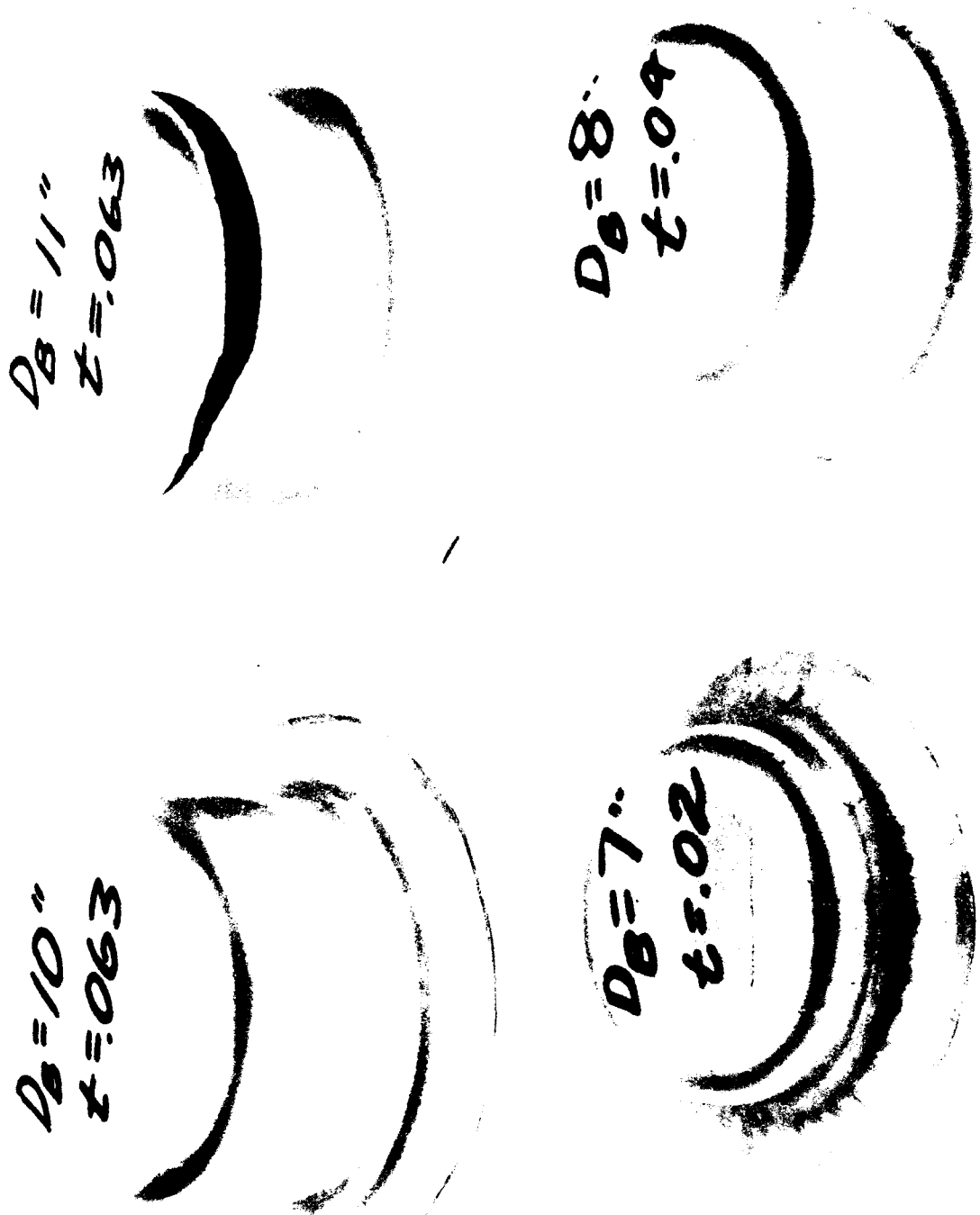


FIGURE I-99 BUCKLING AND SPLITTING OF DEEP DRAW PARTS

SPINNING

Spinning is another method of forming deep recessed parts. The principle difference between spinning and deep drawing is that deep drawing produces a uniform pressure on the drawing flange to prevent buckling whereas spinning has only the pressure of the forming and back-up bars in this area. A 5 horsepower, variable speed, Model 1006 Spin Master, shown in Figure I-100, was used to form cylindrical cups for this program.



FIGURE I-100 MODEL 1006 HAAG SPIN MASTER

The spinning dies, shown in Figure I-101, were used to form spun parts ranging in diameter from 2.5 to 5 inches. Two spinning dies with diameters of 7 and 10 inches were fabricated late in the program to substantiate the forming limits for each material gage used.

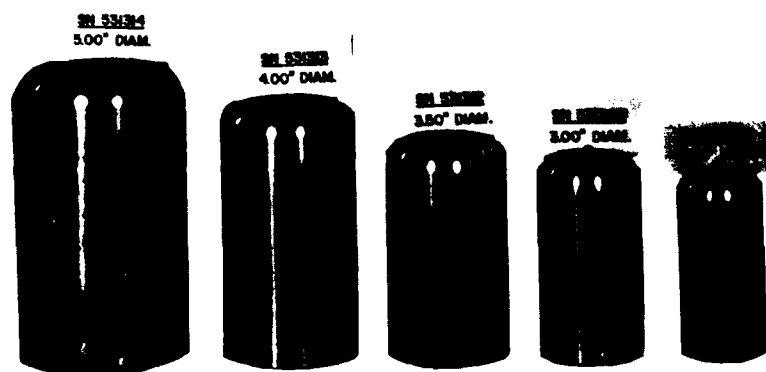


FIGURE I-101 SPINNING DIES

The procedure used for spinning the cylindrical cups is illustrated by the sketches in Figures I-102, I-103, I-104 and I-105. Figure I-102 shows the blank centered over the 1/4 inch pin in the spinning block with the edge trimmed and rounded off with a carbide cutter and sanded with No. 200 and 400 grit sandpaper. Lubriplate is then applied over the complete surface of the part. The part is formed around the die radius and the final friction block inserted to prevent radius hump as shown in Figure I-103. The steady rest is then rotated parallel to the center line of the spinning block and moved closer to the part if necessary. Figure I-104 shows the phenolic tip replaced by a brass tip for the high strength materials. The part is formed to the die by forming a 1/4 to 3/4 inch flange on the edge with the back-up bar, thus enabling the part to be spun flush to the die. For the higher strength materials a ball bearing steel roller can be used to form the flange to the die.

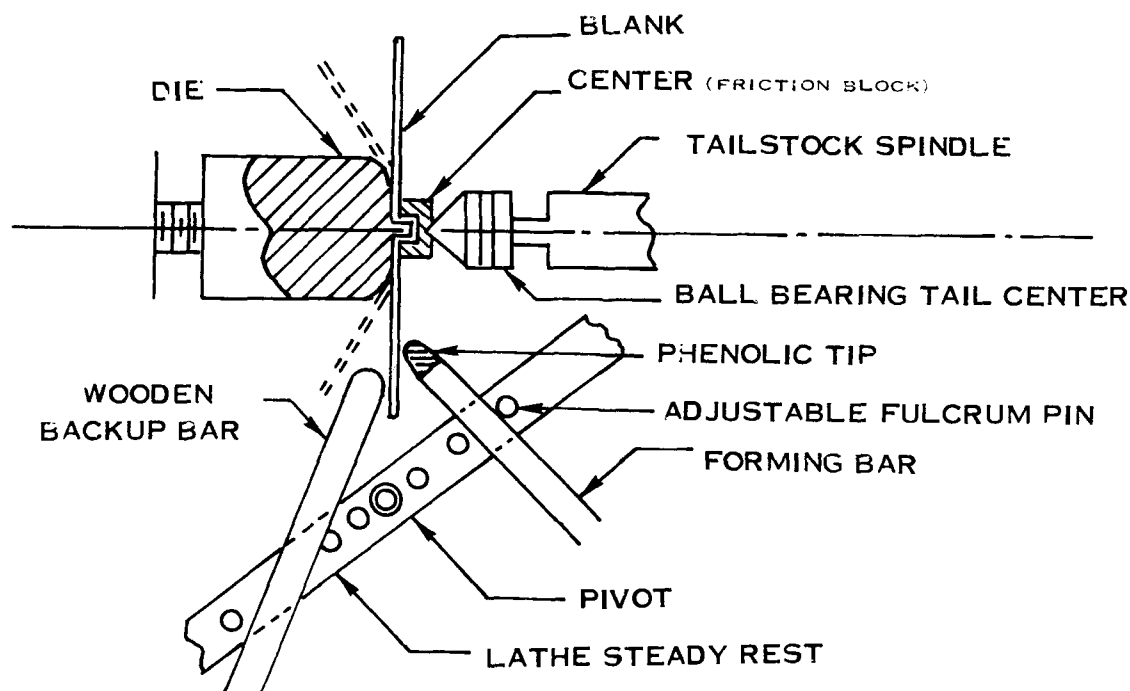


FIGURE I-102 SPINNING PROCEDURE (STEP 1)

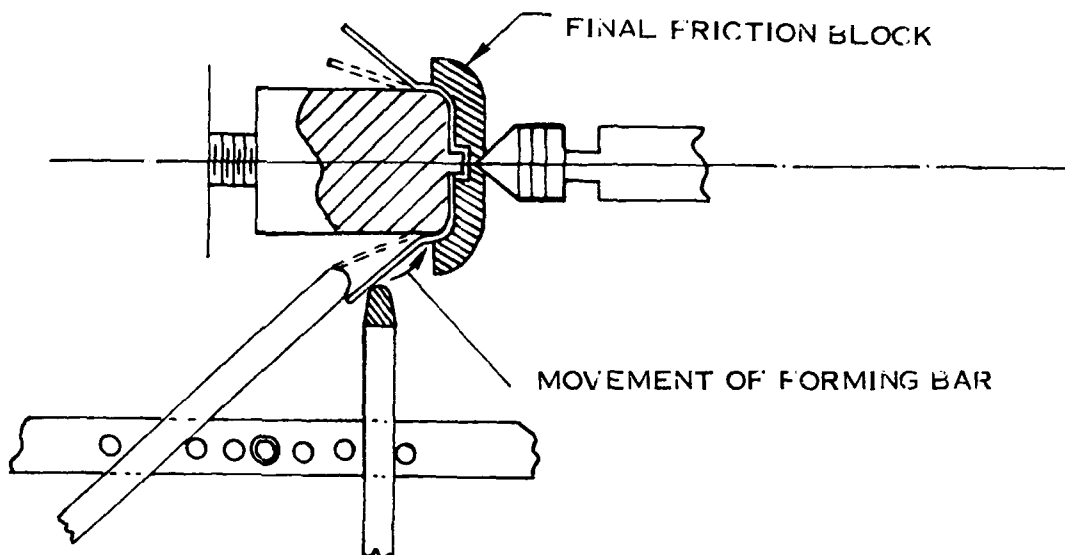


FIGURE I-103 SPINNING PROCEDURE (STEP 2)

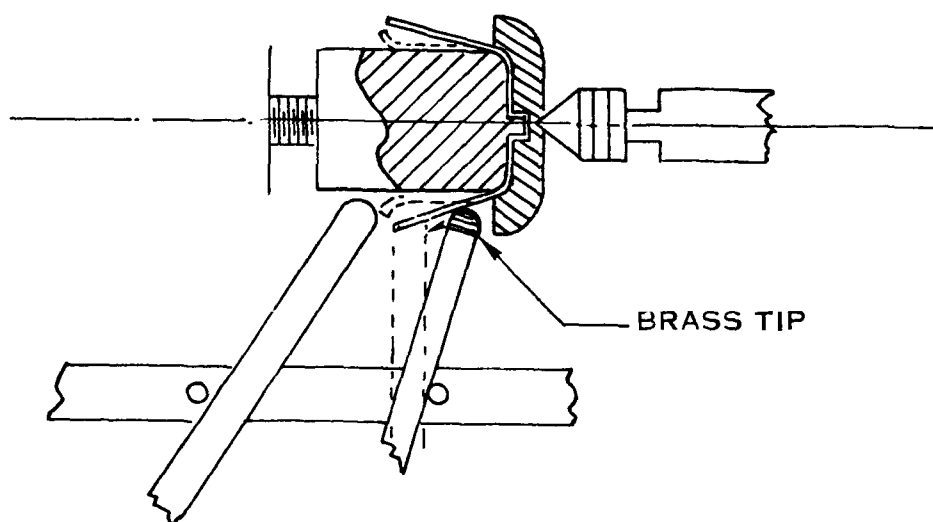


FIGURE I-104 SPINNING PROCEDURE (STEP 3)

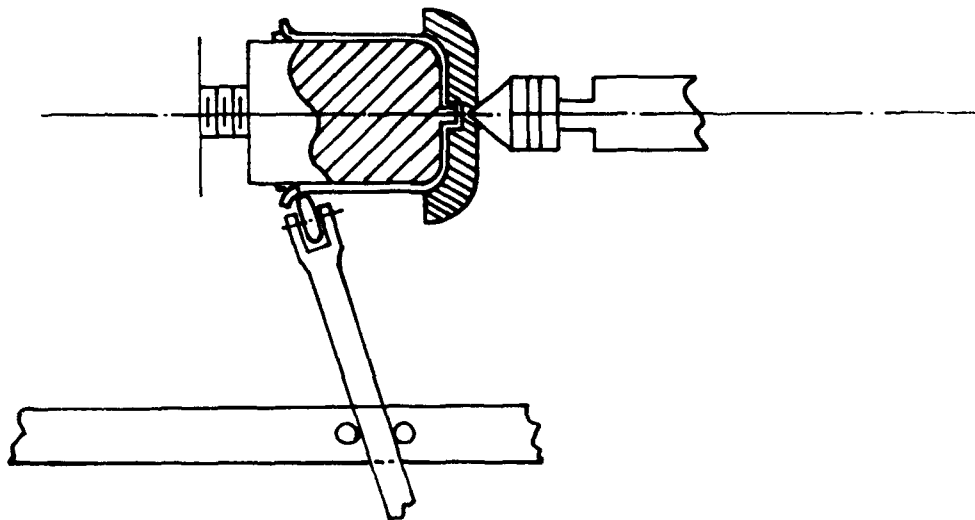


FIGURE I-105 SPINNING PROCEDURE (STEP 4)

The parameters for spinning, as shown in Figure I-106, are blank radius (R_b), flange height before forming (h) and material thickness (t). The relationship of the flange before forming (h) to the final cup depth (H) is developed in Chapter II of this report.

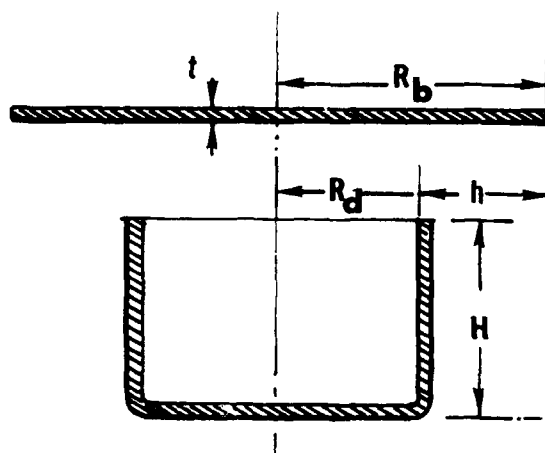


FIGURE I-106 PARAMETERS FOR SPINNING

The sketch in Figure I-107 illustrates the compression that results as a given segment of the blank conforms to the spinning die. As in deep drawing, each segment on the blank compresses a different amount as the part is spun to the die because each segment is at an increasingly larger distance away from the die radius.

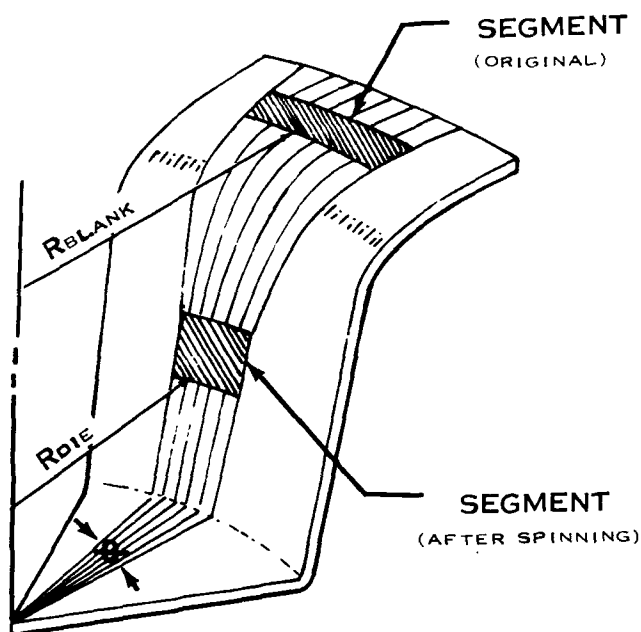


FIGURE I-107 CIRCUMFERENTIAL COMPRESSION IN SPINNING

The maximum principle strain in spinning is defined as the strain that occurs from actually stretching the part and not the "free" strain (Poisson's Effect) that occurs from circumferential compression. The actual compression that occurs after the part has been spun over the die is equal to zero. The "free strain" from circumferential compression is illustrated in Figure I-108.



FIGURE I-108 FREE-STRAIN FROM CIRCUMFERENTIAL COMPRESSION

The failures in spinning are sine wave plate buckling, plastic buckling, circumferential splitting and shear splitting.

Elastic buckling, illustrated in Figure I-109, takes the form of sinusoidal waves and occurs when the critical buckling strength of the material at a given slenderness ratio (h/t) is less than the yield strength.

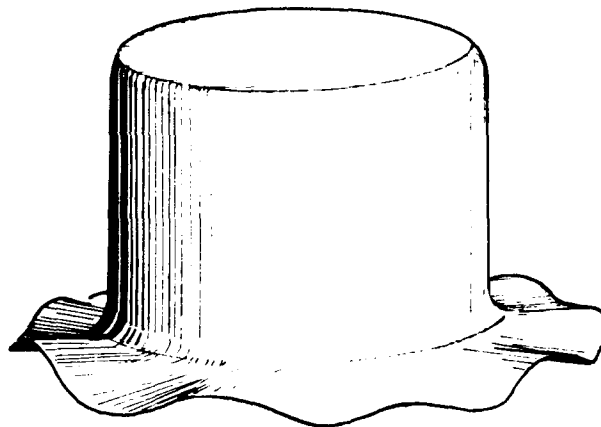


FIGURE I-109 ELASTIC BUCKLING FAILURE FOR SPINNING

Plastic buckling, illustrated in Figure I-110 occurs when the slenderness ratio (h/t) is small and the critical buckling strength of the material is higher than the yield strength. This type of failure is usually accompanied by shear splitting that occurs when the operator tries to remove the plastic buckling.

Circumferential splitting, illustrated in Figure I-111, results when the operator uses excessive wiping action in an attempt to remove previous buckling. However, splitting occurs at a higher value of h/R_b than plastic buckling, therefore, eliminating it as a major failure.

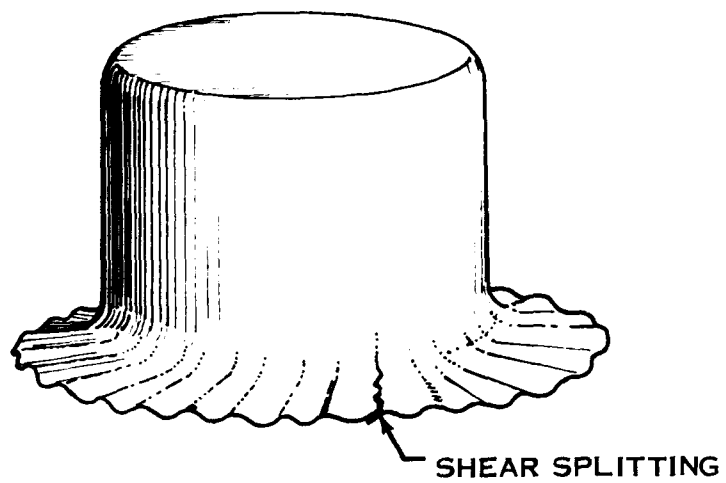


FIGURE 1-110 PLASTIC BUCKLING AND SHEAR SPLITTING FAILURES FOR SPINNING

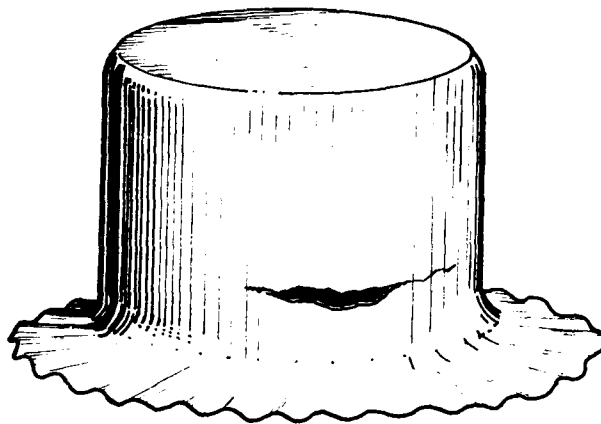


FIGURE 1-111 CIRCUMFERENTIAL SPLITTING FAILURE FOR SPINNING

The spinning curve, illustrated in Figure I-112, is defined by good parts below the curve and failed parts above the curve. Elastic buckling results for high values of h/t while plastic buckling and shear splitting occur for small values of h/t . Circumferential splitting occurs at a higher value of h/R_b than plastic buckling and considered as a secondary failure.

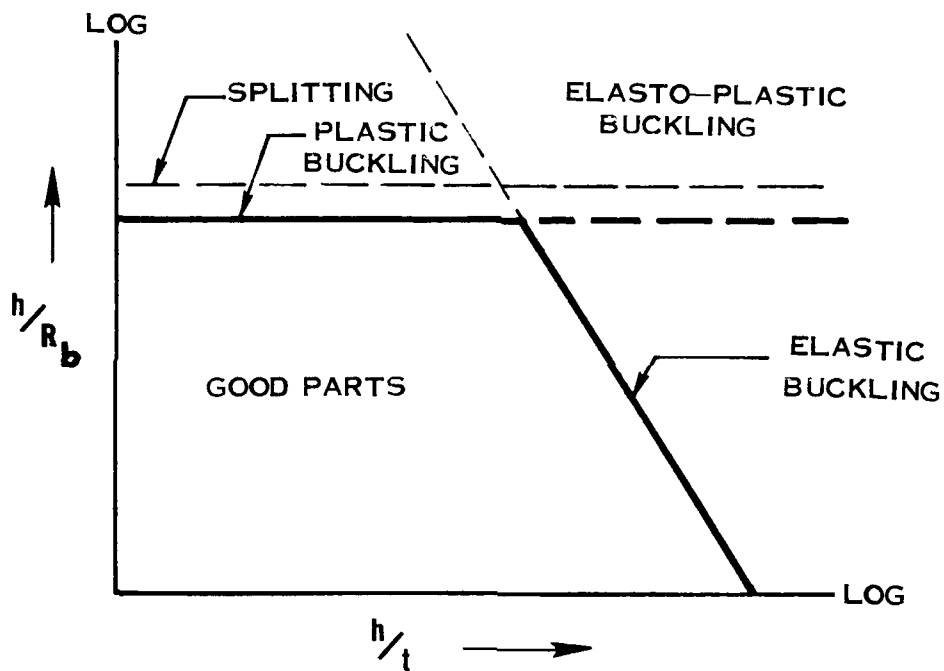


FIGURE I-112 SPINNING LIMIT CURVE

The applied stress and the strain diagram of a spinning sample is illustrated in Figure I-113. The strain diagram shows $\bar{\epsilon}_L = \bar{\epsilon}_t$ and $\bar{\epsilon}_w = 0$; therefore, $\bar{\epsilon}_L / \bar{\epsilon}_w = \infty$. The value for $\bar{\epsilon}_L / \bar{\epsilon}_\theta = 0.866$ was determined by the Energy of Distortion Theory and allows the process to be plotted on the "Effective Strain" Ellipse in Figure I-133 for correlation to the standard tensile specimen.

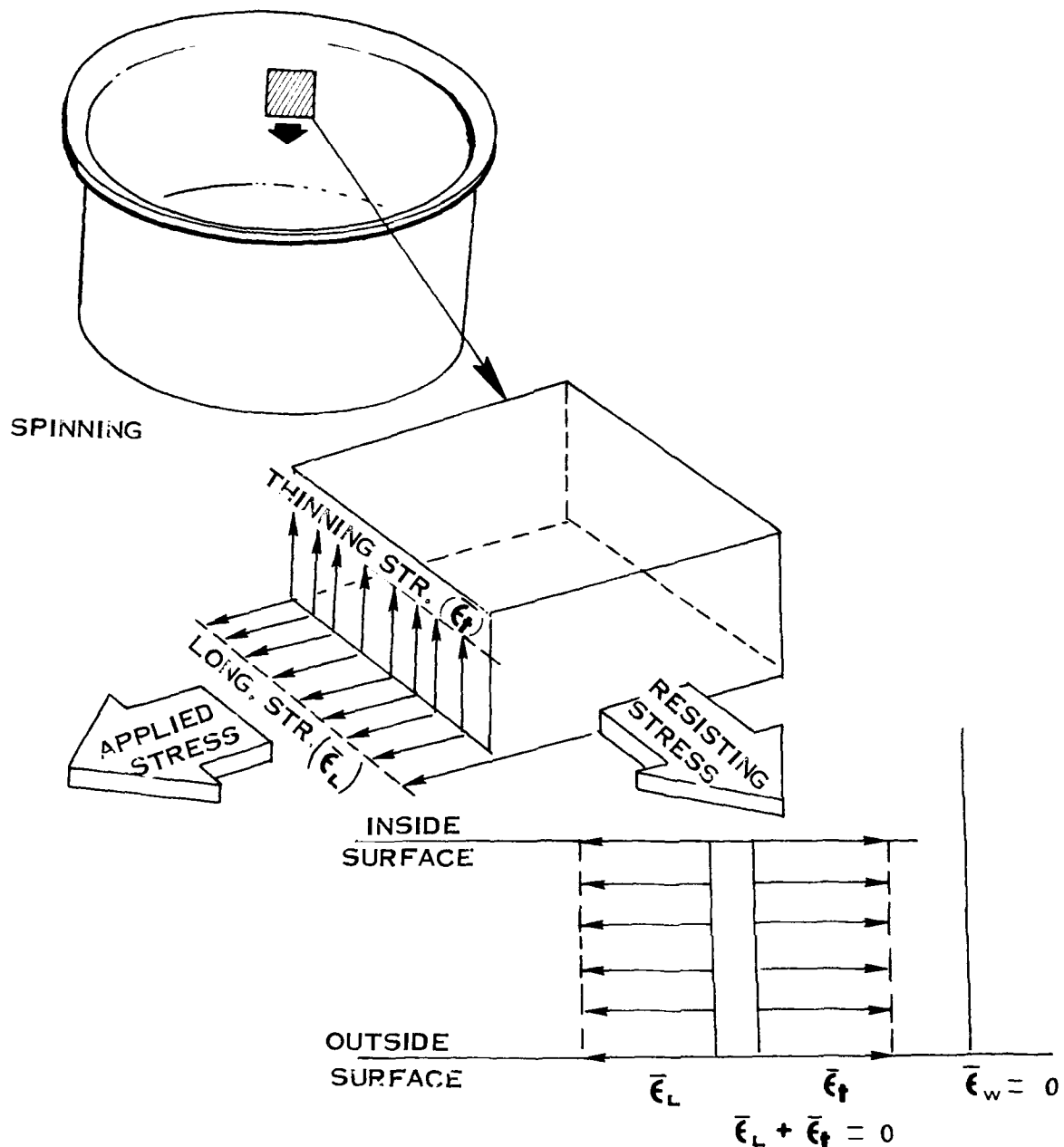


FIGURE I-113 APPLIED STRESS AND STRAIN DIAGRAMS FOR SPINNING



FIGURE I-114 SHEAR SPLITTING (MIDDLE) AND CIRCUMFERENTIAL SPLITTING (RIGHT) OF SPUN PARTS

RUBBER PRESS BEADING

Beading, a shallow recessing process, is the principal method used for achieving stiffness in thin sheet metal panels. Although the rubber beading process is commonly used, drop hammer beading is considered to be a much superior process. A 3,000 psi HPM Die Press, shown in Figure I-115, was used to form the rubber formed beaded panels for this program.



FIGURE I-115 3,000 PSI. HPM DIE PRESS

The tooling for rubber press beading, shown in Figure I-116, consists of a base plate with tooling holes to accommodate different size bead inserts and allow a variable bead spacing in increments of $3/8$ inch. The bead inserts range in radius from $1/4$ to $3/4$ inches.



FIGURE I-116 RUBBER BEAD TOOLING

The parameters for rubber beading are bead radius (R), distance between bead centers (L) and material thickness (t) as shown in Figure I-117.

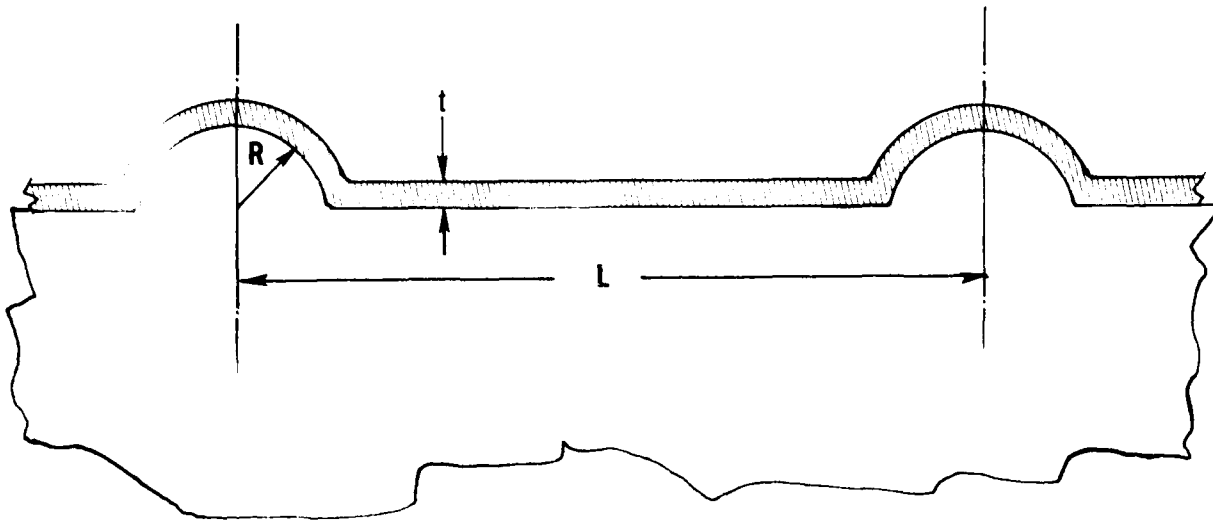


FIGURE I-117 PARAMETERS FOR RUBBER BEADING

The most objectionable limitation of rubber beading is the large free-form bend radius (r) that a given material will form regardless of the bead height or spacing due to insufficient pressure. Since this free-form radius, illustrated in Figure I-118, is independent of the bead radius (R) and the distance between beads (L), it cannot be plotted on the formability curve. However, an expression for this radius is derived in Chapter II.

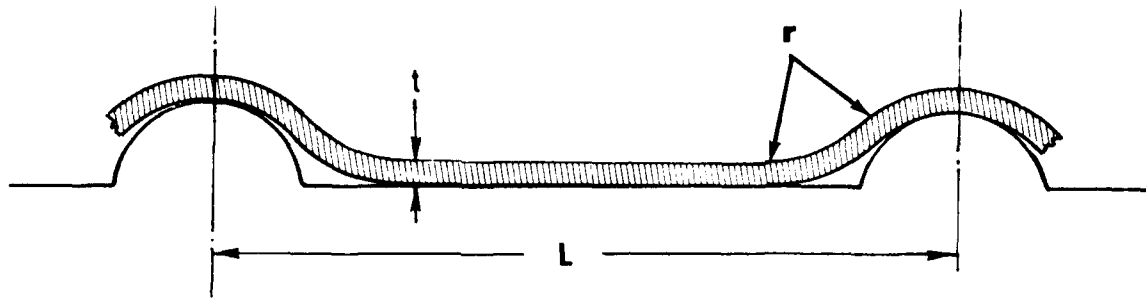


FIGURE I-118 FREE FORM RADIUS IN RUBBER BEADING

The major failure in rubber beading is splitting in the free-form radius area as illustrated in Figure I-119. This failure results when the available elongation of a given material is exceeded.

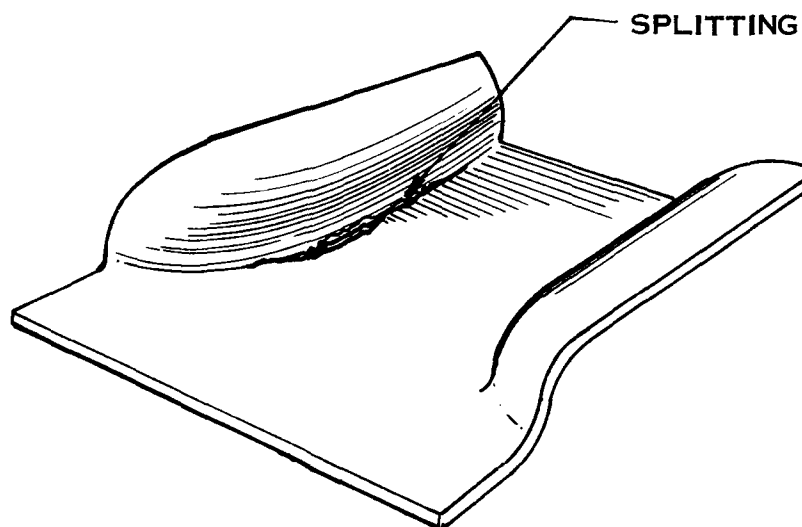


FIGURE I-119 MAJOR SPLITTING FAILURE IN RUBBER BEADING

Splitting failures occurring at the top of the bead, illustrated in Figure I-120, are due to bending strain superimposed on the forming strain. If the forming strain is greater than the allowable bending strain of the material, failure will occur before the part is completely formed.

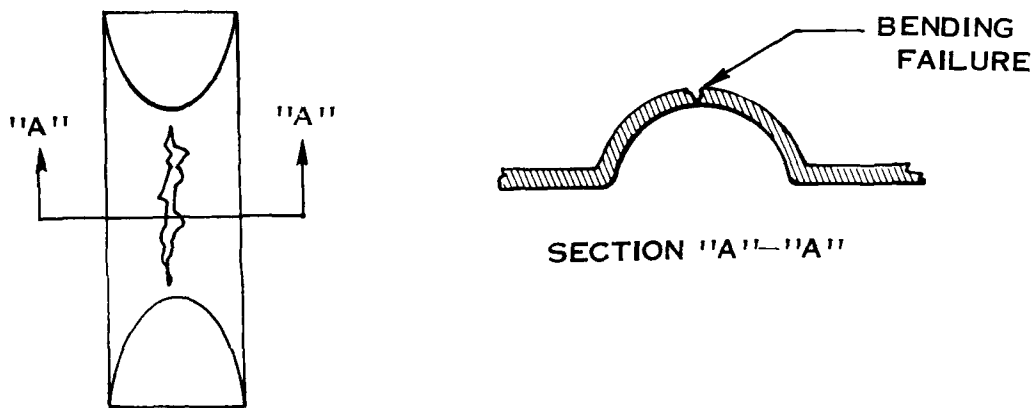


FIGURE I-120 BENDING FAILURES IN RUBBER BEADING

Buckling in the panel between the beads occurred for large bead radii. This buckling was not considered because increasing the bead length to bead radius ratio will eliminate the buckling.

The rubber beading limit curve, illustrated in Figure I-121, is defined by good parts below the curve and failed parts above the curve. Splitting results for high values of R/L and R/t .

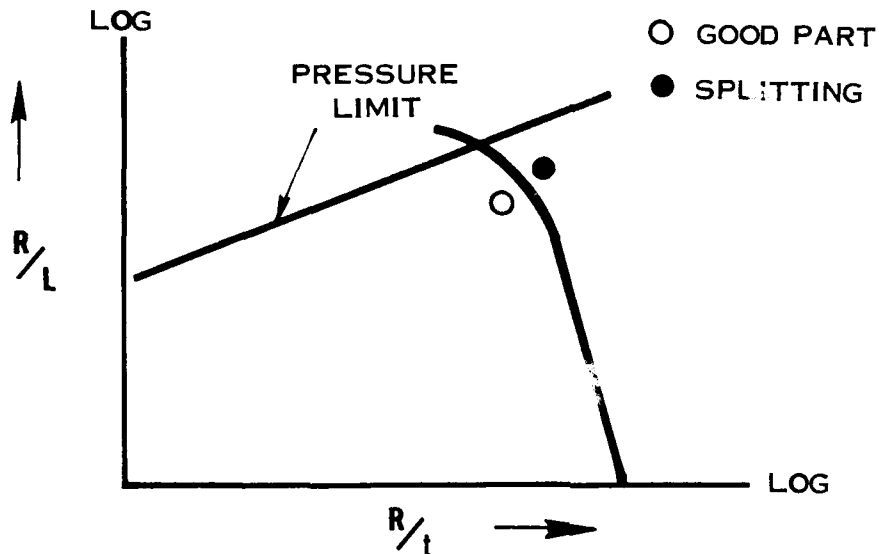
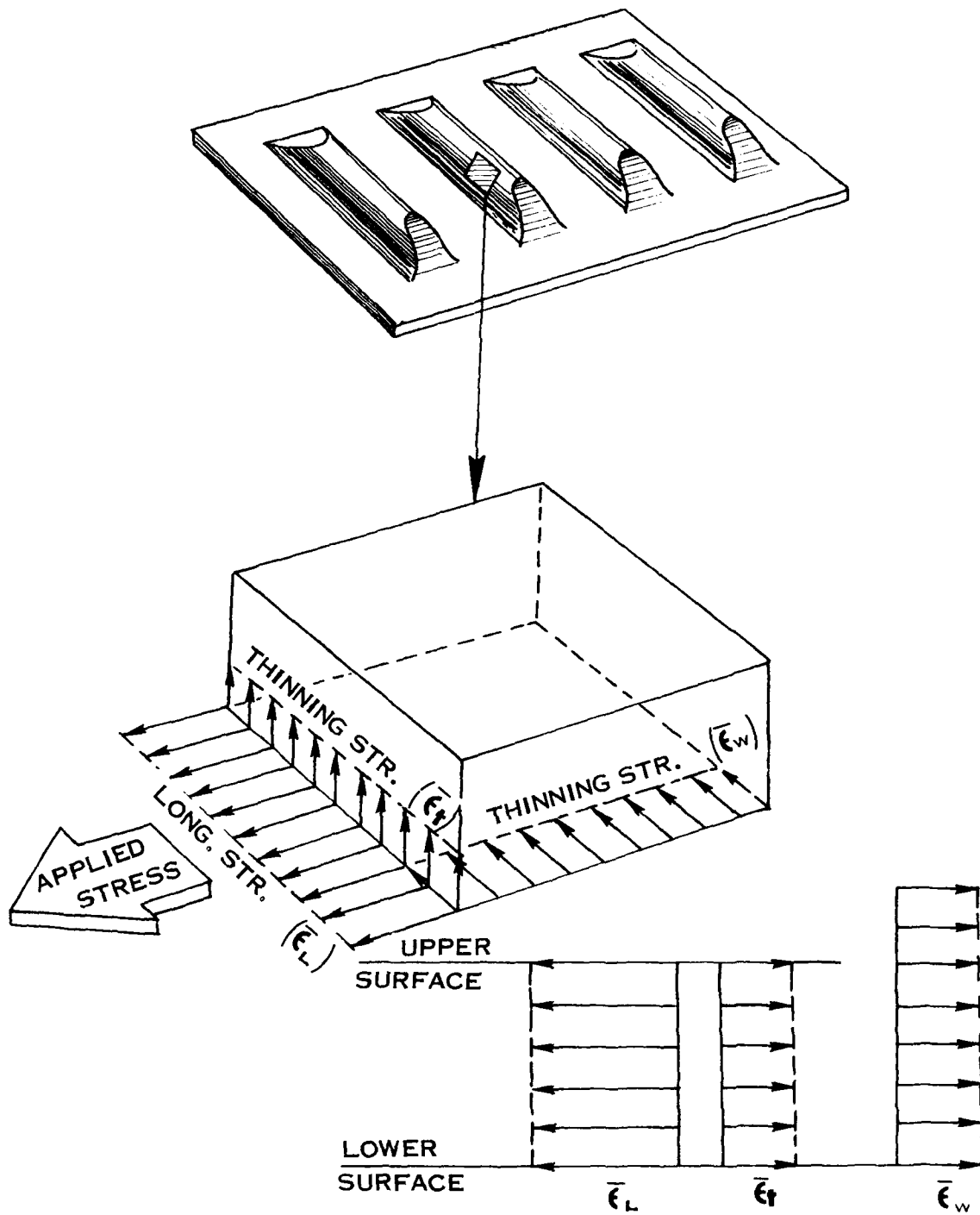


FIGURE I-121 RUBBER BEADING LIMIT CURVE

The applied stress and the strain diagrams for a rubber formed beaded panel is shown in Figure I-122. The strain diagram shows $\bar{\epsilon}_L + \bar{\epsilon}_w + \bar{\epsilon}_t = 0$. The value for $\bar{\epsilon}_L / \bar{\epsilon}_e = 0.925$ was determined by the Energy of Distortion Theory using empirical data and allows the rubber beading process to be plotted on the "Effective Strain" Ellipse in Figure I-133 for correlation to the standard tensile specimen.



$$\bar{\epsilon}_L + \bar{\epsilon}_t + \bar{\epsilon}_w = 0$$

FIGURE 1-122 APPLIED STRESS AND STRAIN DIAGRAM FOR RUBBER BEADING

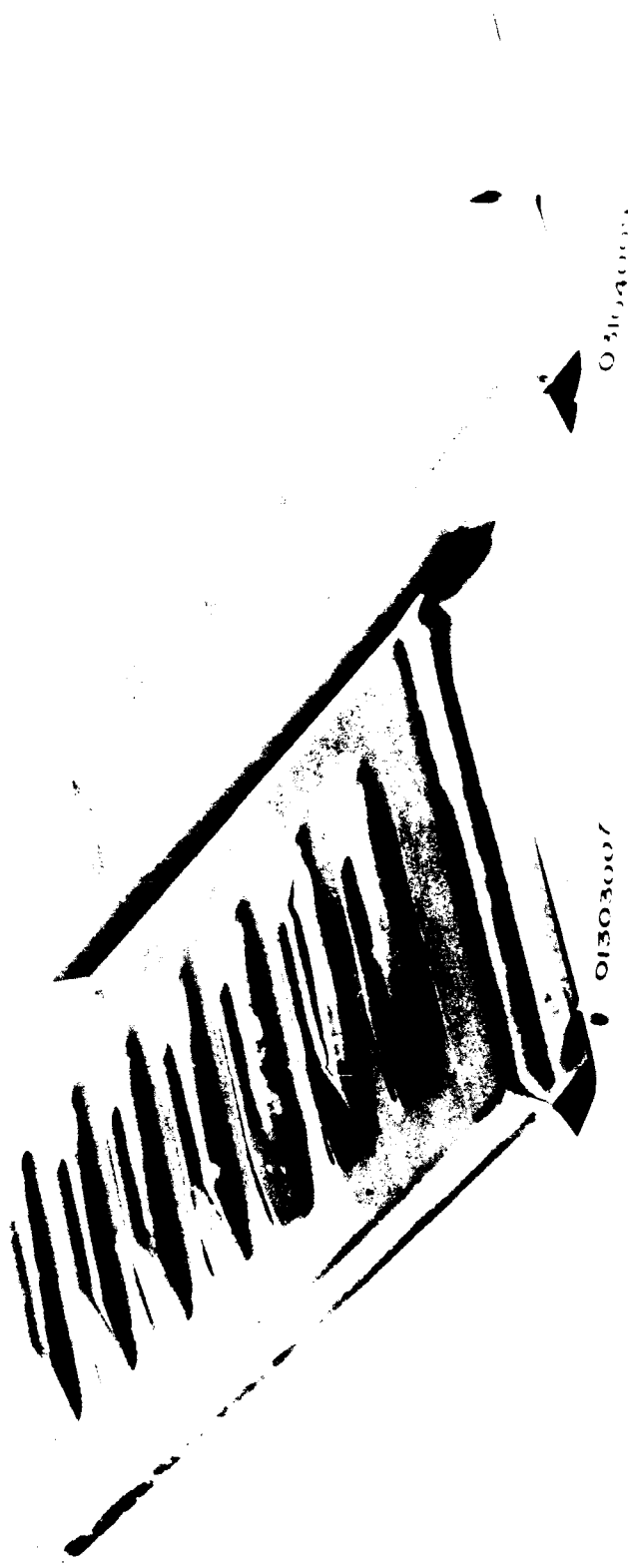


FIGURE I-123 SPLITTING FOR RUBBER FORMED BEADED PANELS

DROP HAMMER BEADING

As previously stated, drop hammer forming is considered to be the superior shallow recessing process for beading. An air operated Cecostamp Drop Hammer shown in Figure I-124, was used to form the drop hammer beaded panels for this program.



FIGURE I-124 CECOSTAMP DROP HAMMER

The drop hammer dies, partially shown in Figure I-125, provide bead spacings of 2 to 5 inches for the $\frac{1}{2}$ inch radius beads and 3 to $5\frac{1}{2}$ inches for the 1 inch radius beads.

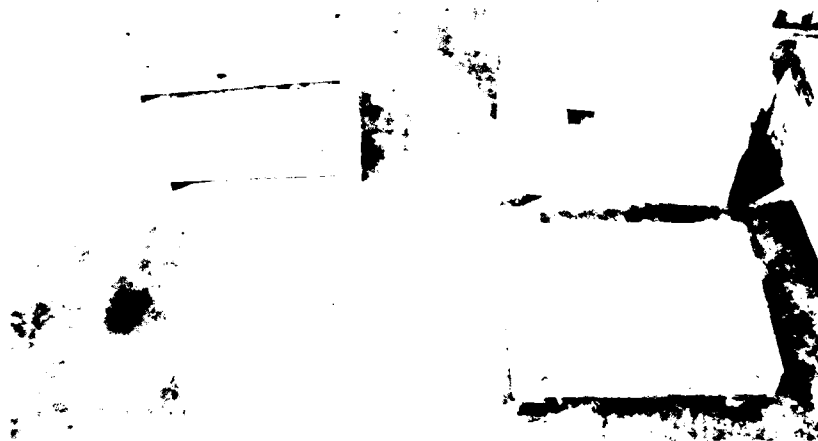


FIGURE I-125 DROP HAMMER BEADING DIES

The parameters for drop hammer beading are bead radius (R), distance between bead centers (L) and material thickness (t), as shown in Figure I-126.

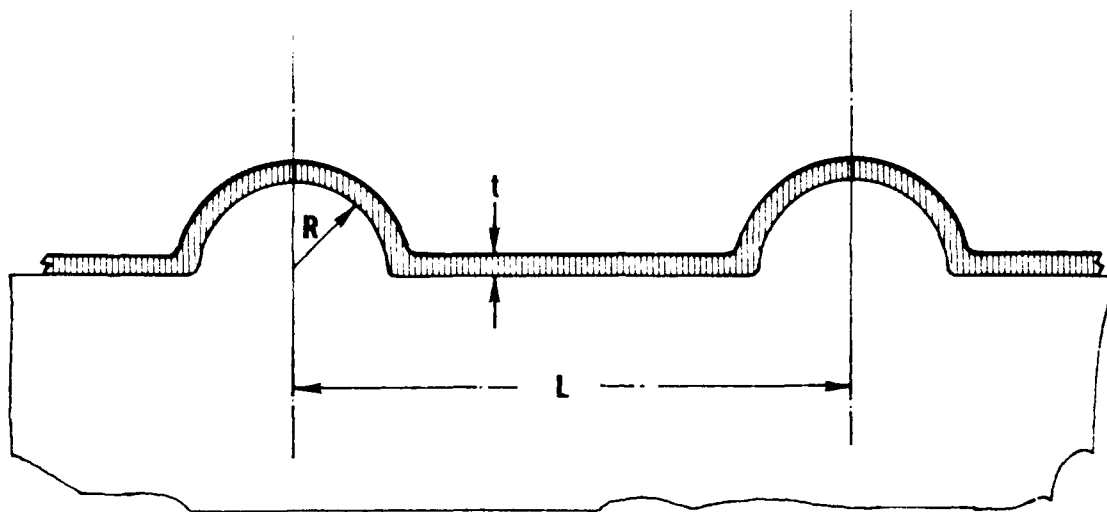


FIGURE I-126 PARAMETERS FOR DROP HAMMER BEADING

The forming process is accomplished in several stages starting with thick rubber strips and reducing the strips at each stage until the final stage which is accomplished without the strips. The sketches in Figure I-127, illustrates only the initial and final stages. As the material is bent around the bead radius in the initial stage (Position A), the bending strain superimposed upon the forming strain (ϵ_1 , total at a) gives a distribution as shown in A. If ϵ_1 is greater than the maximum allowable bending strain of the material, then failure will occur at the top of the bead before the part is completely formed. If ϵ_1 is less than the maximum allowable bending strain of the material the part will develop a strain distribution as shown in B and the part will fail at point (d) where ϵ_2 is maximum strain. The two types of splitting are illustrated in Figure I-128.

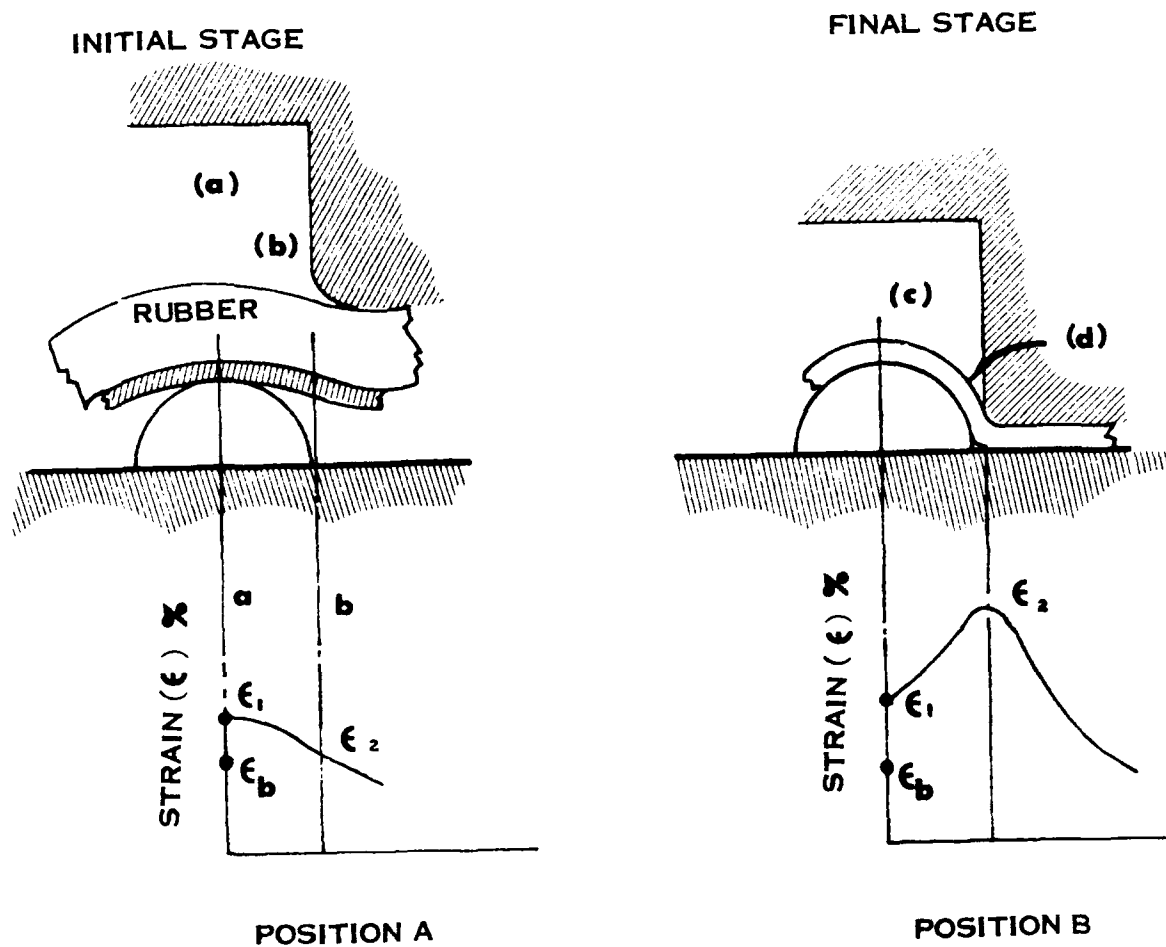
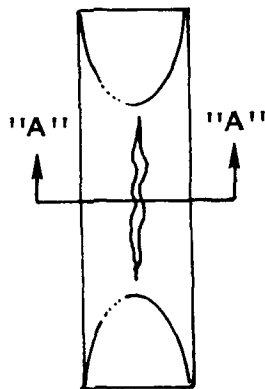


FIGURE I-127 INITIAL AND FINAL STAGES OF DROP HAMMER FORMING

BENDING FAILURE

(BRITTLE)



SECTION "A"-"A"

DUCTILE FAILURE

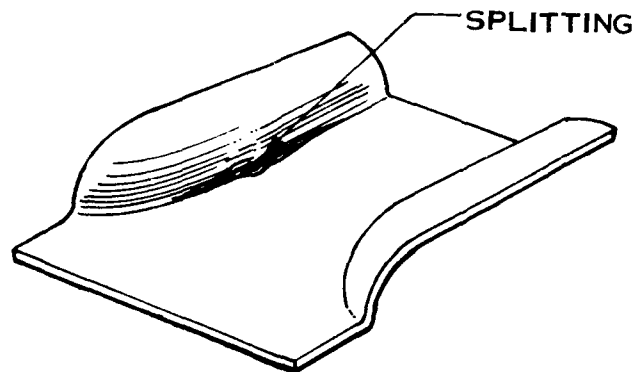


FIGURE I-128 SPLITTING FAILURES IN DROP HAMMER BEADING

The drop hammer limit curve, illustrated in Figure I-129, is defined by good parts below the curve and failed above the curve. Splitting results for high values of R/L and R/t .

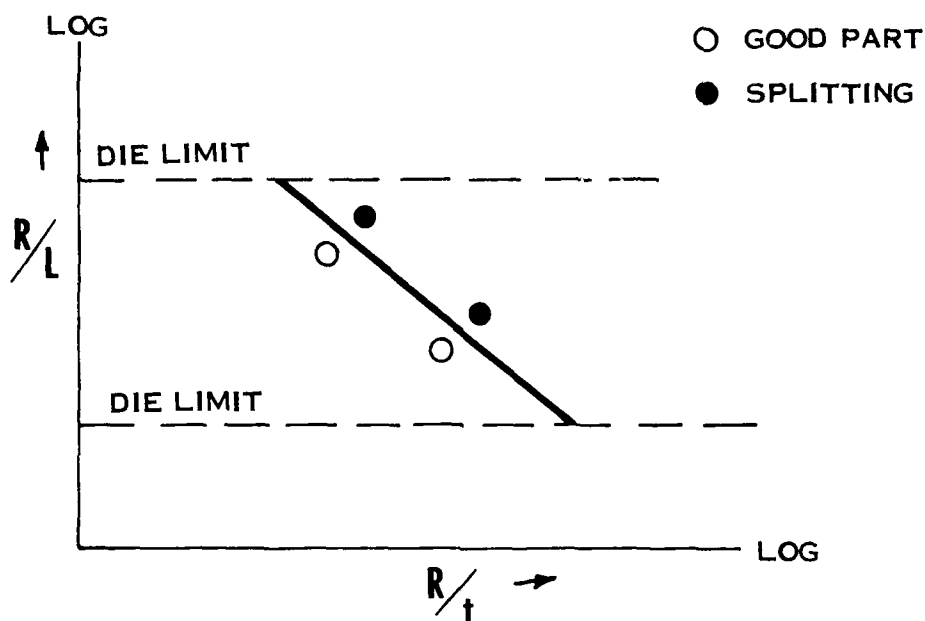


FIGURE I-129 DROP HAMMER BEADING LIMIT CURVE

The applied stress and the strain diagram of a drop hammer beaded part is illustrated in Figure I-130. The strain diagram shows $\bar{\epsilon}_L = \bar{\epsilon}_t$ and $\bar{\epsilon}_w = 0$; therefore, $\bar{\epsilon}_L / \bar{\epsilon}_w = \infty$. The value for $\bar{\epsilon}_L / \bar{\epsilon}_e = 0.866$ was determined by the Energy of Distortion Theory and allows the process to be plotted on the "Effective Strain" Ellipse in Figure I-133 for correlation to the standard tensile specimen.

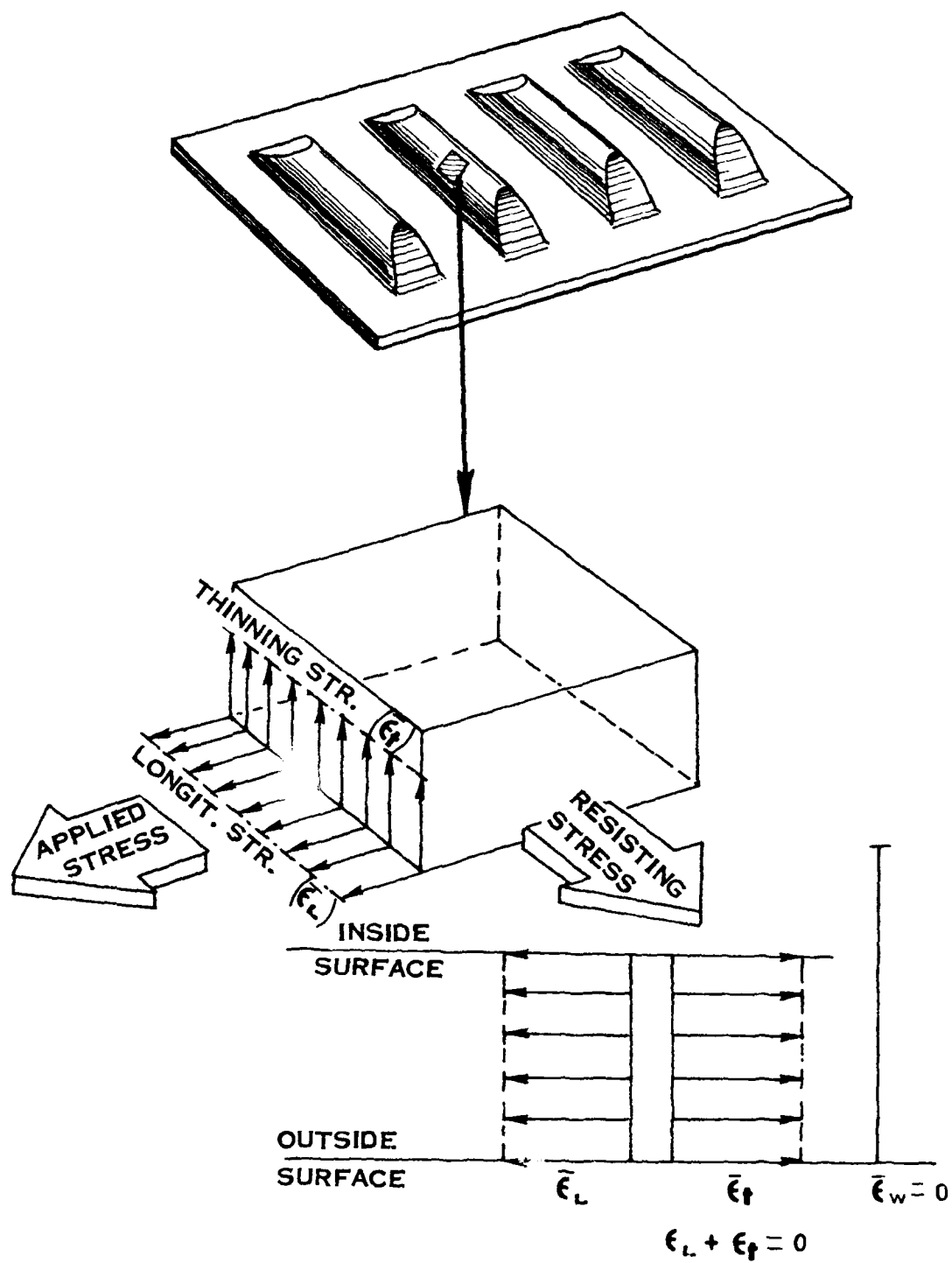


FIGURE I-130 APPLIED STRESS AND STRAIN DIAGRAM FOR DROP HAMMER BEADING

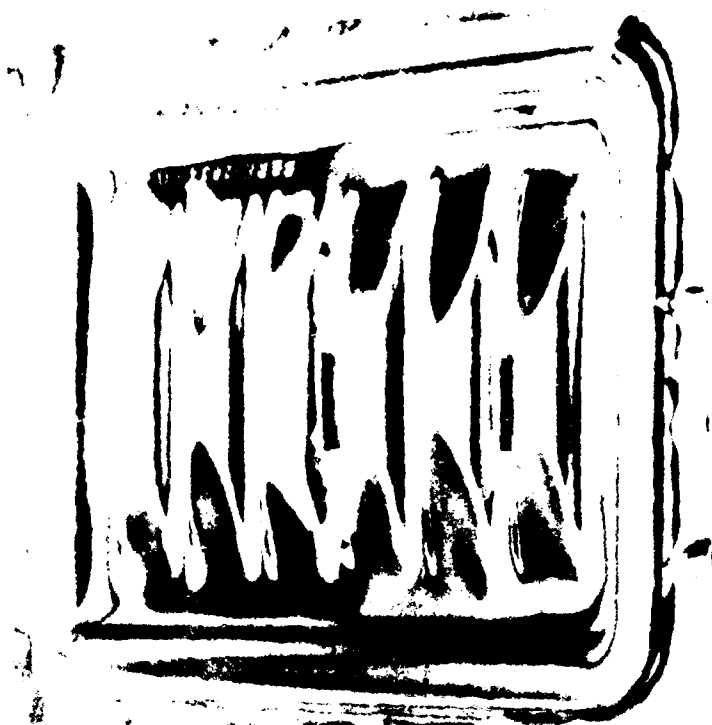


FIGURE I-131 SPLITTING FOR DROP HAMMER BEADED PANELS

EFFECTIVE STRAIN

The table in Figure I-132 gives the ratio of the longitudinal strain to width strain ($\bar{\epsilon}_L / \bar{\epsilon}_w$) and the ratio of longitudinal strain to "effective" strain ($\bar{\epsilon}_L / \bar{\epsilon}_e$) for all the processes with splitting as a major failure except Androforming. Androforming is not plotted on the "Effective Strain" Ellipse because heat treated materials were used that had elongations of only 6 to 8 percent. These small values of elongation allow considerable error in grid measurements for calculation of the "effective" strain.

The "Effective Strain" Ellipse in Figure I-133 is the combined strain condition for uniform strain up to necking. The strains for the processes plotted are uniform strains and do not violate the basic assumptions for the ellipse. The exceptions are strains used for brake forming and joggling that exceed the uniform strain. However, $\bar{\epsilon}_L / \bar{\epsilon}_w$ is equal to infinity (∞) for these processes regardless of the magnitude of the longitudinal strain ($\bar{\epsilon}_L$) since the width strain ($\bar{\epsilon}_w$) is equal to zero. For this reason, the brake forming and joggling processes are plotted with the other eight processes for comparison.

PROCESS	$\bar{\epsilon}_L / \bar{\epsilon}_w$	$\bar{\epsilon}_L / \bar{\epsilon}_e$
Brake Forming	∞	0.866
Joggling	∞	0.866
Dimpling	-2.15	1
Rubber Stretch Flanging	-2.46	0.990
Linear Stretch Forming	-1.48	0.980
Sheet Stretch Forming	-3.70	0.960
Deep Drawing	∞	0.866
Spinning	∞	0.866
Rubber Press Beading	-7.05	0.925
Drop Hammer Beading	∞	0.866

FIGURE I-132 STRAIN RATIOS FOR PLOTTING THE "EFFECTIVE STRAIN" ELLIPSE

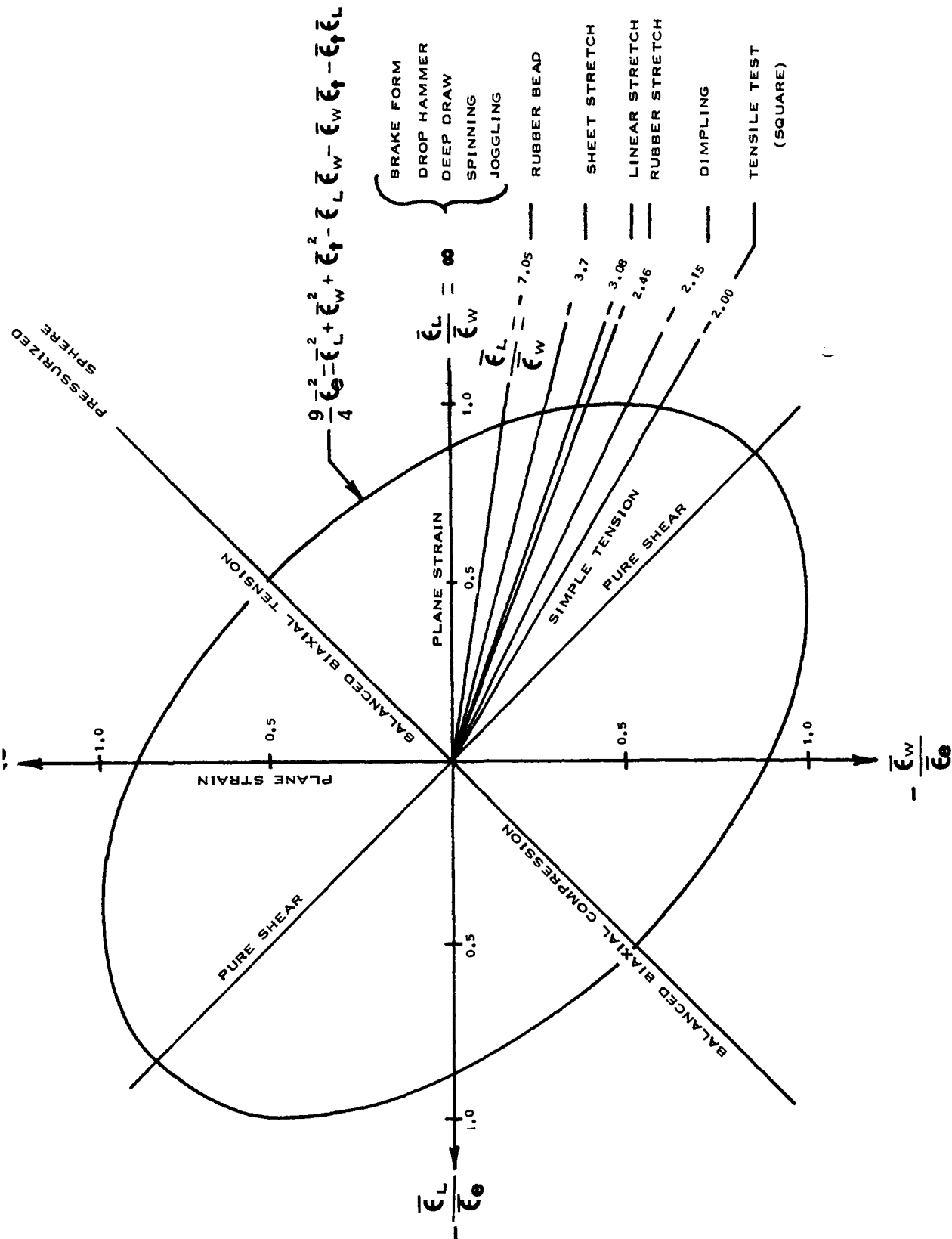


FIGURE I-133 "EFFECTIVE STRAIN" ELLIPSE FOR SHEET METAL FORMING

CHAPTER II
DEVELOPMENT OF BASIC EQUATIONS

SPLITTING THEORY

The factors determining the amount of strain that a part can be subjected to without failure are:

- (1) The material
- (2) Geometry of the part
- (3) The complete stress-strain state of the part (triaxial stress-strain consideration)
- (4) Strain gradients across the part
- (5) Stability against necking.

The material determines the amount of elongation a part can take before fracture. The geometry of the part indicates the amount of strain that has to occur to develop a certain shape. The stress-strain state of the part gives the biaxial effect that takes place during forming. The strain gradients across the part determine the amount of elongation a particular material can take before fracture. Finally, stability against necking determines fracture sensitivity in that the more near maximum elongation is occurring near the free edge and surface of the part, the more near it will be to fracture.

This chapter is concerned principally with the second factor. The other four will be treated elsewhere in this book, either from a theoretical or empirical approach.

BUCKLING THEORY

As shown by the failure analysis in Chapter I, all of the forming methods except five exhibit buckling as a major forming limitation along with splitting. These five exceptions are brake forming, dimpling, sheet stretch forming, rubber bead forming, and drop hammer bead forming. The other seven forming methods will exhibit buckling in the form of rectangular sine wave buckling, sheet shear buckling, circular sheet buckling, and section twist buckling as shown in Figure II-2.

Rectangular sine wave buckling is shown to result when thin gage sheet material is subjected to compressive end stresses. A sine wave buckle will occur where each half wave approximates a square. Shear buckling of sheet material occurs from shearing stresses acting on the part resulting in sine wave type buckling rotated approximately 45° from the long direction of the sheet. Circular sheet buckling is noted to occur from compressive radial stresses as shown (or alternately, from tensile radial stresses on the inside edge) resulting in circumferential sine wave buckling. It should be noted that these buckles are perpendicular to the applied radial stresses; however, resulting circumferential compressive hoop stresses are the direct stresses causing the buckling.

Thin gage sheet metal stabilized by a bend, as shown by the angle section, can buckle in another manner. Twist buckling of this type occurs when the twisting stiffness of the section is below a critical minimum value.

The edge conditions of the sheet elements control the ease of buckling. Practical parts have only two possible edge conditions as shown by the channel in Figure II-1.

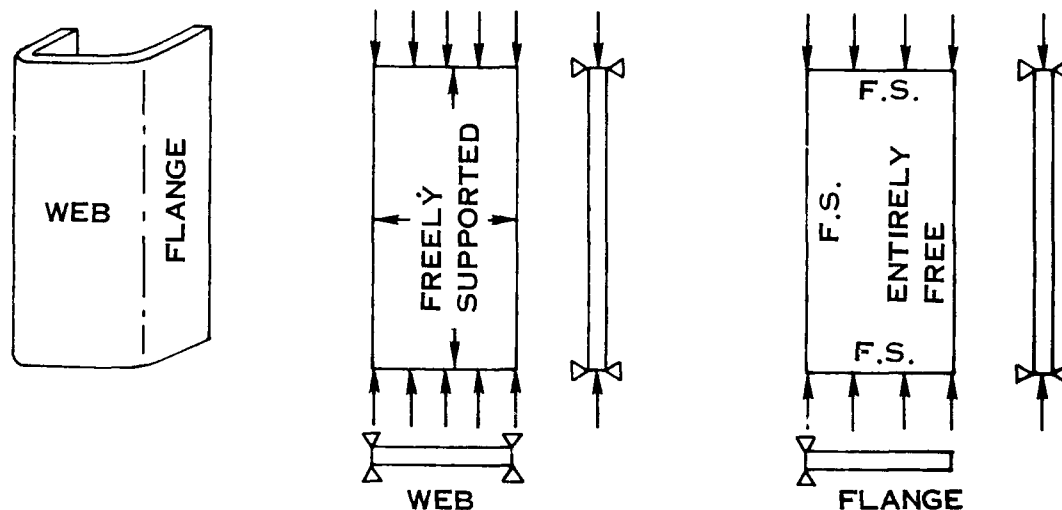


FIGURE II-1 EDGE CONDITIONS OF PRACTICAL PARTS FOR BUCKLING

These edge conditions are designated as freely supported and entirely free as shown by the web and flange of the channel. A freely supported edge condition is one that is free to rotate but is constrained to remain straight, thus taking no bending moment. This is represented by both edges of the web and one edge of the flange because of the stiffening bend along these edges. An entirely free edge condition is one that can bow as well as rotate, represented by the flange with the free edge.

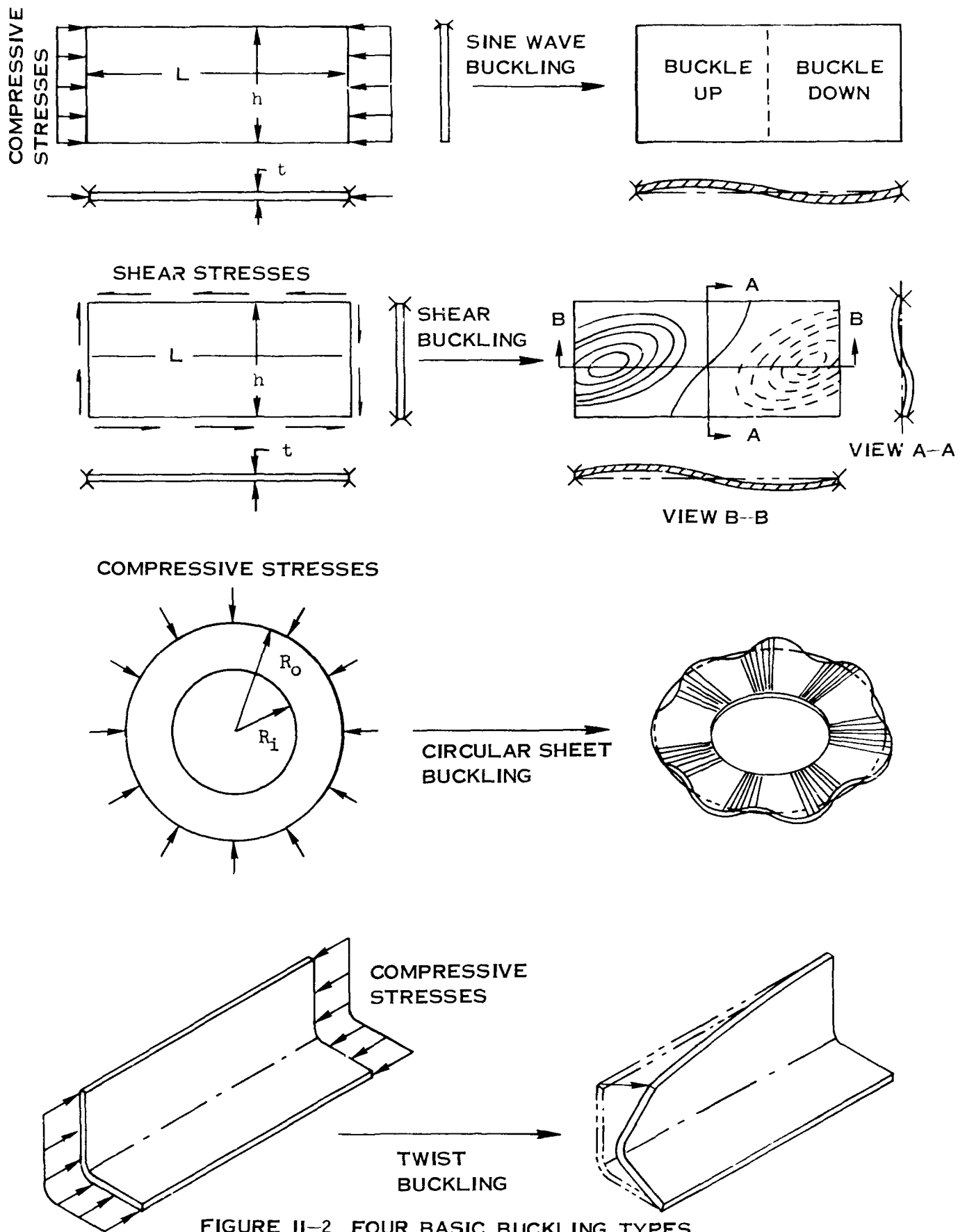


FIGURE II-2 FOUR BASIC BUCKLING TYPES FOR SHEET MATERIAL

Webs with freely supported edges are much more difficult to buckle than flanges. For this reason, only flange type buckling will be considered in the following analysis. Shear buckling and circular sheet buckling will be considered for freely supported edges only because the edge conditions are of secondary importance in these cases. Twist buckling will be analyzed for sections that are completely free to rotate.

The general sheet buckling equation for both sine wave and shear buckling is:

$$(II-1) \quad S_{CR} = k \frac{\pi^2 D}{h^2 t}$$

where S_{CR} is the critical compressive buckling stress, h is the width and t is the thickness of the sheet, k is a numerical factor depending on the width h , the length L , and the edge conditions of the sheet element, and D is the sheet constant as defined by:

$$(II-2) \quad D = \frac{E t^3}{12 (1 - \mu^2)}$$

where E is Young's modulus and μ is Poisson's ratio. Substituting equation (II-2) into equation (II-1) gives:

$$\begin{aligned} S_{CR} &= k \frac{\pi^2 D}{h^2 t} = \frac{k \pi^2}{h^2 t} \left[\frac{E t^3}{12(1 - \mu^2)} \right] \\ S_{CR} &= \frac{k \pi^2}{12(1 - \mu^2)} \frac{E}{(h/t)^2} \end{aligned}$$

$$(II-3) \quad S_{CR} = B_1 \frac{E}{(h/t)^2}$$

where B_1 is a numerical constant:

$$(II-4) \quad B_1 = \frac{k \pi^2}{12(1-\mu^2)}$$

The general buckling equation for circular sheet is:

$$(II-5) \quad S_{CR} = k \frac{D}{R_o^2 t} = \frac{k}{R_o^2 t} \frac{E}{12(1-\mu^2)}$$

$$S_{CR} = \frac{k}{12(1-\mu^2)} \frac{E}{(R_o/t)^2}$$

$$(II-6) \quad S_{CR} = B_2 \frac{E}{(R_o/t)^2}$$

where all of the parameters are the same as before and R_o is the outside radius of the circular sheet. The numerical constant B_2 in this case is seen to be:

$$(II-7) \quad B_2 = \frac{k}{12(1-\mu^2)}$$

The critical buckling stress in (II-3) and (II-6) is seen to be directly proportional to B and E and inversely proportional to $(h/t)^2$ and $(R_o/t)^2$. This means that materials with a high modulus such as the steels and some of the refractory metals are resistant to buckling whereas the titaniums and aluminums are relatively easy to buckle. Also, as the h/t and R_o/t value gets small, it is more buckle resistant as would be the case for thick gage materials.

For a given material, however, equations (II-4) and (II-7) indicate the relative ease of buckling of different shape parts because k is dependent on the length and width of the sheet element, its edge restraints, and types of loading. This constant can be determined for the three types of elements found in sheet forming.

The graph in Figure II-3 gives the k value for these three types of elements:

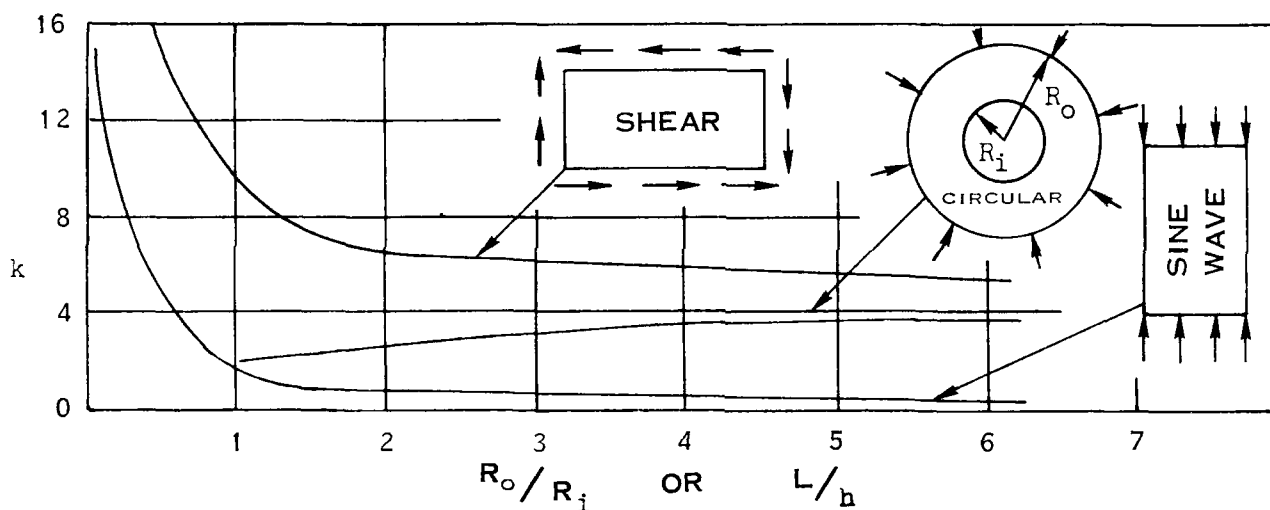
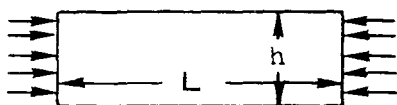


FIGURE II-3 DISTRIBUTION OF " k " FOR BASIC BUCKLING TYPES

These k values can be seen to be fairly constant for values of R_o/R_i and L/h greater than 3; however, the k value rapidly approaches infinity as L/h approaches zero. The k value for a circular plate with a hole in it can be seen to go to 1.9 at $R_o/R_i = 1$ where the flange becomes zero.

By substituting these k values for practical L/h and R_0/R_1 ratios into equation (II-4) and (II-7), the following B values can be computed giving a relative evaluation of the ease of buckling the three fundamental sheet elements for a given material:

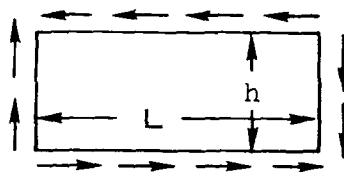
Case A: Rectangular sine wave buckling



for $L/h \geq 2$, $k = 0.5$

$$B = \frac{k \pi^2}{12(1 - \mu^2)} = \frac{(0.5) (3.14)^2}{12(1 - .09)} = 0.45$$

Case B: Rectangular shear buckling



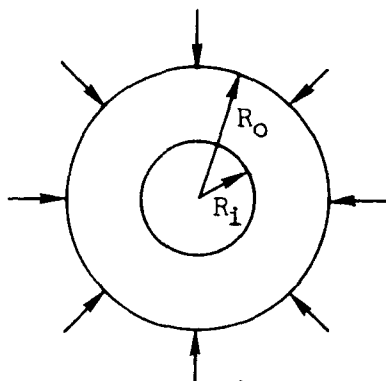
for long parts, $L/h \geq 5$, $k = 5.5$

$$B = \frac{k \pi^2}{12(1 - \mu^2)} = \frac{(5.5) (3.14)^2}{12(1 - .09)} = 5.0$$

for joggling, $L/h = 1$, $k = 20$

$$B = \frac{(20) (3.14)^2}{12(1 - .09)} = 20.0$$

Case C: Circular sheet buckling



for $R_o/R_i = 1.5$, $k = 2.2$

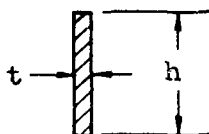
$$B = \frac{k}{12(1 - \mu^2)} = \frac{2.2}{12(1 - .09)} = 0.20$$

The general twist buckling equation is:

$$(II-8) \quad \boxed{S_{CR} = \frac{C}{I_p}}$$

where S_{CR} is the critical compressive buckling stress, C is the twisting stiffness as defined by:

$$(II-9) \quad \boxed{C = f \frac{G h t^3}{3}}$$



for a cross section of f slender rectangles and a modulus of rigidity G , and I_p is the polar moment of inertia of the section as defined by:

$$(II-10) \quad \boxed{I_p = g h^3 t}$$

where g is a numerical constant depending on the shape of the cross section.

Combining equations (II-8), (II-9), and (II-10), and substituting
for $G = \frac{E}{2.5}$:

$$S_{CR} = \frac{C}{I_p} = \frac{f \frac{G h t^3}{3}}{g h^3 t} = \frac{f}{3(2.5)g} \frac{E}{(h/t)^2}$$

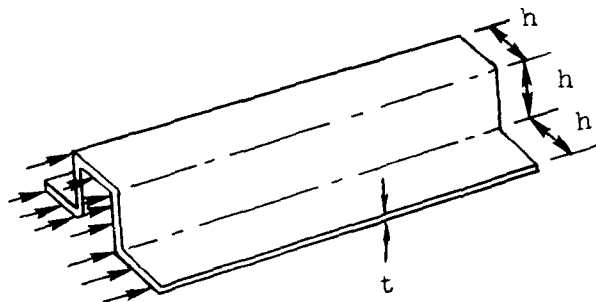
$$(II-11) \quad S_{CR} = B_3 \frac{E}{(h/t)^2}$$

Twist buckling of sections is seen to be equivalent to sine wave and shear buckling by comparing equations (II-11) and (II-3); however, the size constants B in both equations are considerably different as seen by comparing the following equation with equation (II-4):

$$(II-12) \quad B_3 = \frac{f}{7.5g}$$

Evaluating the constant for three typical type sections results in the following:

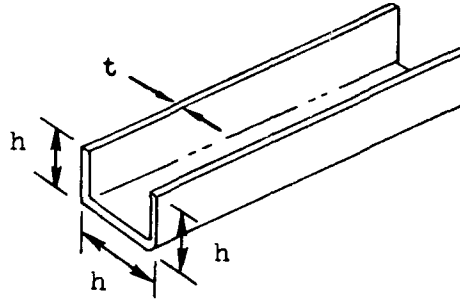
Case A: Twist buckling of hat sections



$f = 5$ rectangles
 h long and t thick
 $g = 3.6$ computed

$$B_3 = \frac{f}{7.5g} = \frac{5}{7.5(3.6)} = 0.19$$

Case B: Twist buckling of channel sections

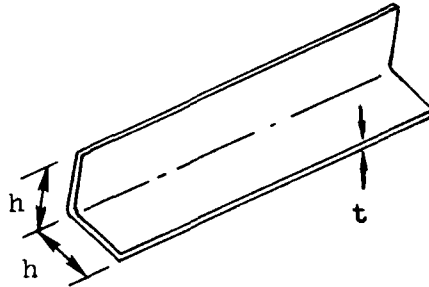


$f = 3$ rectangles

$g = .92$ computed

$$B_3 = \frac{f}{7.5g} = \frac{3}{7.5(.92)} = 0.44$$

Case C: Twist buckling of angle sections



$f = 2$ rectangles

$g = .42$ computed

$$B_3 = \frac{f}{7.5g} = \frac{2}{7.5(.42)} = 0.64$$

Remembering from equation (II-11) that the critical buckling stress is directly proportional to the constant B , it is seen from the above calculations that it is relatively easy to twist buckle hat sections and relatively difficult to twist buckle angle sections.

It should be noticed in equation (II-11) that no k value appears as it did in sheet buckling indicating that twist buckling is independent of the length of the element.

A table of the various types of buckling is shown on the following page in Figure II-4. This table gives a description of the types of buckling with equations and edge conditions for each.

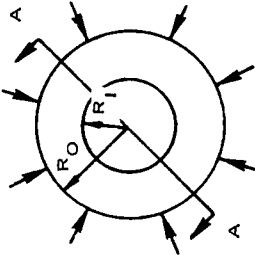
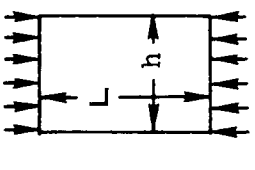
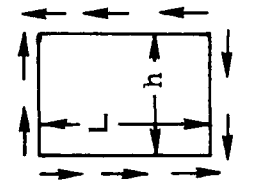

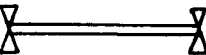
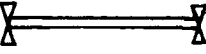

The B value is also shown indicating the relative ease of buckling for each type. It is shown that twist buckling of hats and circular sheet buckling are the easiest because of their low B value; however, deep drawing of circular sheets is stabilized considerably with the aid of pressure plates acting normal to the buckling. Buckling of rectangular plates under end compression and twist buckling of channels is next in ease of buckling as can be seen by the respective B values of .45 and .44. Most of the practical type of parts will buckle under longitudinal compression as shown.

It is shown that angle sections are more difficult to twist buckle than to sine wave buckle whereas the reverse is true for hat sections. For this reason, angles will always buckle as a sine wave, hats will always twist buckle, and channels will buckle either way.

Shear buckling is shown to be much more difficult than the other buckling because of the large B values, particularly for short parts as in joggling.

Deep drawing and spinning are shown to be the applicable types of circular sheet buckling. Rubber forming, linear stretch forming, roll forming, and drop hammer forming are shown to be applicable to buckling of rectangular sheets under longitudinal compression.

BUCKLING OF THIN SHEET

BUCKLING OF CIRCULAR AND RECTANGULAR SHEET			TWIST BUCKLING OF SECTIONS		
GEOMETRY	CIRCULAR		RECTANGULAR		
LOADING	RADIAL COMPRESSION		LONGITUDINAL COMPRESSION	SHEAR	
DESCRIPTION					
EDGE CONDITION	<p>VIEW A-A</p>  <p>SIMPLY SUPPORTED BOTH EDGES</p>		 <p>3 EDGES SIMPLY SUPPORTED ONE EDGE FREE</p>	 <p>4 EDGES SIMPLY SUPPORTED</p>	 <p>FREE TO ROTATE</p>
EQUATIONS	$S_{CR} = B \frac{E}{(R_o/t)}$		$S_{CR} = B \frac{E}{(h/t)^2}$		$S_{CR} = \frac{B}{(h/t)^2}$
$R_o/R_i, L/h$	1.5	2.0	2	.5	INDEPENDENT OF LENGTH
B VALUE	.20	.24	.45	20.0	.19 .44 .64
APPLICABLE FORMING METHODS	DEEP DRAWING SPINNING		RUBBER STRETCH RUBBER SHRINK LINEAR STRETCH ROLL FORMING RUBBER BEAD DROP HAMMER		LINEAR STRETCH ROLL FORMING
RELATIVE IMPORTANCE	HIGHLY IMPORTANT		HIGHLY IMPORTANT	INTERMEDIATE IMPORTANCE	INTERMEDIATE IMPORTANCE SLIGHT IMPORTANCE SLIGHT IMPORTANCE

Shear buckling encompasses both types of rubber press flanging and joggling. Twist buckling of sections occurs in linear stretch forming and roll forming.

The table also shows that circular and rectangular sheet buckling are very important in predicting formability limits. Twist buckling of hat sections and shear buckling are of intermediate importance and twist buckling of channels and angles are only of slight importance as will be brought out in the next section.

The three general plate buckling equations shown in the table can be analyzed together in the development of formability graphs because of their similarity as shown below:

$$(II-3) \quad S_{CR} = B_1 \frac{E}{(h/t)^2} , \text{ sine wave and shear buckling}$$

$$(II-6) \quad S_{CR} = B_2 \frac{E}{(R_o/t)^2} , \text{ circular sheet buckling}$$

$$(II-7) \quad S_{CR} = B_3 \frac{E}{(h/t)^2} , \text{ twist buckling}$$

The shape of the curves illustrating these equations can be better visualized by expanding equation (II-3) by taking the logarithm of both sides:

$$(II-13) \quad \boxed{S_{CR} = \log B_1 E - 2 \log (h/t)}$$

This is an hyperbola, which when plotted on log-log graph paper, will give a straight line with a slope of -2 and an intercept on the S_{CR} axis of $B_1 E$ when $h/t = 1$.

S_{CR} is the critical buckling stress in all types of forming; however, it occurs as elastic buckling from residual stresses left in the part after the forming forces are removed in such processes as rubber stretch flanges, linear stretch forming, and roll forming. S_{CR} is the applied compressive stress that causes buckling during forming in rubber shrink flanges, joggling, deep drawing, spinning, and Androforming. The same type of equation and graph can be used for both cases.

In order to relate S_{CR} to the geometry of the part, it should be remembered that stress and strain are compatible and that no finite jumps in strain will occur. In this way, stress can be related as a definite function of strain as shown by the following equation:

$$(II-14) \quad S_{CR} = f(e) = f(\text{geometry})$$

Then, as will be shown in the following analysis, this strain function can be related to the geometry of the parts considered.

BRAKE FORMING

An analysis for brake forming can be made with the aid of the following sketch:

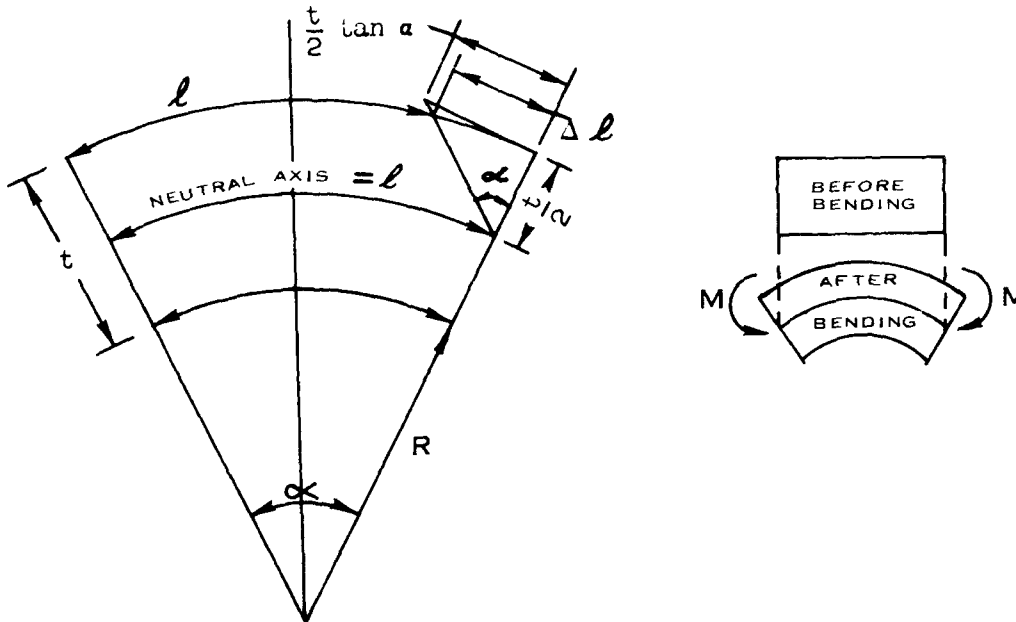


FIGURE II-5 ELONGATION FOR PURE BENDING

It can be seen that the strain equation for pure bending can be computed as follows for small angles:

$$\Delta l \approx t/2 \tan \alpha \quad (\text{for small angles})$$

$$l = (R + t/2) \alpha \quad (\text{original length, assuming the neutral axis remains in the geometric center})$$

$$\epsilon = \frac{\Delta l}{l} = \frac{t/2 \tan \alpha}{(R + t/2) \alpha} = \frac{\tan \alpha}{(2 R/t + 1) \alpha}$$

$$2 R/t + 1 = \frac{1}{\epsilon} \frac{\tan \alpha}{\alpha}$$

$$(II-15) \quad R/t = \frac{1}{2} \left(\frac{1}{\epsilon} - \frac{\tan \alpha}{\alpha} - 1 \right)$$

As shown in the figure, however, the difference between the elongation

Δl and $t/2 \tan \alpha$ increases as the angle α increases. For this reason, it is necessary to compute the strain relationships for large bend angles as shown below:

$$l = (R + t/2) \alpha \quad (\text{original length})$$

$$l_f = (R + t) \alpha \quad (\text{final length})$$

$$\epsilon = \frac{l_f - l}{l} = \frac{l_f}{l} - 1 = \frac{(R+t) \alpha}{(R+t/2) \alpha} - 1 = \frac{R/t + 1}{R/t + \frac{1}{2}} - 1$$

$$\epsilon = \frac{R/t + 1 - R/t - \frac{1}{2}}{R/t + \frac{1}{2}} = \frac{\frac{1}{2}}{R/t + \frac{1}{2}} = \frac{1}{2 R/t + 1}$$

$$2 R/t + 1 = \frac{1}{\epsilon}$$

$$(II-16) \quad R/t = \frac{1}{2} \left(\frac{1}{\epsilon} - 1 \right)$$

This equation shows that the maximum R/t defining the bending limits for a given material is an inverse function of some form of elongation for the material. This means that this equation is a constant for a given material.

In order to draw the complete curve for brake forming limits, it will be necessary to superimpose equations (II-15) and (II-16):

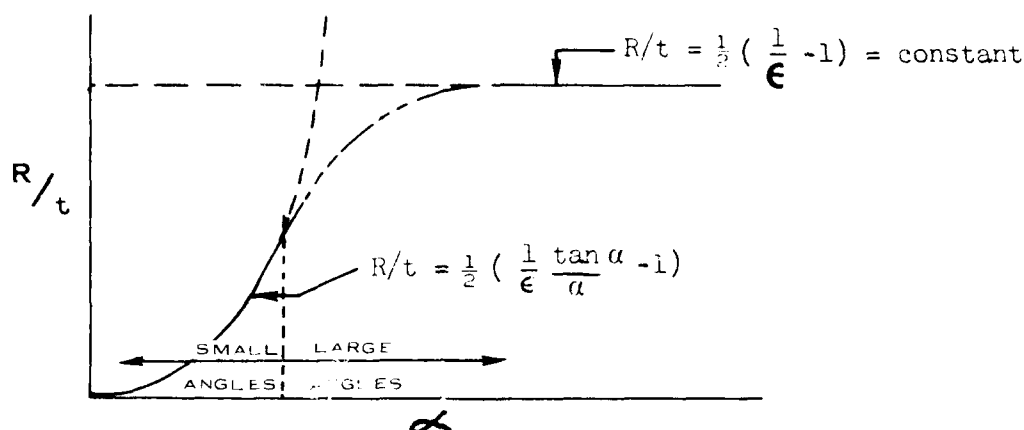


FIGURE II-6 BRAKE FORMING LIMITS

Equation (II-15) represents the forming limits for small bend angles whereas equation (II-16) represents the limits for larger angles. In order to effect the initial point of equation (II-15) at the origin as shown, the arbitrary size constant " ϵ " was chosen as 1.00. A smooth transition curve is drawn between the two in order to form a continuous function as shown by the completed formability limit graph below:

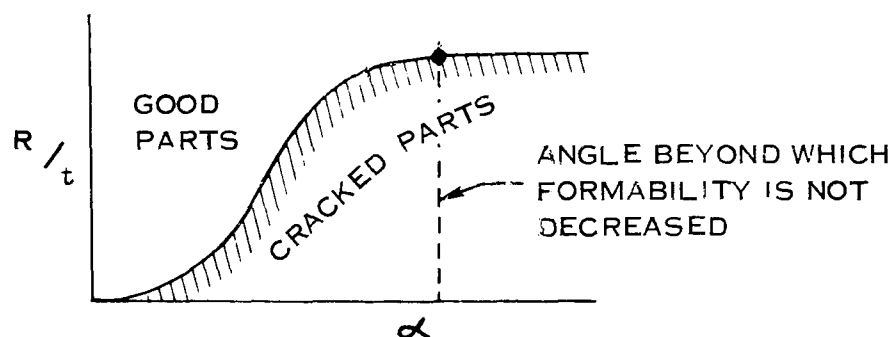


FIGURE II-7 FORMABILITY CURVE FOR BRAKE FORMING

This type of graph illustrating brake forming limits indicates increasing formability with decreasing bend angle α . It also shows a bend angle beyond which formability is not decreased as shown by the horizontal portion of the line. This means that after a certain angle is reached in bending, no more strain can be added in the bend to result in fracture.

Figure II-7 gives the brake forming limits for a single material. In order to illustrate the limits for different materials, the strain " ϵ " in equation (II-16) will have to be treated as a variable as shown by the graph below:

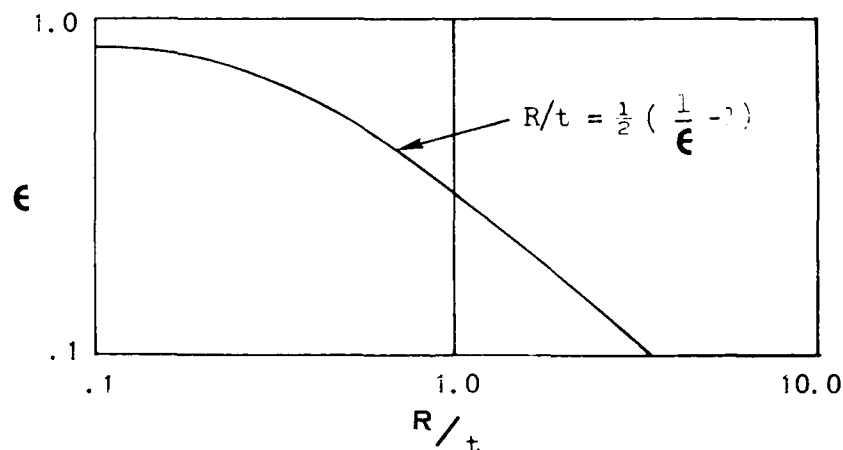


FIGURE II-8 RELATIVE BRAKE FORMABILITY
FOR DIFFERENT MATERIALS

This graph indicates that as the elongation " ϵ " of materials are increased, the R/t necessary to crack a part is decreased. The curve is shown to become a straight line when plotted on log-log paper for the less ductile materials with elongations less than about 50%.

It should be remembered, however, that this curve was developed for the neutral axis remaining congruent with the geometric center during bending. Although this shape of curve will be used for correlating materials for brake formability in subsequent chapters, it will be shown that more precise positioning will be required, particularly for small R/t , because of the movement of the neutral axis away from the geometric center.

JOGGLING

The strain equation for joggling can be determined with the aid of the following sketch:

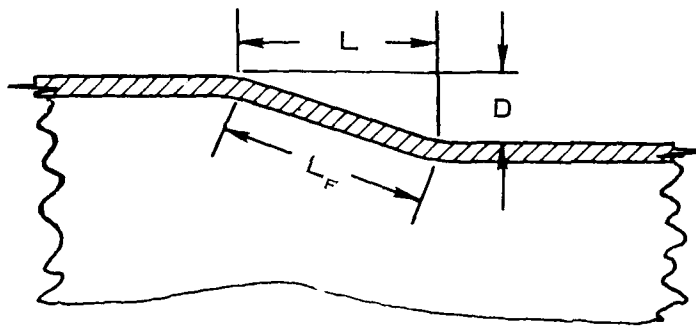


FIGURE II-9 CROSS SECTION OF A JOGGLE

- L = original length of fiber
- L_F = final length of fiber after joggling
- D = depth of joggle

$$L_f = \sqrt{D^2 + L^2}$$

$$\epsilon = \frac{L_f - L}{L} = \frac{L_f}{L} - 1 = \sqrt{\frac{D^2 + L^2}{L^2}} - 1 = \text{elongation}$$

$$\epsilon = \sqrt{(D/L)^2 + 1} - 1$$

$$(\epsilon + 1)^2 = (D/L)^2 + 1, \quad D/L = \sqrt{(\epsilon + 1)^2 - 1}$$

$$(II-17) \quad D/L = \sqrt{\epsilon(\epsilon + 2)}$$

This equation shows that the maximum strain that can be obtained in joggling is a constant for a given material with a strain of ϵ . By combining equation (II-17) for splitting limits with equations (II-3) and (II-14) for shear buckling, the formability envelope can be established for joggling:

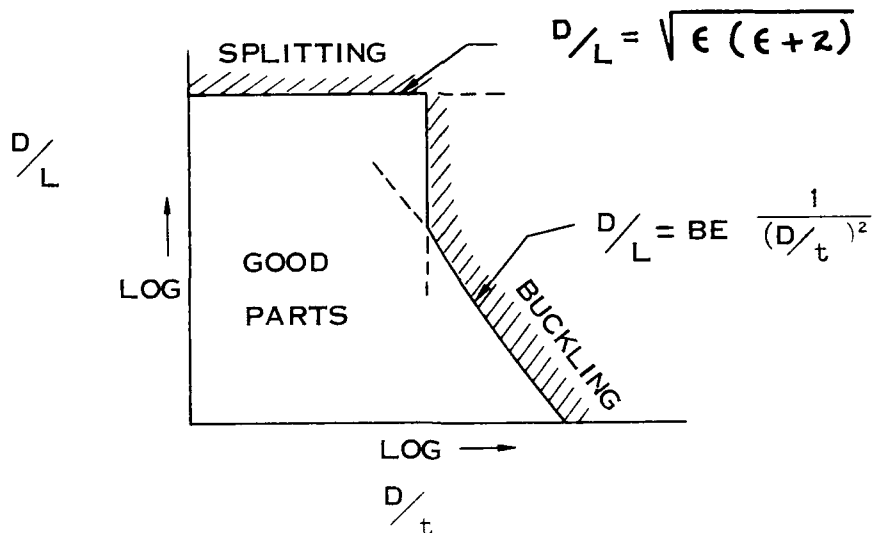


FIGURE II-10 JOGGLING FORMABILITY CURVE

The complete envelope is seen to be bounded by straight lines when plotted on log-log graph paper. The buckling line shown with the slope of -2 is seen to change to a slope of ∞ for large D/L values because of the large increase in the k value discussed previously. The vertical limit line is seen to indicate that formability is independent of D/L , depending only on D/t .

This formability graph was developed based on a material with given mechanical properties. In considering the relative formability for different materials, the material properties in equations (II-17) and (II-3) will have to be considered. Only the elongation equation will be shown below in graph form because the buckling equation will be positioned subsequently using formability indices:

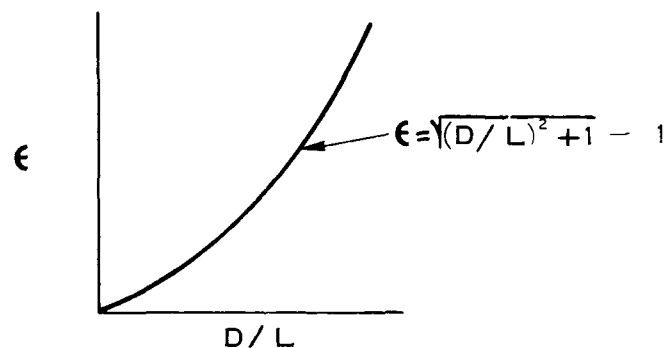


FIGURE II-11 RELATIVE JOGGING FORMABILITY
FOR DIFFERENT MATERIALS

This graph indicates that greater depths can be juggled for materials with higher elongations, ϵ , independent of the gage of the material. This type of curve will be used for correlating splitting limits for different materials in joggling.

DIMPLING

The strains developed during the dimpling operation can be determined from the following sketch:

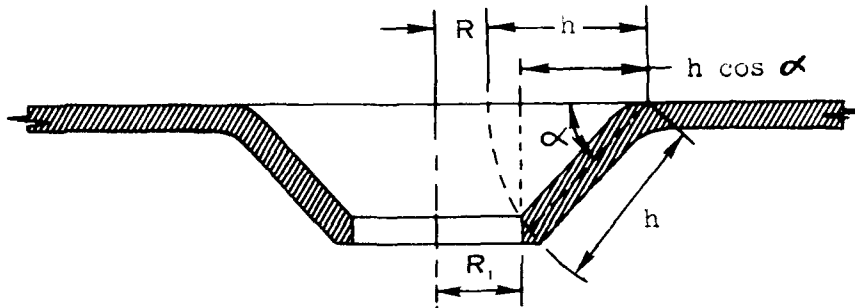


FIGURE II-12 CROSS SECTION OF A DIMPLE

$$R_1 = h + R - h \cos \alpha$$

$$l_0 = 2\pi R = \text{original length of circumferential edge fiber}$$

$$l = 2\pi R_1 = \text{final length of circumferential edge fiber}$$

$$\epsilon = \frac{l - l_0}{l_0} = \frac{2\pi(h + R - h \cos \alpha) - 2\pi R}{2\pi R}$$

$$\epsilon = \frac{h + R - h \cos \alpha - R}{R} = h/R (1 - \cos \alpha)$$

(II-18)

$$h/R = \frac{\epsilon}{1 - \cos \alpha}$$

This equation represents the h/R ratio to which a given material can be stretched for any angle by dimpling before breaking as shown by Figure II-13. It can readily be seen that only small bend angles can be obtained for large h/R ratios while the opposite is true for small h/R ratios.

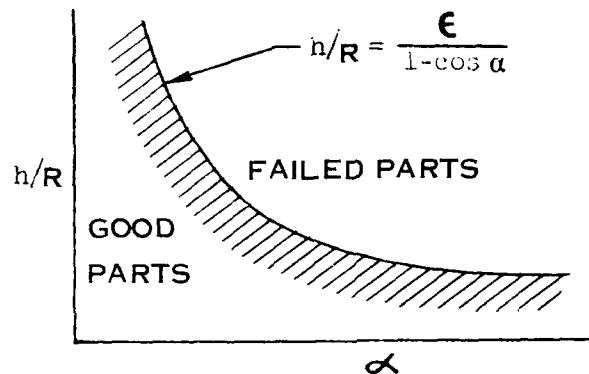


FIGURE II-13 DIMPLING FORMABILITY CURVE

The above formability limit graph is for a single material. In order to evaluate the material as a variable, equation (II-18) will have to be considered with the strain ϵ as a variable for a given constant angle α . By plotting the two major variables h/R and ϵ , the following graph results:

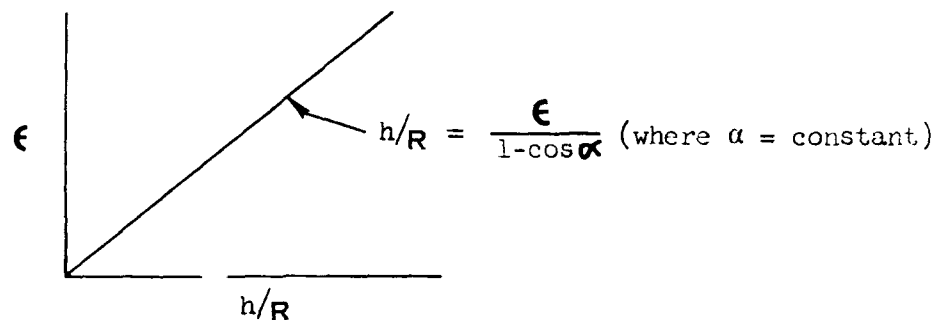


FIGURE II-14 RELATIVE DIMPLING FORMABILITY FOR DIFFERENT MATERIALS

This graph represents the idealized case where the flange remains constant length and thickness; however, in dimpling, the flange will thin and extend its length tending to lower the circumferential hoop strains predicted in equation (II-18). The hole will often remain the same size during dimpling for some materials and, consequently, the dimple will not fail in a radial type split. Generally, the hole will enlarge and the flange will extend during dimpling. This will affect the shape of the graph in Figure II-14.

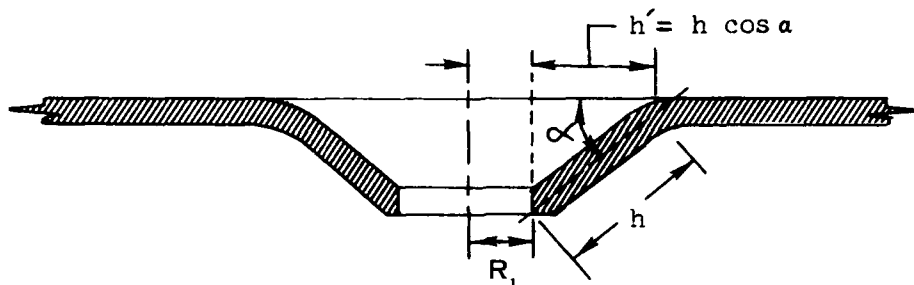


FIGURE II-15 DIMPLE SHOWING FLANGE LENGTHENING

$$\epsilon_L = \frac{h - h \cos \alpha}{h \cos \alpha} = \frac{1 - \cos \alpha}{\cos \alpha}$$

(II-19) $\epsilon_L = \frac{1 - \cos \alpha}{\cos \alpha}$

Superimposing this equation on the graph for equation (II-18) for various angles will result in the curve in Figure II-16. The intersection of the curves for equations (II-18) and (II-19) gives a formability curve representing radial type failures for dimpling. From the above analysis, it is seen that the resulting strain is a compromise between that resulting from a complete circumferential stretch with no flange lengthening to that resulting from no circumferential stretch with complete flange lengthening.

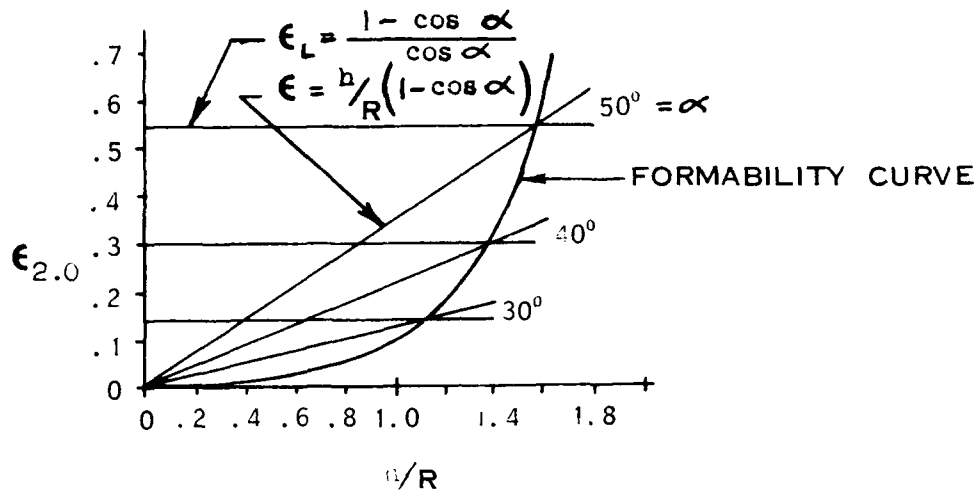


FIGURE II-16 DIMPLING FORMABILITY FOR DIFFERENT MATERIALS

This formability curve will be used to predict maximum dimpling that can be obtained for materials with certain elongation values.

RUBBER FLANGING

The following sketches will be used to determine the strain equations for rubber forming stretch and shrink flanges:

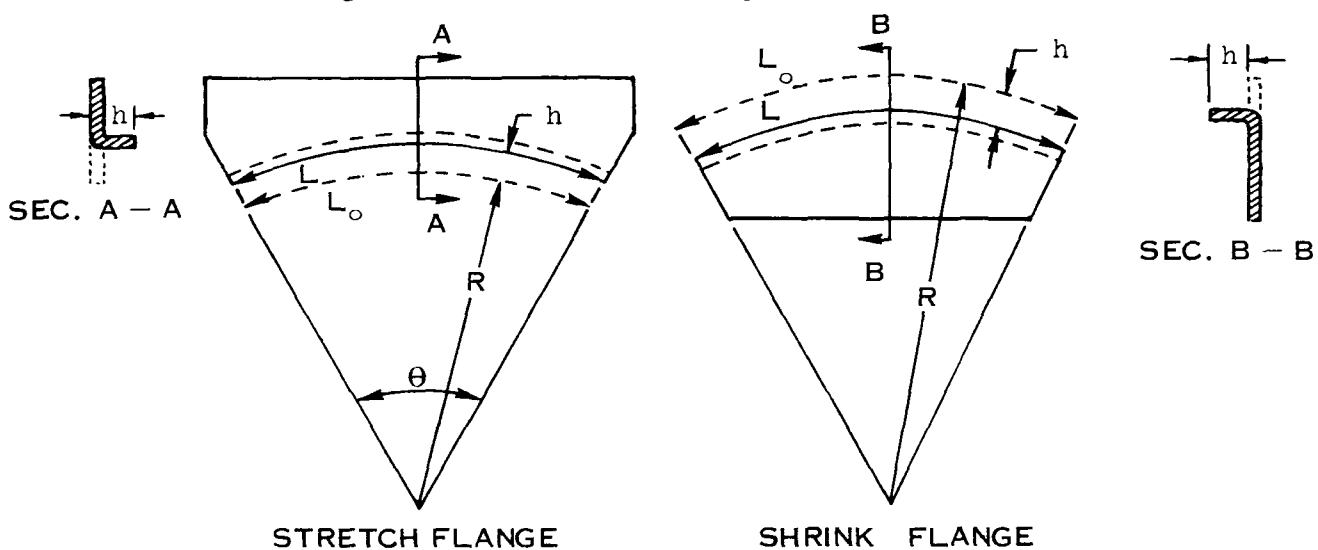


FIGURE II-17 STRETCH AND SHRINK FLANGE PARTS

$L_0 = R \theta$ = original length of fiber

$L = (R+h) \theta$ = final length of fiber for stretch flange

$L = (R - h) \theta$ = final length of fiber for shrink flange

$$\epsilon = \frac{L - L_0}{L_0} = \frac{L}{L_0} - 1 = \frac{(R+h) \theta}{R \theta} - 1$$

(II-20) $\boxed{\epsilon = h/R}$ = elongation for stretch flange

$$\epsilon = \frac{L_0 - L}{L_0} = 1 - \frac{L}{L_0} = 1 - \frac{(R - h) \theta}{R \theta}$$

(II-21) $\boxed{\epsilon = h/R}$ = compression for shrink flange

The shrink and stretch flanges both are defined for percent elongation ϵ by h/R where the contour radius is to the free edge of the flange.

This strain can be related to geometry for buckling by equations (II-3) and (II-14) so that the following graphs can be drawn representing the formability envelopes for rubber press flanging:

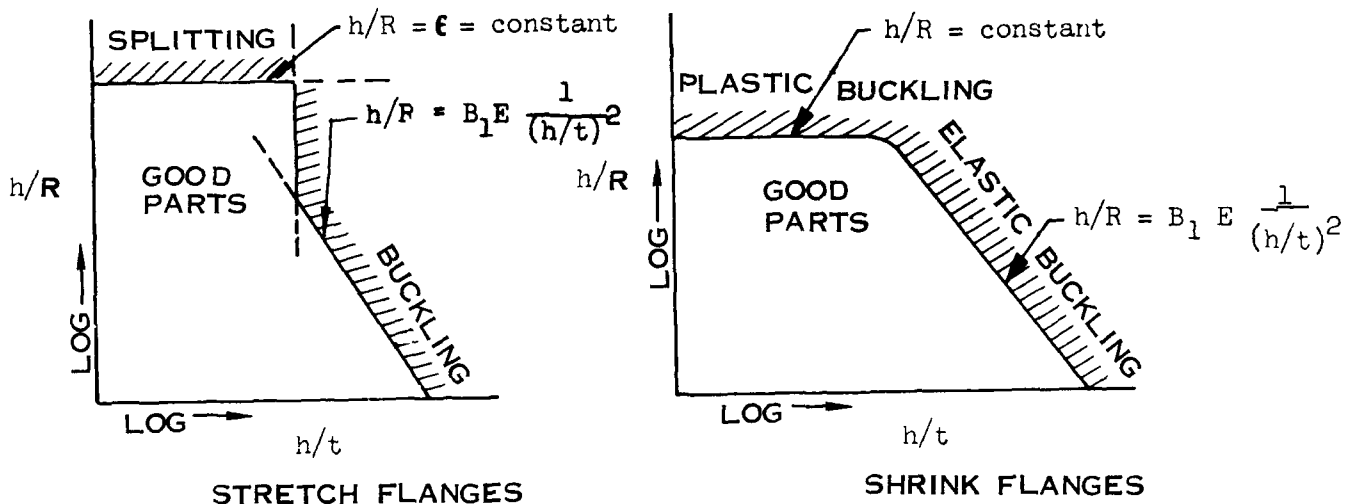


FIGURE II-18 RUBBER PRESS FORMABILITY

In the case of the stretch flanges, formability is seen to be dependent on buckling from residual stresses in the part for large h/t values and on splitting of the flange for large h/R values. The buckling curve is noted to change from a -2 slope to a slope of ∞ for large h/R values because the flange is approaching a shell which is more difficult to buckle than a flat sheet.

The shrink flange curve is similar to the stretch curve in the elastic buckling region, both curves following a slope of -2; however, when the gage gets sufficiently large, the shrink flanges become strictly dependent on h/R which is a function of the plastic buckling properties of the materials. It is seen that failure in the plastic buckling region is independent of the h/t ratio.

Equation (II-20) can also be used to predict the relative formability for all materials as shown in the graph below:

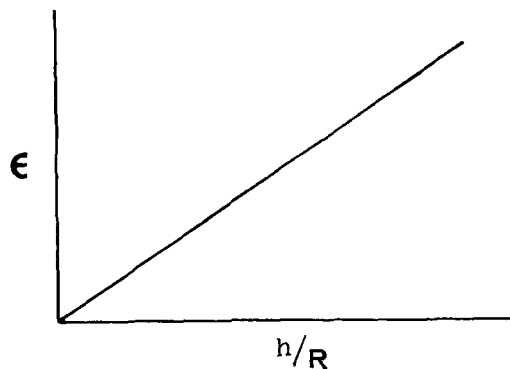


FIGURE II-19 RELATIVE STRETCH FLANGE FORMABILITY
FOR DIFFERENT MATERIALS

This graph shows a straight line relationship between the available elongation in a material and the flange height to radius ratio h/R . Thus, materials with high elongations can be subjected to large flanges before splitting is encountered. This type of curve will be used for splitting correlation of materials for stretch flanges.

LINEAR STRETCH AND ROLL FORMING

This type of part can be defined with a sketch similar to rubber stretch flanging as shown below:

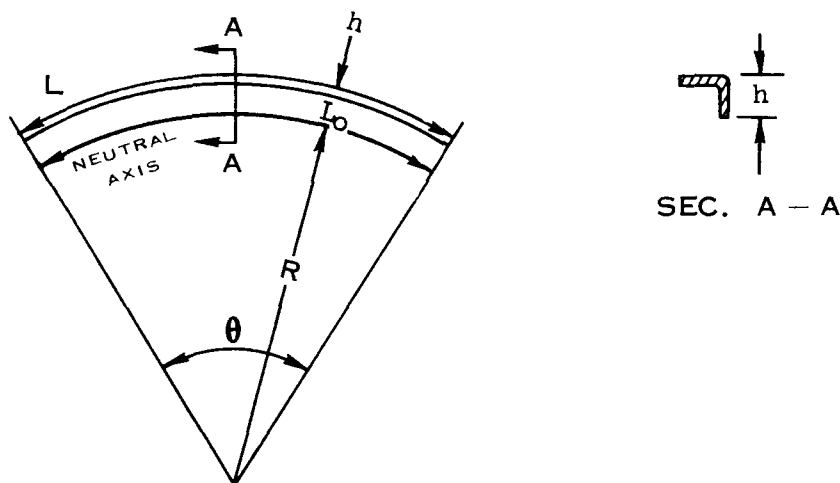


FIGURE II-20 LINEAR STRETCH FORMED PART

$L_0 = R\theta$ = original length of fiber (assuming neutral axis on the concave side of part)

$L = (R+h)\theta$ = final length of fiber

$$\epsilon = \frac{L - L_0}{L_0} = \frac{L}{L_0} - 1 = \frac{(R+h)\theta}{R\theta} - 1$$

(II-22) $\epsilon = h/R$ = elongation of outer fiber

This equation gives the elongation that will occur in a part with a given h/R assuming the contour radius is defined to the edge of the free flange and the neutral axis remains along this free edge.

In order to determine the formability graph for linear stretch forming, equation (II-22) will be combined with equations (II-3), (II-11), and (II-14) in the following manner:

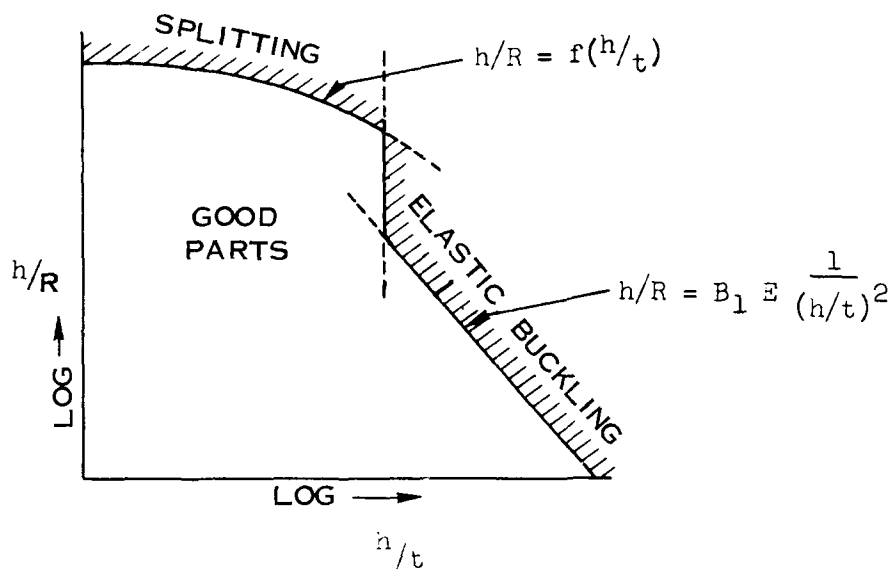


FIGURE II-21 LINEAR STRETCH FORMABILITY CURVE

It can be seen that parts with large h/t values will fail by elastic buckling from residual stresses left in the part. The theoretical curve with a slope of -2 is shown to change to a slope of ∞ for large h/R values because the "k" value in equation (II-4) becomes extremely large for parts of this shape.

Equation (II-22) shows that splitting should be dependent only on the elongation of the material so that the splitting line on the graph would be horizontal; however, it was assumed that the neutral axis was maintained along the concave side of the part. This is true for thin gages; however, thicker gages allow the neutral axis to move toward the convex side of the part without wrinkling of the inner edge, thereby increasing the effective h/R to which the part can be formed without splitting.

The above formability limit graph was developed for a given material with specific material properties. Equation (II-22) can also be used to determine relative formability for splitting for materials with different elongations as shown below:

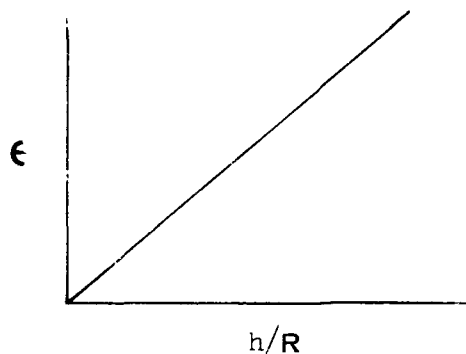


FIGURE II-22 RELATIVE LINEAR STRETCH FORMABILITY
FOR DIFFERENT MATERIALS

This curve shows that materials with large elongation values can be formed to large h/R values. This is the type of curve to be used for correlation of splitting limits for linear stretch forming.

Linear roll forming will have the same type of buckling curve as linear stretch but roll forming will not exhibit splitting as a failure.

SHEET STRETCH

In order to study the strains resulting in double contour sheet stretch forming, the following sketch of a cross section of a spherical segment will be used:

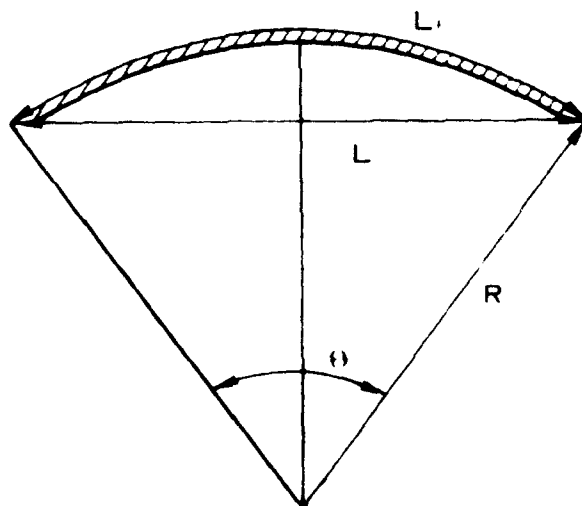


FIGURE II 23 CROSS SECTION OF SPHERICAL SHEET

$L_f = R \theta$ = final circumferential length of fiber

$L = 2 R \sin \frac{\theta}{2}$ = initial circumferential length of fiber

$$\epsilon = \frac{L_f - L}{L} = \frac{L_f}{L} - 1 = \frac{R \theta}{2 R \sin \frac{\theta}{2}} - 1 = \frac{\theta}{2 \sin \frac{\theta}{2}} - 1 = \text{elongation}$$

$$\epsilon = \frac{2 \sin^{-1} L/2R}{L/R} - 1$$

(II-23)

$$2 R/L \csc^{-1} (2 R/L) = \epsilon + 1$$

This is the equation for the meridional strain for a spherical element. In order to extend this to a double contoured skin with different radii in the longitudinal and transverse directions, a new concept of resultant radius will have to be developed as shown below:

$$R_R = \sqrt{R_L R_T} : \text{resultant radius of curvature}$$

$$\frac{R^2}{LT} = \left(\frac{R_L}{L} \right) \left(\frac{R_T}{T} \right) = \text{constant, for a given material}$$

$$(11-24) \quad \boxed{\left(\frac{R_L}{L} \right) \left(\frac{R_T}{T} \right) = \text{constant}}$$

R_L : longitudinal radius of curvature

R_T : transverse radius of curvature

L : longitudinal chord length

T : transverse chord length

This equation will plot as a straight line with a slope of -1 on log-log graph paper as shown below:

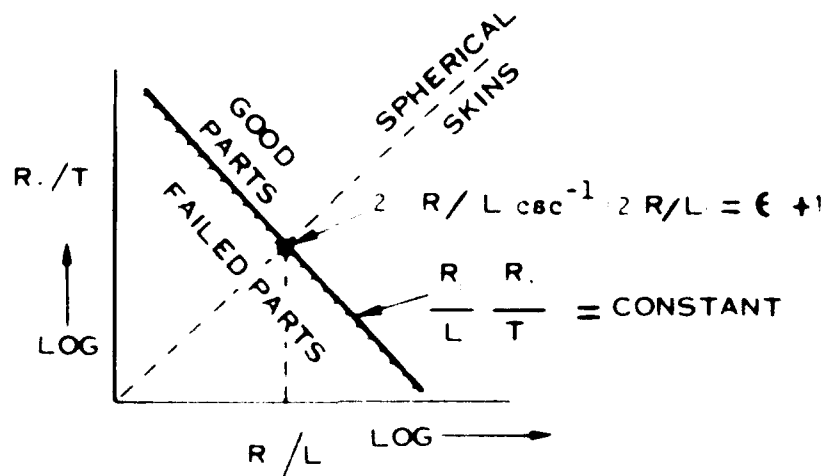


FIGURE 11-24 SHEET STRETCH FORMABILITY CURVE

The graph shows that when the longitudinal radius chord length ratio R_L/L is small, the transverse radius chord length ratio R_T/T must be large to form a given material and vice versa.

This graph gives the formability limits for a given material because the strain ϵ was considered a constant. In order to determine the relative formability for different materials, the strain ϵ in equation (11-24) must be considered a variable as shown below:

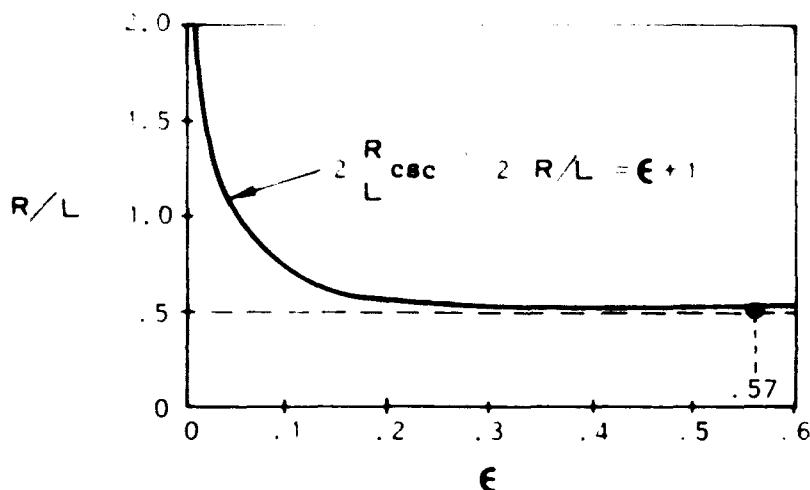


FIGURE 11-25 RELATIVE SHEET STRETCH FORMABILITY
FOR DIFFERENT MATERIALS

This graph shows that the spherical radius to chord length ratio R/L can be decreased toward .5 as the elongation ϵ of a material is increased. This means that materials with good elongations can be formed approaching a half sphere. This is not true in practice, however, because of die friction and resulting non-uniform strain across the part. The shape of the above curve will be used to predict sheet stretch formability.

ANDROFORMING

The strains produced in Androforming are similar to those produced in sheet stretch forming as given by equation (II-23). However, very severe bending strains are superimposed on these from the curved forming element described in Chapter I. This makes a complex strain situation that has to be developed empirically.

In the same manner that sheet stretch forming was handled, a resultant radius of curvature will have to be defined as:

$$(II-25) \quad R_R = \sqrt{R_L R_T} = \text{resultant radius of curvature}$$

R_L = longitudinal radius of curvature

R_T = transverse radius of curvature

It has been found experimentally that the smaller the contour radii and the greater the gage of material, the greater will be the strain developed in the part. This suggests the following relationship:

$$R_R^2 = R_L R_T$$

$$\frac{R_R^2}{t} = \left(\frac{R_L}{\sqrt{t}} \right) \left(\frac{R_T}{\sqrt{t}} \right) = \text{constant}$$

$$(II-26) \quad \left(\frac{R_L}{\sqrt{t}} \right) \left(\frac{R_T}{\sqrt{t}} \right) = \text{constant}, \text{ for a given material}$$

This equation is seen to be derived by first squaring equation (II-25) and then dividing both sides by the material gage "t".

This equation plots as a straight line on log-log graph paper as shown below:

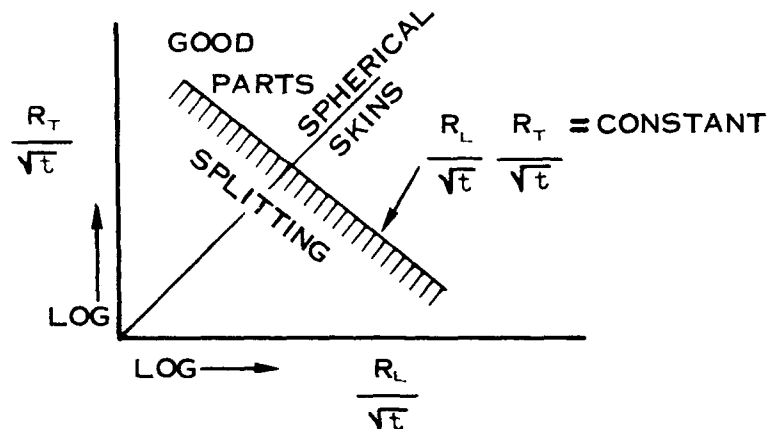


FIGURE II-26 ANDROFORMING FORMABILITY CURVE

The graph indicates that large longitudinal radii are needed to produce parts that have small transverse radii for a given material with a given gage. It is also shown on the graph that large gages have lower formability limits.

In addition to splitting, buckling is also a limitation in Androforming. This type of failure becomes noticeable only for small contour radii and gages. It has been found experimentally that the smaller the contour radii and the smaller the gage, the greater the tendency for buckling. This suggests the following relationship with equation (II-25):

$$R_R^2 = R_L R_T$$

$$R_R^2 t^2 = (R_L t) (R_T t)$$

(II-27) $(R_L t) (R_T t) = \text{constant,}$ for a given material

Plotting this on log-log graph paper will give a straight line with a slope of -1 as shown below:

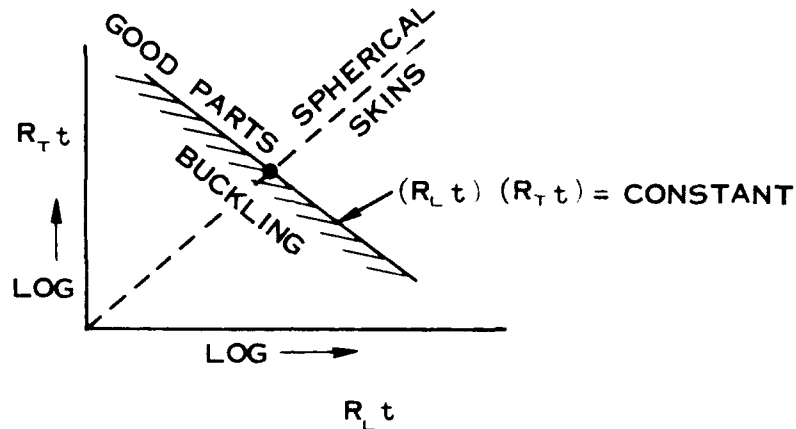


FIGURE II-27 ANDROFORMING FORMABILITY CURVE

This graph indicates that large longitudinal radii are necessary for small transverse radii and vice versa in order to form good parts. Heavy gages also increase formability.

Formability in Androforming can thus be seen to be a compromise for material gage considerations. Thin gages will buckle more easily while heavy gages will split more easily. Intermediate gages will form best for the more severely contoured parts.

DEEP DRAWING WITH MECHANICAL
DIES AND MANUAL SPINNING

The simplest type of deep drawing can be analyzed best for cylindrical cupping as shown below:

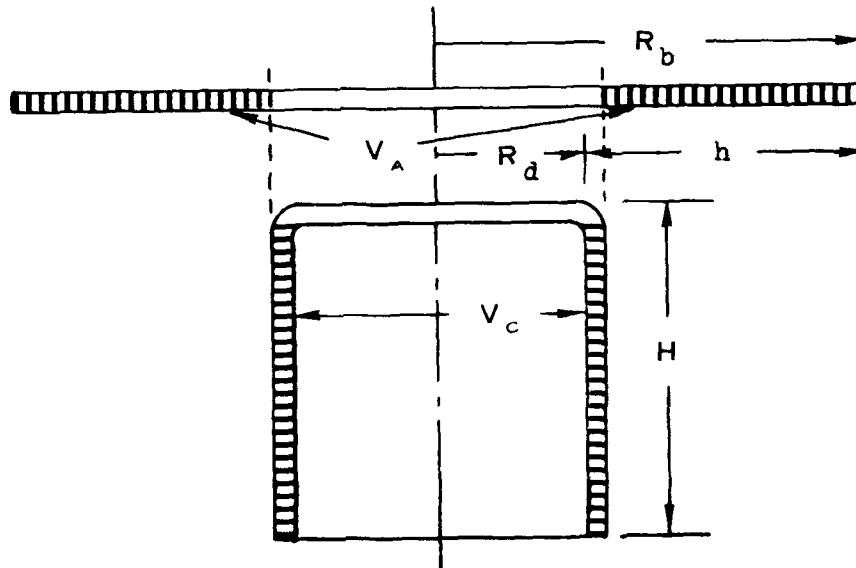


FIGURE II-28 CROSS SECTION OF DEEP RECESSED PART

R_b = radius of the blank

R_d = radius of the die

$h = R_b - R_d$ = overhang flange height

H = cup depth

A geometrical relationship exists for cupping with both mechanical dies and manual spinning based on a constant volume relationship during the drawing operation.

It has been found experimentally that the thickness strain for both methods of deep recessing are approximately as shown below for most materials currently in use:

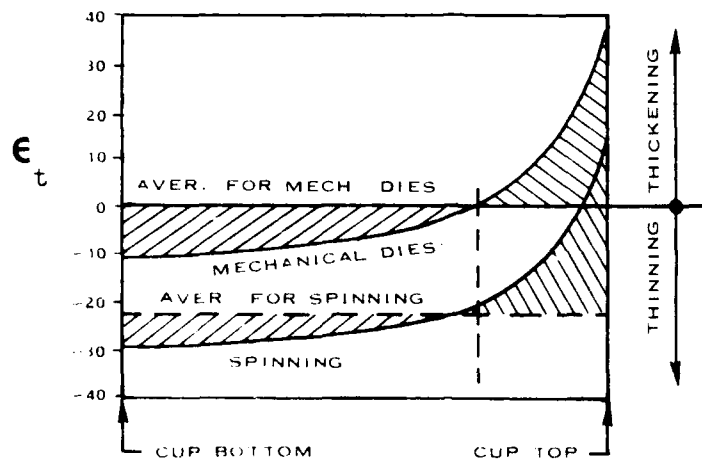


FIGURE II-29 THICKNESS STRAINS FOR DEEP RECESSING

Mechanical die cupping will thin the cup to a small amount near the bottom to a fairly large amount of thickening near the cup top resulting in a near zero average thickness change. Manual spinning, however, will thin the cup considerably for most of the cup depth generally increasing to a slight thickening near the top of the cup resulting in an average of 22% thinning. Although these values vary slightly with material, the averages are close enough for the following derivations.

The cup depth (H) will be considerably greater than the overhang (h) by the constant volume relationship. Consider first that the cup bottom and the associated volume within the blank bounded by R_d as unchanged during forming. This means that the cylindrical volume of metal bounded by H will equal the annulus volume bounded by h as shown by the cross hatched areas in the sketch above.

$$V_A = \pi (R_b^2 - R_d^2) t = \text{volume of annulus of blank}$$

$$V_A = \pi t (R_b - R_d) (R_b + R_d) = \pi t h (R_b + R_d)$$

$$V_C = 2 \pi R_d H t = \text{volume of cylinder of cup}$$

$$V_A = V_C = \pi t h (R_b + R_d) = 2 \pi R_d H t = \text{constant volume}$$

$$\frac{h}{h} = \frac{R_b + R_d}{2 R_d}$$

$$(II-28) \quad \boxed{\frac{H}{h} = .500 \left(\frac{R_b}{R_d} + 1 \right)} \quad \text{for mechanical dies}$$

This is the relationship of the cup depth to the overhang width for mechanical die recessing because no average thickness strain will occur for this process.

It was mentioned, however, that an average of 22% thinning will result in spinning, so the equation will change as follows:

$$V_A = \pi t h (R_b + R_d) = \text{same as for mechanical dies}$$

$$V_C = 2 \pi R_d H (1 - .22)t, \text{ to allow for 22\% thinning}$$

$$V_C = 1.56 \pi R_d H t$$

$$V_A = V_C = \pi t h (R_b + R_d) = 1.56 \pi R_d H t$$

$$\frac{H}{h} = \frac{R_b + R_d}{1.56 R_d}$$

$$(II-29) \quad \boxed{\frac{H}{h} = .641 \left(\frac{R_b}{R_d} + 1 \right)} \quad \text{for manual spinning}$$

These two equations for mechanical die and spinning are identical except for a constant and consequently can be plotted on the same graph as shown below:

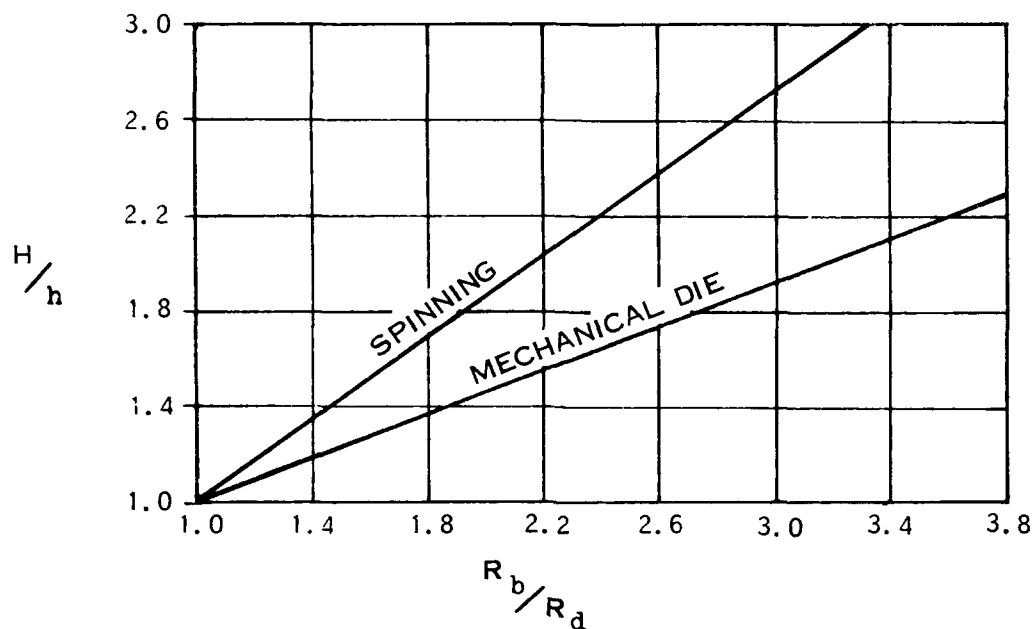


FIGURE II-30 OVERHANG FLANGE TO CUP DEPTH RATIO

This graph shows that, for a given material with a given blank and die, spinning will produce somewhat deeper cups because of the greater thinning. The graph also shows that larger ratios of H/h can be obtained for larger R_b/R_d ratios for both processes. The significance of this is that greater depth ratios H/h can be produced for the smaller dies.

Because deep recessing is a process of drawing metal, formability is based on the ability of the metal to withstand buckling during the drawing action. This formability does not depend on the elongation characteristics of a material but on the strength in the cup and the stability of the flange against buckling. For this reason, the formability graphs will be obtained strictly from equations (II-6) and (II-14).

The overhang flange (h) can be used with the material gage to determine the buckling ratio h/t instead of the R_o/t developed in equation (II-6) as shown below:

$$h = R_b - R_d = R_o - R_d$$

because h is a function of R_o minus a constant. Also, the stress and strain build-up in the flange during drawing as shown by equation (II-14) can be represented by h/R_b as shown by the formability graph below:

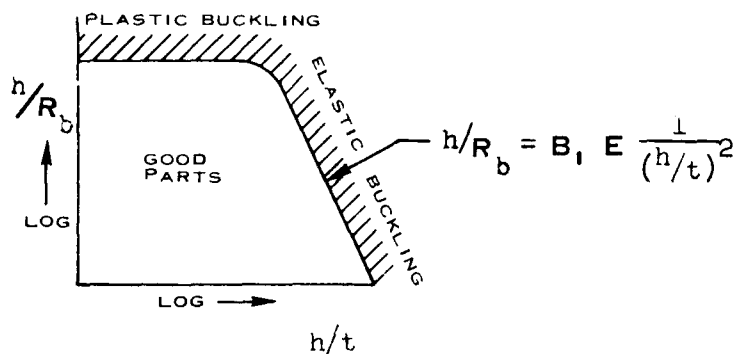


FIGURE II-31 DEEP RECESSING FORMABILITY

Elastic buckling occurs for large h/t values as predicted by the equation; however, when sufficiently heavy gages are formed, considerable plastic strain occurs in the flange before buckling is initiated as shown by the horizontal limit line. After this occurs, the formability becomes independent of h/t .

RUBBER PRESS BEADING

Beading on the rubber press is somewhat different than on the drop hammer, chiefly due to the limiting pressure of the former. The following sketch illustrates rubber press beading and the accompanying free forming radius:

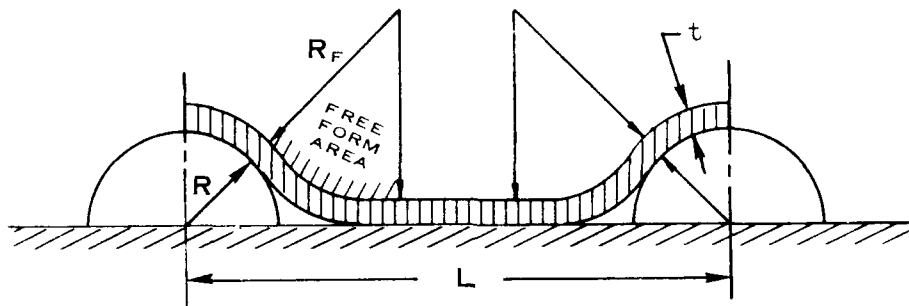
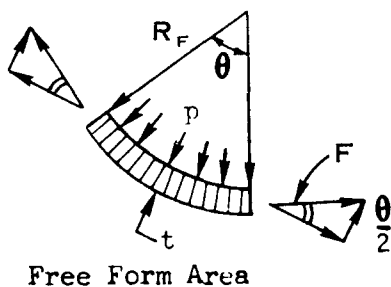


FIGURE II-32 CROSS SECTION OF RUBBER FORMED BEAD

R_F = free forming radius



$$2 F \frac{\theta}{2} = p R_F \theta \cdot 1$$

$$S t \cdot 1 \cdot \theta = p R_F \theta$$

$$S = p R_F \frac{1}{t}$$

(II-30)

This equation shows that for a given material with a given rubber pressure, a free forming radius R_F will result and the resulting stress developed will be inversely proportional to the material gage. The free form radius is almost entirely independent of the bead radius and spacing, R and L , so that the following formability graph results for rubber beading:

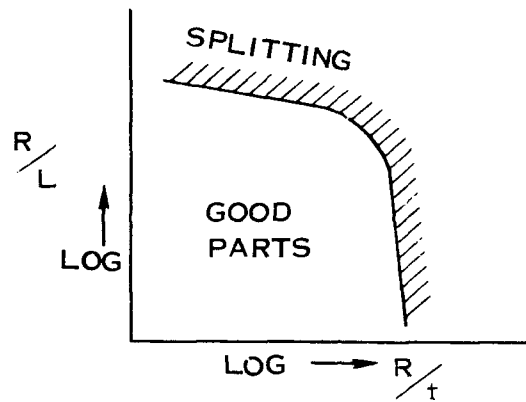


FIGURE II-33 RUBBER PRESS BEAD FORMABILITY LIMITS

This graph shows that formability is very dependent on the material gage for small R/L values. For a given material and a given rubber forming pressure, there exists a material gage below which parts cannot be formed independent of these small R/L values. For large R/L values, the splitting limits are seen to depend only on R/L almost independent of the gage. This is because bending is superimposed on tension for the heavy gages.

DROP HAMMER BEADING

The forming of beaded panels on the drop hammer can be analyzed with the aid of the following sketch:

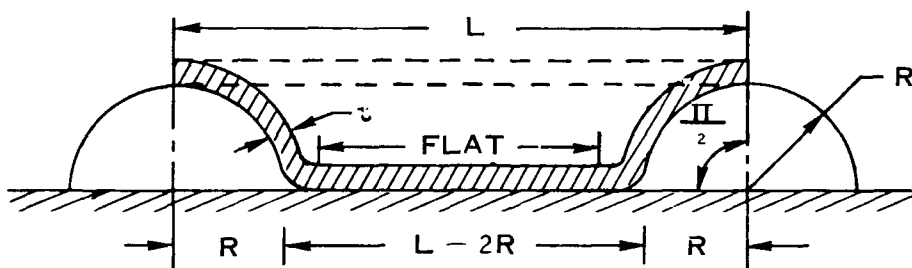


FIGURE II-34 CROSS SECTION OF DROP HAMMER FORMED BEAD

L = original length before forming

$$L_f = 2R \frac{\pi}{2} + L - 2R = \pi R + L - 2R$$

$L_f = R (\pi - 2) + L$ = final length after forming

$$\epsilon = \frac{L_f - L}{L} = \frac{L_f}{L} - 1 = \frac{R (\pi - 2) + L}{L} - 1 = \frac{R}{L} (\pi - 2) + 1 - 1$$

$$(II-31) \quad \boxed{\epsilon = 1.14 R/L} = \text{average strain during forming}$$

This equation shows that the strain developed during drop hammer forming is a function of the bead radius to spacing ratio R/L .

The development of the above equation is based on a uniform strain occurring across the formed L_f ; however, the strain distribution is very unequal because of drawing and friction between the die and the rubber used in drop hammer forming. The amount of drawing out of the flat area of the bead, noted in the sketch, is a function of material gage as shown below:

Assume one square inch of flat area

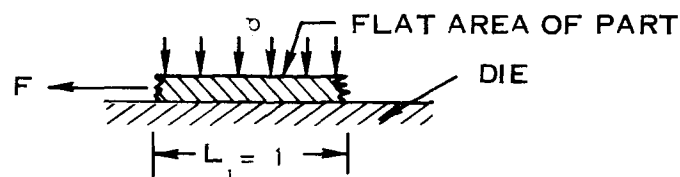


FIGURE II-35 CROSS SECTION OF FLAT AREA IN BEADING

$F = \mu N =$ force to pull material out of flat area

$\mu =$ coefficient of friction, $N =$ normal force resulting
from rubber pressure

$$F = S \cdot t \cdot l = \mu p \cdot l \cdot l$$

(II-32) $S = \mu p \frac{1}{t} =$ stress resulting in the flat
area of the bead

The stress build-up can thus be seen to be inversely proportional to the material gage. This equation will plot as shown below:

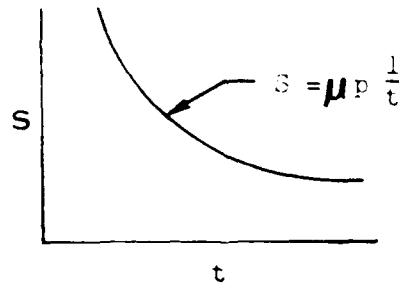


FIGURE II-36 STRESS VERSUS GAGE FOR DROP HAMMER BEADING

For a given pressure and coefficient of friction, it can be seen that thin gages build up a very high stress in the part; this is the reason that thin gages exhibit poor formability in this type of drop hammer forming.

Because the strain equation was a function of R/L and the stress equation was a function of $1/t$, the following graph can be drawn for formability of beading on the drop hammer:

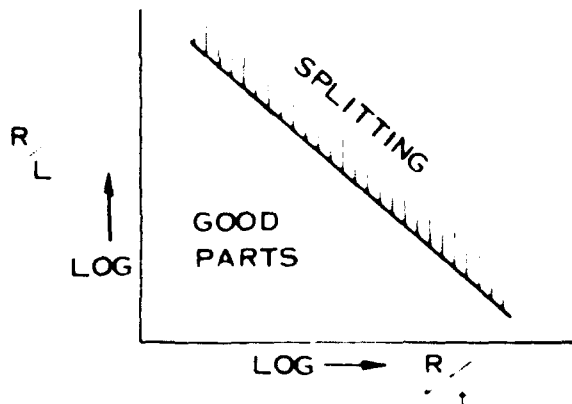


FIGURE II 37 DROP HAMMER FORMABILITY LIMITS

This graph shows that the R/L drops considerably as the gage is decreased. Also, heavy gages exhibit good formability with a high R/L .

CHAPTER III
FORMABILITY INDICES

FORMABILITY INDICES

The last chapter comprised the development of formability limits for splitting and buckling based on the geometry of the parts. This chapter will be devoted to developing the effect of material mechanical properties on these same limits. In a majority of cases, the indices that are developed are obtained from the equations developed in the previous chapter; in a few cases however, the indices will be developed based on the laws of dimensional analysis.

By taking any one of the three basic buckling equations developed in the last chapter, (II-3), (II-6), and (II-11), it can be shown that the material variables can be isolated on one side of the equation and the geometrical variables on the other as shown by equation (II-3) below:

$$(II-3) \quad S_{CR} = B_1 E \frac{1}{(h/t)^2} \quad \text{or} \quad \frac{E}{S_{CR}} = \frac{(h/t)^2}{B_1}$$

$$(III-1) \quad \boxed{\frac{E}{S_y} = \frac{(h/t)^2}{B_1}} \quad \text{where} \quad S_{CR} = S_y$$

This equation isolates the material buckling variables on the left in dimensionless form to give the position of the curve to the geometrical variables on the right in dimensionless form to give the shape of the curve.

The function E/S_y is the buckling index that will be used to position all curves for processes exhibiting buckling as a failure. It means that materials with a high modulus and low yield strength have good buckling resistance and, consequently, good formability in this regard.

The strain equations developed in Chapter II will be used to position all curves for processes exhibiting splitting as a failure. These equations are: (II-16, -17, -18, -20, -21, -22, -23, and -31) which indicate the amount of strain a material will withstand before failure.

Some of the forming processes will have formability graphs positioned only by splitting or strain indices while others will be positioned only by buckling indices. A third group will be positioned by both as shown schematically below:

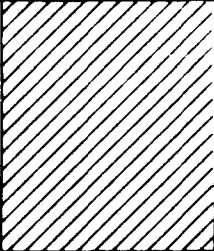
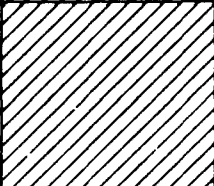
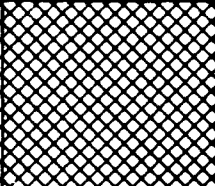
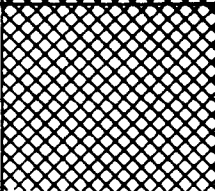
Process	Splitting Index	Buckling Index
1. Brake Forming 2. Dimpling 3. Drop Hammer Bead 4. Rubber Press Beading 5. Sheet Stretch		
6. Androform 7. Jogging 8. Linear Stretch 9. Rubber Stretch		
10. Rubber Shrink 11. Roll Forming 12. Spinning 13. Deep Drawing		

FIGURE III-1 APPLICATION OF INDICES

This chart shows that five processes are defined by elongation indices alone and four by buckling indices alone while four processes are defined by both. These indices are developed for each forming process in the succeeding pages.

BRAKE FORMING

The brake forming limit curve for a given material was developed in the preceding chapter and was shown to have the following shape:

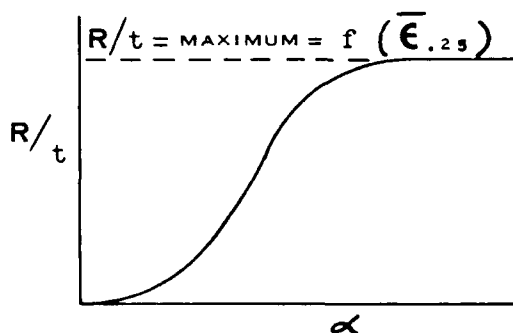


FIGURE III-2 BRAKE FORMING LIMIT CURVES

The limit curve was shown to reach a maximum R/t at a given bend angle (α) for a given material. This maximum R/t value has been found to correlate best with the corrected value of the .25 gage length strain on a simple tension test, $\bar{\epsilon}_{.25}$. This strain will be defined in Chapter IV. The correlation is in conformance with the strain equation (II-16) developed in Chapter II for this process.

The significance of this relationship between the maximum bending strain in the outer fiber in brake forming to the maximum tension strain in a .25 gage length tensile test is that bending strains can be correlated to tensile strains for different materials.

DIMPLING

The dimpling curve developed in Chapter II was shown to have the following shape:

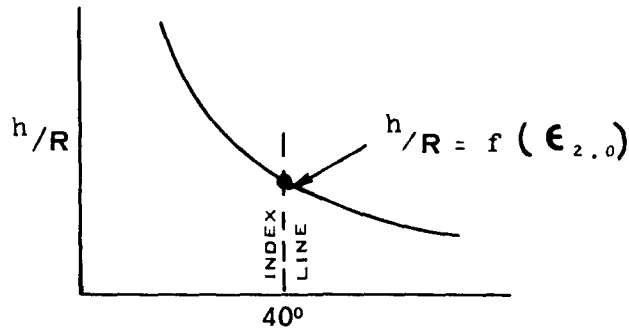


FIGURE III-3 DIMPLING LIMIT CURVES

By using equation (II-18) from the preceding chapter and experimental data, it was found that the 2.0 inch gage length elongation, $\epsilon_{2.0}$, correlated best to the standard 40° dimple. This means that the complete dimpling curves for all materials can be positioned by relating the maximum h/R to $\epsilon_{2.0}$ for the standard 40° dimple.

DROP HAMMER BEADING

The formability curve for this process was developed in the preceding chapter and is shown below:

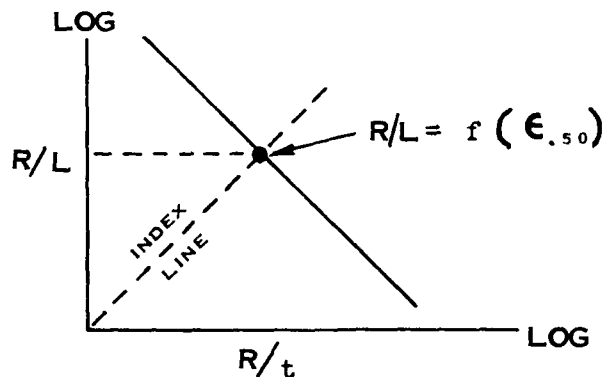


FIGURE III-4 DROP HAMMER BEADING CURVE

Equation (II-31) showed that the limits of this process were defined by R/L being a function of some strain. This strain function was found empirically to be the corrected strain for a .50 inch gage length. This strain will be developed in the next chapter.

Curves for different materials can be positioned by relating this R/L as a function of $\epsilon_{.50}$ along an index line with a slope of +1.

RUBBER PRESS BEADING

The theoretical curve for rubber press beading was developed in Chapter II and had the following shape:

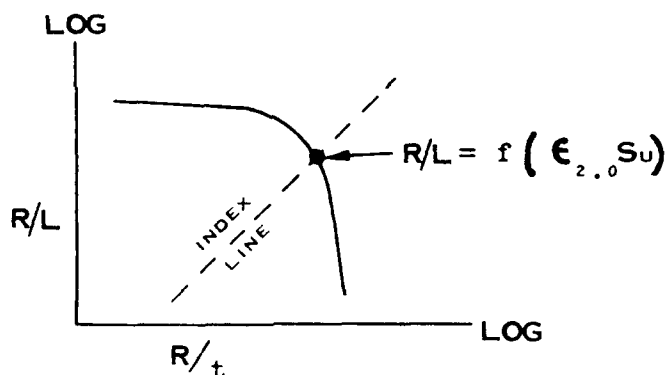


FIGURE III-5 RUBBER PRESS BEADING CURVE

The splitting limits were shown to be limited by a definite gage for a given material and forming pressure for small R/L values because of the resulting free forming radius. The formability index for this process is not a simple function of material elongation because of this free forming radius. The larger this radius, the less strain the material is subjected to resulting in an index that is related to both the elongation and strength of the material.

This index was found to be the 2.0 inch gage length elongation times the ultimate strength of the material, $\epsilon_{2.0} S_u$. This means that materials with large elongations and high strength values will form readily before splitting for a given pressure. The resulting free forming radius will, of course, be large for strong materials.

The rubber press beading curves for all materials can thus be positioned with $\epsilon_{2.0} S_u$ plotted along the index line with a slope of + 1.5.

SHEET STRETCH

Sheet stretch forming was shown to have the following shape from the preceding chapter:

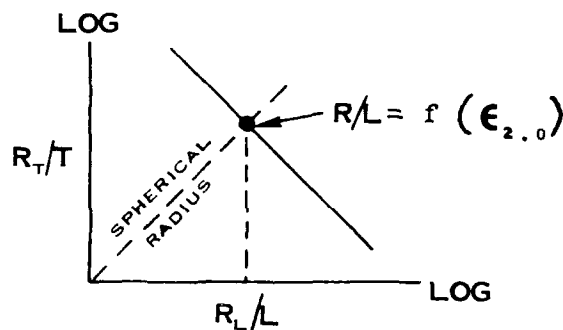
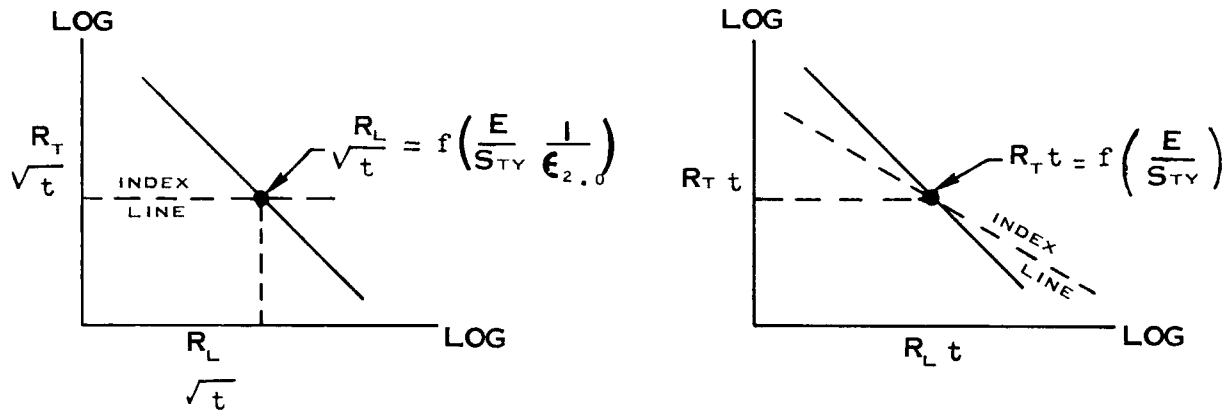


FIGURE III-6 SHEET STRETCH FORMABILITY CURVE

Equation (II-23), developed in the last chapter, showed that the spherical radius to chord length ratio would be a function of elongation. This elongation value has been found to be the 2.0 inch gage length elongation ($\epsilon_{2.0}$) so that curves for all materials can be positioned along the spherical radius index line by using these elongation values.

ANDROFORMING

Androforming was found in the last chapter to have a formability curve similar in shape to the sheet stretch formability curve for splitting except that different parameters were plotted on the graph as shown below:



**FIGURE III-7 ANDROFORMING SPLITTING AND BUCKLING
LIMIT CURVES**

The splitting formability line has been found to be dependent on more than just the elongation of a material. This type of limit was found to be a function of springback $\left(\frac{E}{S_{TY}} \frac{1}{\epsilon_{2.0}}\right)$ so that the ratio of longitudinal radii to the material gage can be written as a function of this index:

$$R_L / \sqrt{t} = f\left(\frac{E}{S_{TY}} \frac{1}{\epsilon_{2.0}}\right)$$
 This means that the lower E/S_{TY} (greater spring-back) and the larger $\epsilon_{2.0}$, the greater the formability of a material. The result is that formability increases as the index $\left(\frac{E}{S_{TY}} \frac{1}{\epsilon_{2.0}}\right)$ decreases, pointing out the fact that the Androforming process depends strongly on the ability of a material to springback to a severe curvature. It is, therefore, for all practical purposes, mandatory that materials be formed in the heat treated condition. Although severe curvatures cannot be formed by this process when compared with sheet stretch forming, it can readily be recognized that Androforming has definite advantages over sheet stretch forming.

The buckling limits are not dependent on the same geometrical parameters as splitting, so another formability graph is needed for these limits as shown above. Again, buckling limits are seen to be governed by the buckling index, E/S_{ty} , so that formability limit lines can be drawn for all materials based on $R_T t = f(E/S_{ty})$.

JOGGLING

Jogging is the second process where formability is limited by both splitting and buckling indices as shown by the limit graph developed in Chapter II and reproduced below:

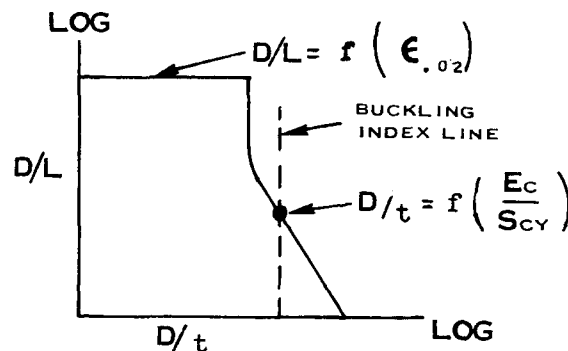


FIGURE III-8 JOGGLING FORMABILITY LIMITS

The splitting limits were shown to be dependent on some form of elongation limits of a material by equation (II-17). This parameter has been found empirically to be the .02 gage length elongation ($\epsilon_{.02}$), so that formability curves for all materials may be drawn by relating the D/L ratio to the .02 elongation: $D/L = f(\epsilon_{.02})$.

Buckling is a function of the compressive modulus to yield strength index, E_c/S_{cy} , so that curves for all materials may be drawn by the following relation: $D/t = f(E_c/S_{cy})$.

LINEAR STRETCH

The formability limits were seen to be dependent on the following curve from Chapter II.

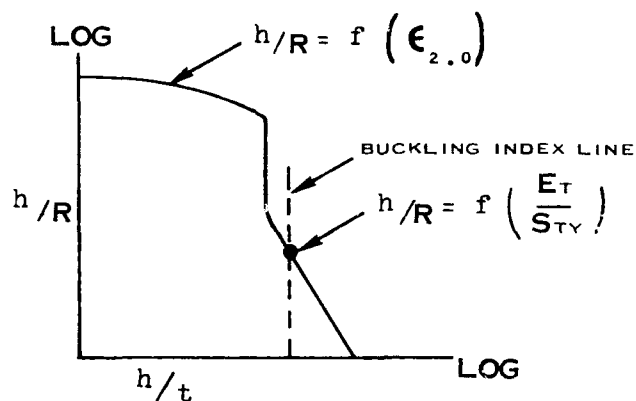


FIGURE III-9 LINEAR STRETCH FORMING LIMITS

Equation (II-22) predicted the splitting limits based on the elongation of a material. Splitting formability for any material has been found empirically to be a function of the 2.0 inch gage length elongation $h/R = f(\epsilon_{2.0})$.

As mentioned at the beginning of this chapter, buckling is dependent on the index E/S_{ty} so that linear stretch buckling limits for any material can be found with the following relation: $h/R = f(E_T/S_{ty})$.

RUBBER PRESS STRETCH FLANGES

These types of stretch flanges are represented by almost an identical formability curve to linear stretch forming as developed in Chapter II and shown below:

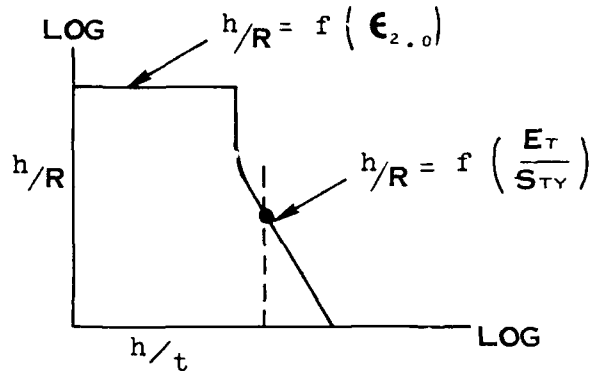


FIGURE III-10 RUBBER PRESS STRETCH FLANGE LIMIT GRAPH

The elongation equation developed in Chapter II, (II-20), was shown to depend on an elongation factor of material. This has been found empirically to be the 2.0 inch elongation, $\epsilon_{2.0}$, so that all materials can be related by the following function, $h/R = f(\epsilon_{2.0})$.

The buckling limits are again dependent on the buckling index E_T/S_{ty} so that all materials can be related by the function: $h/R = f(E_T/S_{ty})$. This index is the tensile modulus divided by the tensile yield stress.

RUBBER PRESS SHRINK FLANGES

Because shrink flanges are formed with resulting compressive hoop stresses in the flange, splitting failures will not result in this type of forming. Looking at the formability limit curve developed in the last chapter, the index for shrink flanging can be determined:

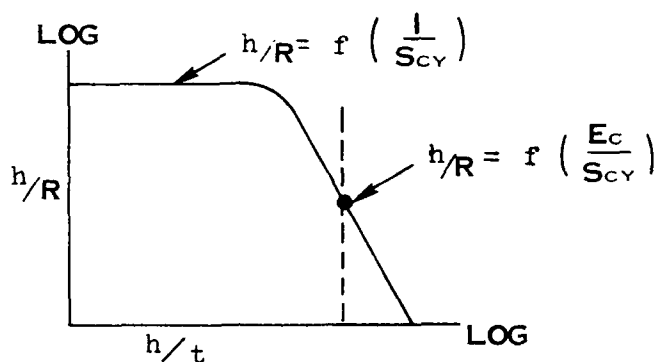


FIGURE III-11 RUBBER PRESS SHRINK FLANGE LIMIT GRAPH

Buckling in the elastic region can be seen to be defined by the same buckling index as for most of the previous cases; i.e. $h/R = f(E_C/S_{Cy})$, where both the modulus and yield are compressive values. The plastic buckling for heavy gages is shown to depend on the index $1/S_{Cy}$ so that $h/R = f(1/S_{Cy})$. This indicates that the heavy gages wrinkle independent of the modulus of elasticity of a material.

ROLL FORMING

Roll forming curves developed in Chapter II indicated formability limits were dependent only on the buckling characteristics of a material as shown below:

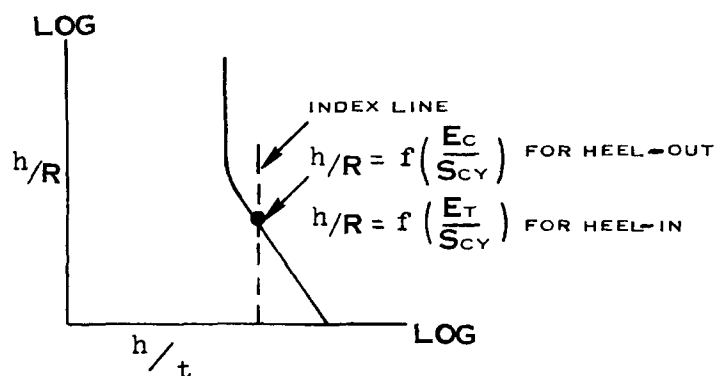


FIGURE III-12 ROLL FORMING LIMIT GRAPH

Because buckling instabilities are so great for this forming process, strains necessary for splitting are never encountered. Buckling indices for this process are again the ratio of modulus to the yield strength; however, the compressive ratio defines buckling for heel-out sections and the tensile ratio for heel-in sections: $h/R = f(E_C/S_{CY})$, for heel-out, $h/R = f(E_T/S_{ty})$, for heel-in. These two indices can be used to draw the limit curves for any material for this process.

MANUAL SPINNING

Spinning is another process, the formability of which is independent of the elongation limits of the material as shown by the graph developed in Chapter II below:

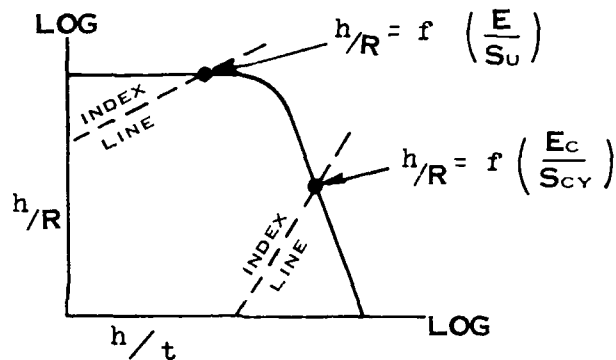


FIGURE III-13 FORMABILITY LIMIT GRAPH FOR SPINNING

The elastic portion of the graph can be seen to be a function of the compressive ratio of modulus to yield strength, E_c/S_{cy} , while the plastic portion of the curve can be seen to be a function of the ratio of the modulus to the ultimate strength of the material, E/S_u . Formability graphs can be drawn for all materials once these two material indices are determined.

DEEP DRAWING WITH MECHANICAL DIES

This process is the fourth one to have formability limits independent of the elongation properties of a material as shown by the graph developed in Chapter II and below:

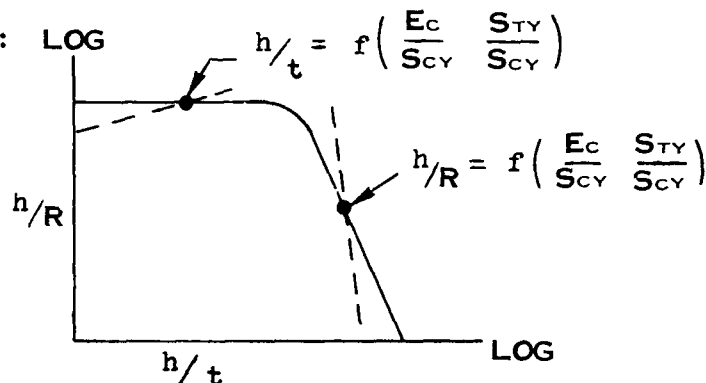


FIGURE III-14 FORMABILITY LIMITS FOR DEEP DRAWING

The index for formability in this process was found to be a complex function of the normal buckling ratio (E_c/S_{cy}) times a tensile yield to compressive yield ratio (S_{ty}/S_{cy}). In this way, formability for different materials for both elastic and plastic buckling limits is governed by the index $(E_c/S_{cy}) \left(\frac{S_{ty}}{S_{cy}} \right)$.

The reasoning for this index is seen to be quite simple by first realizing that the stability of the flange during drawing is a function of E_c/S_{cy} ; however, the tensile strength in the cylindrical portion of the cup determines the ability of the flange to be drawn and the compressive flow stress in the flange determines the relative ease for the flange to be drawn.

The result is that the higher E_c and S_{ty} and the lower S_{cy} , the better the formability. This means that the higher the index, $\frac{E_c}{S_{cy}} \frac{S_{ty}}{S_{cy}}$, the greater will be the formability.

For elastic buckling, $h/R = f\left(\frac{E_c}{S_{cy}} \frac{S_{ty}}{S_{cy}}\right)$, and for plastic buckling, $h/t = f\left(\frac{E_c}{S_{cy}} \frac{S_{ty}}{S_{cy}}\right)$. Using this index, formability curves for any material can be drawn.

SUMMARY

In summary of the formability indices to be used for predicting formability for any material, the following table is presented. (Figure III-15).

It can be seen from the table that most of the processes depending at least partially on the elongation of a material can be correlated to the standard 2.0 inch gage length elongation, $\epsilon_{2.0}$. Also, most of the processes depending at least partially on the buckling characteristics of a material can be correlated to the basic index E/S_y . Some of the processes use both of these indices for prediction of formability; however, it is necessary to use only one of the two for some processes.

FORMING PROCESS	SPLITTING INDICES		BUCKLING INDICES		
	$\epsilon_{2.0}$	OTHERS	E_T / S_{TY}	E_C / S_{CY}	OTHERS
1. BRAKE FORMING		$\bar{\epsilon}_{.25}(\text{CORR.})$			
2. DIMPLING	FOR $\alpha < 40^\circ$				
3. DROP HAMMER BEADING		$\epsilon_{.50}(\text{CORR.})$			
4. RUBBER PRESS BEADING		$\epsilon_{2.0} S_U$			
5. SHEET STRETCH	FRACTURE IN FREE AREA				
6. ANDROFORM		$\frac{E_T}{S_{TY}} \frac{1}{\epsilon_{2.0}}$	BOTH LONGITUDINAL AND TRANSVERSE		
7. JOGGLING		$\epsilon_{.02}$		SHEAR BUCKLING	
8. LINEAR STRETCH	VARIES WITH "t"		FROM SPRINGBACK		
9. RUBBER STRETCH	INDEPENDENT OF "t"		FROM SPRINGBACK		
10. RUBBER SHRINK				FROM APPLIED ELASTIC STRESS	$\frac{1}{S_{CY}}$ FOR PLASTIC BUCKLING
11. ROLL FORMING			HEEL-IN	HEEL-OUT	
12. SPINNING				FROM APPLIED ELASTIC STRESS	E/S_U FOR PLASTIC BUCKLING
13. DEEP DRAWING					$\frac{E}{S_{CY}} \frac{S_{TY}}{S_{CY}}$ FOR ELASTIC AND PLASTIC BUCKLING

FIGURE III-15 APPLICATION OF FORMABILITY INDICES

CHAPTER IV
FORMABILITY TESTS

STANDARD TENSILE SPECIMENS

Standard tensile specimens were tested to obtain the modulus of elasticity (E_T), tensile yield strength (S_{TY}), ultimate tensile strength (S_U) and strain distribution for the materials considered in this program. The specimens were tested with the Model FGT-SR4 T/M Tensile Test Machine shown in Figure IV-1.

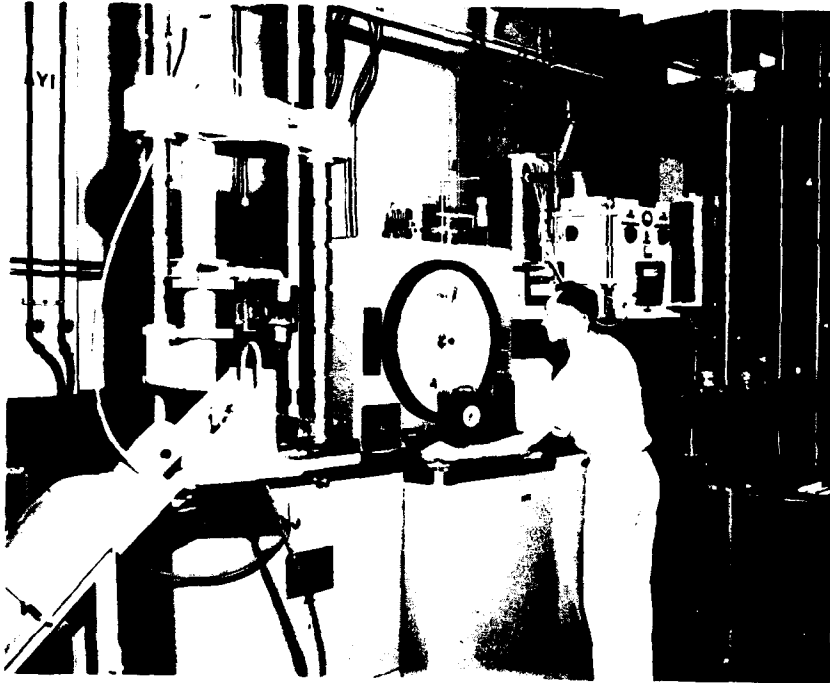


FIGURE IV-1 MODEL FGT — SR4 T/M BALDWIN TENSILE
TEST MACHINE

The tensile specimens were fabricated to the requirements of CVL specification 1922-82A, shown in Figure IV-2, from the same sheet material available for forming experimental parts so that correlation of the forming processes to the tensile specimens would be valid.

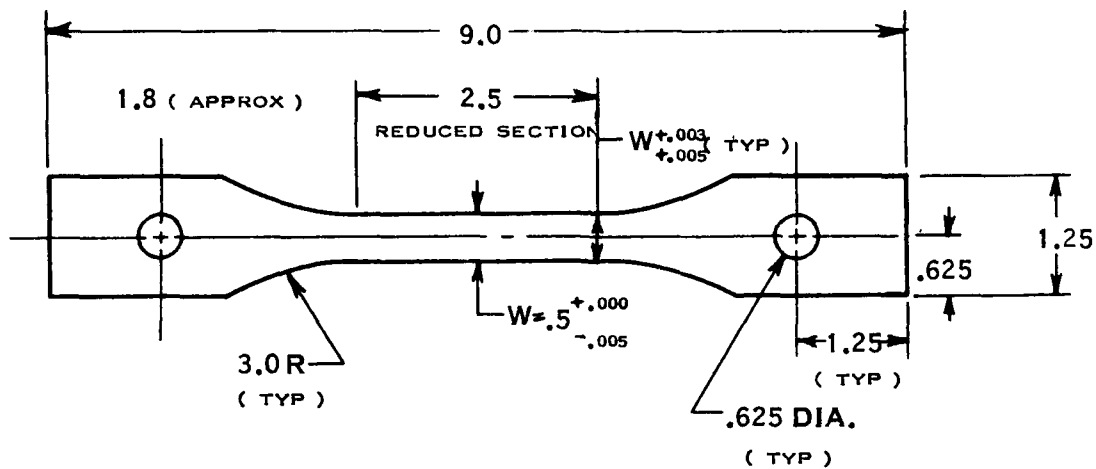


FIGURE IV-2 CVL 1922 - 82A (TENSILE SPECIMEN)

Two types of load-strain curves were obtained for each material as shown in Figure IV-3. The curve in Figure IV-3(a) was obtained with an SRE-1 extensometer using calibrated SR-4 beams to give high magnification curves for the modulus of elasticity and the yield strength. The curve in Figure IV-3(b) was obtained with the TSMD dual range extensometer shown in Figure IV-4. This extensometer does not have the high magnification in the elastic region as the SRE-1 extensometer, but it records the entire plastic region of the curve showing the strain

hardening and necking characteristics of a given material.

The SRE-1 extensometer with SR-4 beams has a magnification of 500 to 1 until the beams are removed. The magnification of the TSMD extensometer is 200 to 1 from zero to 0.01 in/in strain (4" chart) and 20 to 1 from 0.01 in/in strain to fracture.

All tensile tests were controlled at a strain rate of 0.005 in/in/min in the elastic region and 0.05 in/in/min in the plastic region with an O.S. Peters Strain Pacer.

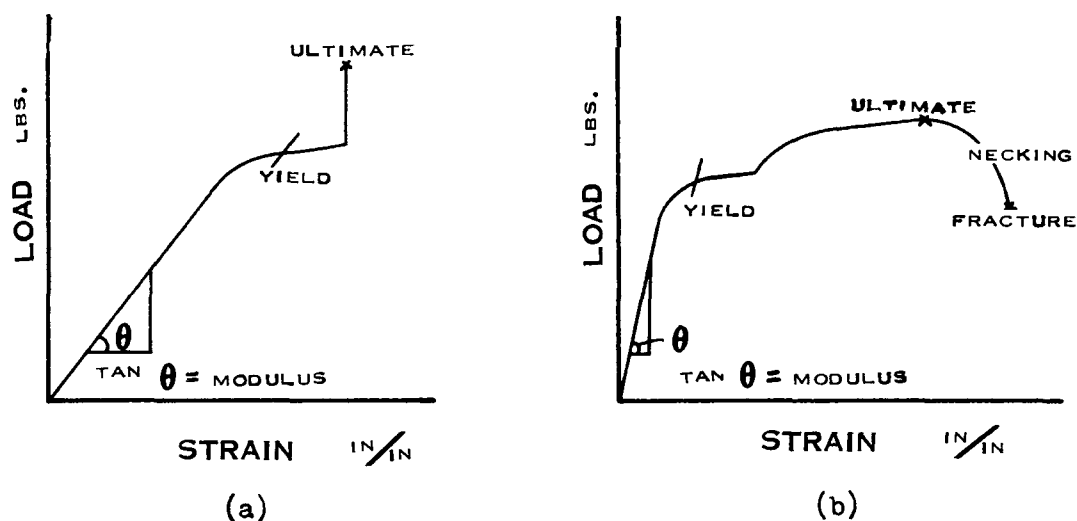


FIGURE IV-3 TYPES OF TENSILE LOAD - STRAIN CURVES



FIGURE IV-4
TSMD EXTENSOMETER

Elevated temperature testing was accomplished with the same instrumentation as the room temperature testing previously discussed except for the heating system. Arc Weld furnaces were first used, but it was found that radiant heat lamps with an Ignitron Control System provided excellent control of the temperature gradient over the two inch gage length and provided a testing time of approximately 1/2 the time due to decreased set-up time. Three thermocouples were attached to the heat zone of the specimen to accurately determine the temperature conditions and the specimen was allowed to heat soak for a predetermined period of time.

The factors that determine the amount of strain that a sheet metal part can take before fracture during forming are the material, the geometry of the part and the strain gradient across the part.

The geometry determines the stability of a part against necking. Stresses can be applied in only two directions in a tensile specimen which is classed as a sixteenth-infinite plate illustrated in Figure IV-5. This type of part is very unstable and nearly all failures are preceded by considerable necking.

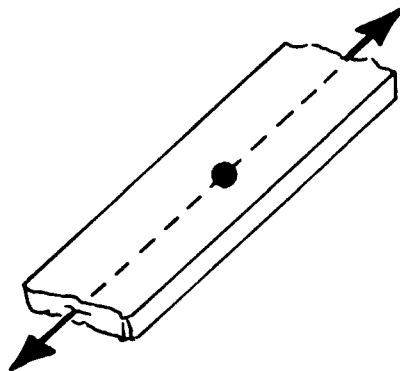


FIGURE IV-5 SIXTEENTH INFINITE PLATE
(TENSILE SPECIMEN)

The thinner a part and the nearer plastic flow is occurring to a free edge, the higher the instability and the more of a tendency toward necking. The tensile specimen is the most unstable part since it has two flat surfaces very close together, in thin gage material, and two edges that are close together.

The reason for this geometric instability is illustrated in Figure IV-6. Stability against necking in plastic deformation is the compensation of the increased stress due to reduction of area by the strain hardening in the necked area. When strain hardening increases as fast as the stress increases due to reduction in area, stability is reached and necking does not occur.

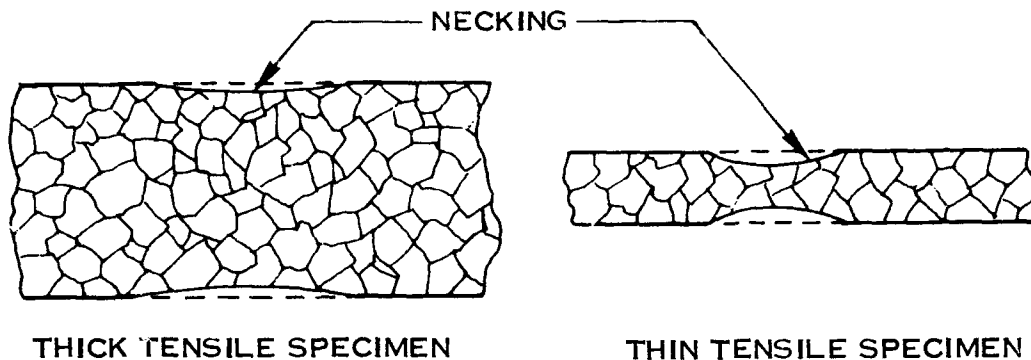


FIGURE IV-6 INSTABILITY OF TENSILE SPECIMEN

Strain hardening is due to dislocation pile-up at grain boundaries and is somewhat greater in the thick specimen than in the thin specimen. The plastic flow surfaces in the thick specimen strain harden faster than the stress increases due to reduction in cross sectional area resulting in a more stable condition than in the thin specimen.

Strain hardening across the width of a tensile specimen is greater than across the thickness, thereby making the width more stable against necking than the thickness. Plastic thinning does occur across the width of the tensile specimen but not enough to result in instability and failure.

Two types of shear flow occur simultaneously when tensile specimens are pulled as illustrated in Figure IV-7. The specimens thin in both directions during the initial pulling, the width thinning according to Figure IV-7(a) and the thickness thinning according to Figure IV-7(b).

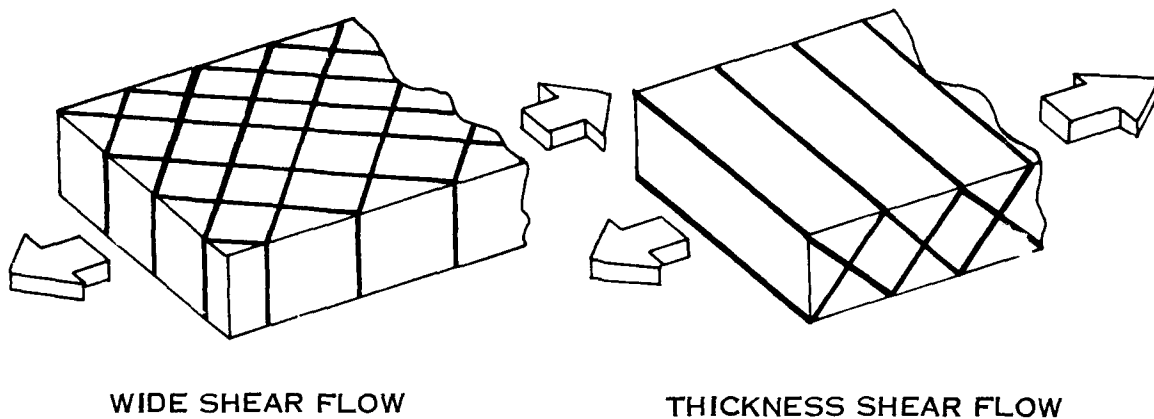


FIGURE IV-7 SHEAR FLOW IN TENSILE SPECIMENS

As previously stated, thick tensile specimens are impeded against necking in the thickness direction and will reduce in width enough to insure failure across this reduced width. Then the shear failure will occur approximately 50° to 60° across the thickness as illustrated in Figure IV-8.

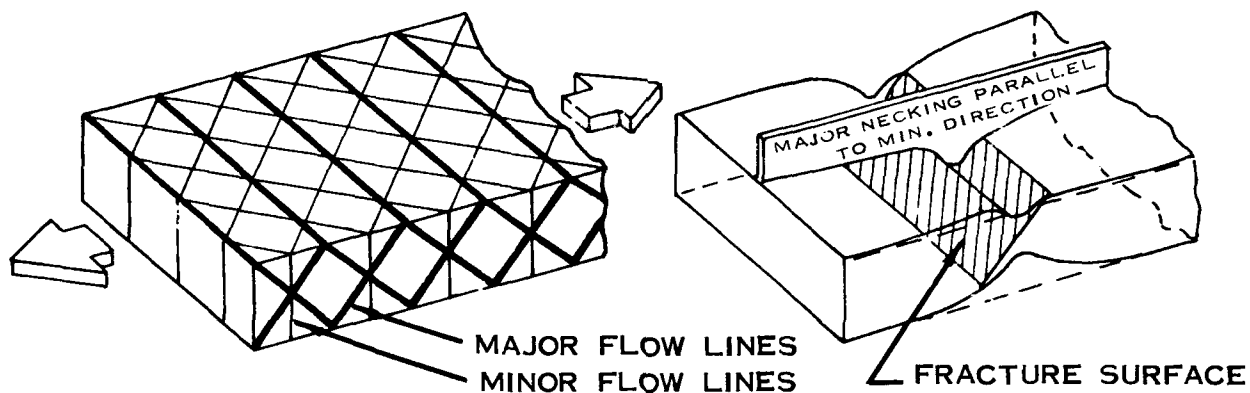


FIGURE IV-8 FAILURE OF THICK TENSILE SPECIMENS

The thin tensile specimen necks readily across the thickness as illustrated in Figure IV-9. This necking occurs at approximately 50° to 60° across the width and 90° across the thickness because this is where the maximum shear stress occurs.

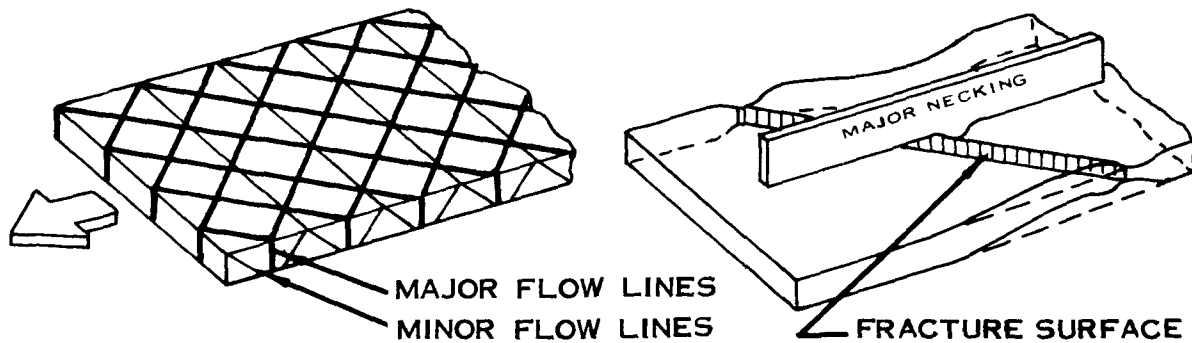


FIGURE IV-9 FAILURE OF THIN TENSILE SPECIMENS

Strain gradients occurring across plastically deformed tensile specimens also affect stability. Figure IV-10 illustrates the strain gradients in the three principal directions which are longitudinal (ϵ_L) transverse or width (ϵ_w) and thickness (ϵ_t).

From the laws of plasticity for constant volume, the equation for conventional strain (ϵ) is:

$$(IV-1) \quad (\epsilon_L + 1)(\epsilon_w + 1)(\epsilon_t + 1) = 1$$

Where the equation for conventional strain is defined by:

$$(IV-2) \quad \epsilon = \frac{\Delta l}{l_0} = \frac{l - l_0}{l_0} = \frac{l}{l_0} - 1$$

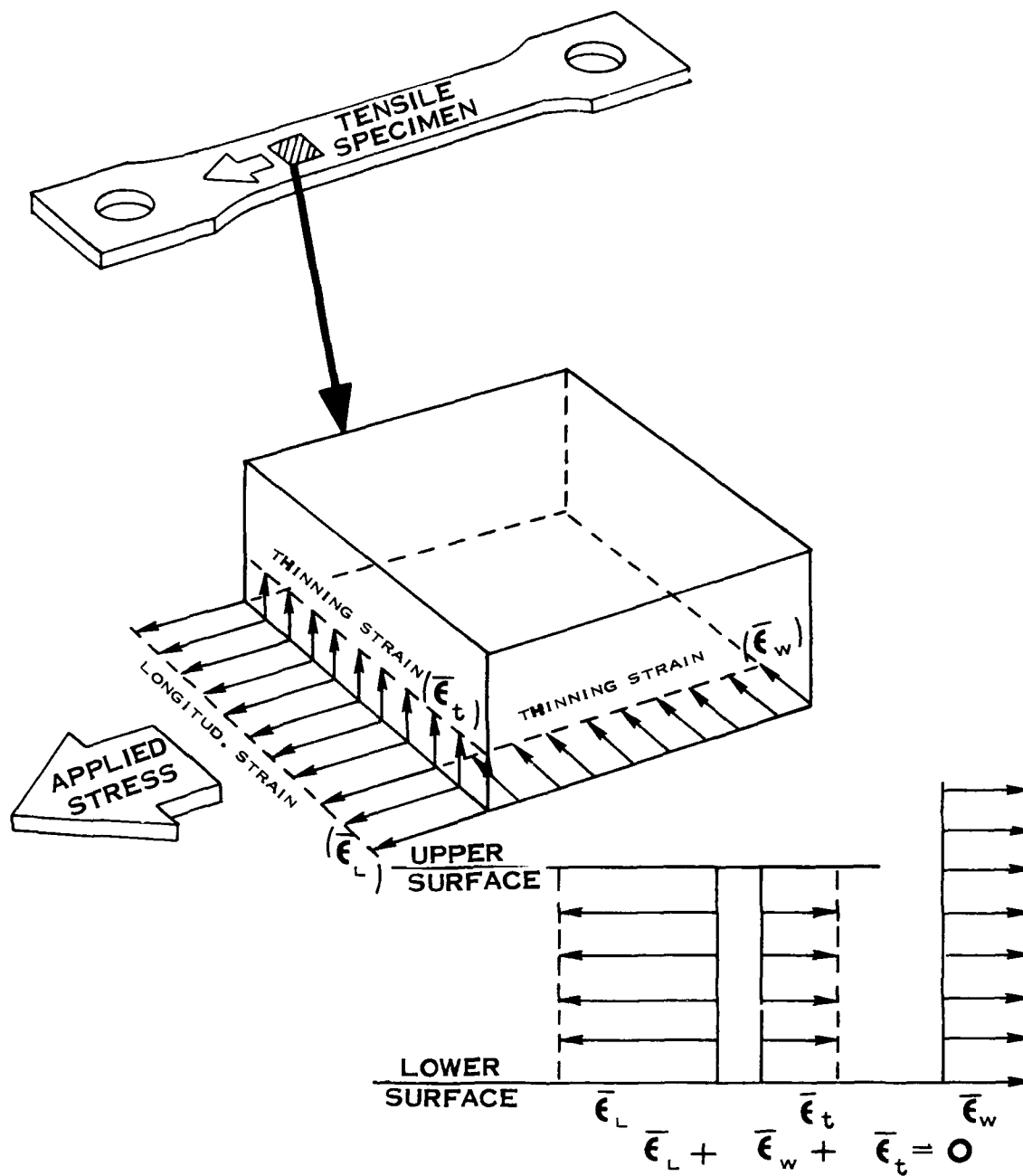


FIGURE IV-10 UNIFORM STRAIN DISTRIBUTION FOR TENSILE SPECIMENS

The conventional strain equation is valid as long as the elongations are uniform within the gage length. However, when instability is initiated by necking, the equation only gives an average strain throughout the gage length. In order to define absolute strains for the necked region, a logarithmic strain ($\bar{\epsilon}$) is defined:

(IV - 3)

$$\bar{\epsilon} = \int_{l_0}^l \frac{dl}{l} = \ln \frac{l}{l_0} = \ln \frac{A_0}{A} = \ln (1 + \epsilon)$$

All of these forms of the natural or true strain describe the strain condition within the necked region during plastic deformation.

The constant volume equation for natural strain is:

(IV - 4)

$$\bar{\epsilon}_L + \bar{\epsilon}_w + \bar{\epsilon}_t = 0$$

Where $\bar{\epsilon}_L$, $\bar{\epsilon}_w$ and $\bar{\epsilon}_t$ are the principal natural strains.

In order to determine the three principal natural strains in terms of the three principal stresses, it is necessary to define the three rules of yielding. These rules are based upon isotropy and constant volume:

- (a) The direction of principal strains coincide with those of the principal stresses: (isotropy).
- (b) The volume remains constant:

$$\bar{\epsilon}_L + \bar{\epsilon}_w + \bar{\epsilon}_t = 0$$

(Equation IV-4)

- (c) The Mohr's circles for stresses and strains are geometrically similar: (isotropy).

(IV - 5)

$$\frac{\bar{\epsilon}_L - \bar{\epsilon}_w}{\sigma_L - \sigma_w} = \frac{\bar{\epsilon}_w - \bar{\epsilon}_t}{\sigma_w - \sigma_t} = \frac{\bar{\epsilon}_t - \bar{\epsilon}_L}{\sigma_t - \sigma_L} = \text{CONSTANT}$$

Combining equation (IV-4) with each set of the three equations in (IV-5) gives:

(IV - 6)

$$\begin{aligned}\epsilon_L &= A \left[\sigma_L - 1/2 (\sigma_w + \sigma_t) \right] \\ \epsilon_w &= A \left[\sigma_w - 1/2 (\sigma_L + \sigma_t) \right] \\ \epsilon_t &= A \left[\sigma_t - 1/2 (\sigma_w + \sigma_L) \right]\end{aligned}$$

The coefficient "A" in each case is a constant for a given stress level, but it varies for different stress levels. Since these three equations were derived on the basis of equation (IV-4), they are limited to small plastic strains up to the onset of necking. However, these equations are valid beyond necking provided the gage lengths are small enough to satisfy equation (IV-4) and provided the directions of the principal stresses and strains are identical and do not rotate during straining.

One of the most prominent criterion developed for stressing a metal into the plastic region based on the three principal stresses is the "effective" stress and strain theory:

(IV - 7)

$$\sigma_e = \frac{1}{\sqrt{2}} \sqrt{(\sigma_L - \sigma_w)^2 + (\sigma_w - \sigma_t)^2 + (\sigma_t - \sigma_L)^2}$$

(IV - 8)

$$\bar{\epsilon}_e = \sqrt{\frac{2}{3}} \sqrt{(\bar{\epsilon}_L - \bar{\epsilon}_w)^2 + (\bar{\epsilon}_w - \bar{\epsilon}_t)^2 + (\bar{\epsilon}_t - \bar{\epsilon}_L)^2}$$

These are the resultant of the diameters of the Mohr's circles times an arbitrary constant. The arbitrary constants were chosen so that the following results are obtained for simple tension (square specimen):

$$\begin{aligned}\sigma_w &= \sigma_t = 0 & : & \sigma_e = \sigma_L \\ \bar{\epsilon}_w &= \bar{\epsilon}_t = -\frac{\bar{\epsilon}_L}{2} & : & \bar{\epsilon}_e = \bar{\epsilon}_L\end{aligned}$$

Equation (IV-8), representing the effective strain, can be expanded to give equation (IV-9) which represents the amount of yielding that occurs for various conditions of plane stress.

(IV-9)

$$\frac{9}{4} \bar{\epsilon}_e^2 = \bar{\epsilon}_L^2 + \bar{\epsilon}_W^2 + \bar{\epsilon}_T^2 - \bar{\epsilon}_L \bar{\epsilon}_W - \bar{\epsilon}_W \bar{\epsilon}_T - \bar{\epsilon}_T \bar{\epsilon}_L$$

The equations in (IV-6) reduce to the equations in (IV-10) for the types of loading that occur in sheet metal forming where $\sigma_t = 0$ for plane stress.

(IV-10)

$$\begin{aligned} \bar{\epsilon}_L &= A \left[\sigma_L - 1/2 \sigma_W \right] \\ \bar{\epsilon}_W &= A \left[\sigma_W - 1/2 \sigma_L \right] \\ \bar{\epsilon}_T &= A \left[-1/2 (\sigma_L + \sigma_W) \right] \end{aligned}$$

Using the equations in (IV-10), equation (IV-9) can be plotted in Figure IV-11.

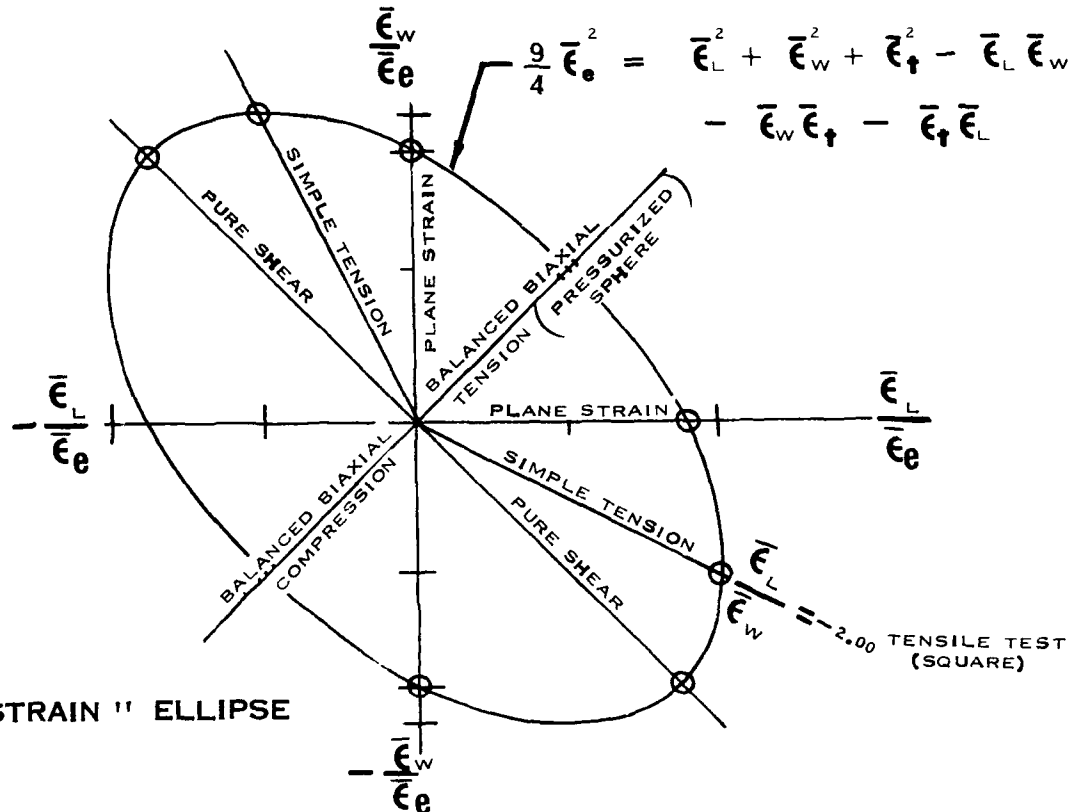


FIGURE IV-11
"EFFECTIVE STRAIN" ELLIPSE

The significant aspects of this ellipse are that the available strains are reduced in the upper right and lower left quadrants for balanced biaxial tension and compression. The quadrants in the lower right and upper left show increased strains for pure shear and simple tension (square specimen) where the sheet is reduced in width with longitudinal extension. It should be noted that the 1/2 inch wide tensile specimen (CVL 1922-82A) will have values of $\frac{\bar{\epsilon}_L}{\bar{\epsilon}_e} < 1$ and will have varying values of $\frac{\bar{\epsilon}_L}{\bar{\epsilon}_w}$ for different materials. Plane strain is shown to result in strains 13.4% lower than that for simple tension (square specimen) because the former is restricted to zero reduction in width by a lateral 2 to 1 stress acting on the part.

It should be emphasized again that the strain ellipse is limited to small strains of the order of uniform strain. Forming operations displaying larger strains will not be predicted by such an ellipse.

In order to obtain the values of $\frac{\bar{\epsilon}_L}{\bar{\epsilon}_w}$ and $\frac{\bar{\epsilon}_L}{\bar{\epsilon}_e}$ for the different materials, tensile specimens were photographically gridded using a negative with 0.02 inch grids furnished by the Bureau of Standards.

The specimens were tested to failure and the strained grids were measured with a Stocker and Yale Optical Comparator using a 50 to 1 magnification factor. An optical comparator view of a fractured tensile specimen is shown in Figure IV-12.

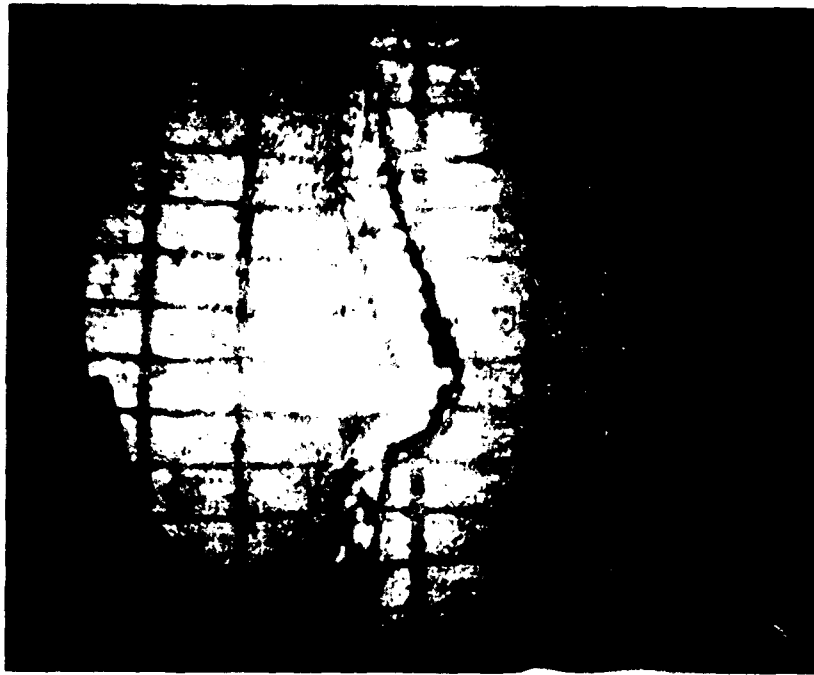


FIGURE IV-12 TENSILE SPECIMEN FRACTURE ON THE SCOPE OF THE OPTICAL COMPARATOR

Measurements of the longitudinal strains (ϵ_L) across fracture and width strains (ϵ_w) perpendicular to the longitudinal strains were made for each of the materials to obtain the values for correlation of tensile specimens to the forming processes.

All processes using splitting indices with the exceptions of brake forming, drop hammer forming and joggling correlated to the standard 2 inch elongation $(\epsilon_L)_{2.0}$. Joggling was correlated to the 0.02 inch gage length elongation, but for brake forming and drop hammer forming it was necessary to use $(\bar{\epsilon}_L)_{.25}$ and $(\epsilon_L)_{.5}$, respectively, and correct for lateral contraction.

The correction for lateral contraction is obtained from the following analysis illustrated in Figure IV-13.

$$\bar{\epsilon}_{L \text{ (CORRECTED)}} = \bar{\epsilon}_L - \bar{V} \bar{\epsilon}_w$$

$$\text{WHERE: } \bar{V} = \frac{\bar{\epsilon}_w}{\bar{\epsilon}_L}$$

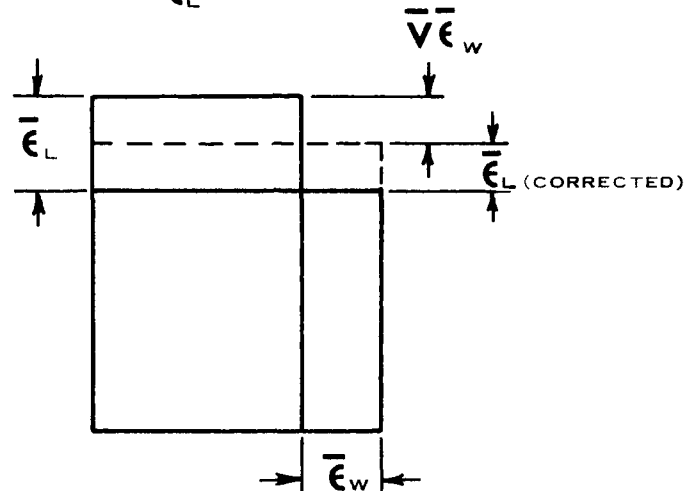
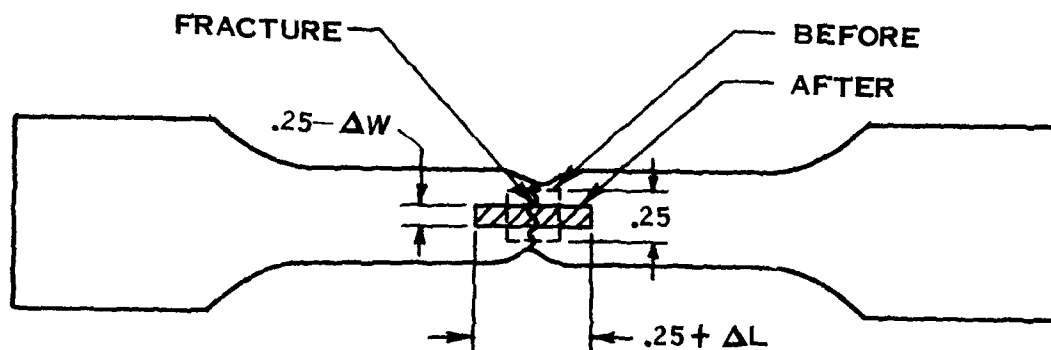


FIGURE IV-13 CORRECTION FOR LATERAL CONTRACTION

The equation for the corrected longitudinal elongation is given by:

$$(IV - 11) \quad \bar{\epsilon}_{L \text{ (CORRECTED)}} = \bar{\epsilon}_L - \frac{\bar{\epsilon}_w^2}{\bar{\epsilon}_L}$$

The 0.25 inch gage length was corrected for lateral contraction, as illustrated in Figure I-14, and used for the brake forming index for splitting. Since the gage length for brake forming is small, the corrected elongations were left in terms of natural strain.



$$(\epsilon_L)_{.25} = \frac{\Delta L}{.25} ; (\bar{\epsilon})_{.25} = \ln [1 + (\epsilon_L)_{.25}]$$

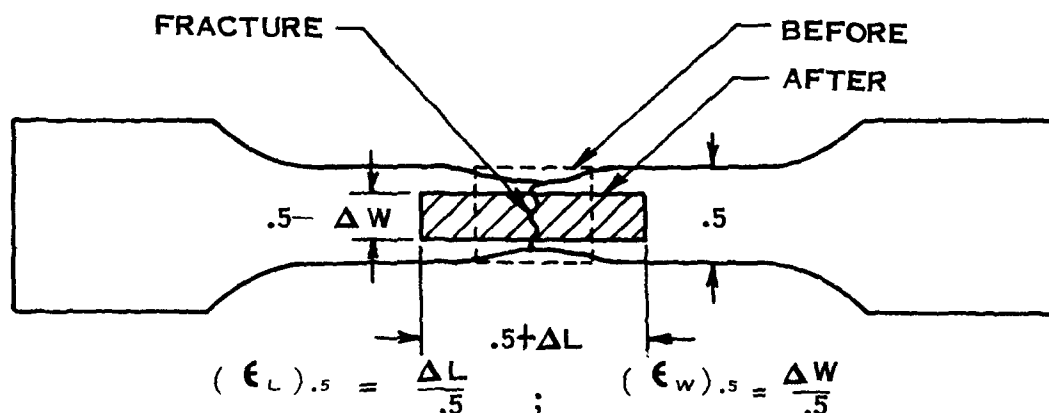
$$(\epsilon_W)_{.25} = \frac{\Delta W}{.25} ; (\bar{\epsilon})_{.25} = \ln [1 + (\epsilon_W)_{.25}]$$

FIGURE IV-14 CORRECTION FOR LATERAL CONTRACTION
(.25" GAGE LENGTH)

The corrected value for the longitudinal strain $\bar{\epsilon}_{L, .25(CORR.)}$ is given by equation (IV-12).

$$(IV-12) \quad (\bar{\epsilon}_{L, .25(CORR.)}) = (\bar{\epsilon}_L)_{.25} - \frac{(\bar{\epsilon}_W)_{.25}^2}{(\bar{\epsilon}_L)_{.25}}$$

The 0.5 inch gage length was corrected for lateral contraction, as illustrated in Figure IV-15, and used for the drop hammer forming index for splitting. Since the gage length for drop hammer beading is relatively large, the corrected elongations were found in terms of conventional strain.



$$(\epsilon_L)_{.5} = \frac{\Delta L}{.5} ; (\epsilon_W)_{.5} = \frac{\Delta W}{.5}$$

FIGURE IV-15 CORRECTION FOR LATERAL CONTRACTION
(.5" GAGE LENGTH)

The corrected value for the longitudinal strain $(\epsilon_L)_{.5(CORR.)}$ is given by equation (IV-13).

$$(IV - 13) \quad (\epsilon_L)_{.5(CORR.)} = \ln^{-1} \left[(\epsilon_L)_{.5} - \frac{[\bar{\epsilon}_w]_{.5}^2}{[\bar{\epsilon}_L]_{.5}} \right] - 1$$

STANDARD COMPRESSION SPECIMENS

Standard compression specimens were tested to obtain the modulus of elasticity (E_c) and the compressive yield strength (S_{cy}) for the materials considered in this program. The specimens were tested with the Baldwin Tensile and Compression Machine shown in Figure IV-16.

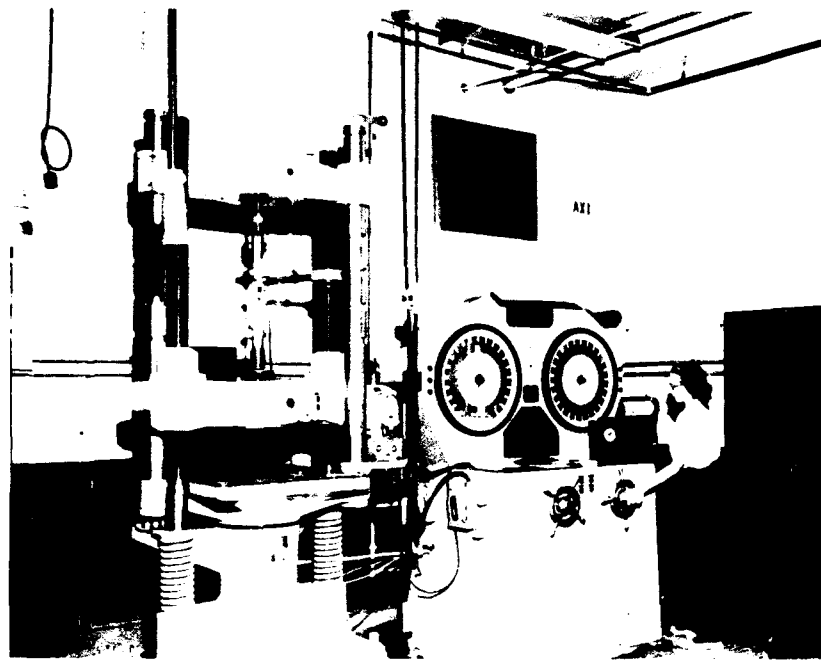


FIGURE IV-16 BALDWIN TENSILE AND COMPRESSION MACHINE

The compression specimens were fabricated to the requirements of CVL specification 1922-58 from the same sheet material available for forming experimental parts so that indices based on the compressive properties would be valid.

Load-strain curves, as illustrated in Figure IV-17, were obtained for each material using an extensometer with calibrated SR-4 beams and a lateral supporting compression jig with 0.0625 inch Kentanium balls.

All compression tests were controlled at a strain rate of 0.005 in/in/min in the elastic region and 0.05 in/in/min in the plastic region with an O.S. Peters Strain Pacer.

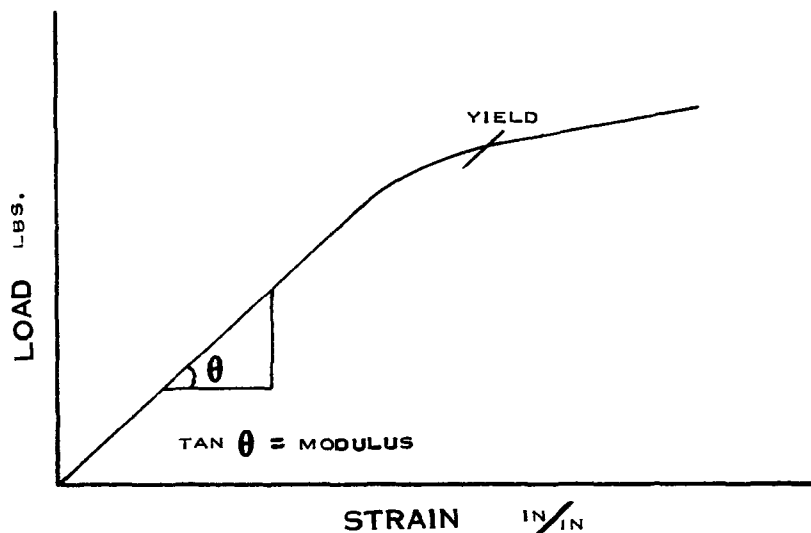


FIGURE IV-17 COMPRESSIVE LOAD - STRAIN CURVE

Elevated temperature testing was accomplished with the same instrumentation as the room temperature testing except for the heating system. An Arc Weld furnace enclosing the lateral support jig was used with a

temperature control and recording system. Thermocouples were attached to the heat zone of the specimen to accurately determine the temperature conditions and the specimen was allowed to heat soak for a predetermined period of time.

SPECIAL TESTS

All of the experimental parts fall into one of the three basic types of combined loading conditions: (1) uniaxial stress, (2) plane stress and (3) plane strain. This consideration led into special types of tensile specimens that would simulate these loading conditions. In order to simulate the plane strain condition and, to a lesser extent, the plane stress condition, three types of the 2 inch gage length by 12 inch wide tensile specimens were devised as illustrated in Figure IV-18. Since a number of different materials were involved, three types of this specimen were used to insure the proper type of failure in the gridded zone.

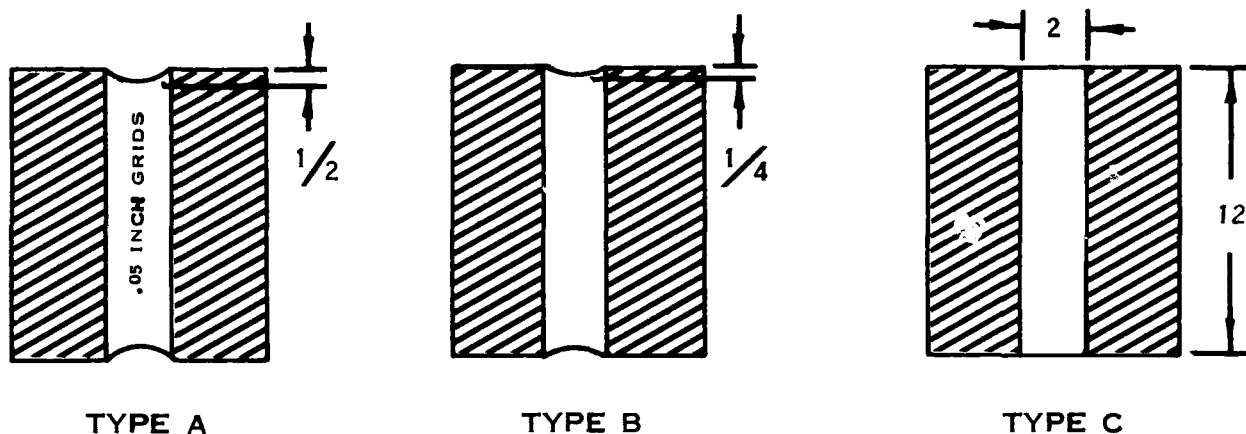
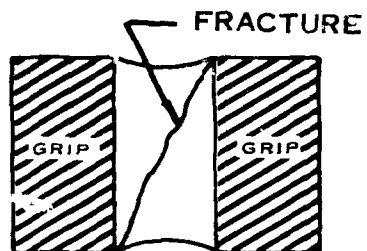


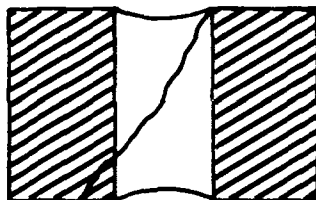
FIGURE IV-18 THREE TYPES OF 12 INCH WIDE TENSILE SPECIMENS

The wide specimens could not be evaluated for some materials because of the following reasons:

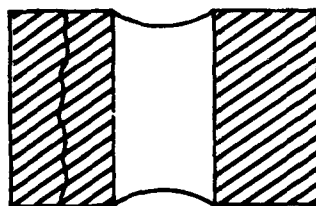
- (1) Diagonal failure



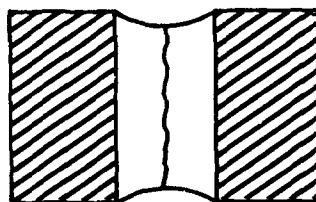
- (2) Failure initiated in jaws (notch sensitive material)



- (3) Slippage in the jaw



- (4) The type of failure that yield good results is illustrated below.



Since it was difficult to pull successful 12 inch wide tensile specimens and impossible for some materials, this type of testing was terminated. However, correlations for brake forming and drop hammer forming were made for eleven materials yielding fractures that could be evaluated. In addition, correlation was made with the standard tensile specimen (1/2" wide) by correcting the longitudinal strain(ϵ_L) for lateral contraction(ϵ_w)

A special eccentric test, as illustrated in Figure IV-19, was developed to simulate varying strain conditions across formed experimental parts. Considerable transverse flow is noted in the sketch illustrating the similarity to uniaxial stress conditions. This type of testing was terminated because satisfactory results were not being obtained and correlation with the standard tensile specimen (1/2" wide) was possible.

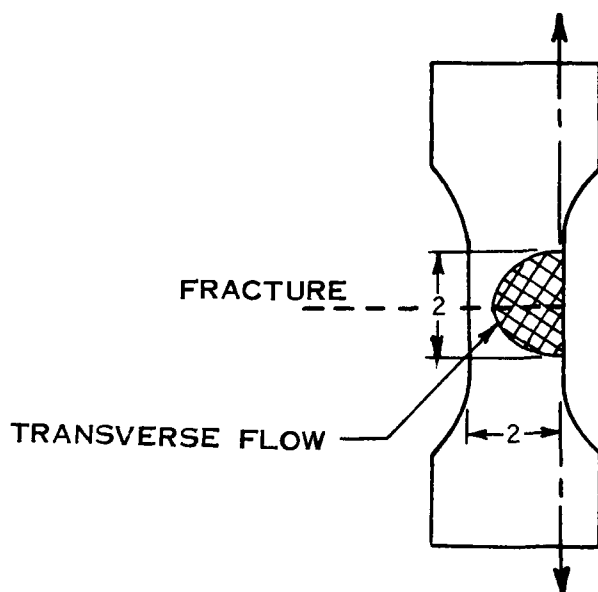


FIGURE IV-19 ECCENTRIC TENSILE TEST

GRIDDED PARTS

Part blanks were gridded and formed for ten processes displaying splitting as a major failure to verify the mathematical plasticity equations and the "Effective Strain" theory for sheet metal forming.

The purpose of the analysis was to determine the maximum principal strains, $\bar{\epsilon}_L$ and $\bar{\epsilon}_W$, for use in the plasticity equations (IV-10) which define the types of loading that occur in sheet metal forming.

$$(IV-10) \quad \begin{array}{l} \bar{\epsilon}_L = A \left[\sigma_L - 1/2 \sigma_W \right] \\ \bar{\epsilon}_W = A \left[\sigma_W - 1/2 \sigma_L \right] \\ \bar{\epsilon}_t = A \left[-1/2 (\sigma_L + \sigma_W) \right] \end{array}$$

The effective strain is given by equation (IV-9).

$$(IV-9) \quad \frac{9}{4} \bar{\epsilon}_e^2 = \bar{\epsilon}_L^2 + \bar{\epsilon}_W^2 + \bar{\epsilon}_t^2 - \bar{\epsilon}_L \bar{\epsilon}_W - \bar{\epsilon}_W \bar{\epsilon}_t - \bar{\epsilon}_t \bar{\epsilon}_L$$

The following sample calculation for sheet stretch forming, utilizing the measured values for $\bar{\epsilon}_L$ and $\bar{\epsilon}_W$ and the plasticity equations, is typical of the analysis used for each process having splitting as a major failure.

Sample Calculation (Sheet Stretch Forming):

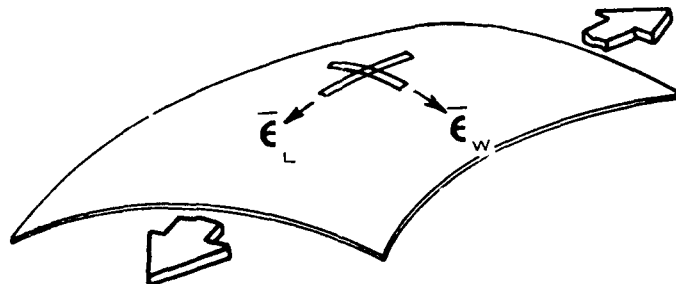


FIGURE IV - 20 SHEET STRETCH FORMED PART

The plasticity equations (IV-10) are used to determine $\frac{\sigma_L}{\sigma_w}$ and $\frac{\bar{\epsilon}_L}{\bar{\epsilon}_t}$.

$$\frac{\bar{\epsilon}_L}{\bar{\epsilon}_w} = \frac{A [\sigma_L - 1/2 \sigma_w]}{A [\sigma_w - 1/2 \sigma_L]} = -3.7$$

$$\sigma_L = 3.76 \sigma_w \quad ; \quad \sigma_t = 0$$

$$\frac{\bar{\epsilon}_L}{\bar{\epsilon}_t} = \frac{A [\sigma_L - 1/2 \sigma_w]}{A [-1/2 (\sigma_L + \sigma_w)]} = -1.37$$

The effective strain is calculated by substituting known relationships into equation (IV-9).

$$\frac{9}{4} \bar{\epsilon}_e^2 = \bar{\epsilon}_L^2 + \bar{\epsilon}_w^2 + \bar{\epsilon}_t^2 - \bar{\epsilon}_L \bar{\epsilon}_w - \bar{\epsilon}_w \bar{\epsilon}_t - \bar{\epsilon}_t \bar{\epsilon}_L$$

$$\frac{9}{4} \bar{\epsilon}_e^2 = 2.408 \bar{\epsilon}_L^2$$

$$\frac{\bar{\epsilon}_L}{\bar{\epsilon}_e} = 0.968$$

The calculation of $\frac{\bar{\epsilon}_L}{\bar{\epsilon}_e}$ allows the Sheet Stretch Forming process to be plotted on the "Effective Strain" Ellipse as shown in Figure IV-21. All processes having splitting as a major failure are plotted in Chapter I, Figure I-133.

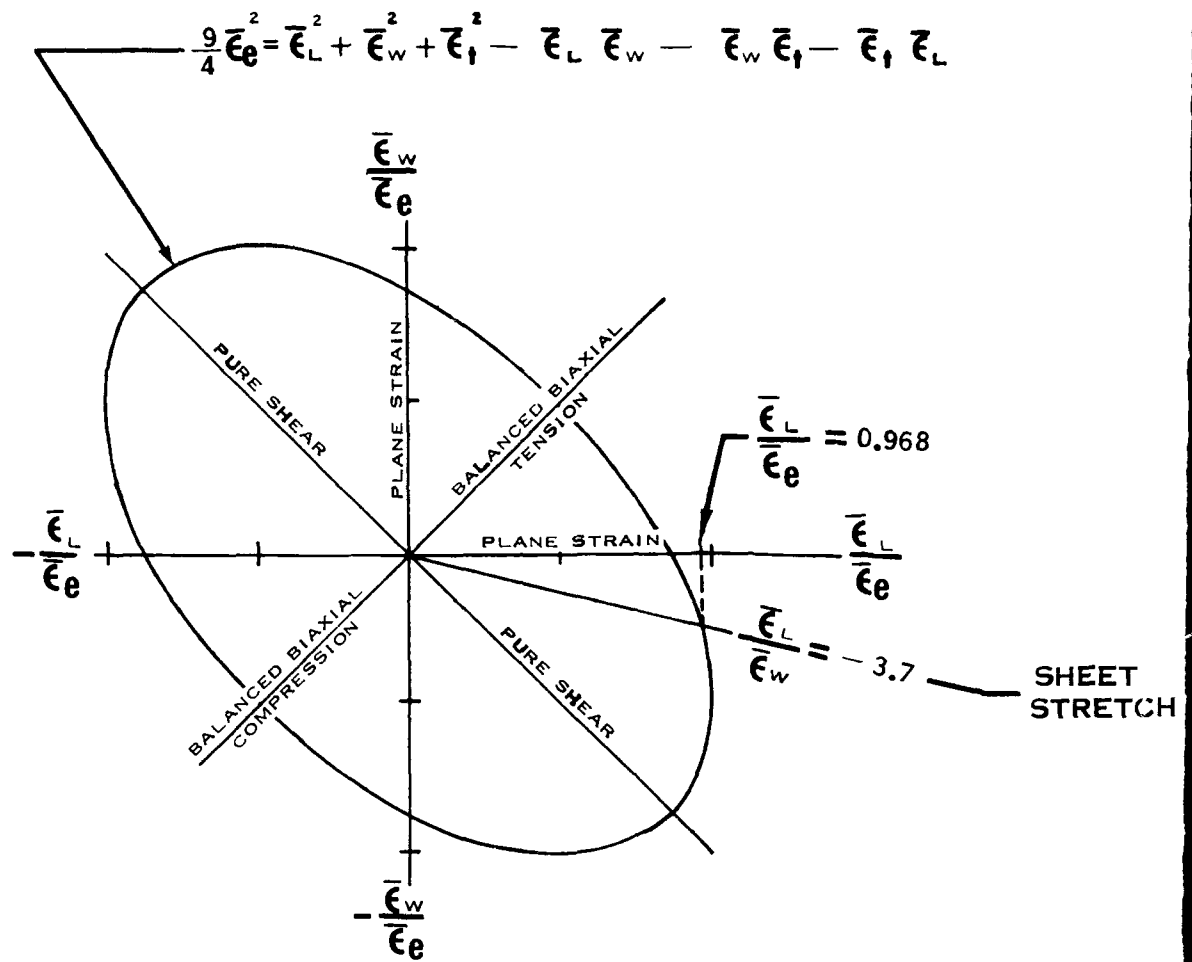


FIGURE IV - 21 "EFFECTIVE STRAIN" ELLIPSE

CHAPTER V
COMPOSITE GRAPHS, PREDICTABILITY
EQUATIONS AND DESIGN TABLES

BRAKE FORMING

The fundamental shape equations for brake forming, which define the shape of the formability limit curve, were developed in Chapter II. A composite graph composed of the empirically determined forming limit curves of all materials was developed as shown in Figure V-1.

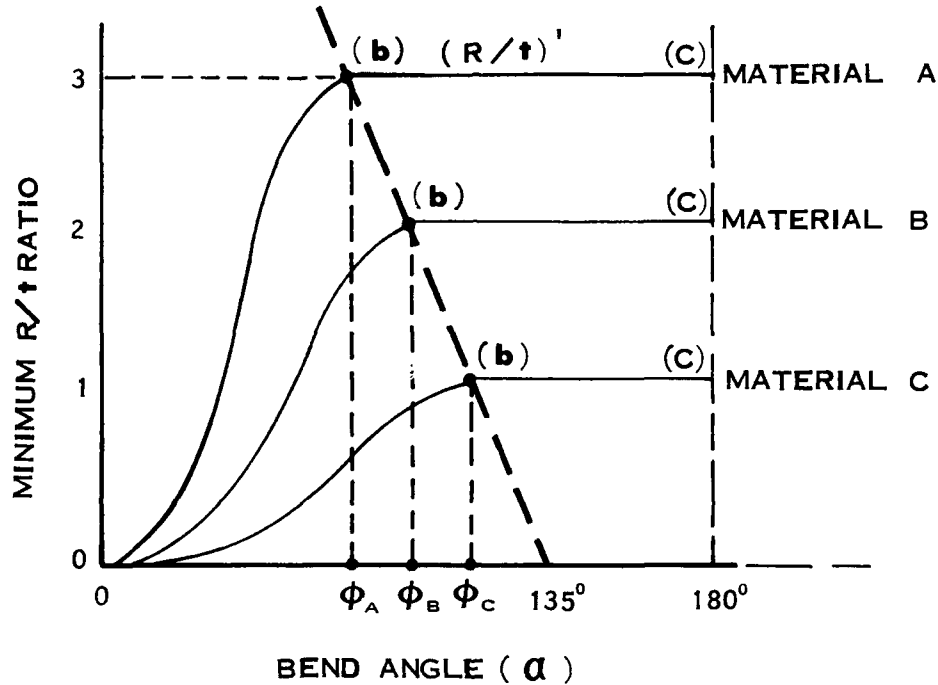


FIGURE V-1 COMPOSITE GRAPH FOR BRAKE FORMING

The minimum R/t ratio for any material is a function of the bend angle α up to a certain angle $\alpha = \phi$. From the angle ϕ to 180° the R/t ratio is constant and at its maximum value $(R/t)'$.

The natural strain in the outer fiber of a bend specimen is calculated as follows:

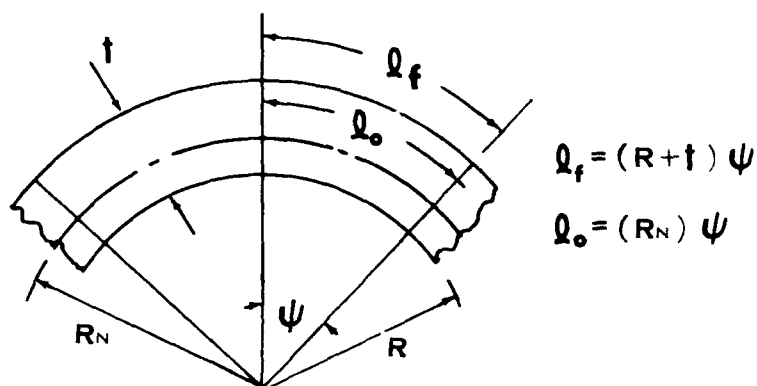


FIGURE V-2 STRAIN IN A BEND SPECIMEN

From Progress Report No. 1, the basic equation for the shift in neutral axis is:

$$(V-1) \quad R_N = \sqrt{R(R+t)}$$

The natural strain from Figure V-2 is:

$$(V-2) \quad \bar{\epsilon} = \ln \frac{l_f}{l} = \ln \left[\frac{(R+t) \psi}{\sqrt{R(R+t)} \psi} \right] = \ln \left[\frac{R+t}{\sqrt{R(R+t)}} \right] = \ln \sqrt{1 + \frac{t}{R}}$$

Solving for R/t :

$$(V-2A) \quad \frac{R}{t} = \frac{1}{e^{2\bar{\epsilon}} - 1}$$

The one-quarter inch (0.25") gauge length natural strain from the standard tensile specimen, corrected to a condition of plane strain (See Chapter IV), was found by correlation to be equal to the natural bending strain at $(R/t)^{1/2}$. Therefore:

(V-3)

$$\left(\frac{R}{t}\right)' = \frac{1}{e^{2(\bar{\epsilon}_{.25}) \text{ CORRECTED}} + 1}$$

From equation (V-3) the minimum R/t limit for bend angles from ϕ to 180° for any material can be predicted if $(\bar{\epsilon}_{.25}) \text{ CORRECTED}$ is determined. The equation is for the section of the curve from (b) to (c). (See Figure V-1).

For bend angles less than ϕ , an empirical equation was developed. The section of the curve from (a) to (b) takes the form of a sine wave. The basic equation to be developed takes the following form:

(V-4)

$$\frac{R}{t} = f\left[\alpha, (\bar{\epsilon}_{.25}) \text{ CORRECTED}\right]$$

Figure V-3 illustrates the type of sine curve that fits the composite graphs very well.

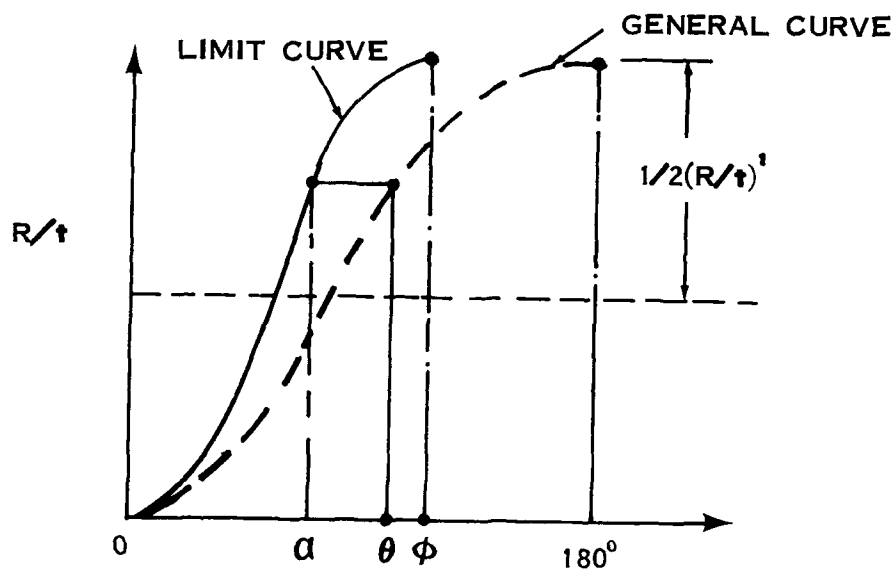


FIGURE V-3 SINE WAVE CURVE

The equation for the general curve is:

$$(V-5) \quad \frac{R}{t} = \left(\frac{1}{2}\right)\left(\frac{R}{t}\right)' [1 + \sin(\theta - 90)]$$

Expressing θ in terms of α and ϕ from Figure V-3:

$$(V-6) \quad \frac{180^\circ}{\phi} = \frac{\theta}{\alpha}$$

Solving for θ :

$$(V-6A) \quad \theta = \frac{180\alpha}{\phi}$$

ϕ is a function of (R/t) and α . It was empirically determined as follows:

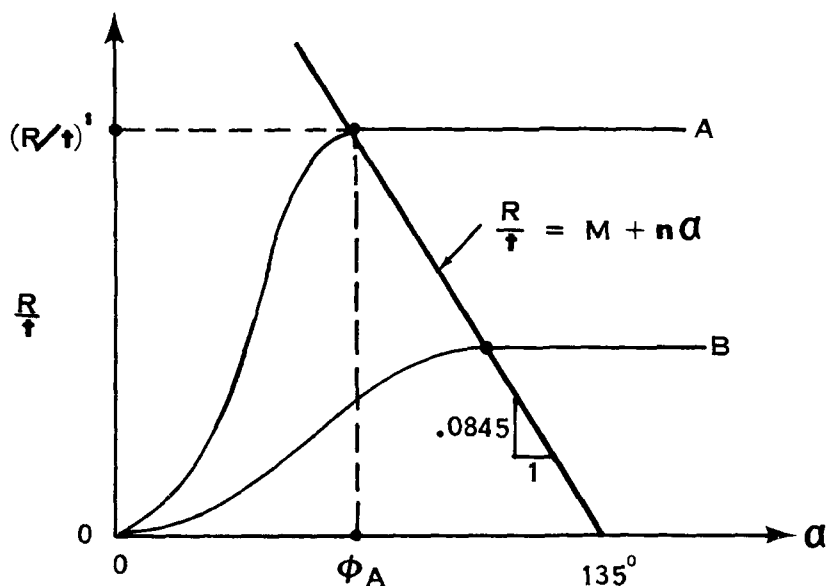


FIGURE V-4 COMPOSITE GRAPH FOR BRAKE FORMING

The equation of the line in Figure V-4 has the general slope and intercept form:

(V-7)

$$\frac{R}{t} = M + n\alpha$$

Solving for M and n from Figure V-4:

(V-8)

$$\frac{R}{t} = 11.4 - .0845\alpha$$

At $\alpha = \phi$:

(V-9)

$$\left(\frac{R}{t}\right)' = 11.4 - 0.0845\phi$$

Solving for ϕ :

(V-9a)

$$\phi = \frac{11.4 - (R/t)'}{.0845}$$

Substituting equation (V-9a) into equation (V-6a):

(V-10)

$$\theta = \frac{180 \alpha}{11.4 - (R/t)'} = \frac{15.21 \alpha}{11.4 - (R/t)'}$$

Substituting equations (V-10) and (V-3) into (V-5) gives:

V-11)

$$\frac{R}{t} = \frac{1}{2} \left[e^{2(\bar{\epsilon}_{.25}) \text{ CORRECTED}} - 1 \right]^{-1} \left[1 + \sin \left[\frac{15.21 \alpha}{11.4 - (e^{2\bar{\epsilon}_{.25} \text{ CORRECTED}} - 1)^{-1}} - 90 \right] \right]$$

Equation (V-11) is therefore the predictability equation for angles less than ϕ .

DESIGN TABLES

Design tables can be developed for any material from the composite graph.

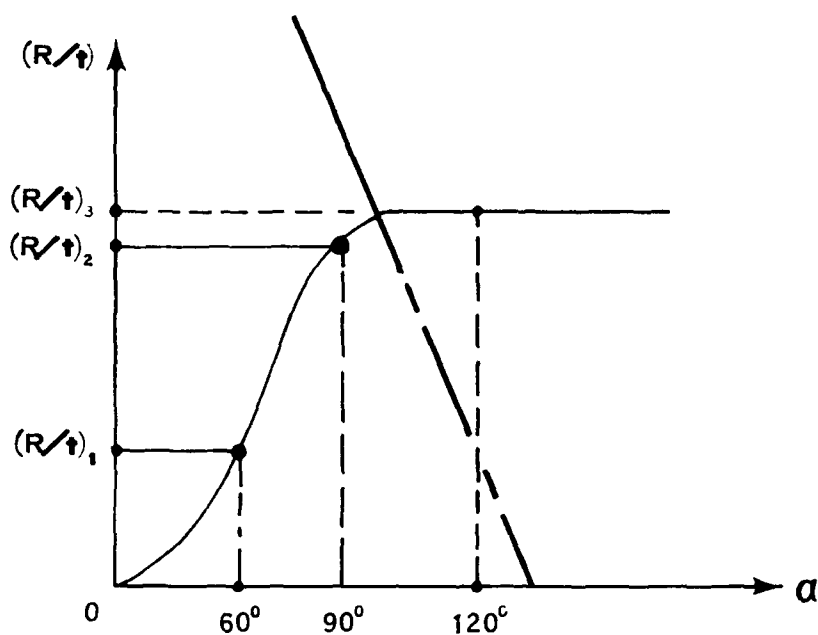


FIGURE V-5 FORMABILITY CURVE FOR BRAKE FORMING

The design table format is illustrated in Figure V-6.

$\alpha = 60^\circ$		$\alpha = 90^\circ$		$\alpha = 120^\circ$	
t	R	t	R	t	R
0.016	R_1	0.016		0.016	
0.020	R_2	0.020		0.020	
0.187		0.187		0.187	

FIGURE V-6 DESIGN TABLE FORMAT FOR BRAKE FORMING

The R is determined from Figure V-5 for each angle and gauge at $\alpha = 60^\circ$:

$$\frac{R}{t} = \frac{R}{t_1}$$

Therefore:

$$\frac{R_1}{.016} = \frac{R_2}{0.02} = \frac{R}{0.187}$$

JOGGLING

The fundamental shape equations for joggling, which define the shape of the formability limit curve, were developed in Chapter II. Two types of failure occur in joggling - splitting and buckling. A composite graph composed of the empirically determined forming limit curves of all materials was developed as shown in Figure V-7.

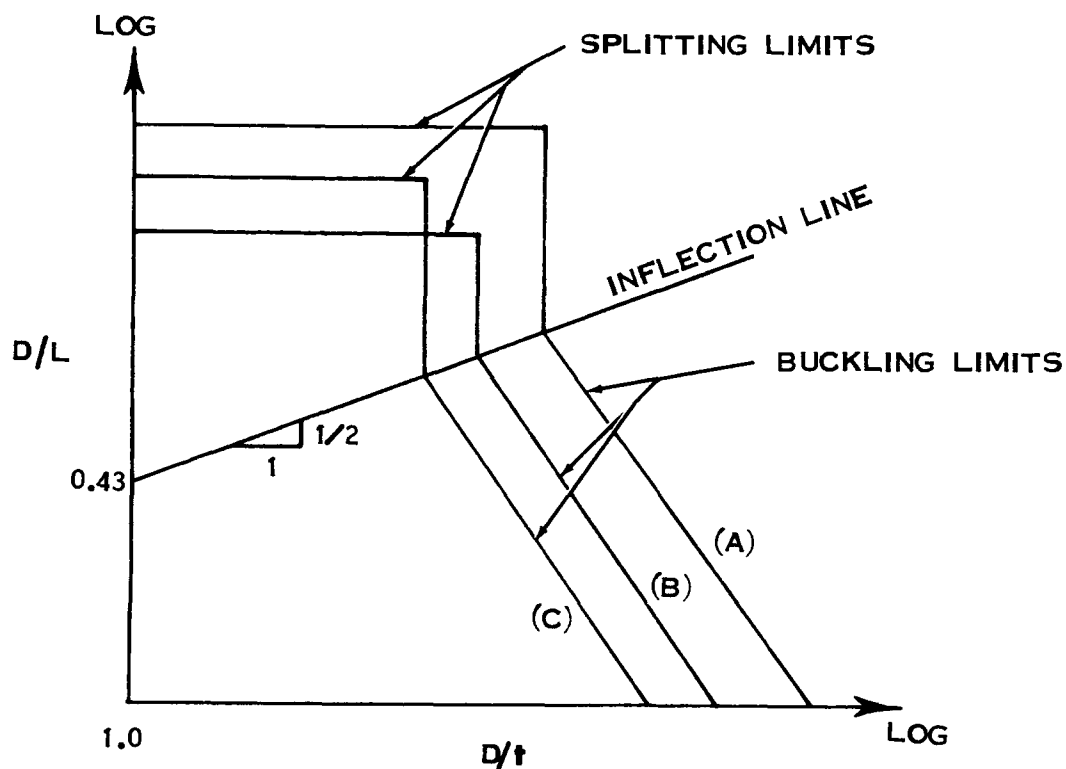


FIGURE V-7 COMPOSITE GRAPH FOR JOGGLING

The basic geometric parameters are defined by Figure V-8.

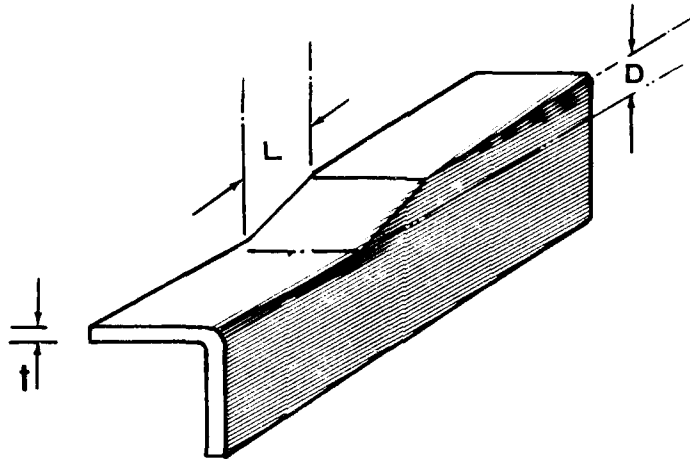


FIGURE V-8 JOGGLE SECTION PARAMETERS

The basic equation for elastic buckling is:

$$(V-12) \quad S_{CR} = f\left(\frac{D}{L}\right) = \frac{E_C}{S_{CY}} \left[\frac{B}{(D/t)^2} \right]$$

or :

$$(V-13) \quad \frac{D}{L} = \frac{E_C}{S_{CY}} \left[\frac{K}{(D/t)^2} \right]$$

Where $\frac{E_C}{S_{CY}}$ is the buckling index developed in Chapter III which positions the curves according to their formability. K is a forming process constant.

The buckling formability index line which positions materials according to their mechanical properties is at $D/t = 2.25$ as shown in Figure V-9.

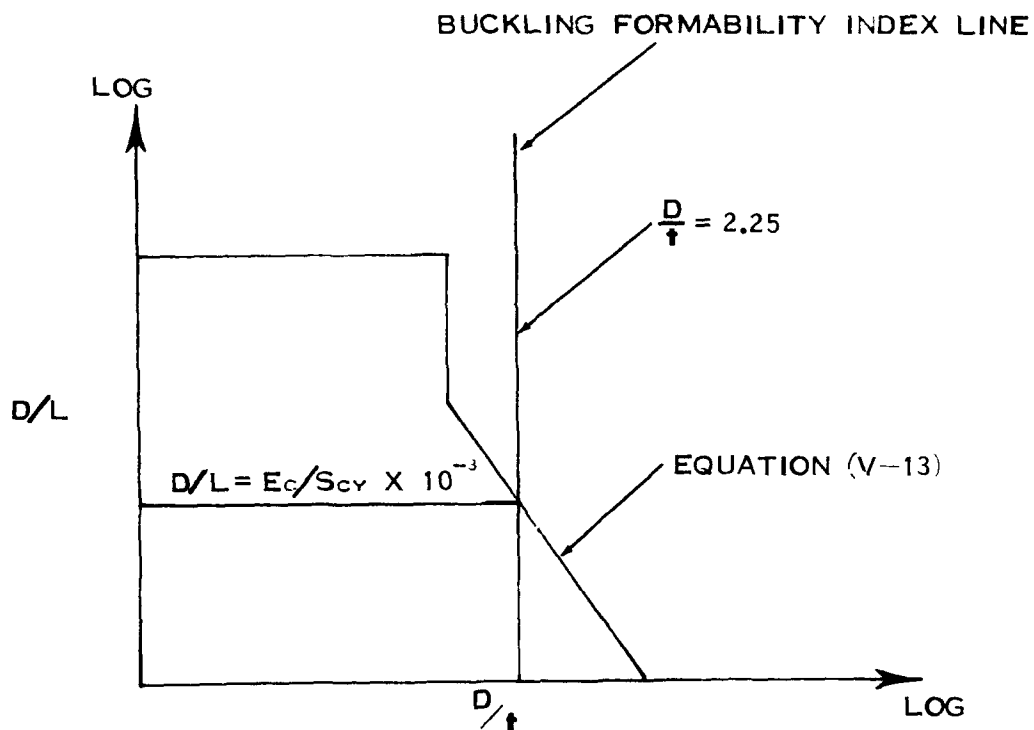


FIGURE V-9 BUCKLING FORMABILITY INDEX LINE

At the intersection of $D/t = 2.25$ and the buckling formability curve with a slope of -2:

(V - 14)

$$\frac{D}{L} = \frac{E_c}{S_{cy}} \times 10^{-3}$$

Solving for K:

(V - 15)

$$\frac{E}{S_{cy}} \times 10^{-3} = \frac{E_c}{S_{cy}} \left[\frac{K}{(2.25)^2} \right]$$

$$K = (2.25)^2 \times 11^{-3} = .0050625$$

Equation V-13 now becomes:

$$(V - 16) \quad \frac{D}{L} = \frac{E_c}{S_{cy}} \left[\frac{0.0050625}{(D/t)^2} \right]$$

The inflection line has a slope of $+1/2$ and intersects the D/L axis at 0.43 when $D/t = 1.0$. See Figure V-7. The equation for the inflection line has the form:

$$(V - 17) \quad \frac{D}{L} = M \left[\frac{D}{t} \right]^n$$

Solving for M and n using the slope and intercept in Figure V-7 gives:

$$(V - 17A) \quad \frac{D}{L} = 0.43 \left[\frac{D}{t} \right]^{1/2}$$

Above the intersection of the elastic buckling curves and the inflection line, the buckling limit is given by a vertical (constant D/t) line up to the splitting limit. By solving equation (V-16) and (V-17a) simultaneously the point of intersection, and therefore the equation for the vertical line is:

$$(V - 18) \quad \frac{D}{t} = \left[0.0118 \frac{E_c}{S_{cy}} \right]^{2/5}$$

The splitting limit in joggling is a function of the available elongation in the material. The basic equation for the strain in joggled specimens as developed in Chapter II is:

$$(V - 19) \quad \epsilon = \sqrt{(D/L)^2 + 1} - 1$$

The maximum D/L that can be formed without splitting is therefore a function of the available strain in the material. Since the part is strained over a very short gauge length, the strain on a tensile specimen over a gauge length of .02 in. was correlated as follows:

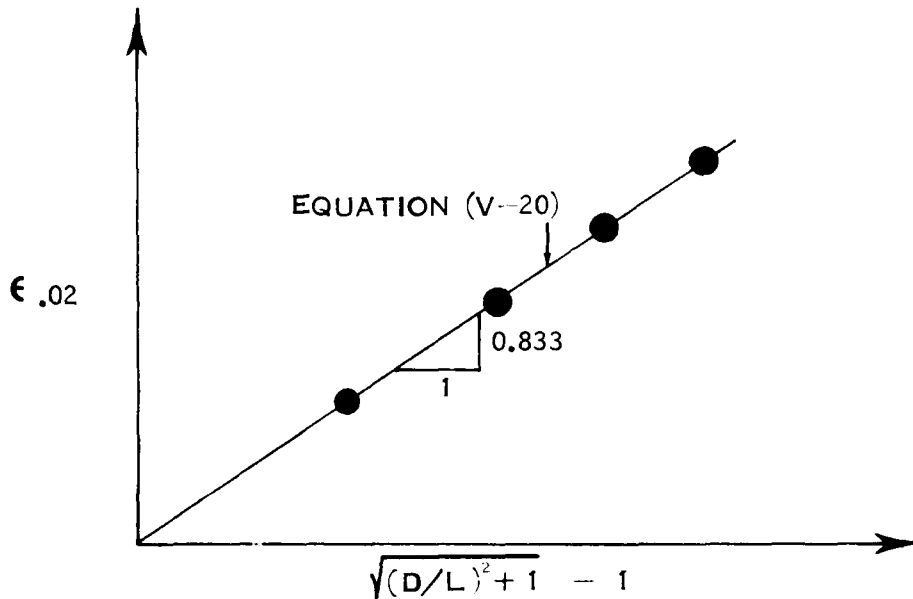


FIGURE V-10 SPLITTING LIMIT CORRELATION CURVE FOR JOGGING

The equation of the correlation line in Figure V-10 has the form:

$$(V-20) \quad \epsilon_{.02} = M' + n' \left(\sqrt{(D/L)^2 + 1} - 1 \right)$$

Solving for M' and n' using the slope and intercept in Figure V-10 gives:

$$(V-21) \quad \epsilon_{.02} = 0.833 \left(\sqrt{(D/L)^2 + 1} - 1 \right)$$

Solving for D/L:

(V - 21A)

$$\frac{D}{L} = \left[\epsilon_{.02} (1.44 \epsilon_{.02} + 2.4) \right]^{1/2}$$

In summary, the predictability equations for joggling are shown in Figure V-11.

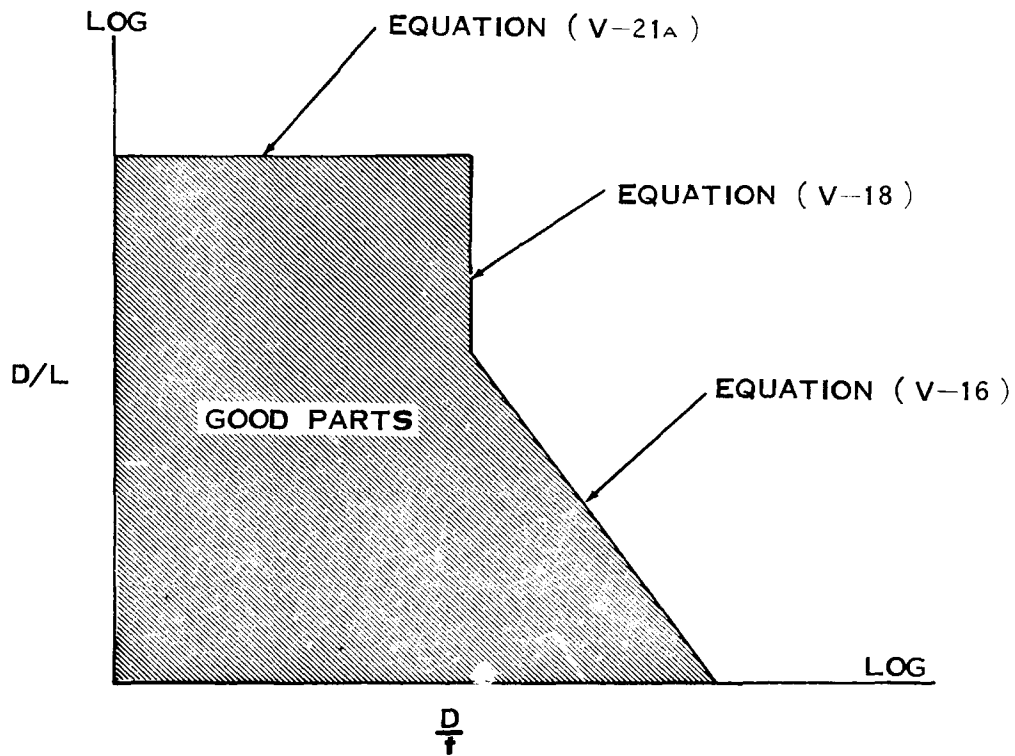


FIGURE V-11 PREDICTABILITY EQUATIONS FOR JOGGLING

DESIGN TABLES

Design tables for joggling limits were established for each material by using the composite graph and an overlay graph with constant L/t curves plotted on it as shown in Figure V-12.

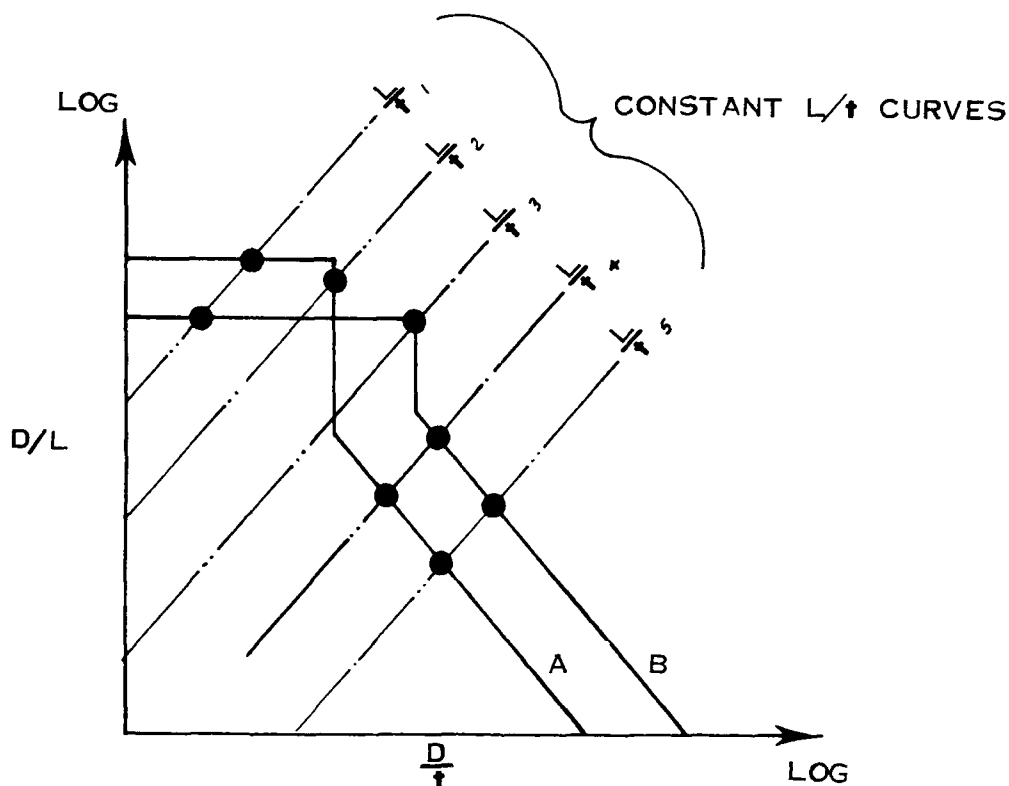


FIGURE V-12 COMPOSITE GRAPH FOR JOGGLING

For any particular L and t value (L/t), the corresponding limiting value of D/t can be read directly from Figure V-12 for any material. The value of D is found simply by multiplying the D/t times the material's gage. Tables can then be developed for each material as illustrated in Figure V-13.

L / t	t_1	t_2	t_3	t_4		
D						
L_1	D_1	D_2	D_3	D_4		
L_2						
L_3						

FIGURE V-13 DESIGN TABLE FORMAT FOR JOGGLING

DIMPLING

The fundamental shape equation for dimpling, which defines the shape of the formability limit curve, was developed in Chapter II. Two types of failure occur in dimpling--radial splitting caused by the circumferential hoop stresses in the outer fibers and circumferential splitting along the bend of the dimple. Circumferential splitting can be eliminated by adjusting the dimple pressure and increasing the temperature; therefore, it is considered secondary.

A composite graph, as illustrated in Figure V-14, was constructed from the empirically determined forming limit curves of all materials.

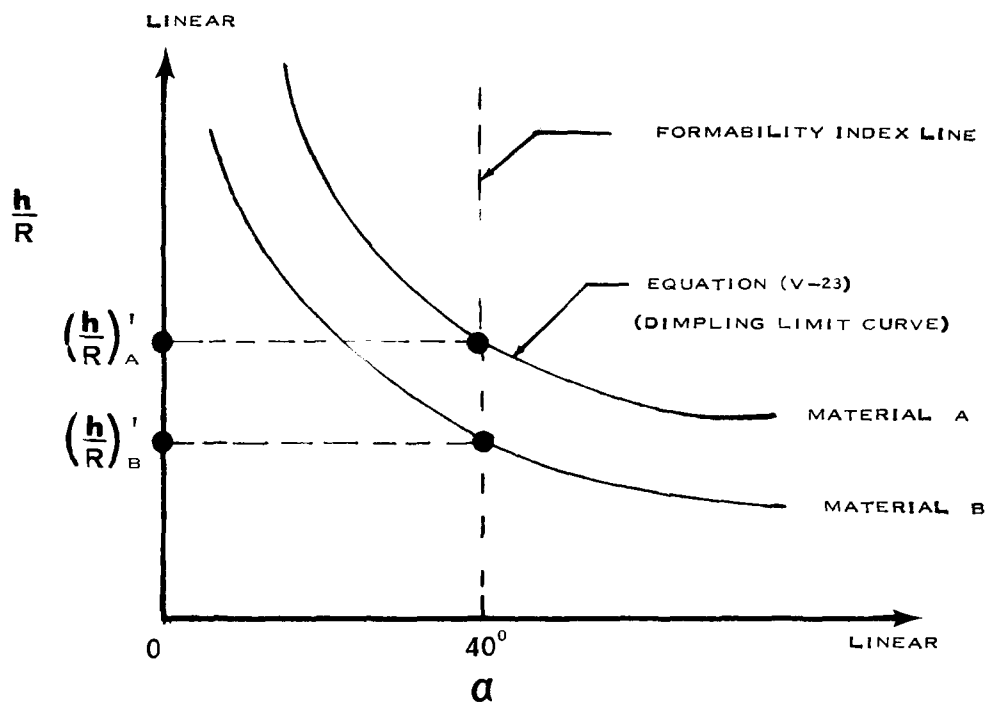


FIGURE V-14 COMPOSITE GRAPH FOR DIMPLING

A successful dimple can be formed if its geometric variables place it at a point below the dimpling limit curve. Radial failure occurs when

the point falls above the curve.

The basic equation for circumferential hoop strain in the outer fiber of the dimple is:

(V - 22)

$$\epsilon = \frac{h}{R} (1 - \cos \alpha)$$

The geometric parameters are defined by Figure V-15.

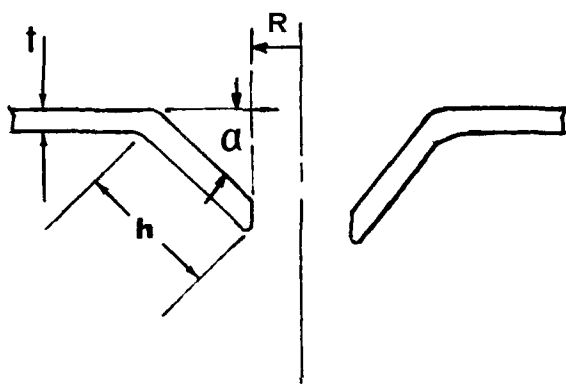


FIGURE V-15 GEOMETRIC PARAMETERS IN DIMPLING

The equation for a family of limiting curves, positioned by some function of the available elongation in the material, is of the form:

(V - 23)

$$f(\epsilon) = \frac{h}{R} (1 - \cos \alpha)$$

In order to determine the actual equation, a formability index line was established at $\alpha = 40^\circ$. (See Figure V-14). At the intersection of the index line and $f(\epsilon_{2.0}) = h/R (1 - \cos \alpha)$; $h/R = (h/R)'$. Plotting $(h/R)'$ vs. $\epsilon_{2.0}$ for various materials the following theoretical curve was developed:

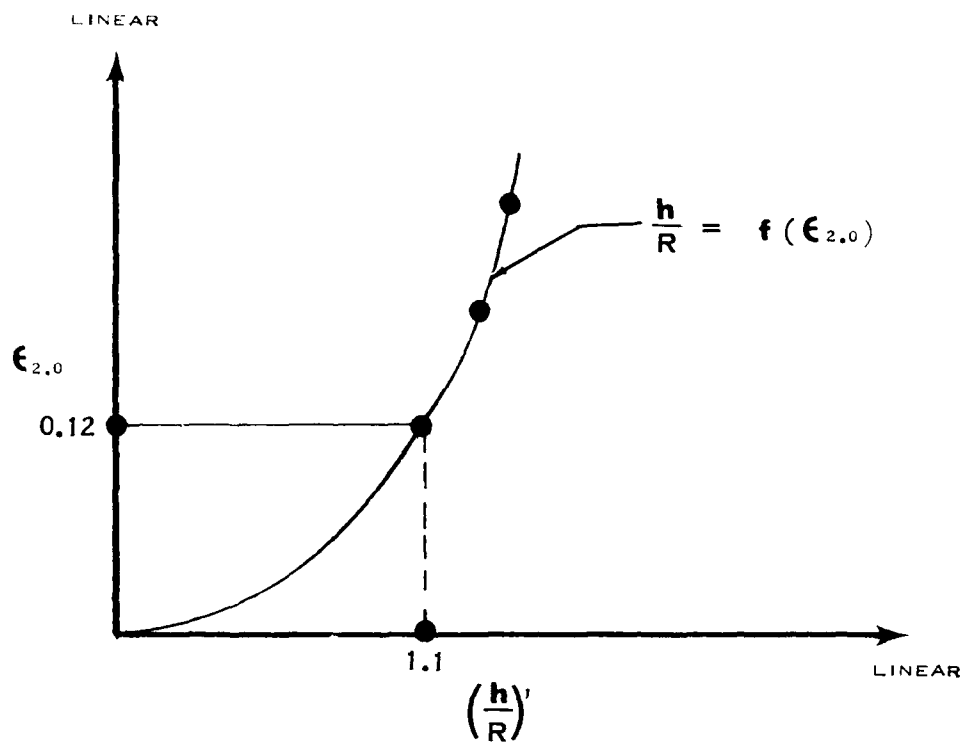


FIGURE V-16 CORRELATION CURVE FOR DIMPLING

The curve in Figure V-16 plots a straight line on log - log graph paper as shown in Figure V-17.

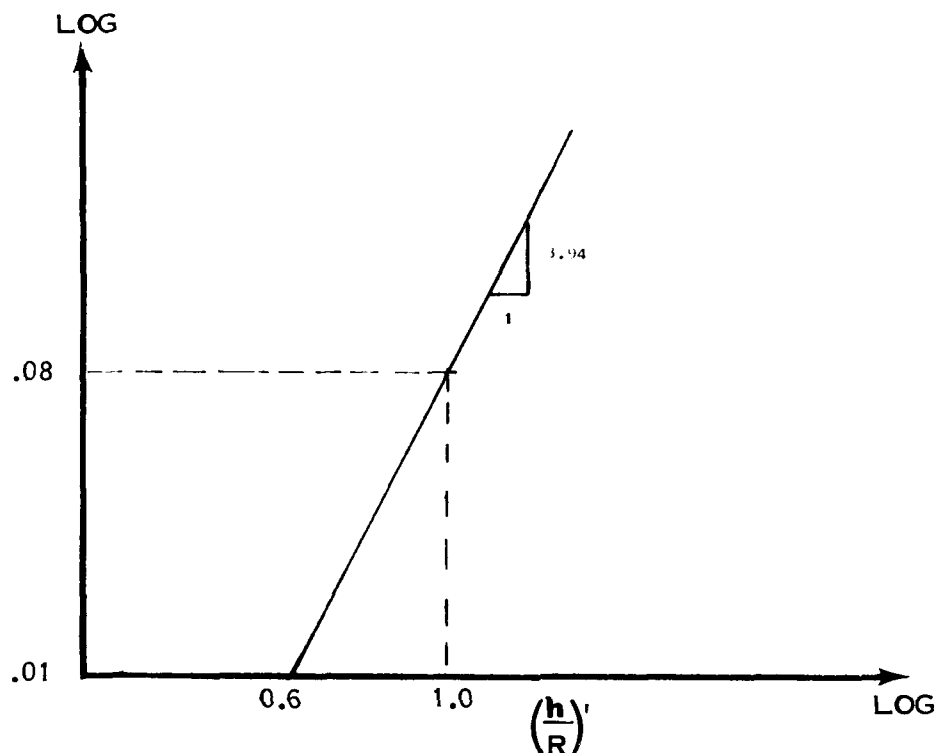


FIGURE V-17 CORRELATION CURVE FOR DIMPLING PLOTTED ON LOG-LOG GRAPH PAPER

The equation for curve in Figure V-17 is therefore:

$$(V - 24) \quad \epsilon_{2.0} = .08 \left[\left(\frac{h}{R} \right)' \right]^{3.94}$$

$$(V - 24_A) \quad \left[\frac{h}{R} \right]' = \left[\frac{\epsilon_{2.0}}{.08} \right]^{0.253}$$

Solving for h/R from equation (V-23):

(V - 23A)

$$\frac{h}{R} = \frac{f(\epsilon)}{1 - \cos \alpha}$$

AT $\alpha = 40^\circ$

$$\frac{h}{R} = \left[\frac{h}{R} \right]'$$

Therefore, setting equation (V-24a) equal to (V-23a) at $\alpha = 40^\circ$:

(V - 25)

$$\frac{f(\epsilon)}{1 - \cos 40^\circ} = [\epsilon_{2.0}]^{0.253}$$

(V - 25A)

$$f(\epsilon) = 0.444 [\epsilon_{2.0}]^{0.253}$$

Substituting back into equation (V-23):

(V - 26)

$$0.444 [\epsilon_{2.0}]^{0.253} = \frac{h}{R} [1 - \cos \alpha]$$

(V - 26A)

$$\frac{h}{R} = \left[\frac{(0.444) (\epsilon_{2.0})^{0.253}}{1 - \cos \alpha} \right]$$

The predictability equation for dimpling is equation (V-26a). The h/R limit can be determined for any angle if α is known.

DESIGN TABLES

A design table was developed for dimpling the standard dimple only. The formability limits for non-standard dimples can be predicted from the preceding equation; however, since at present there is a standard type aircraft dimple with a constant α of 40° and approximate h/R of 1.2, the design tables were developed on a go, no - go basis, as illustrated in Figure V-18.

MATERIAL	CONDITION	ROOM TEMP. R.T.	EXPERIMENTAL TESTS		RECOMMENDED ELEVATED TEMPERATURE
			TEMP.	RESULTS	

FIGURE V-18 DESIGN TABLE FORMAT FOR DIMPLING

RUBBER STRETCH FLANGES

The fundamental shape equations for rubber forming stretch flanges, which define the shape of the formability limit curve, were developed in Chapter II. Splitting and buckling failures occur in stretch flanges. A composite graph composed of the empirically determined forming limit curves of all materials was developed as shown in Figure V-19.

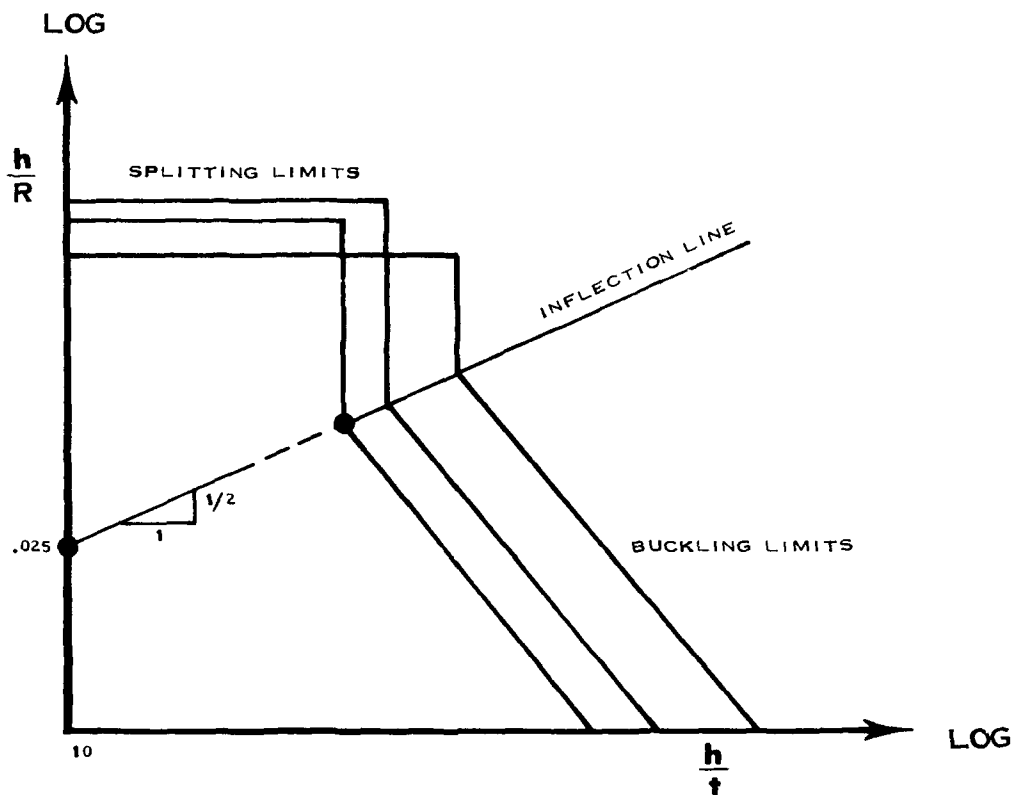


FIGURE V-19 COMPOSITE GRAPH FOR STRETCH FLANGES

The basic geometric parameters are defined by Figure V-18.

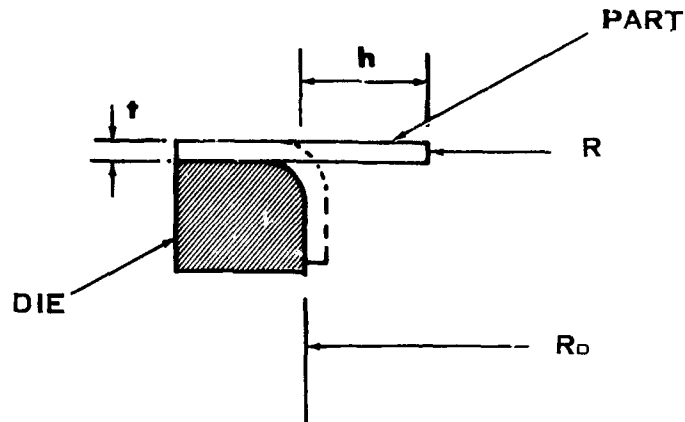


FIGURE V-20 GEOMETRIC PARAMETERS FOR STRETCH FLANGES

The basic equation for elastic buckling is:

$$(V-27) \quad S_{CR} = f\left(\frac{h}{R}\right) = \frac{E_T}{S_{TY}} \left[\frac{B}{(h/t)^2} \right]$$

h/R is a linear function of stress in the elastic region, therefore:

$$(V-28) \quad \frac{h}{R} = \left[\frac{E_T}{S_{TY}} \right] \left[\frac{B'}{(h/t)^2} \right]$$

The buckling formability index line which positions materials according to their mechanical properties is at $h/t = 30$ as shown in Figure V-21.

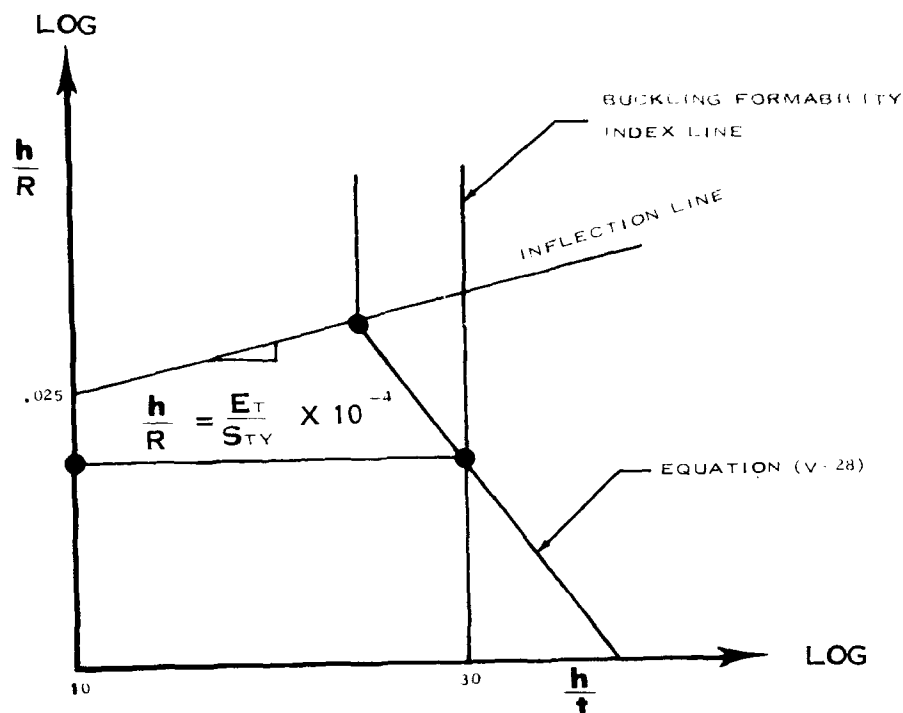


FIGURE V-21 BUCKLING FORMABILITY INDEX LINE FOR RUBBER STRETCH FLANGES

The procedure as shown under joggling was used and the following equations were developed:

Elastic Buckling Limit:

$$(V-29) \quad \frac{h}{R} = \frac{E_T}{S_{TY}} \left[\frac{.09}{(h/t)^2} \right]$$

Inflection Line:

$$(V-30) \quad \frac{h}{R} = 0.0079 \sqrt{h/t}$$

Buckling limit from inflection line to splitting limit:

$$(V-31) \quad \frac{h}{t} = \left[11.4 \frac{E_T}{S_{TY}} \right]^{2/5}$$

The splitting limit in rubber stretch forming is a function of the available elongation in the material. The basic equation for strain as developed in Chapter II is:

(V - 32)

$$\epsilon = \frac{h}{R}$$

Correlating to the elongation in 2 inches from the standard tensile specimen would give an equation of the form:

(V - 33)

$$\frac{h}{R} = f(\epsilon_{2.0})$$

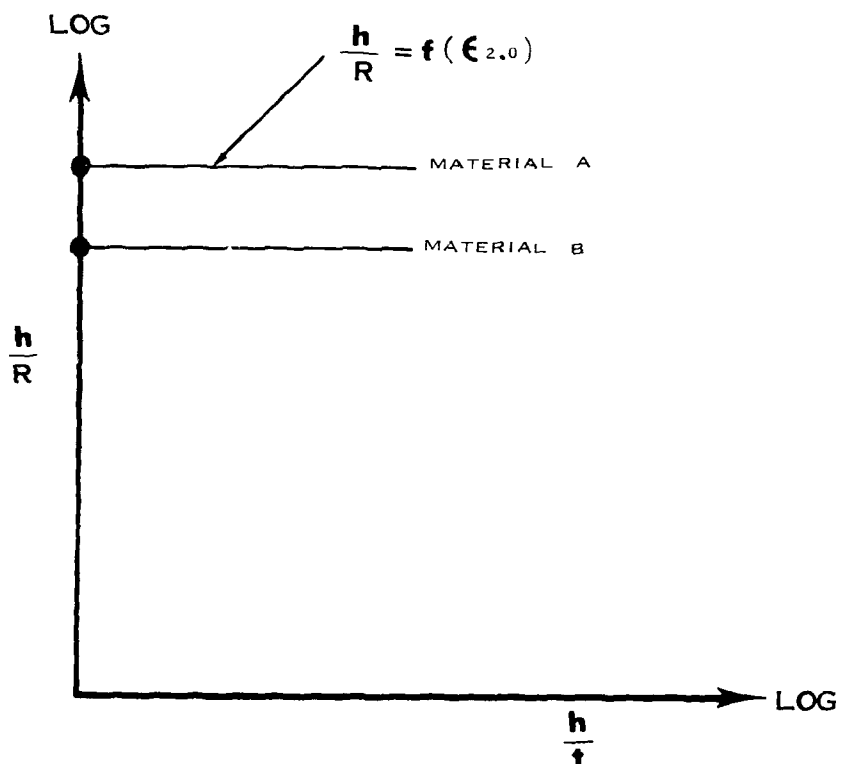


FIGURE V-22 SPLITTING LIMITS IN RUBBER STRETCH FLANGES

Plotting $\epsilon_{2.0}$ vs. the h/R splitting limit gives a straight line on semi-log paper as shown in Figure V-23.

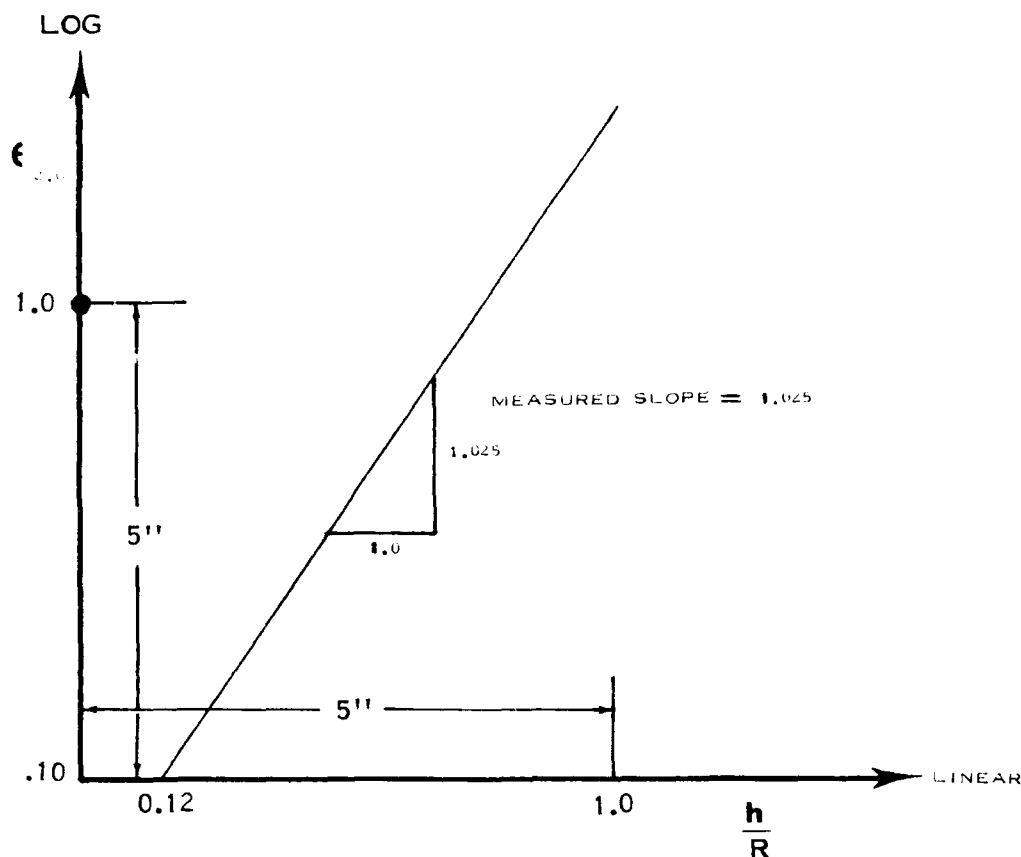


FIGURE V-23 CORRELATION CURVE FOR RUBBER STRETCH FLANGE LIMITS

The general equation for a curve that plots a straight line on semi-log graph paper is:

$$(V-34) \quad \epsilon_{2.0} = [B][d]^{\frac{mh}{R}}$$

Solving for the constants in equation (V-34) by using Figure (V-21) gives:

(V - 35)

$$\epsilon_{2.0} = [.074][2]^{3.42} \frac{h}{R}$$

Solving for h/R to give the predictability equation for splitting:

(V - 35A)

$$\frac{h}{R} = 0.421 \ln (13.5 \epsilon_{2.0})$$

In addition to splitting and buckling, there is a minimum flange height limit below which the flange will not form down to the die. This limit is based upon a machine pressure limit of 1925 psi. The following type composite graph was developed from the experimentally established minimum flange limits for all materials.

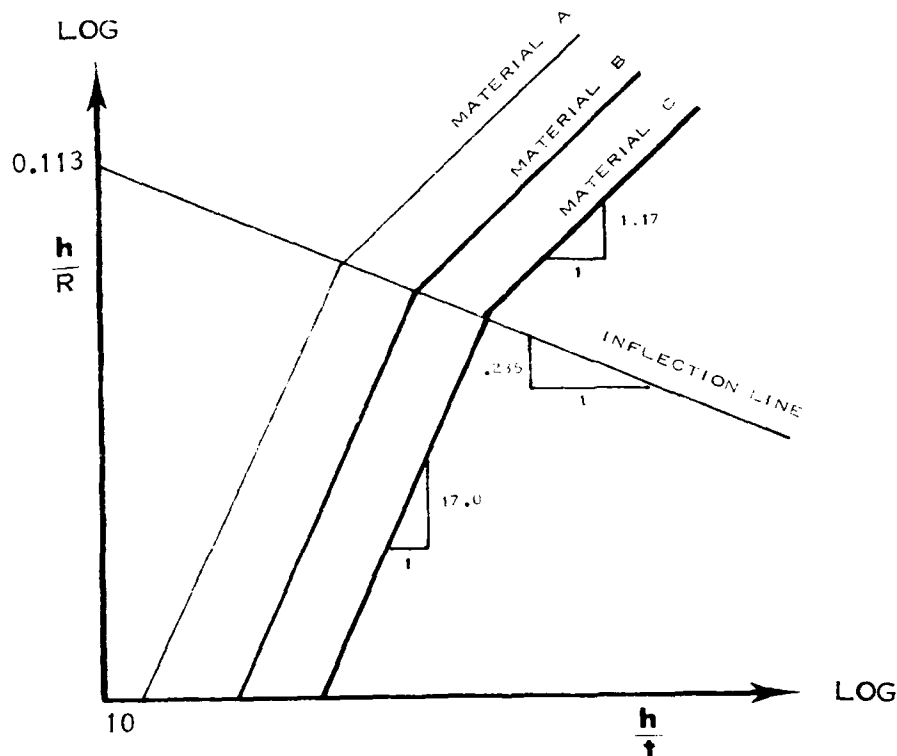


FIGURE V-24 COMPOSITE OF MINIMUM FLANGE LIMITS IN RUBBER STRETCH FORMING

Any part whose geometric variables placed it to the left of the limiting curve had flanges that did not form to the die.

The formability index for minimum flange limits is $\frac{1}{S_{TY}}$. An index line was established by correlation, as shown in Figure V-25.

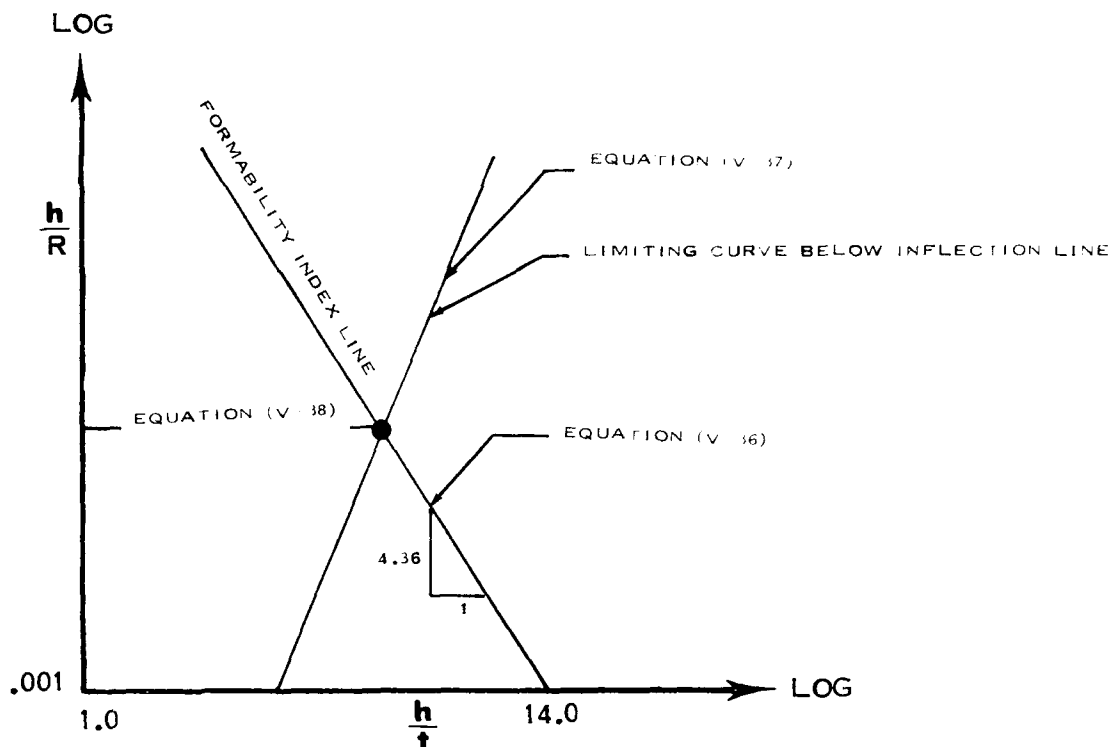


FIGURE V-25 FORMABILITY INDEX LINE FOR RUBBER STRETCH FLANGES

The equation for the index line, as determined from Figure V-25, is:

$$(V-36) \quad \boxed{\frac{h}{R} = 102 \left[\frac{h}{t} \right]^{-4.36}}$$

The equation for the limiting curve is:

(V-37)

$$\frac{h}{R} = \frac{1}{S_{TY}} \left[B \right] \left[\frac{h}{t} \right]^{17.0}$$

At the intersection of equation (V-36) and (V-37):

(V-38)

$$\frac{h}{R} = \frac{1}{S_{TY}} \times 10^3$$

Solving equations (V-36), (V-37), and (V-38) simultaneously to find B and substituting the value of B back into equation (V-37) gives:

(V-39)

$$\frac{h}{R} = \frac{6.99 \times 10^6}{(S_{TY})^{4.9}} \left[\frac{h}{t} \right]^{17.0}$$

Equation (V-39) is the equation for the minimum flange height curve below the inflection line.

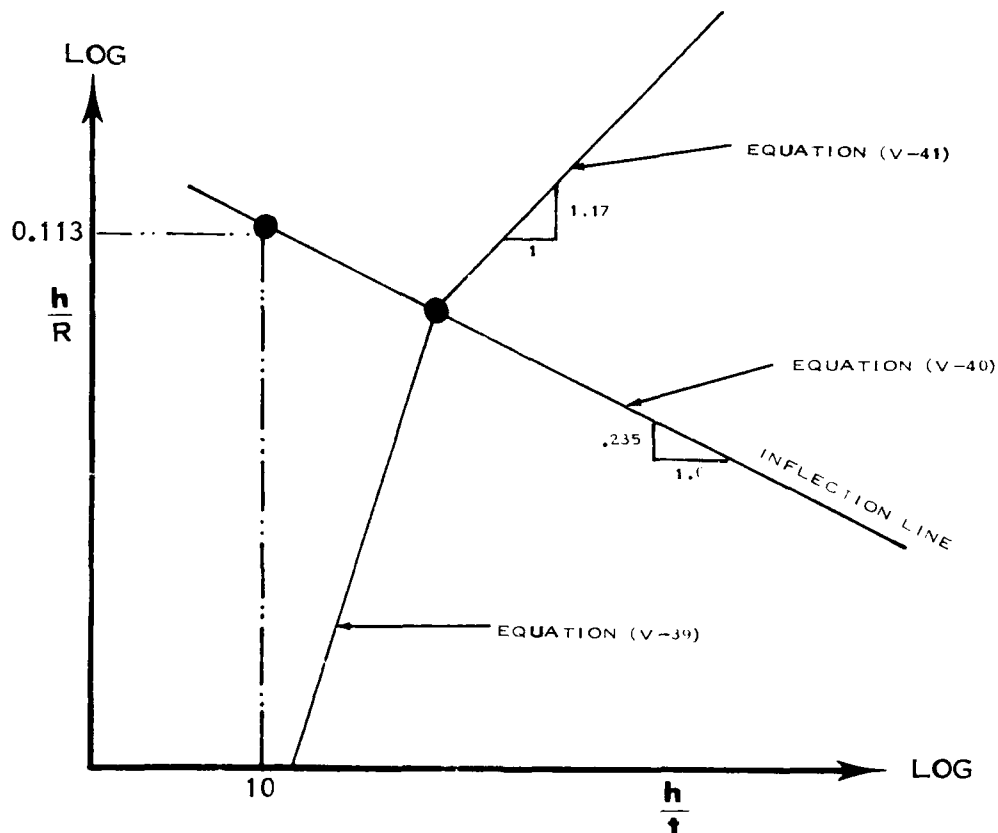


FIGURE V-26 MINIMUM FLANGE LIMIT CURVES FOR RUBBER STRETCH FLANGES

The equation for the inflection line as established from Figure V-26 is:

$$(V-40) \quad \frac{h}{R} = 0.19 \left[\frac{h}{t} \right]^{-0.235}$$

The equation for the limiting formability curve above the inflection line has the form:

$$(V-41) \quad \frac{h}{R} = \frac{1}{S_{TY}} \left[C \right] \left[\frac{h}{t} \right]^{1.17}$$

Solving equations (V-39), (V-40) and (V-41) simultaneously to find C and substituting the value of C back into (V-41) gives:

$$(V-42) \quad \frac{h}{R} = \left[\frac{0.19}{[2.72 \times 10^{-8} (S_{TY})^{4.9}]^{.0816}} \right] \left[\frac{h}{t} \right]^{1.17}$$

Equation (V-42) is the equation for the minimum flange limits above the inflection line.

A summary of all equations is shown in Figure V-27.

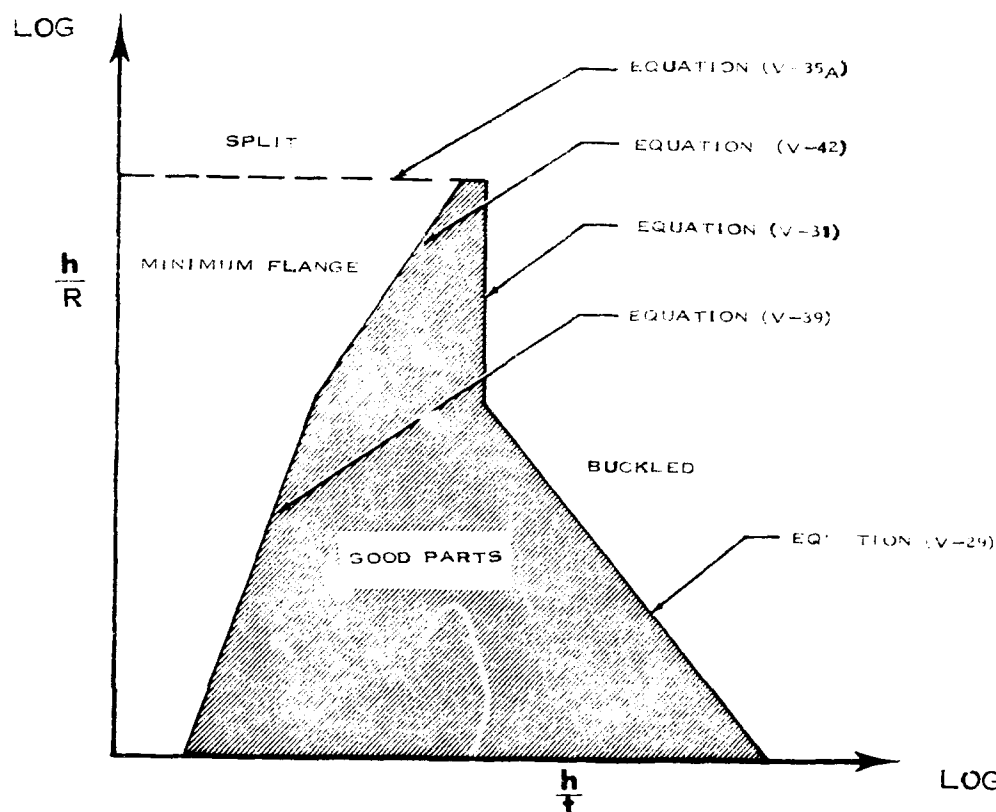


FIGURE V-27 PREDICTABILITY EQUATIONS FOR RUBBER STRETCH FLANGES

DESIGN TABLES

Design tables for rubber formed stretch flanges were established for each material by using the composite graph and an overlay graph with constant R_D/t curves plotted on it, as shown in Figure V-28.

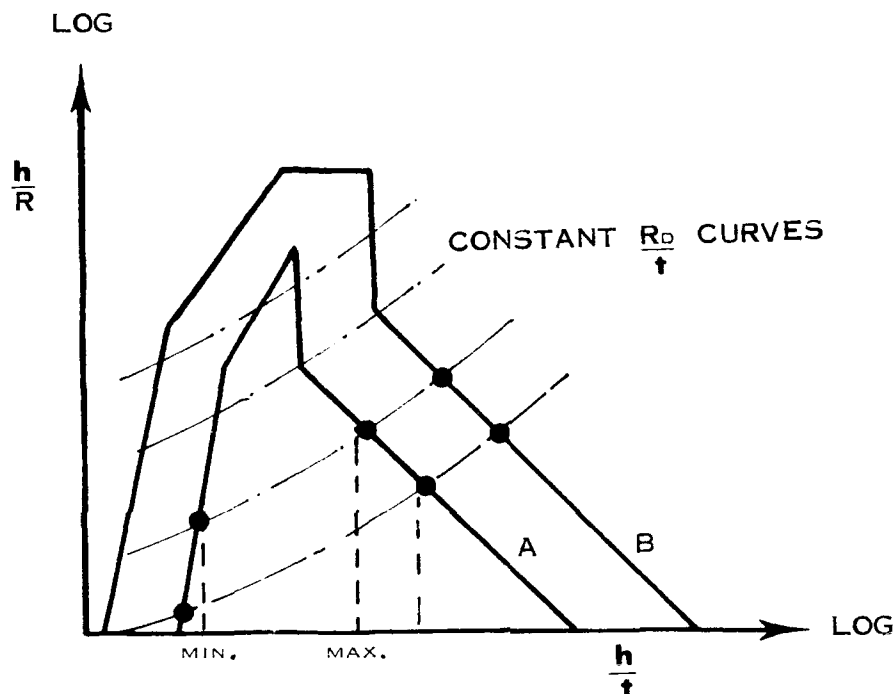


FIGURE V-28 COMPOSITE GRAPH AND CONSTANT R_D/t OVERLAY
GRAPHS FOR RUBBER STRETCH FLANGES

For any particular R_D and t value (R_D/t) the corresponding minimum and maximum value of h/t can be read directly from the graph in Figure V-28 for any material. The values of h maximum and h minimum are found by multiplying the h/t values by the selected t .

Tables can then be developed for each material as illustrated in Figure V-29.

R_D	\uparrow	\uparrow_1	\uparrow_2	\uparrow_3	\uparrow_4	\uparrow_5	\uparrow_6	
R_1	h_{MIN}							
	h_{MAX}							
R_2								

FIGURE V-29 DESIGN TABLE FORMAT FOR RUBBER
STRETCH FLANGES

RUBBER FORMED SHRINK FLANGES

The fundamental shape equations for rubber forming shrink flanges, which define the shape of the formability limit curve, were developed in Chapter II. Two types of buckling occur—elastic and plastic. A composite graph composed of the empirically determined forming limit curves of all materials was developed as illustrated in Figure V-30.

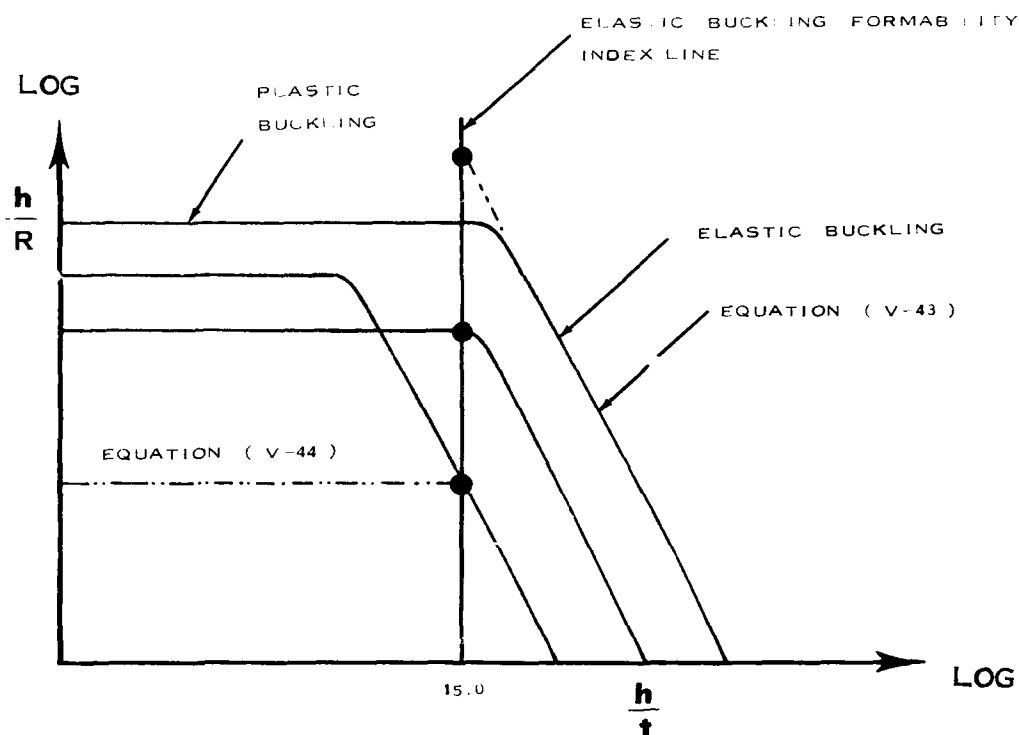


FIGURE V-30 COMPOSITE GRAPH FOR RUBBER SHRINK
FLANGE LIMITS

The general elastic buckling equation is:

$$(V - 43) \quad \boxed{\frac{h}{R} = \frac{E_c}{S_{CY}} B \left[\frac{h}{t} \right]^{-2}}$$

At the intersection of the index line ($h/t = 15$) and equation (V-43):

$$(V-44) \quad \boxed{\frac{h}{R} = \frac{E_c}{S_{CY}} \times 10^{-4}}$$

Solving equations (V-43) and (V-44) simultaneously at $h/t = 15$ gives:

$$(V-45) \quad \boxed{\frac{h}{R} = \frac{E_c}{S_{CY}} \left[\frac{0.0225}{(h/t)^2} \right]}$$

The equation for the plastic buckling limit curve was found experimentally to be:

$$(V-46) \quad \boxed{\frac{h}{R} = \frac{1.4}{S_{CY}}}$$

In addition to elastic buckling and plastic buckling there is a minimum flange height limit for the 1925 psi rubber press. The equations are the same as established for stretch flanges; however, S_{CY} is used rather than S_{TY} .

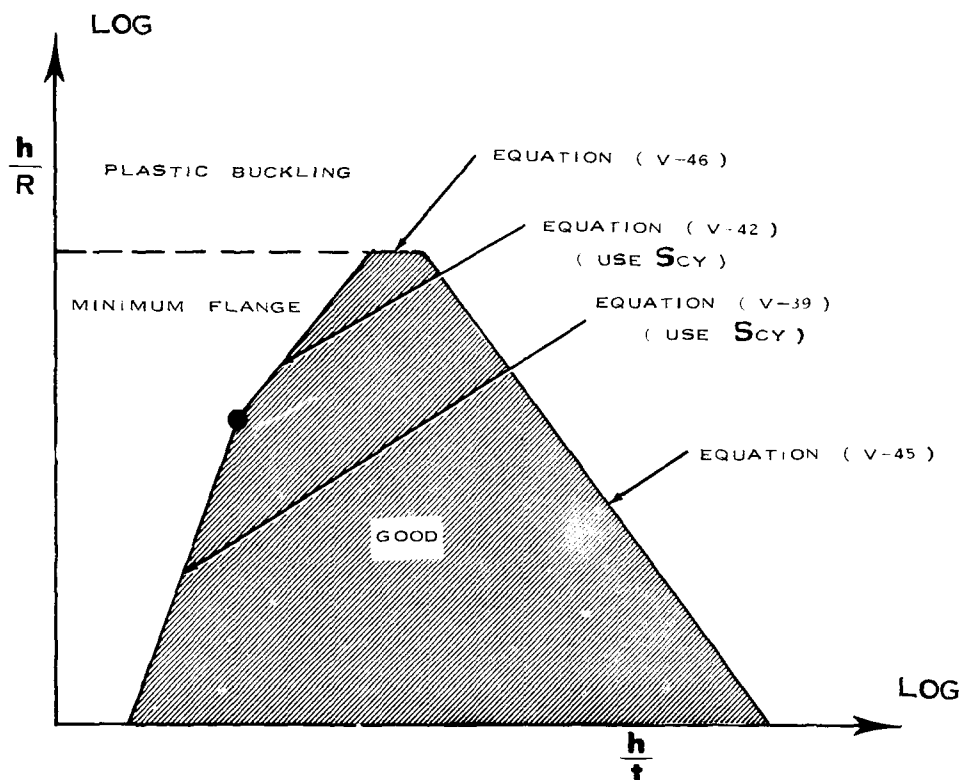


FIGURE V-31 PREDICTABILITY EQUATIONS FOR RUBBER SHRINK FLANGES

DESIGN TABLES

Design tables for rubber formed shrink flanges were established for each material by using the composite graph and an overlay graph with constant R_D/t curves plotted on it as shown in Figure V-32.

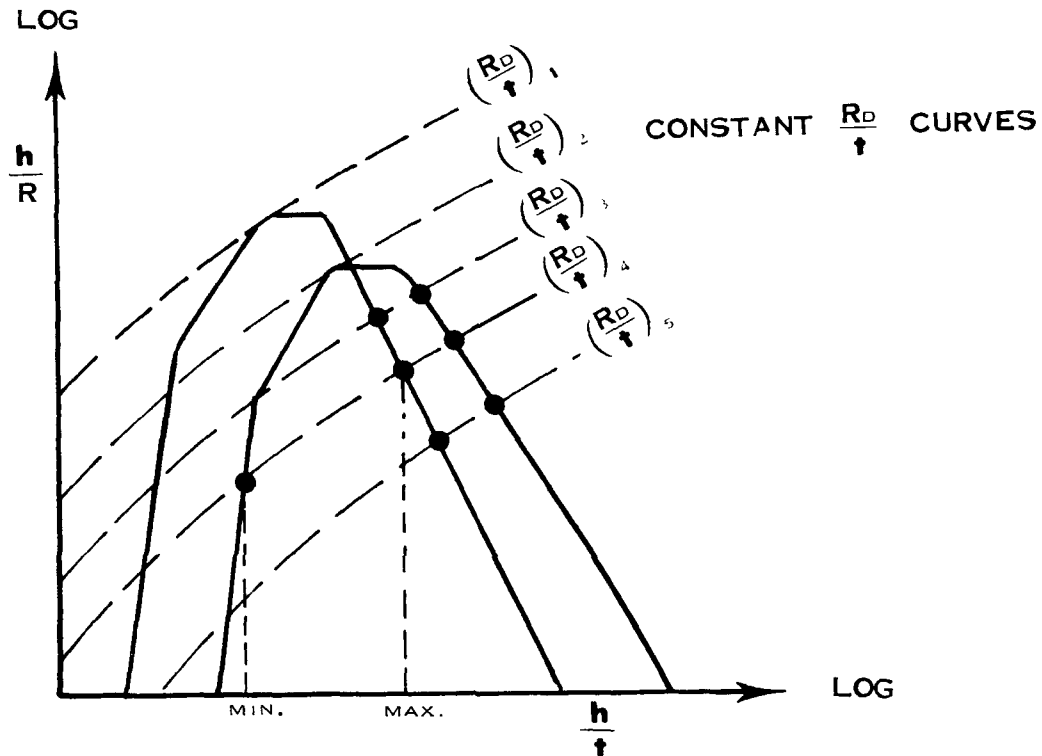


FIGURE V-32 COMPOSITE GRAPH AND CONSTANT R_D/t OVERLAY GRAPHS FOR RUBBER SHRINK FLANGES

For any particular R_D and t value (R_D/t) the corresponding minimum and maximum value of h/t can be read directly from the graph in Figure V-32 for any material. The values of h (maximum) and h (minimum) are found by multiplying the h/t values by the selected t .

Tables can then be developed for each material as illustrated in Figure V-33.

R_D	t_1	t_2	t_3	t_4	t_5	t_n	
R_1	h_{MIN}						
	h_{MAX}						
R_2							

FIGURE V-33 DESIGN TABLE FORMAT FOR RUBBER FORMED SHRINK FLANGES

LINEAR STRETCH FORMING

The fundamental shape equations for linear stretch forming various cross-sections, which define the shape of formability limit curve, were developed in Chapter II. Five geometric cross-sections, as shown in Figure V-34, were investigated. These five cross-sections were further divided into three types.

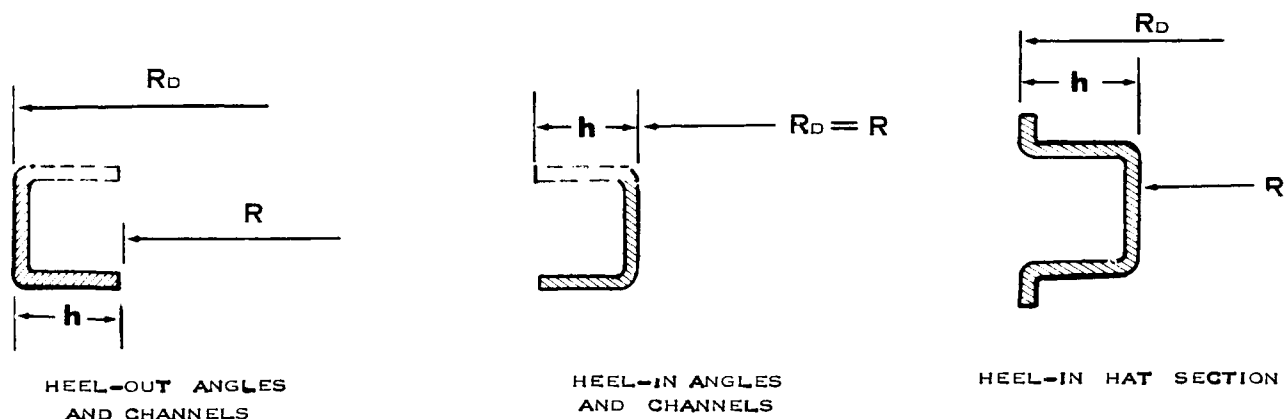


FIGURE V-34 LINEAR STRETCH FORMING GEOMETRIC SHAPES

The development of the equations for the three types of cross-sections were very similar; therefore, heel-out angles and channels will be completely developed and the final results of the other two given.

Two types of failure occur when linear stretch forming (heel-out angles and channels) --elastic buckling and splitting. A composite graph composed of the empirically determined forming limit curves of all materials was developed as illustrated in Figure V-35.

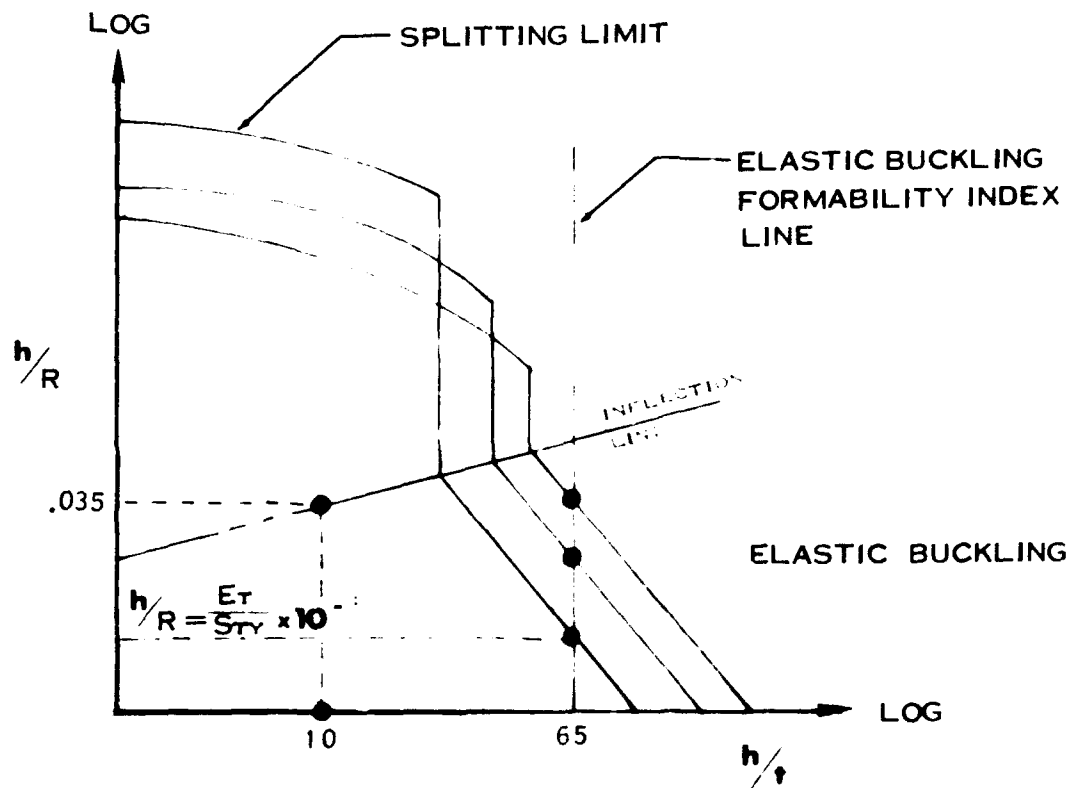


FIGURE V 35 COMPOSITE GRAPH FOR LINEAR STRETCH FORMING

The elastic buckling limit equations were developed in the same manner as is presented in the joggling section. The following equations were developed.

Elastic-Buckling Limit for Heel-Out Angles and Channels below the inflection line:

(V 47

$$\frac{h}{R} = \frac{E}{S} \cdot 0.4225 \frac{h}{t}$$

Elastic Buckling Limit for Heel-Out Angles and Channels above the inflection line:

(V 48

$$\frac{h}{t} = 38.2 \frac{E}{S}$$

The splitting limit in linear stretch forming is a function of the available elongation in the material. The basic equation for strain as developed in Chapter II is:

(V 49

$$\epsilon = \frac{h}{R}$$

Correlating to the elongation in a two inch gauge length from the standard tensile specimen would give an equation of the form:

(V 50

$$\frac{h}{R} = f(\epsilon_{2in}, \frac{h}{t})$$

The splitting limit line was established at $\epsilon_{2in} = 0.1$, as shown in Figure V-36.

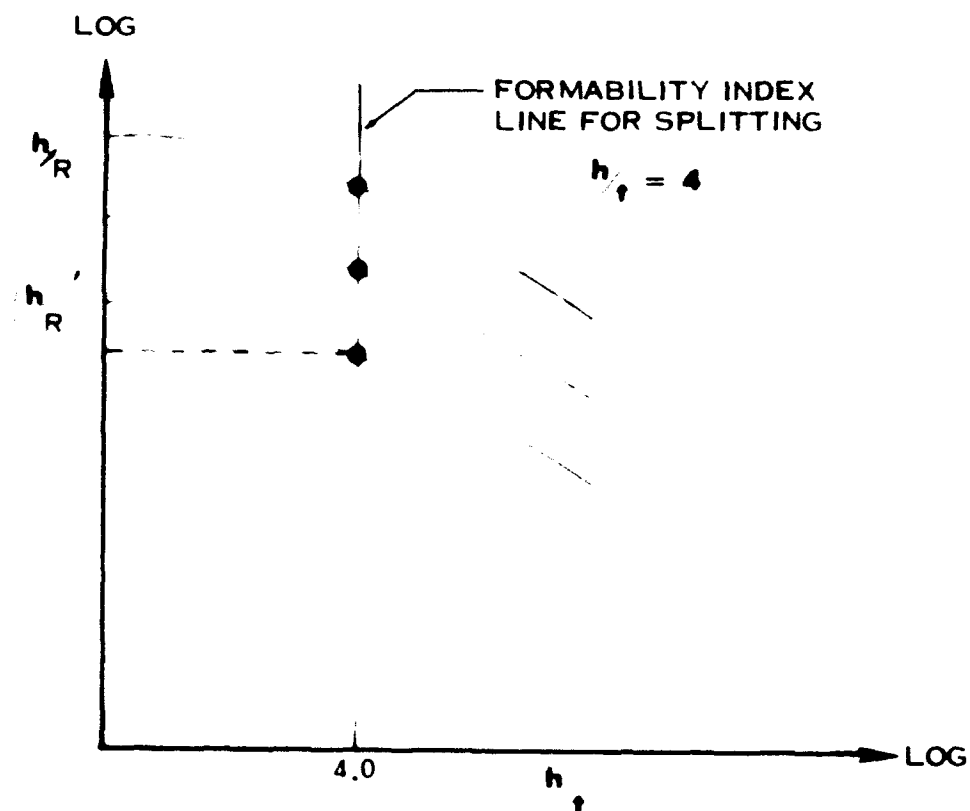


FIGURE V 36 SPLITTING LIMITS IN LINEAR STRETCH FORMING

Plotting $(h/R)^{1/2}$ from Figure V-36 vs. ϵ gives a straight line on linear graph paper as shown in Figure V-37.

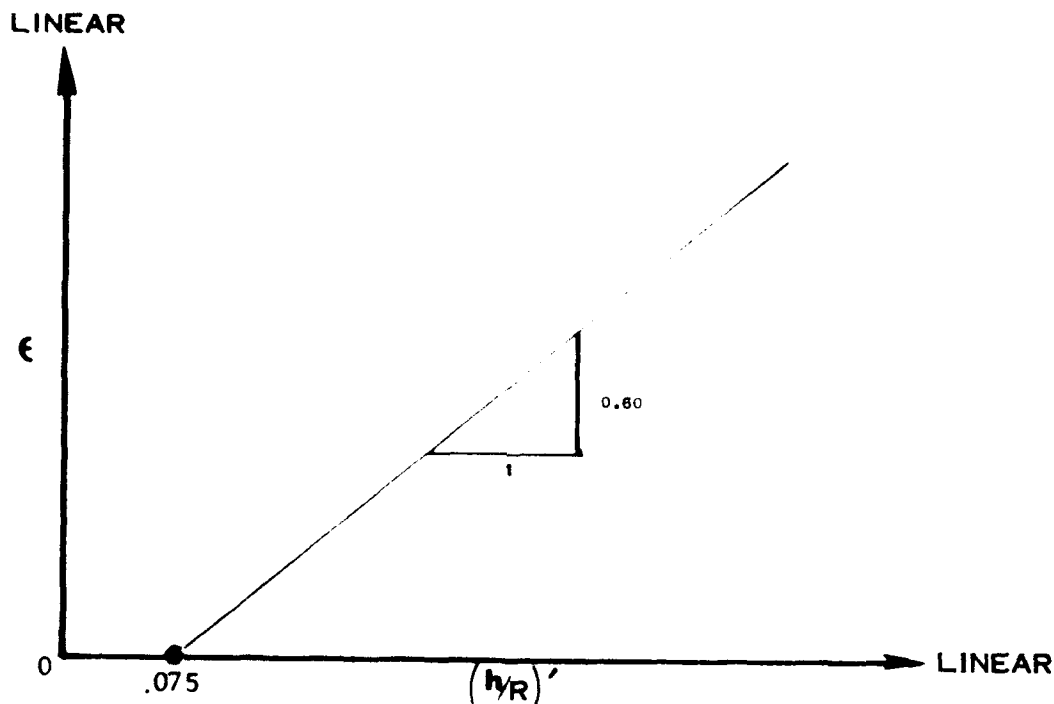


FIGURE V 37 CORRELATION CURVE FOR SPLITTING IN LINEAR STRETCH FORMING

The equation for the curve in Figure V-37 by using the slope and intercept is:

$$\epsilon_{2,0} = 0.6 \left(\frac{h}{R} \right)' - .0450$$

$$\left(\frac{h}{R} \right)' = \frac{\epsilon_{2,0} + .0450}{0.6}$$

Plotting the curves in Figure V-36 on semi-log graph paper gives the results as shown in Figure V-38.

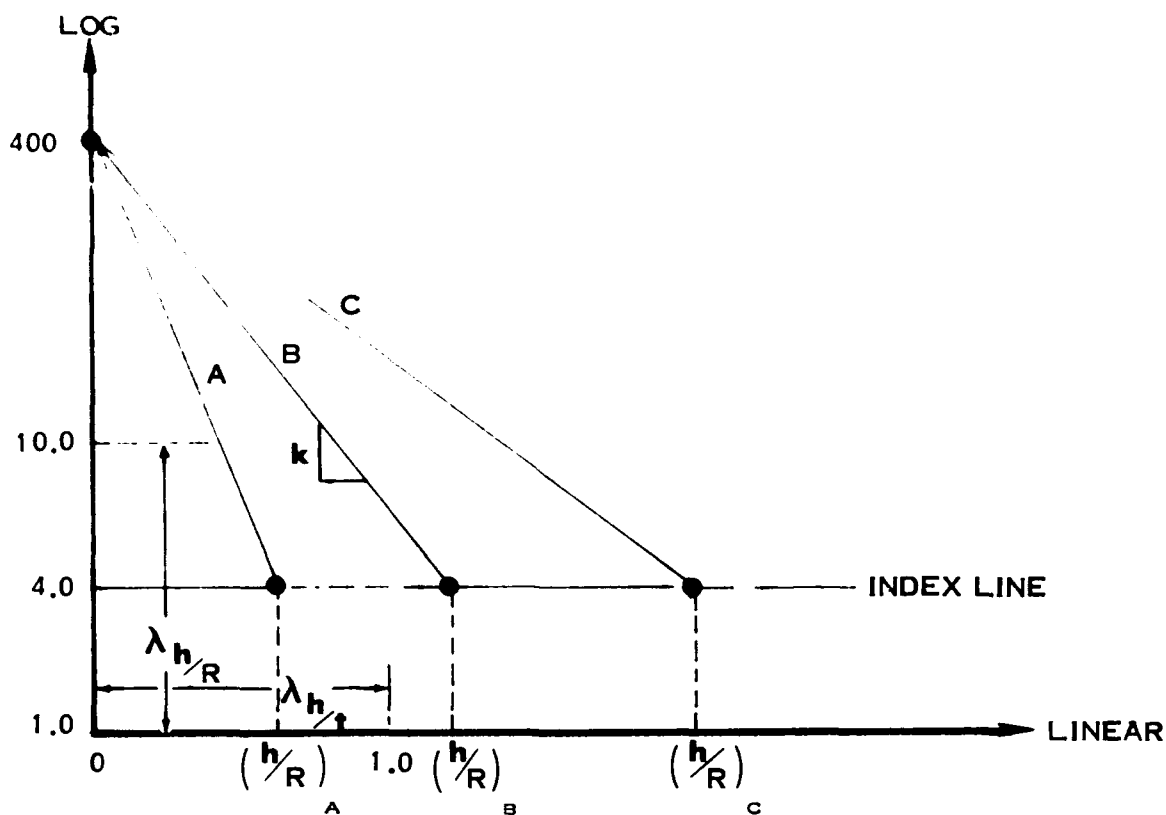


FIGURE V-38 COMPOSITE OF SPLITTING LIMITS FOR LINEAR STRETCH FORMING ON SEMI-LOG GRAPH PAPER

The equation for the curves in Figure V-38 has the form:

(V - 52)

$$\frac{h}{t} = (B)(d)^{m \frac{h}{R}}$$

The slope, however, varies with the $(h/R)^{\frac{1}{2}}$, which is a function of ϵ as defined by equation (V-31a). Changing equation (V-52) to log form:

(V-52a)

$$\log \frac{h}{t} = \log B + \frac{h}{R} m \log d$$

B is constant and equal to 100 for all curves since they all intersect the h/R axis at 100.

The slope of the curve is $m \log d$ which varies with $(h/R)^{\frac{1}{2}}$.

(V - 53)

$$(m \log d) \left(\frac{h}{R} \right)^{\frac{1}{2}} = \text{CONSTANT}$$

Therefore:

(V - 53a)

$$m \log d = \frac{\text{CONSTANT}}{\left(\frac{h}{R} \right)^{\frac{1}{2}}}$$

The expression $m \log d$ can be determined from Figure (V-38).

(V - 54)

$$m \log d = \left(\frac{\lambda_{h/R}}{\lambda_h} \right) K$$

where $\lambda_{h/R}$ = actual measured length of a cycle from 0 to 1 on the linear scale

$\lambda_{h/t}$ = actual measured length of a cycle on log log scale from 1.0 to 10.0

K = actual measured slope

The constant in equation (V-53a) was found to be equal to -1.99.

Substituting values back to equation (V-52) gives:

$$(V-55) \quad \log \frac{h}{t} = \log 400 - \frac{1.99}{\left(\frac{h}{R}\right)^{2.0}} \left[\frac{h}{R} \right]$$

Substituting equation (V-51a) into (V-55) gives:

$$(V-56) \quad \log \frac{h}{t} = \log 40 - \frac{1.99 (0.6)}{\epsilon_{2.0} + .045} \left[\frac{h}{R} \right]$$

Solving for h/R :

$$(V-57) \quad \frac{h}{R} = - \left[0.836 \epsilon_{2.0} + .045 \right] \left[\log .0025 \frac{h}{t} \right]$$

Equation (V-57) is the splitting limit predictability equation for Heel-Out Angle and Channel sections in linear stretch forming.

A summary of all equations is shown in Figures V-39 through V-41.

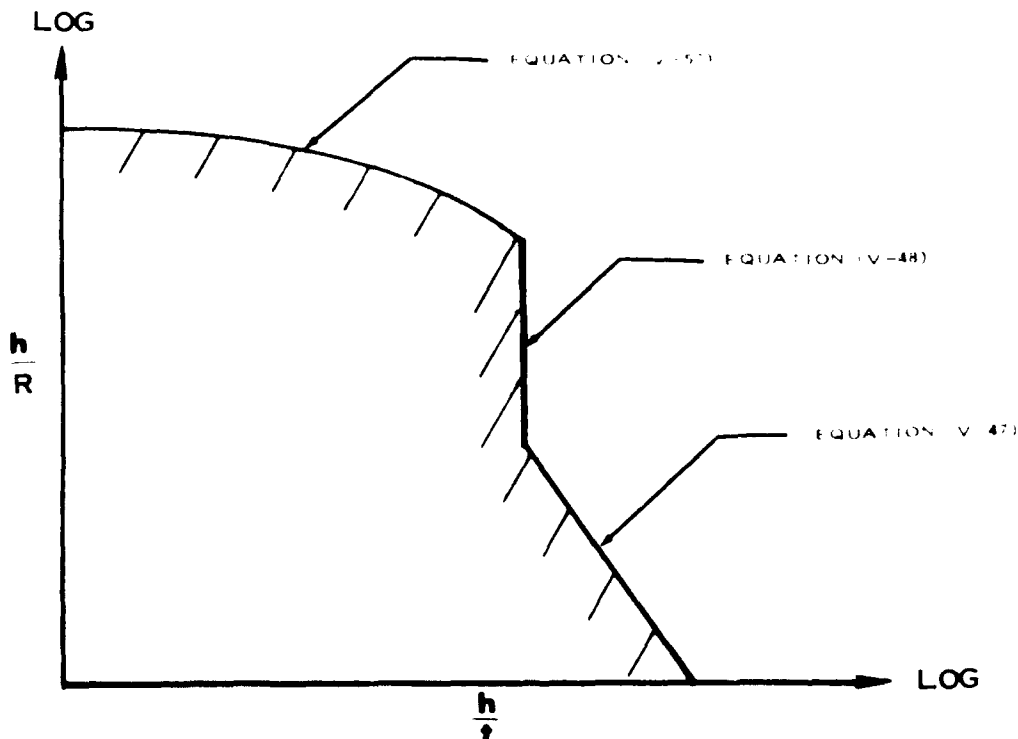


FIGURE V-39 EQUATIONS FOR LINEAR STRETCH FORMED HEEL-OUT ANGLES AND CHANNELS

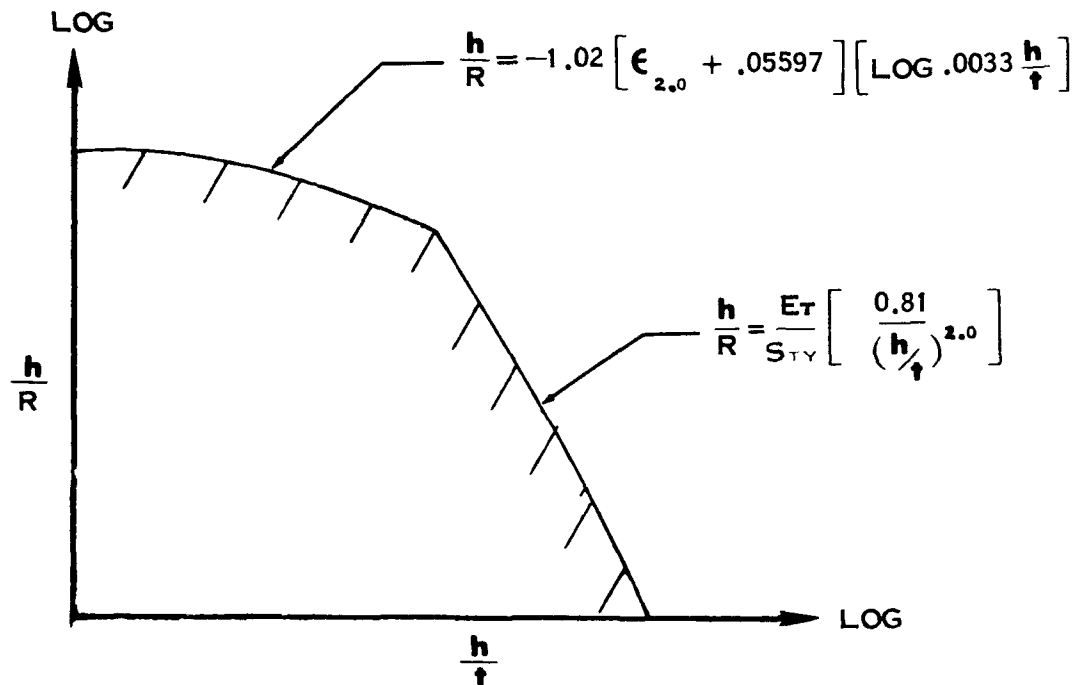


FIGURE V-40 EQUATIONS FOR LINEAR STRETCH FORMED HEEL-IN ANGLES AND CHANNELS

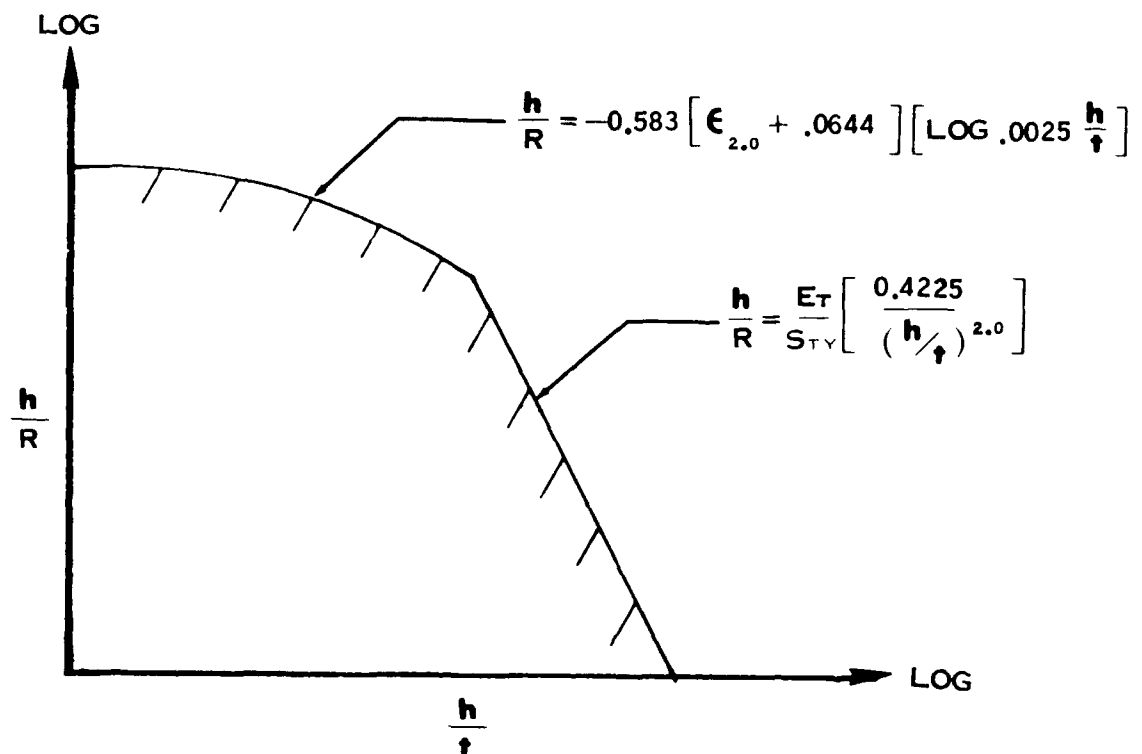


FIGURE V-41 EQUATIONS FOR LINEAR STRETCH FORMED HEEL-IN HAT SECTIONS

DESIGN TABLES

Design tables for the three types of cross-sections in linear stretch forming were established for each material by using the composite graphs and an overlay graph with constant R_D/t curves plotted on it. This was accomplished in the same manner as was shown in the previous sections of this chapter. The overlay graphs are constructed graphically with constant R_D/t curves and vary for each type of cross-section as shown in Figure V-42.

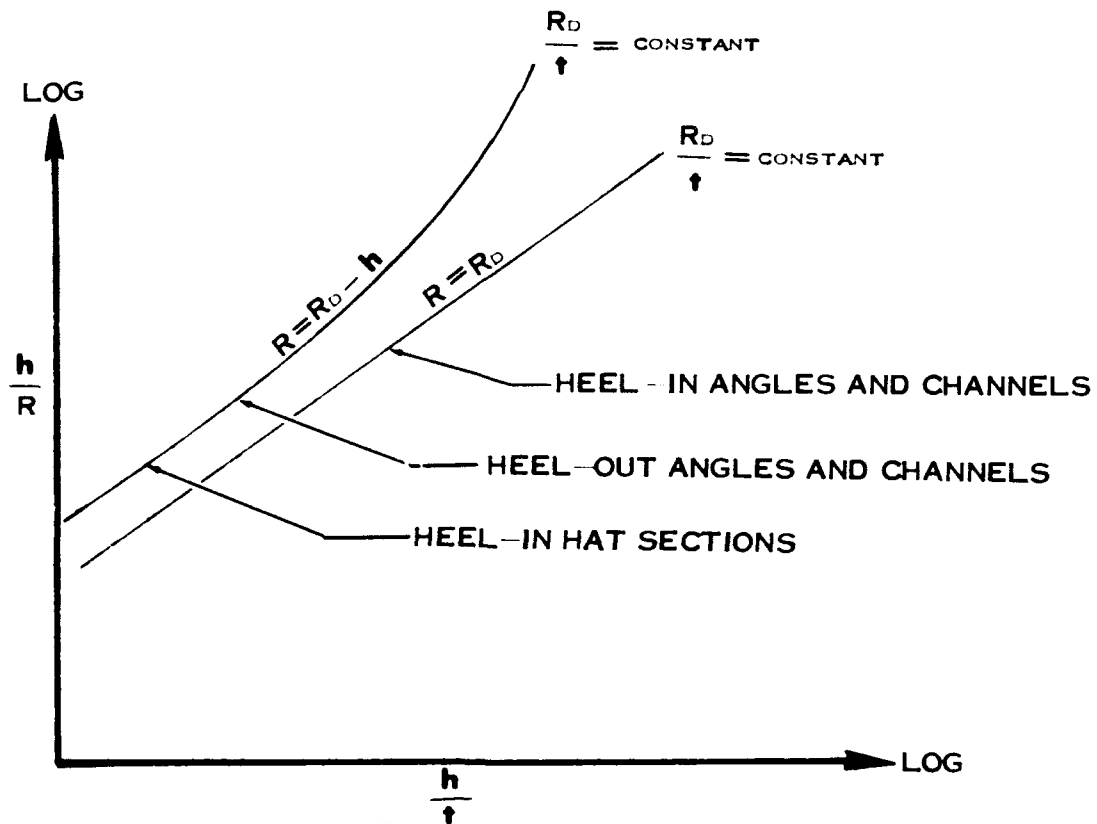


FIGURE V-42 CONSTANT $\frac{R_D}{t}$ CURVES FOR OVERLAY GRAPHS FOR LINEAR STRETCH FORMED PARTS

Design tables can then be developed for each material as illustrated in Figure V-43.

R_D	t	t_1	t_2	t_3	t_4	
	h					
R_1	h_1	h_3				
R_2	h_2	h_4				

FIGURE V-43 DESIGN TABLE FORMAT FOR LINEAR STRETCH FORMING

LINEAR ROLL FORMING

Two geometric shapes were investigated--Heel-In and Heel-Out Channels as shown in Figure V-44.

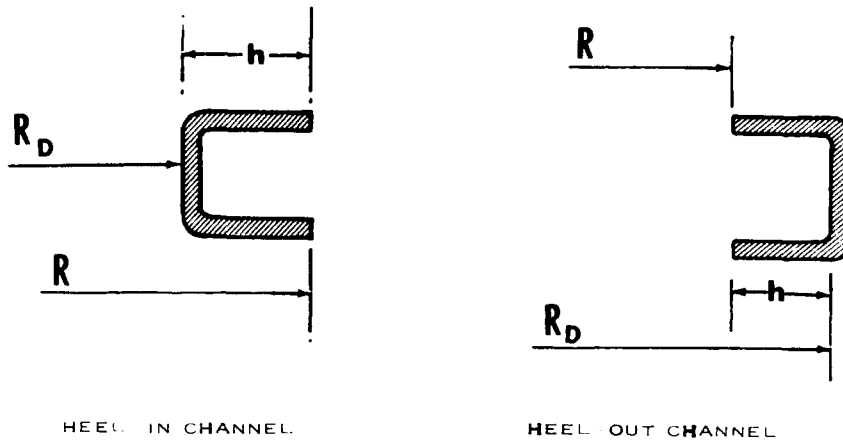


FIGURE V-44 GEOMETRIC PARAMETERS FOR ROLL FORMING

Elastic buckling is the only formability limit involved in linear roll forming. The graphs for Heel-In and Heel-Out Channels were developed from the empirically determined forming limit curves of all materials as illustrated in Figures V-45 and V-46.

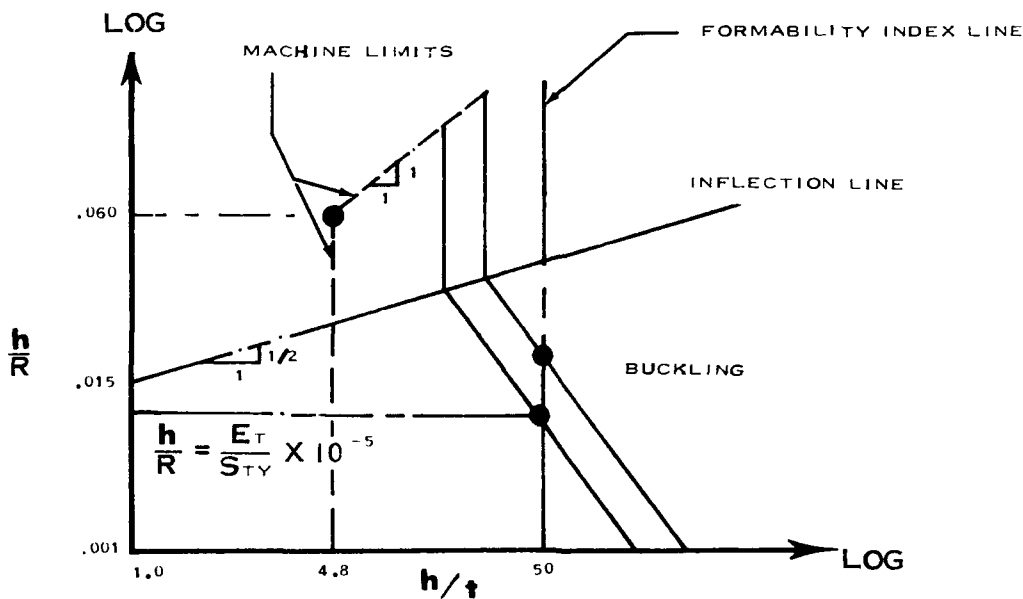


FIGURE V-45 COMPOSITE FOR ROLL FORMED HEEL-IN CHANNELS

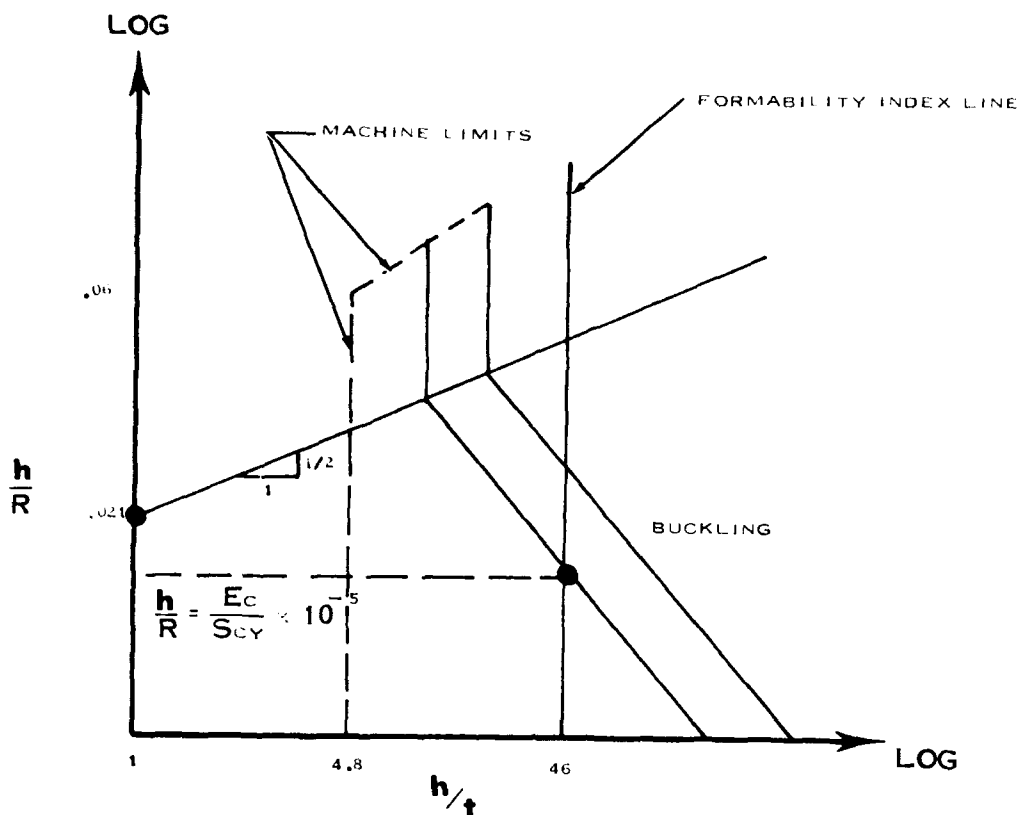


FIGURE V-46 COMPOSITE FOR ROLL FORMED HEEL-OUT CHANNELS

The same type development as was used in joggling was used to develop the following equations for linear roll forming.

Heel-In Channels (below the inflection line):

$$(V - 58) \quad \frac{h}{R} = \frac{E_T}{S_{TY}} \left[\frac{.025}{(h/t)^2} \right]$$

Heel-In Channels (above the inflection line):

$$(V - 59) \quad \frac{h}{t} = \left[1.713 \frac{E_T}{S_{TY}} \right]^{2/5}$$

Heel-Out Channels (below the inflection line):

$$(V - 60) \quad \frac{h}{R} = \frac{E_C}{S_{CY}} \left[\frac{.02116}{(h/t)^2} \right]$$

Heel-Out Channels (above the inflection line):

$$(V - 61) \quad \frac{h}{t} = \left[1.01 \frac{E_C}{S_{CY}} \right]^{2/5}$$

The machine limits are constant and defined by a vertical line at $h/t = 4.8$ up to $h/R = .060$. At that point it slopes to the right with a (+1) slope until it intersects the buckling curve.

DESIGN TABLES

Design tables for Heel-In and Heel-Out Channels in roll forming were established for each material by using the composite graph and an overlay graph with constant R_D/t curves plotted on it. This was accomplished in the same manner as was shown previously in this chapter. The overlay graphs are illustrated in Figure V-47.

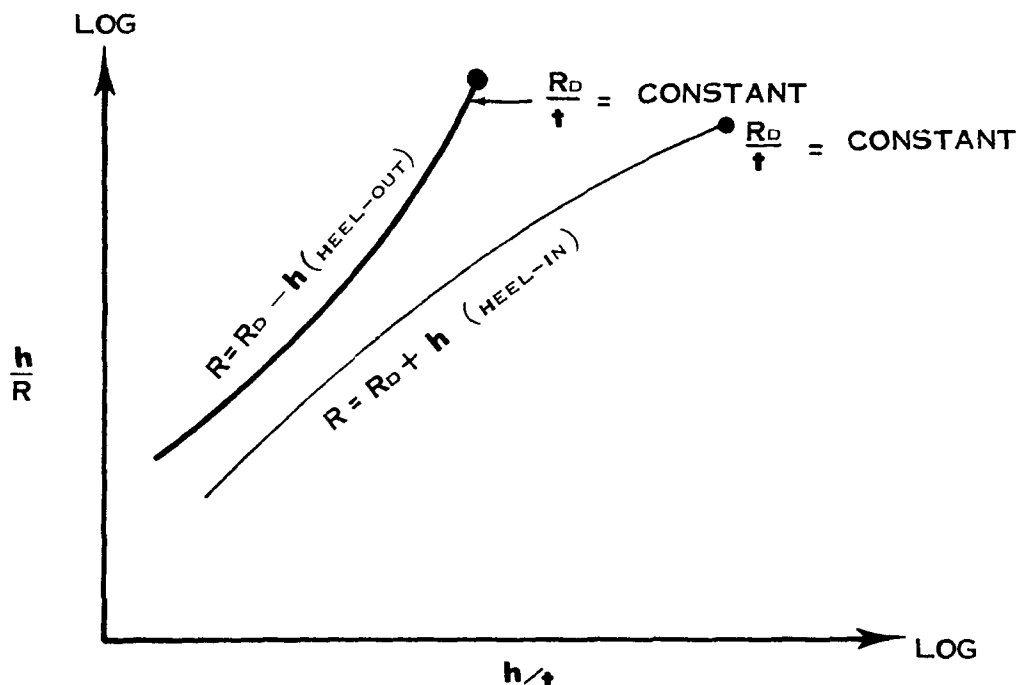


FIGURE V-47 CONSTANT $\frac{R_D}{t}$ CURVES FOR OVERLAY GRAPHS FOR LINEAR ROLL FORMING

Design tables can then be developed for each material as illustrated in Figure V-48.

$R_D \backslash t$	t_1	t_2	t_3	t_4	t_5	t_6
R_1	h_1	h_3				
R_2	h_2					

FIGURE V-48 DESIGN TABLE FORMAT FOR LINEAR ROLL FORMING

SHEET STRETCH FORMING

The fundamental shape equations for sheet stretch forming which define the shape of the formability limit curve were developed in Chapter II. Failure occurs by splitting. A composite graph composed of the empirically determined forming limit curves of all materials was developed as shown in Figure V-49.

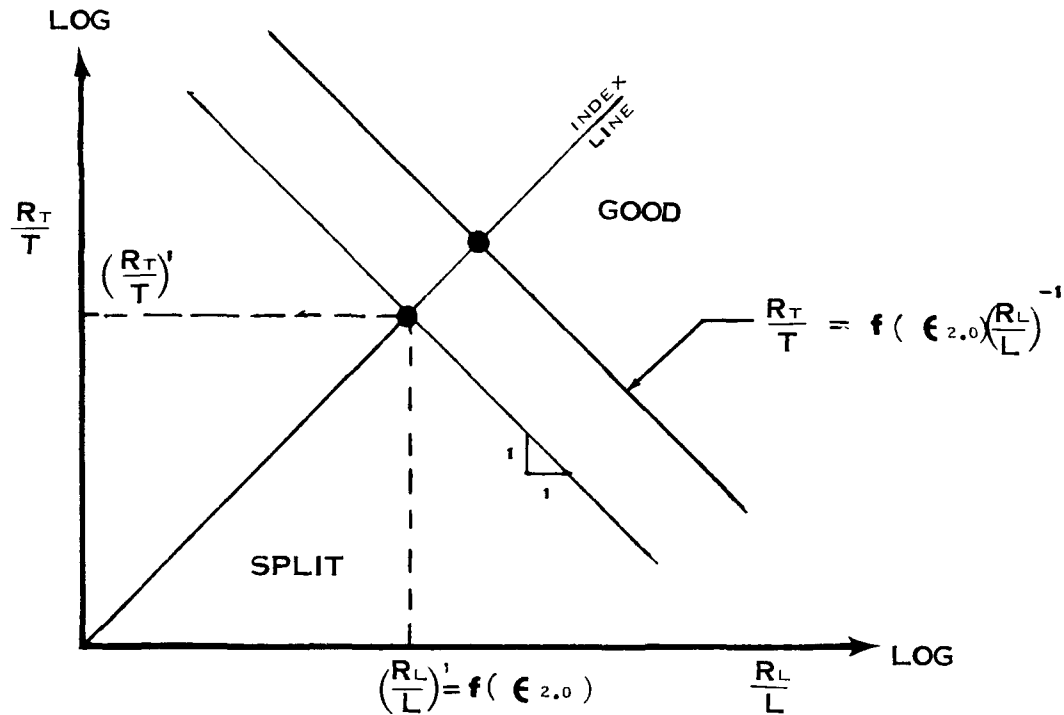


FIGURE V-49 COMPOSITE GRAPH FOR SHEET STRETCH FORMING

The geometric parameters are defined by Figure V-50.

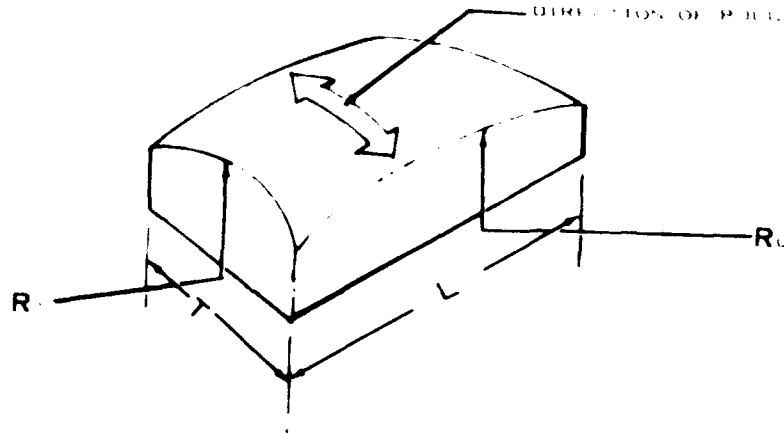


FIGURE V-50 GEOMETRIC PARAMETERS IN SHEET STRETCH FORMING

The index has the equation:

(V - 62)

$$\frac{R_T}{T} = \frac{R_L}{L}$$

The splitting limit in sheet stretch is a function of the available elongation in the material. The basic equation for strain as developed in Chapter II is:

(V - 63)

$$\epsilon = 2 \left(\frac{R_L}{L} \right)^2 \csc^{-1} 2 \left(\frac{R_L}{L} \right)^2 - 1$$

Plotting $\epsilon_{2.0}$ vs. $(R_L/L)^2$ gives the following type curve:

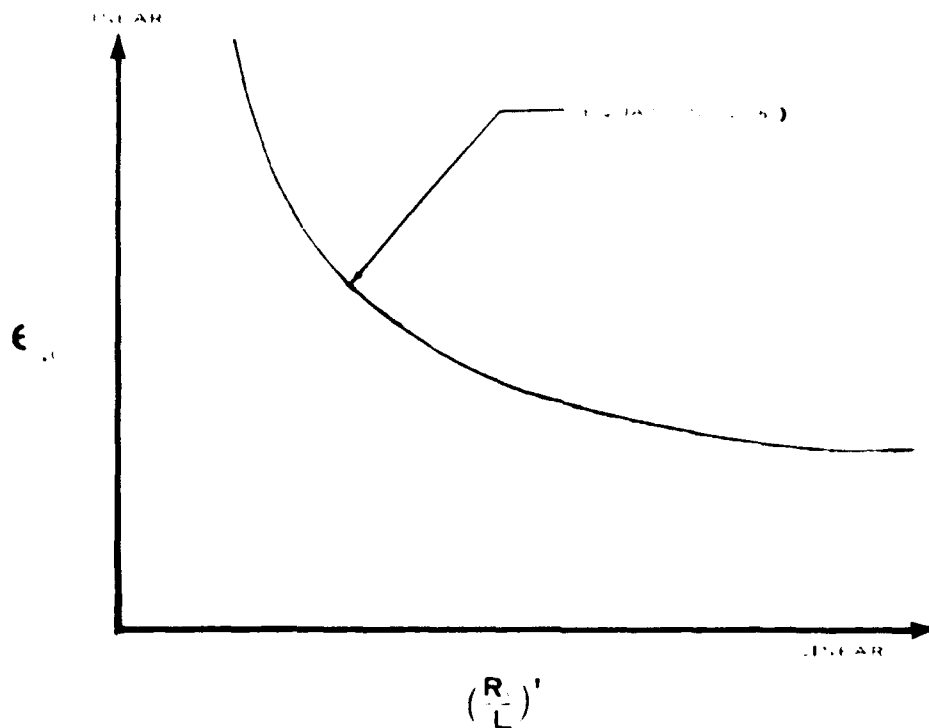


FIGURE V-51 CORRELATION CURVE FOR SHEET STRETCH FORMING

Plotting actual values of $\epsilon_{2,0}$ vs. $(R_L/L)^{-1}$ limits for various materials gives the following curve:

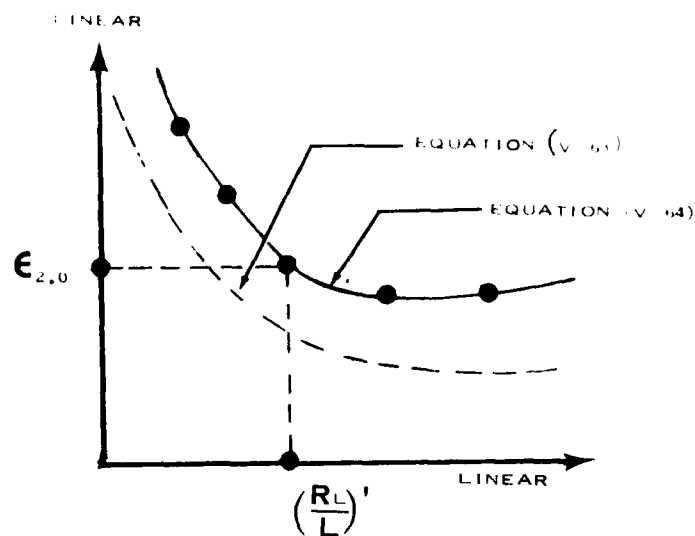


FIGURE V-52 CORRELATION CURVE FOR SHEET STRETCH FORMING

The equation for the curve in Figure V-52 was found to be:

$$(V - 64) \quad \epsilon_{2.0} = 4 \left[2 \left(\frac{R_L}{L} \right)^1 \csc^{-1} 2 \left(\frac{R_L}{L} \right)^1 - 1 \right]$$

Solving equation V-64 for $(R_L/L)^1$ gives a very complex series function.

The limiting curve in Figure V-49 can be constructed very simply by finding $\epsilon_{2.0}$ and using Figure V-52 to find $(R_L/L)^1$. $(R_L/L)^1$ can then be plotted on Figure V-49 up to the index line and then a limiting curve with a slope of (-1) can be constructed.

DESIGN TABLES

Design tables for sheet stretch forming were established for each material directly from the composite graph as illustrated in the Figure V-53.

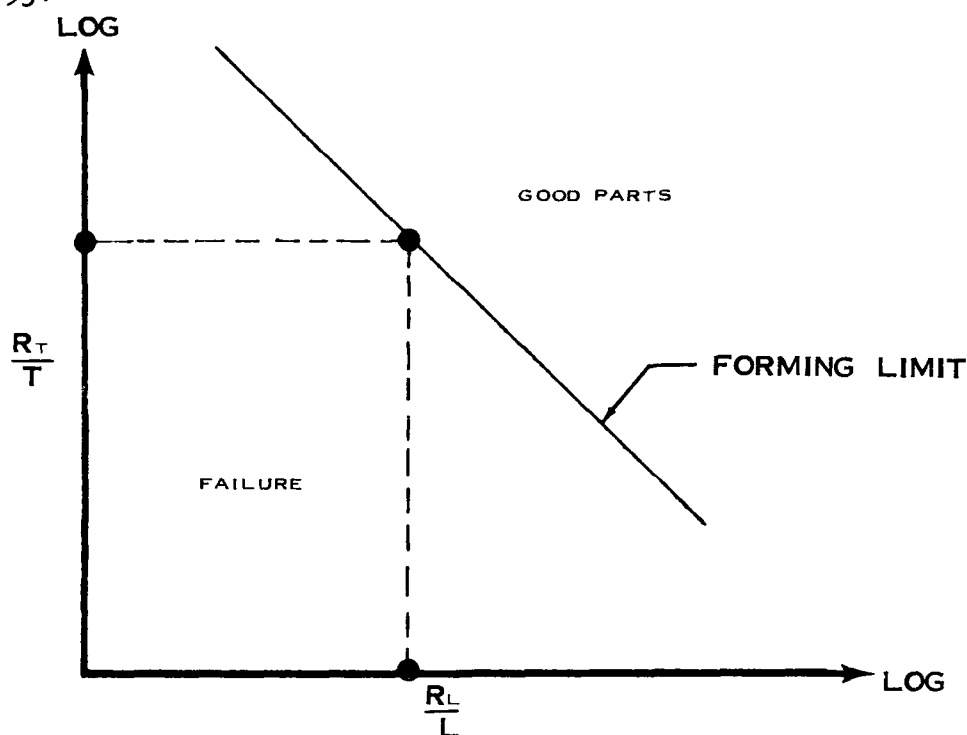


FIGURE V-53 FORMING LIMIT CURVE AND METHOD TO DETERMINE THE FORMING LIMITS FOR SHEET STRETCH FORMING

There are four variables involved--three known parameters R_T , T , R_L and the unknown parameter L ; i.e., the forming limit. Values of R_T , T , and R_L were selected and the L value calculated directly from the composite. R_T should always be considered the smallest radius since it is the general procedure to pull the sheet across the smallest radius. The forming limit curve can be expressed in tabular form as shown in Figure V-54.

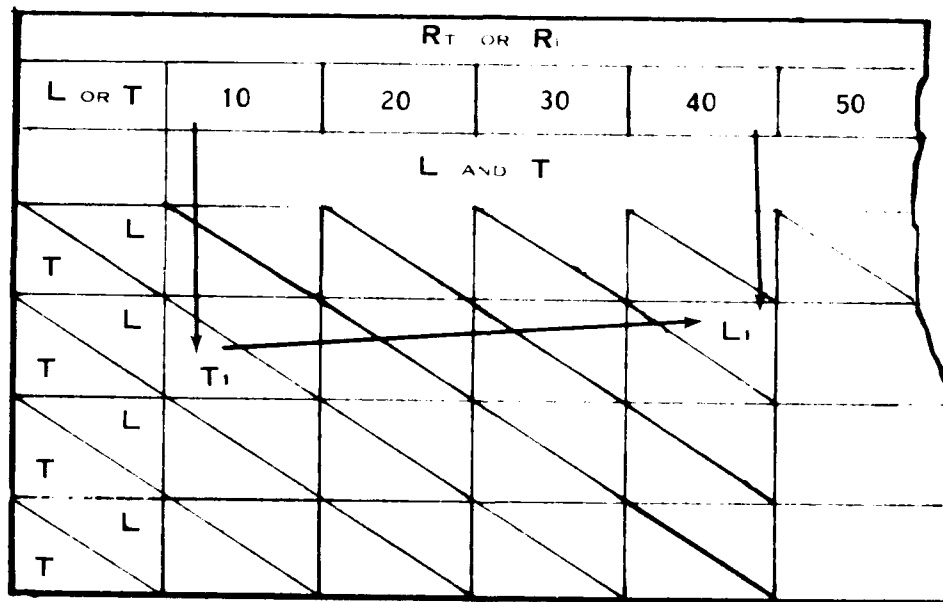


FIGURE V-54 DESIGN TABLE FORMAT FOR SHEET STRETCH FORMING

The forming limit (L) can be determined from the table in Figure V-54 by selecting the values of R_T , R_L and T , and following the arrows as shown in Figure V-54. R_T should always be selected less than R_L .

ANDROFORMING

The fundamental shape equations for Androforming, which define the shape of the formability limit curve, were developed in Chapter II. Two types of failure occur--buckling and splitting. The geometric variables involved are illustrated in Figure V-55.

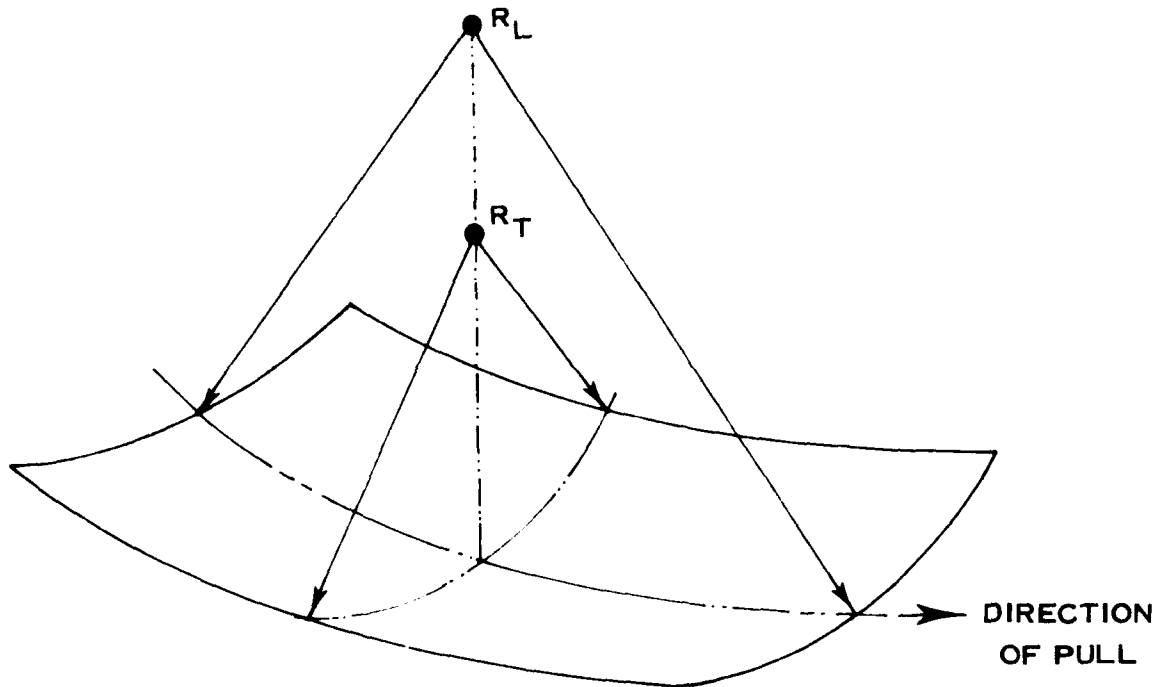


FIGURE V 55 GEOMETRIC PARAMETERS FOR ANDROFORMING

Buckling is inversely proportional to R_L , R_T and t , whereas splitting is inversely proportional to R_L and R_T and directly proportional to t . Two composite graphs are therefore necessary to define the limits, as illustrated in Figures V-56 and V-57.

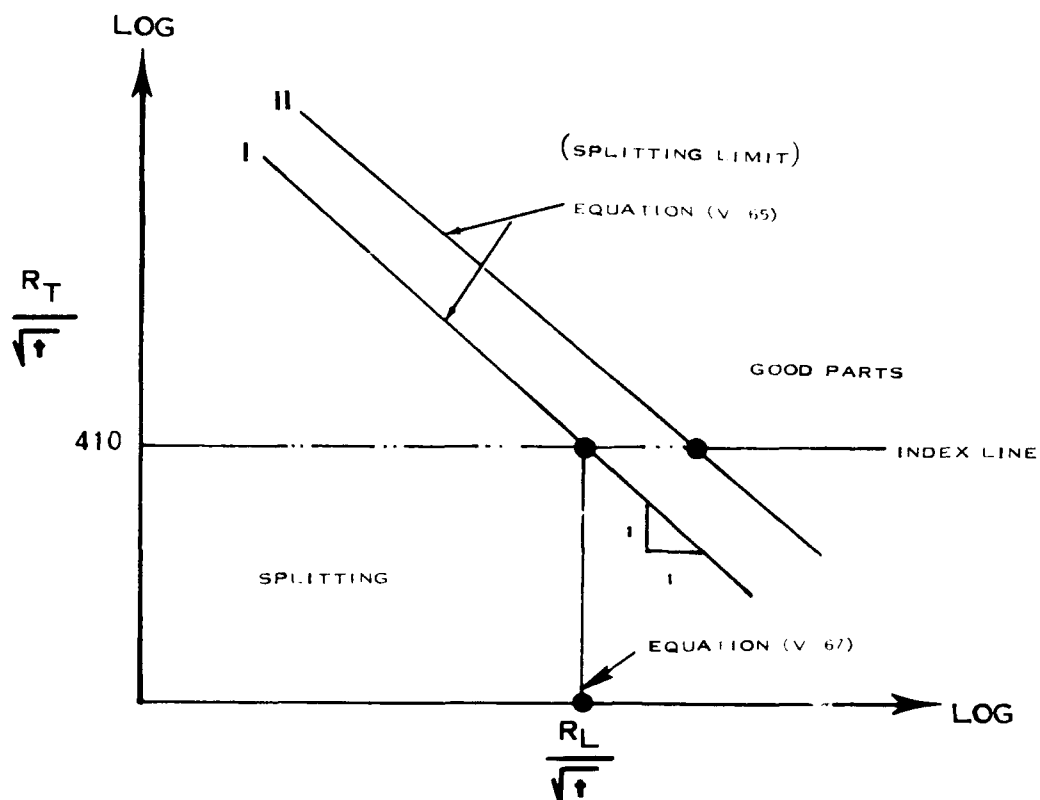


FIGURE V-56 ANDROFORM SPLITTING LIMIT (50'' DIE)

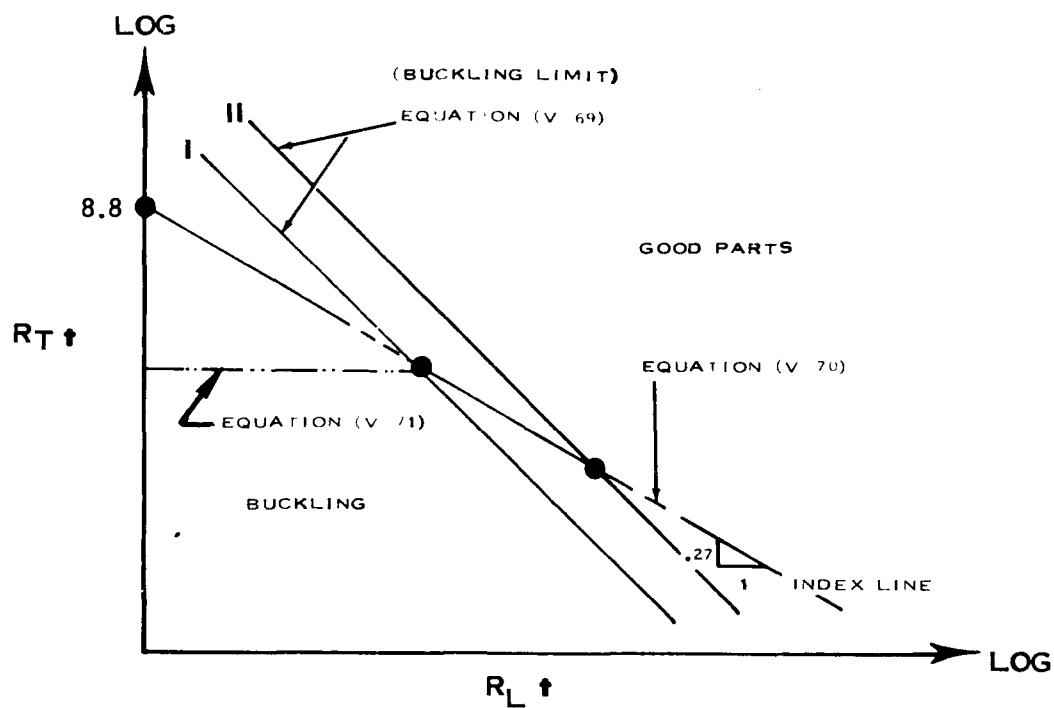


FIGURE V-57 ANDROFORM BUCKLING LIMITS (50'' DIE)

The basic equation for the splitting limit in Androforming is
(See Figure V-56):

$$(V - 65) \quad \boxed{\frac{R_T}{\sqrt{f}} = \frac{E_T}{\epsilon_{2.0} S_{TY}} \left[B \right] \left[\frac{R_L}{\sqrt{f}} \right]^{-1}}$$

The splitting formability index is $\frac{E_T}{\epsilon_{2.0} S_{TY}}$ as developed in Chapter III.
The splitting formability index line which positions materials according to their mechanical properties for the 50" die is:

$$(V - 66) \quad \boxed{\frac{R_T}{\sqrt{f}} = 410}$$

At the intersection of the index line and the splitting limit curve:

$$(V - 67) \quad \boxed{\frac{R_L}{\sqrt{f}} = \frac{E_T}{\epsilon_{2.0} S_{TY}} \times 10^{-1}}$$

Solving for B by substituting equation (V-66) and (V-67) into (V-65):

$$(V - 68) \quad \boxed{B = 41}$$

Equation (V-65) now becomes:

$$(V - 65A) \quad \boxed{\frac{R_T}{\sqrt{f}} = \left[\frac{E_T}{\epsilon_{2.0} S_{TY}} \right] \left[41 \right] \left[\frac{R_L}{\sqrt{f}} \right]^{-1}}$$

The basic equation for the buckling limit in Androforming is
(See Figure V-57):

$$(V - 69) \quad \boxed{R_T f = \left[\frac{S_{TY}}{E_T} \right] \left[C \right] \left[R_L f \right]^{-1}}$$

The buckling formability index is $\left(\frac{E_T}{S_{TY}} \right)$ as developed in Chapter III. The buckling formability index line which positions materials according to their mechanical properties has the equation (For the 50" die):

(V - 70)

$$R_{Tf} = 4.75 [R_{Lf}]^{-0.27}$$

the intersection of the index line and the buckling limit curve:

(V - 71)

$$R_{Tf} = \frac{S_{TY}}{E_T} \times 10^3$$

Using equations (V-70) and (V-71), solve for C in (V-69):

(V - 72)

$$C = \left[\left(\frac{.00475}{\frac{S_{TY}}{E_T}} \right)^{\frac{1}{0.27}} \right] \times 10^3$$

Substituting the value of C back into equation (V-69) gives:

(V - 69a)

$$R_{Tf} = 2.51 \times 10^{-6} \left[\frac{S_{TY}}{E_T} \right]^{-2.7} [R_{Lf}]^{-1}$$

The equations for the 20 inch dies were developed in the same manner and are:

Splitting Limit For 20" Die

(V - 73)

$$\frac{R_T}{\sqrt{f}} = 5.0 \left[\frac{E_T}{\epsilon_{2.0} S_{TY}} \right] \left[\frac{R_L}{\sqrt{f}} \right]^{-1}$$

Buckling Limit For 20" Die

(V - 74)

$$R_{Tf} = 1.471 \times 10^{-6} \left[\frac{S_{TY}}{E_T} \right]^{-2.7} [R_{Lf}]^{-1}$$

In summary, the splitting and buckling limits for the 50" die are given by equations (V-65a) and (V-69a), and the equations for 20" die are given by (V-73) and (V-74).

DESIGN TABLES

Design tables for any material can be established from the buckling and splitting limit formability curve as defined by the predictability equations. Knowing R_T and t , the limiting value of R_L can be obtained easily by finding the limiting value of R_L/\sqrt{t} from the splitting curve and $R_L t$ from the buckling curve. If the R_L value from the buckling curve is larger than the R_L value from the splitting curve, the buckling limit is the primary limit since any value less would buckle. If the reverse is true, the splitting limit is the primary limit since any value less would split. The resulting design table is illustrated in Figure V-58.

TRANS RADIUS	MATERIAL THICKNESS									
	↑ ₁	↑ ₂	↑ ₃	↑ ₄	↑ ₅	↑ ₆	↑ ₇			
R_T	LONGITUDINAL RADIUS (R_L)									
	BUCKLING					SPLITTING				
R_{T1}										
R_{T2}										
R_{T3}										

FIGURE V-58 DESIGN TABLE FORMAT FOR ANDROFORMING

DEEP DRAWING WITH MECHANICAL DIES

The fundamental shape equations for deep drawing, which define the shape of the formability limit curve, were developed in Chapter II. The limiting failure is buckling, as shown in Chapter III. A composite graph composed of the empirically determined forming limit curves of all materials was developed as illustrated in Figure V-59.

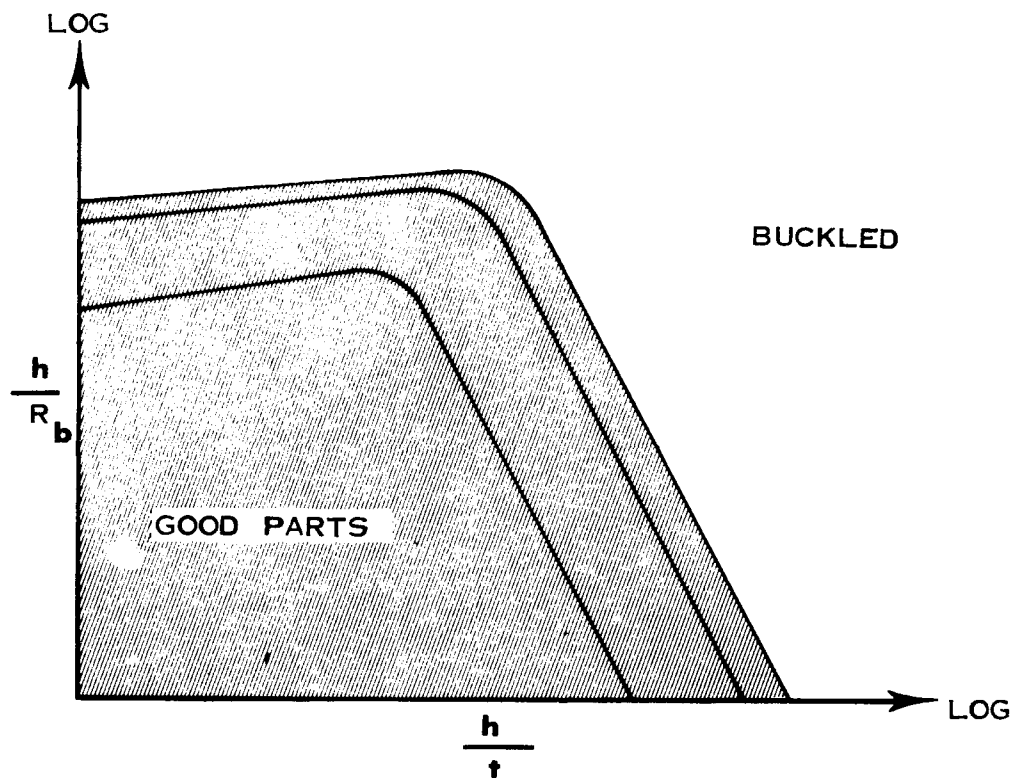


FIGURE V - 59 COMPOSITE GRAPH FOR DEEP DRAWING

The basic geometric parameters are defined by Figure V-60.

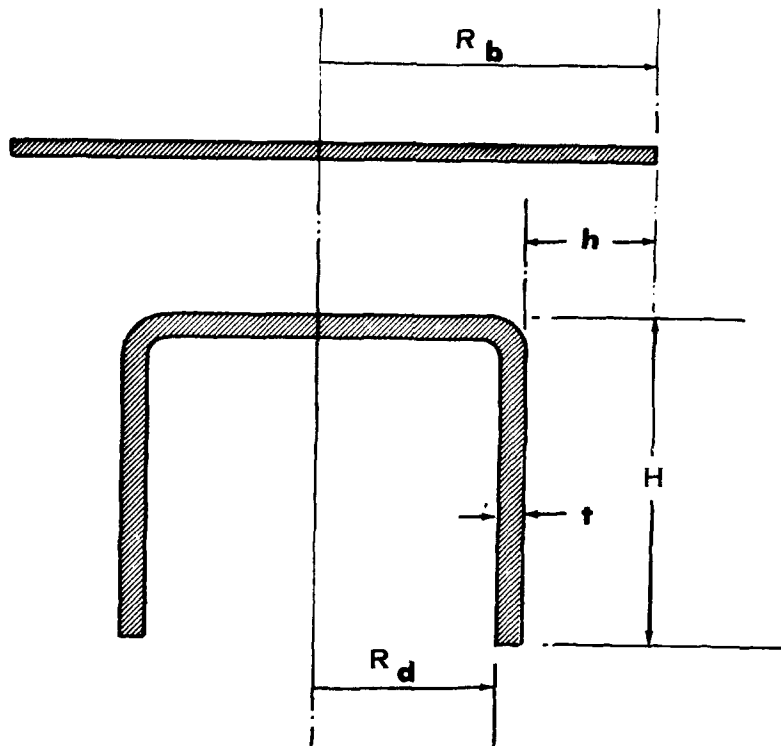


FIGURE V - 60 GEOMETRIC PARAMETERS FOR DEEP DRAWING

The buckling index for deep drawing as developed in Chapter III is:

(V - 75)

$$\text{BUCKLING INDEX} = \left(\frac{E_c}{S_{cy}} \right) \left(\frac{S_{ty}}{S_{cy}} \right)$$

The buckling limit curves and index lines are illustrated in Figure V-61.

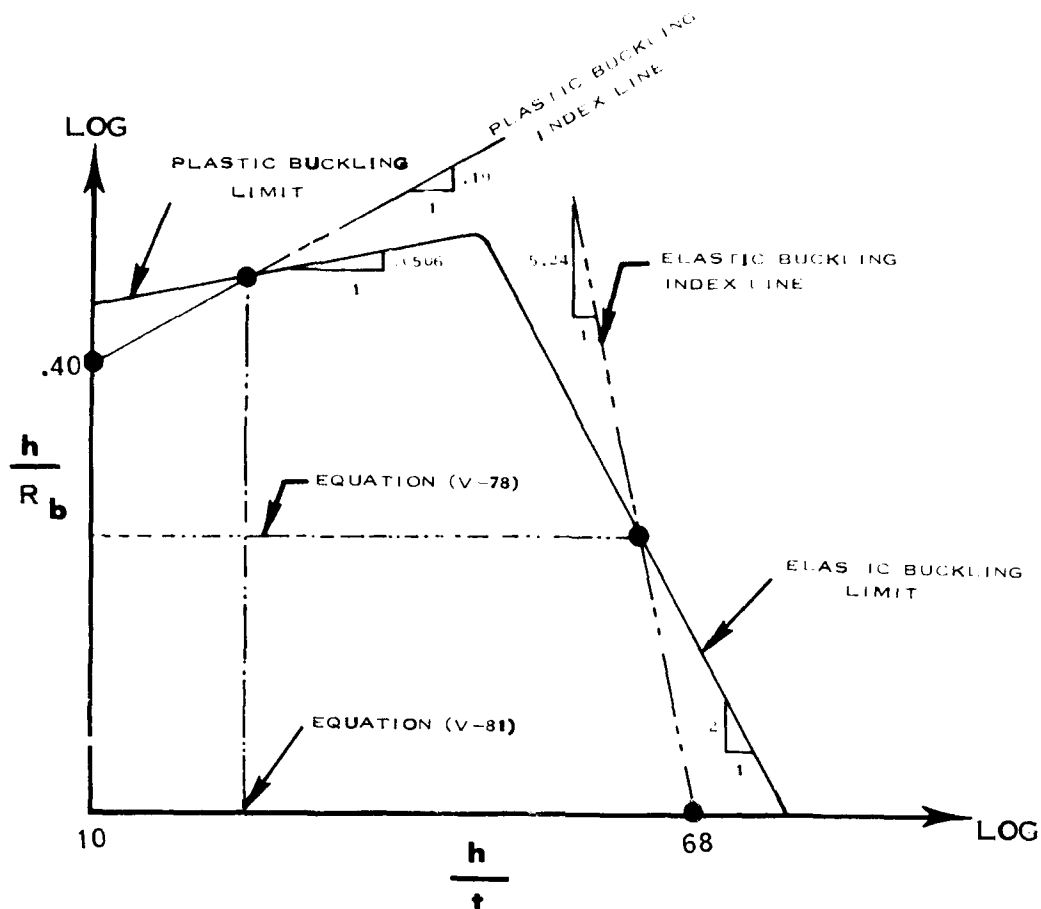


FIGURE V-61 BUCKLING CURVES AND INDEX LINES FOR DEEP DRAWING

The equation for the elastic buckling index line was found from Figure V-61 by the slope and intercept method to be:

$$(V-76) \quad \frac{h}{R_b} = 3.96 \times 10^8 \left(\frac{h}{t} \right)^{-5.24}$$

The general equation for the elastic buckling limit is:

$$(V-77) \quad \frac{h}{R_b} = \left(\frac{E_c}{S_{CY}} \right) \left(\frac{S_{TY}}{S_{CY}} \right) B \left(\frac{h}{t} \right)^{-2}$$

The intersection of the index line and forming limit curve is:

$$(V-78) \quad \frac{h}{R_b} = \left(\frac{E_c}{S_{CY}} \right) \left(\frac{S_{TY}}{S_{CY}} \right) \times 10^{-3}$$

Solving for B from equations (V-76), (V-77) and (V-78) and substituting back into equation (V-77).

$$(V - 77A) \quad \frac{h}{R_b} = 27.0 \left[\left(\frac{E_C}{S_{CY}} \right) \left(\frac{S_{TY}}{S_{CY}} \right) \right]^{0.618} \left(\frac{h}{t} \right)^{-2}$$

The equation for the plastic buckling index line is:

$$(V - 79) \quad \frac{h}{R_b} = 0.258 \left(\frac{h}{t} \right)^{0.19}$$

The general equation for the plastic buckling limit is:

$$(V - 80) \quad \frac{h}{R_b} = \left(\frac{E_C}{S_{CY}} \right) \left(\frac{S_{TY}}{S_{CY}} \right) C \left(\frac{h}{t} \right)^{0.0506}$$

The intersection of the index line and the forming limit curve is:

$$(V - 81) \quad \frac{h}{t} = \left(\frac{E_C}{S_{CY}} \right) \left(\frac{S_{TY}}{S_{CY}} \right) \times 10^{-1}$$

Solving for C from equations (V-79), (V-80) and (V-81) and substituting back into equation V-80 gives:

$$(V - 80A) \quad \frac{h}{R_b} = 0.258 \left[\left(\frac{E_C}{S_{CY}} \right) \left(\frac{S_{TY}}{S_{CY}} \right) \times 10^{-1} \right]^{0.139} \left(\frac{h}{t} \right)^{0.0506}$$

The elastic and plastic buckling limit predictability equations are (V-77a) and (V-80a).

DESIGN TABLES

Design tables for deep drawing limits were established for each material by using the composite graph and an overlay graph with constant R_d/t curves as illustrated in Figure V-62.

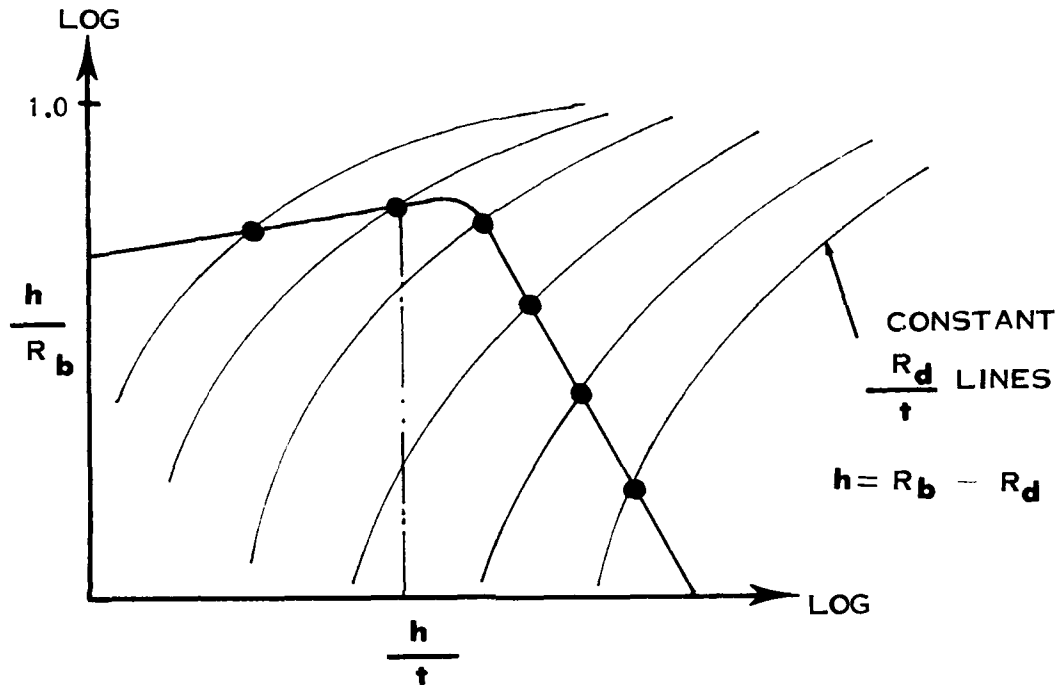


FIGURE V - 62 DEEP DRAWING LIMIT CURVE AND OVERLAY GRAPH

Selecting a particular die radius (R_d) and gage (t) gives a particular R_d/t . At the intersection of the R_d/t line and the limiting curve a vertical line is drawn down to the limiting h/t . The value of the blank diameter limit (D_b) can then be obtained since $h = R_b - R_d$ and $D_b = 2R_b$. The flange height can then be determined from the H/h versus D_b/D_d curve developed for deep drawing in Chapter II. Design tables as illustrated in Figure V-63 can then be developed.

GAGE (↑)		↑ ₁	↑ ₂	↑ ₃	↑ ₄	↑ ₅	↑ ₆	
DIE DIA. D_d		FLANGE HEIGHT (H) : BLANK DIAMETER D						
1	D b							
	H							
2	D b							
	H							
3	D b							
	H							
4	D b							
	H							

FIGURE V - 63 DESIGN TABLE FORMAT FOR DEEP DRAWING

MANUAL SPINNING

The fundamental shape equations for manual spinning, which define the shape of the formability limit curve, were developed in Chapter II. Two types of buckling occur--elastic and plastic. In addition to the elastic and plastic buckling limit there is a machine limit based upon the gage of material being spun. A composite graph composed of the empirically determined forming limit curves of all materials was developed as illustrated in Figure V-64.

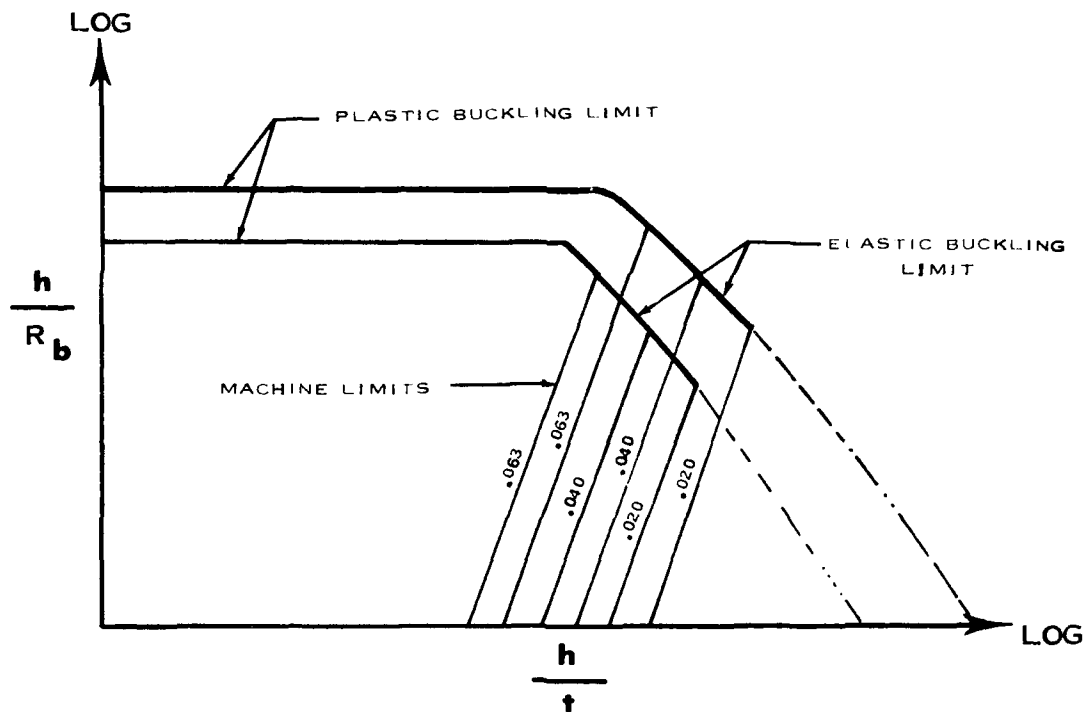


FIGURE V - 64 MANUAL SPINNING LIMIT COMPOSITE

The basic geometric parameters are defined by Figure V-65.

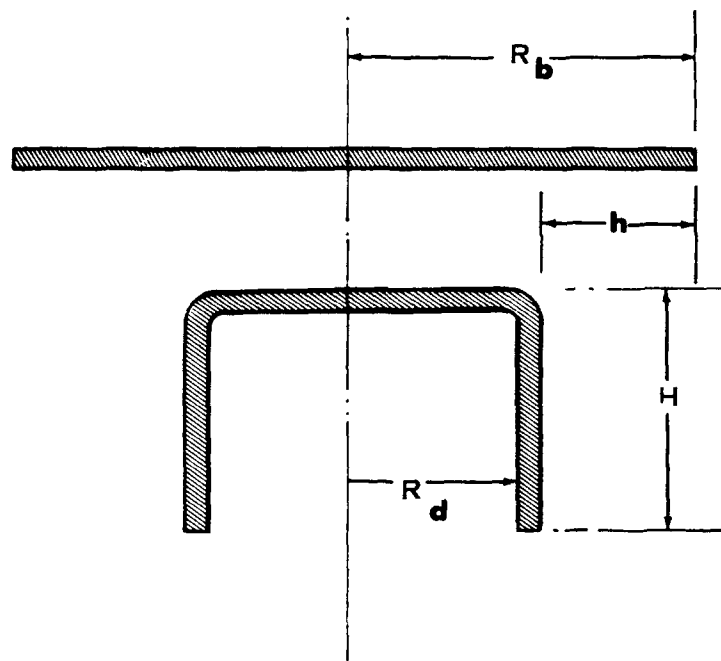


FIGURE V - 65 GEOMETRIC PARAMETERS FOR SPINNING

The general equation for the plastic buckling limit is:

$$(V - 82) \quad \frac{h}{R_b} = f \left[\frac{E_T}{S_u} \right]$$

The plastic buckling index as developed in Chapter III is (E_T/S_u) . The plastic buckling index line was developed experimentally as illustrated in Figure (V-66).

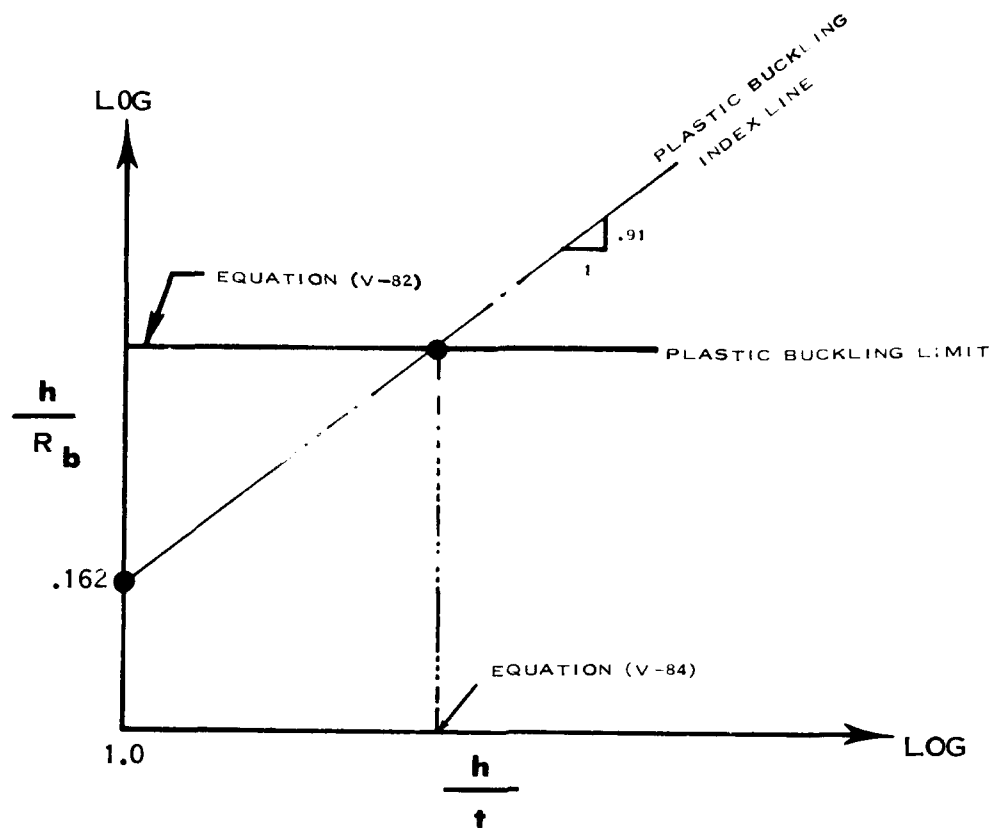


FIGURE V-66 PLASTIC BUCKLING LIMITS FOR SPINNING

The equation for the plastic buckling index line from Figure (V-66) is:

$$(V-83) \quad \frac{h}{R_b} = 0.162 \left[\frac{h}{t} \right]^{0.91}$$

At the intersection of equation (V-82) and (V-83):

$$(V-84) \quad \frac{h}{t} = \left[\frac{E_T}{S_U} \right] \times 10^{-2}$$

Solving equations (V-82), (V-83) and (V-84) simultaneously gives:

$$(V-82A) \quad \frac{h}{R_b} = 0.162 \left[\frac{E_T}{S_U} \times 10^{-2} \right]^{0.91}$$

The general equation for elastic buckling limit is:

$$(V-85) \quad \frac{h}{R_b} = \left[\frac{E_C}{S_{CY}} \right] \left[\frac{B}{h/t^2} \right]$$

The elastic buckling index line was developed experimentally as illustrated in Figure V-67.

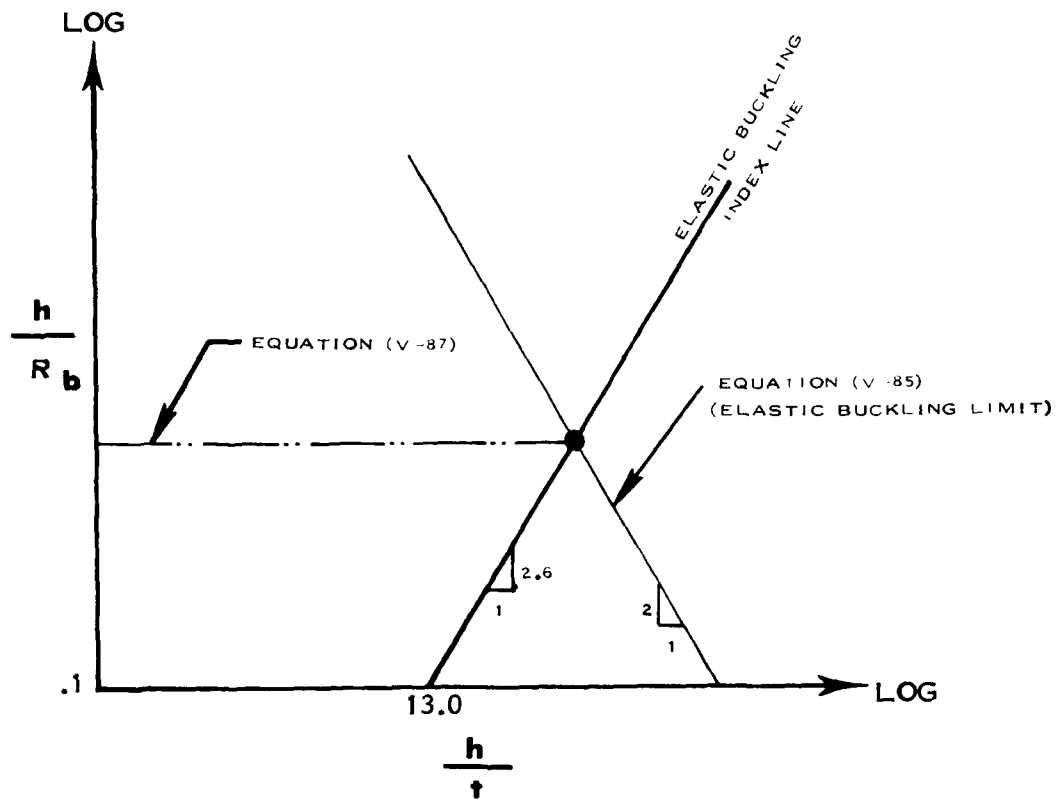


FIGURE V-67 ELASTIC BUCKLING LIMITS FOR SPINNING

The equation for the elastic buckling index line from Figure (V-67) is:

(V-86)

$$\frac{h}{R_b} = 1.279 \times 10^{-4} \left[\frac{h}{t} \right]^{2.6}$$

At the intersection of equation (V-85) and (V-86):

(V-87)

$$\frac{h}{R_b} = \frac{E_c}{S_{cy}} \times 10^{-3}$$

Solving equations (V-85), (V-86), and (V-87) simultaneously for B and substituting back into (V-85) gives:

$$(V - 85A) \quad \boxed{\frac{h}{R_b} = \left[\frac{E_c}{S_{CY}} \right]^{1.769} \left[\frac{.00485}{(h/t)^2} \right]}$$

The machine limits are a function of the material properties and the thickness. In order to develop the equation for the machine limits, two index lines must be determined. Index line I positions index line II on the basis of material properties (E_T/S_U). Index line II, positions the machine limits on the basis of thickness of material. (See Figure V-68).

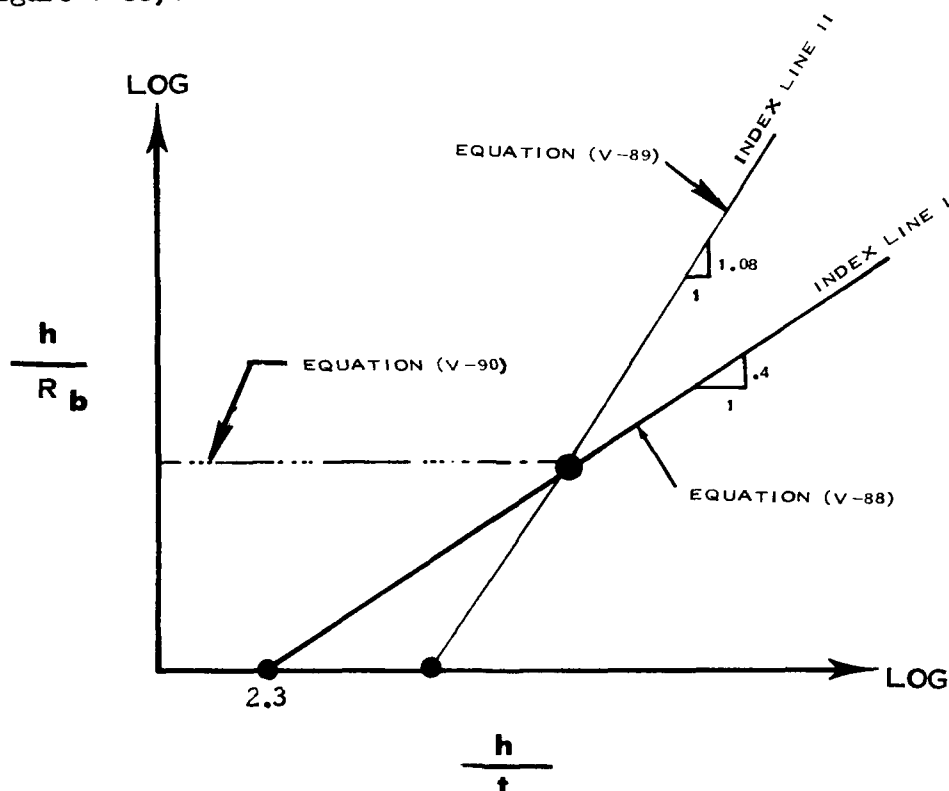


FIGURE V - 68 MACHINE LIMIT INDEX LINES FOR SPINNING

The equation of index line I from the slope and intercept (Figure V-68) is:

$$(V-88) \quad \frac{h}{R_b} = .072 \left(\frac{h}{t} \right)^{0.40}$$

The equation of index line II has the form:

$$(V-89) \quad \frac{h}{R_b} = B \left[\frac{E_T}{S_u} \right] \left[\frac{h}{t} \right]^{1.08}$$

At the intersection of equations (V-88) and (V-89):

$$(V-90) \quad \frac{h}{R_b} = \left[\frac{E_T}{S_u} \right] \times 10^{-3}$$

Solving equations (V-88), (V-89) and (V-90) simultaneously for B and substituting back into (V-89) gives:

$$(V-89_A) \quad \frac{h}{R_b} = 8.13 \times 10^{-4} \left[\frac{E_T}{S_u} \times 10^{-3} \right]^{-1.7} \left[\frac{h}{t} \right]^{1.08}$$

It is now possible to get the equation for the machine limit for each gage. (See Figure V-69).

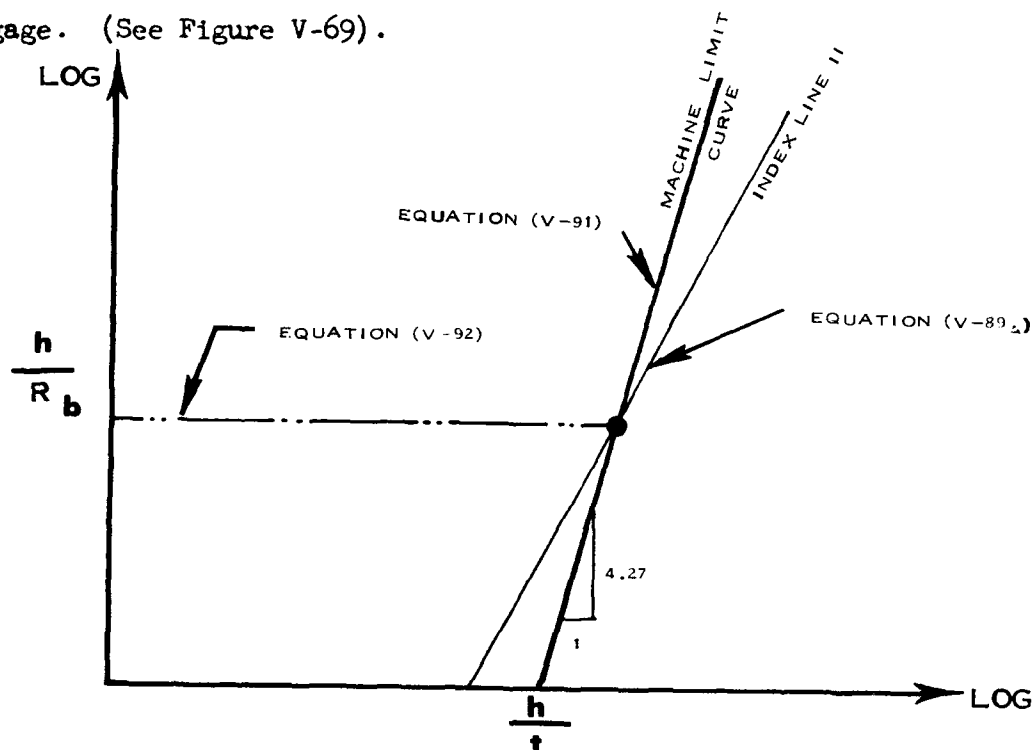


FIGURE V-69 MACHINE LIMIT CURVE FOR SPINNING

The equation of the machine limit curve has the form:

$$(V-91) \quad \frac{h}{R_b} = C \left[\frac{E_T}{S_U} \right] \left[\frac{h}{t} \right]^{4.27}$$

At the intersection of equations (V-89a):

$$(V-92) \quad \frac{h}{R_b} = \frac{1}{t} \times 10^{-2}$$

Solving equations (V-89a), (V-91) and (V-92) simultaneously for C and substituting back into equation (V-91) gives:

$$(V-91_A) \quad \frac{h}{R_b} = \frac{[4.787 \times 10^{-7}] [t]^{2.96} \left[\frac{h}{t} \right]^{4.27}}{\left[\frac{E_T}{S_U} \times 10^{-3} \right]^{6.74}}$$

In summary the predictability equations for spinning are illustrated in Figure V-70.

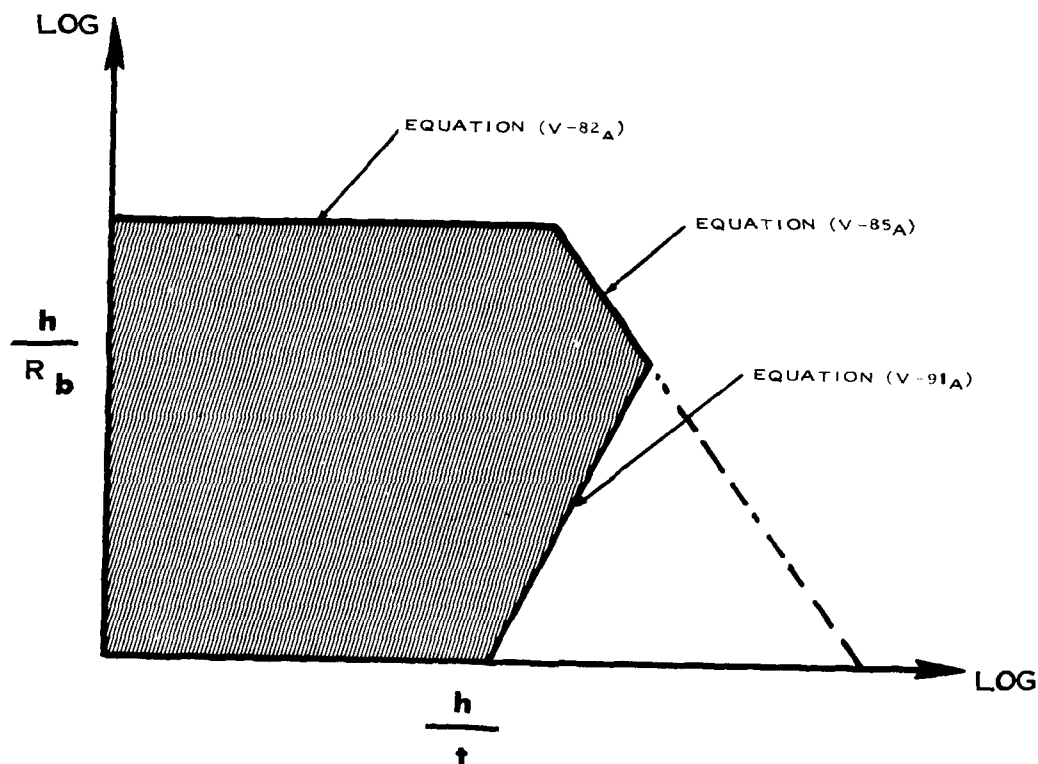


FIGURE V - 70 SPINNING PREDICTABILITY EQUATIONS

DESIGN TABLES

Design tables for manual spinning limits were established for each material by using the composite graph and an overlay graph with constant R_d/t curves as illustrated in Figure V-71.

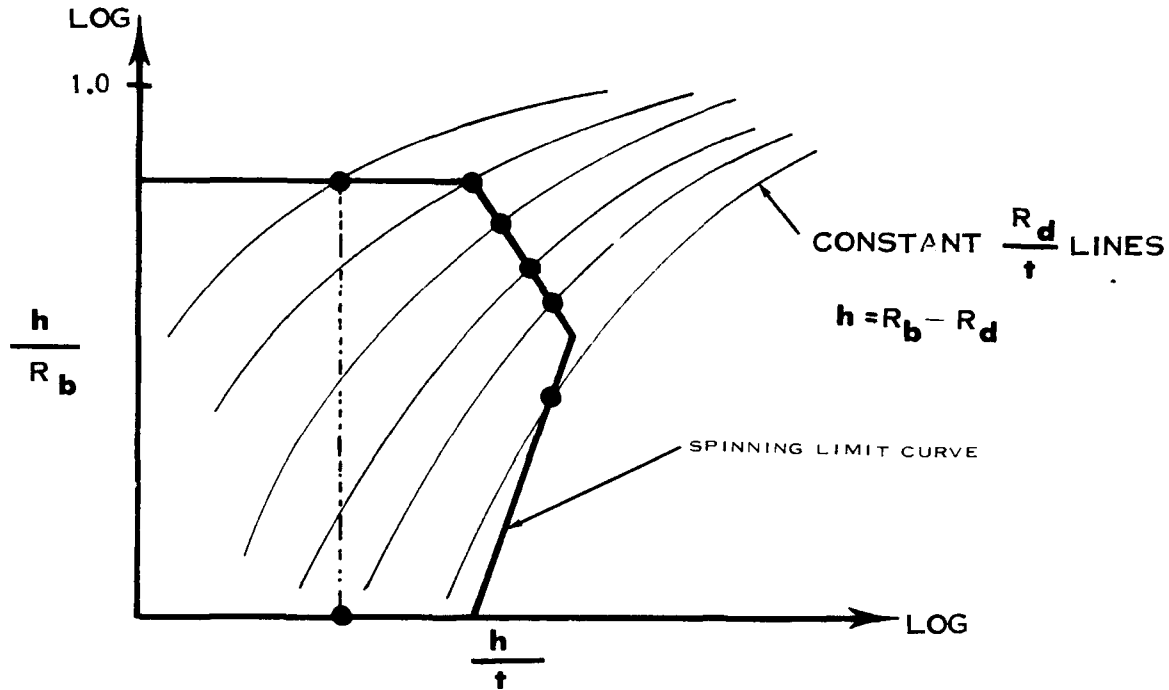


FIGURE V - 71 SPINNING LIMIT CURVE AND OVERLAY GRAPH

Selecting a particular die radius (R_d) and gage (t) gives a particular R_d/t . Where this particular R_d/t line intersects the limiting curve a vertical line is drawn down to the limiting h/t . The value of the limiting blank diameter (D_b) can then be obtained since $h = R_b - R_d$ and $D_b = 2R_b$. The flange height (H) can then be determined from the H/h vs. D_b/D_d curve developed for spinning in Chapter II. Design tables as illustrated in Figure V-72 can then be developed.

GAGE (↑)		↑ ₁	↑ ₂	↑ ₃	↑ ₄	↑ ₅	
D _d		FLANGE HEIGHT (H):BLANK DIAMETER(D _b)					
1	D _b						
	H						
2	D _b						
	H						
3	D _b						
	H						

FIGURE V - 72 DESIGN TABLE FORMAT FOR SPINNING

BEADING ON THE RUBBER PRESS

The fundamental shape equations for rubber formed beads, which define the shape of the formability limit curve, were developed in Chapter II. In addition to the splitting limit there is an insufficient pressure limit based upon a rubber pad pressure of 3000psi. A composite graph composed of the empirically determined forming limits curves of all materials was developed as shown in Figure V-73.

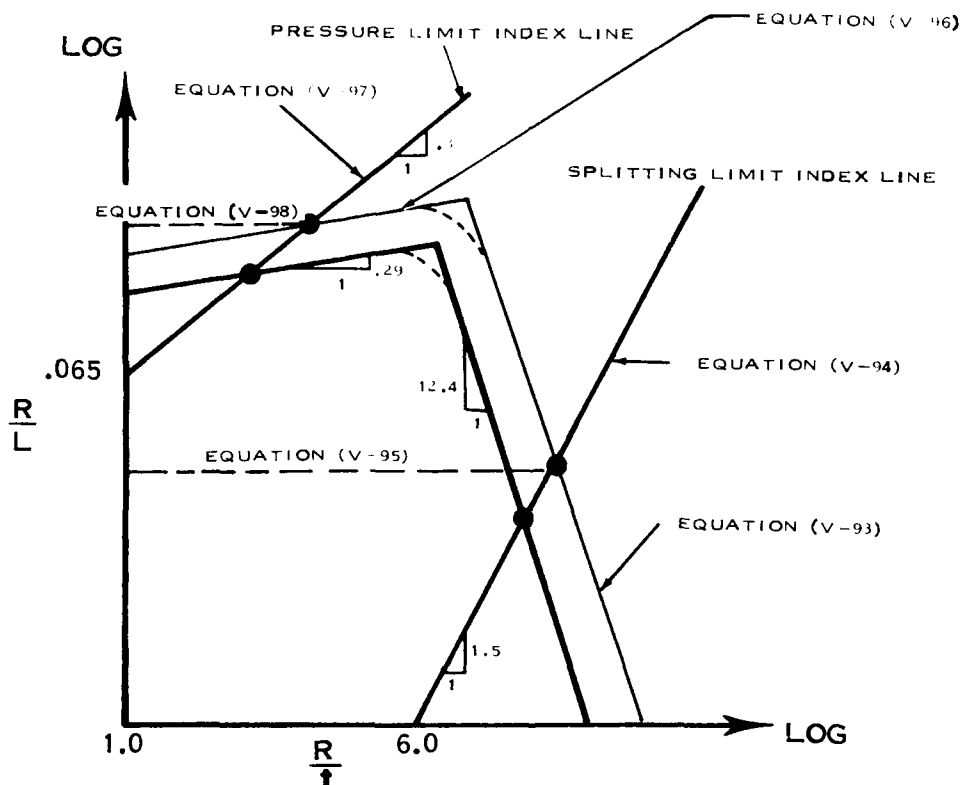


FIGURE V-73 COMPOSITE GRAPH FOR RUBBER FORMED BEAD LIMITS

The geometric parameters are defined by Figure V-74.

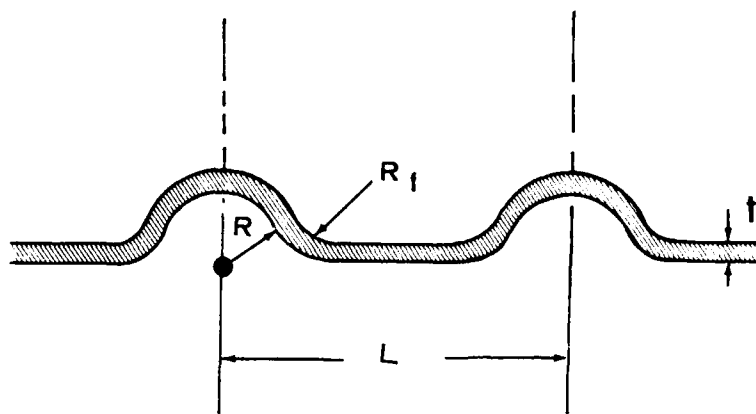


FIGURE V-74 GEOMETRIC PARAMETERS FOR RUBBER BEAD FORMING

The general equation for the splitting limit is:

$$(V-93) \quad \frac{R}{L} = \epsilon_{2.0} S_U [B] \left[\frac{R}{t} \right]^{-12.4}$$

The equation of the splitting limit index line from the slope and intercept (See Figure V-73) is:

$$(V-94) \quad \frac{R}{L} = 6.84 \times 10^{-4} \left(\frac{R}{t} \right)^{1.5}$$

At the intersection of equations (V-93) and (V-94):

$$(V-95) \quad \frac{R}{L} = \epsilon_{2.0} S_U \times 10^{-5}$$

Solving equations (V-93), (V-94) and (V-95) simultaneously for B and substituting back into equation (V-93):

$$(V-93A) \quad \frac{R}{L} = \left[6.0 \times 10^{-21} \right] \left[\epsilon_{2.0} S_U \right]^{9.3} \left[\frac{R}{t} \right]^{-12.4}$$

The equation for the rubber pressure limit has the form:

$$(V-96) \quad \frac{R}{L} = \frac{1}{S_{TY}} \left[C \right] \left[\frac{R}{t} \right]^{0.29}$$

The equation for the pressure limit index line from the slope and intercept (See Figure V-73) is:

$$(V-97) \quad \frac{R}{L} = .065 \left(\frac{R}{t} \right)^{0.37}$$

At the intersection of equations (V-96) and (V-97):

$$(V-98) \quad \frac{R}{L} = \frac{1}{S_{TY}} \times 10^4$$

Solving equation (V-96), (V-97) and (V-98) simultaneously for C and substituting back into equation (V-96):

$$(V-96A) \quad \frac{R}{L} = .065 \left[\frac{\frac{1}{S_{TY}} \times 10^4}{.065} \right]^{0.216} \left[\frac{R}{t} \right]^{0.29}$$

Equations (V-93a) and (V-96a) are the predictability equations for rubber bead forming.

DESIGN TABLES

Design tables for rubber bead forming were established for each material directly from the composite graph as illustrated in Figure V-75.

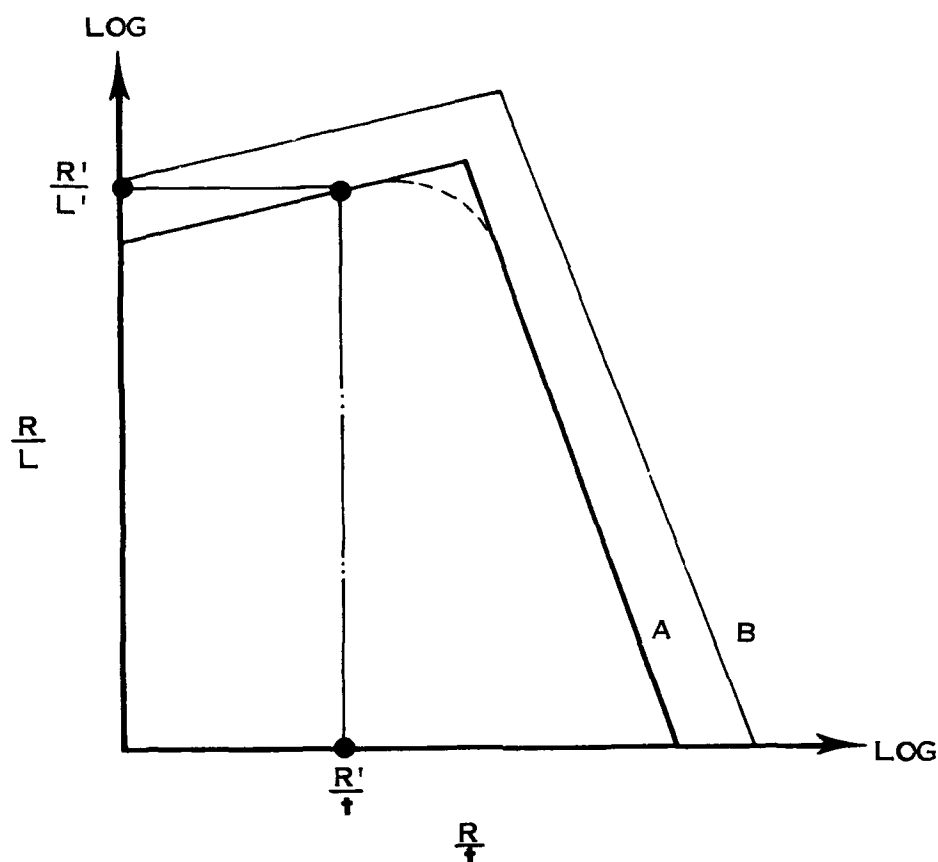


FIGURE V-75 COMPOSITE GRAPH USED TO ESTABLISH DESIGN LIMITS FOR RUBBER BEAD FORMING

A particular R and t (R^1 , t^1) are selected and the R^1/L^1 limit is read directly from the curve. Since R^1 is known L^1 is calculated directly. For each gage and material the free form radius (R_f) is calculated from the equation (V-99).

(V - 99)

$$R_f = \frac{S_u t}{p}$$

Design tables can then be established as illustrated in Figure V-76.

GAGE (t)	t_1	t_2	t_3				
RADIUS (R_f)							
RADIUS (R)	L (DISTANCE BETWEEN CENTERS)						
.25							
.30							
↓							

FIGURE V-76 DESIGN TABLE FOR RUBBER BEAD FORMING

DROP HAMMER BEADING

The equations for drop hammer bead forming, which define the shape of the formability limit curve, were developed in Chapter II. A composite graph composed of the empirically determined forming limits curves of all materials was developed as illustrated in Figure V-77.

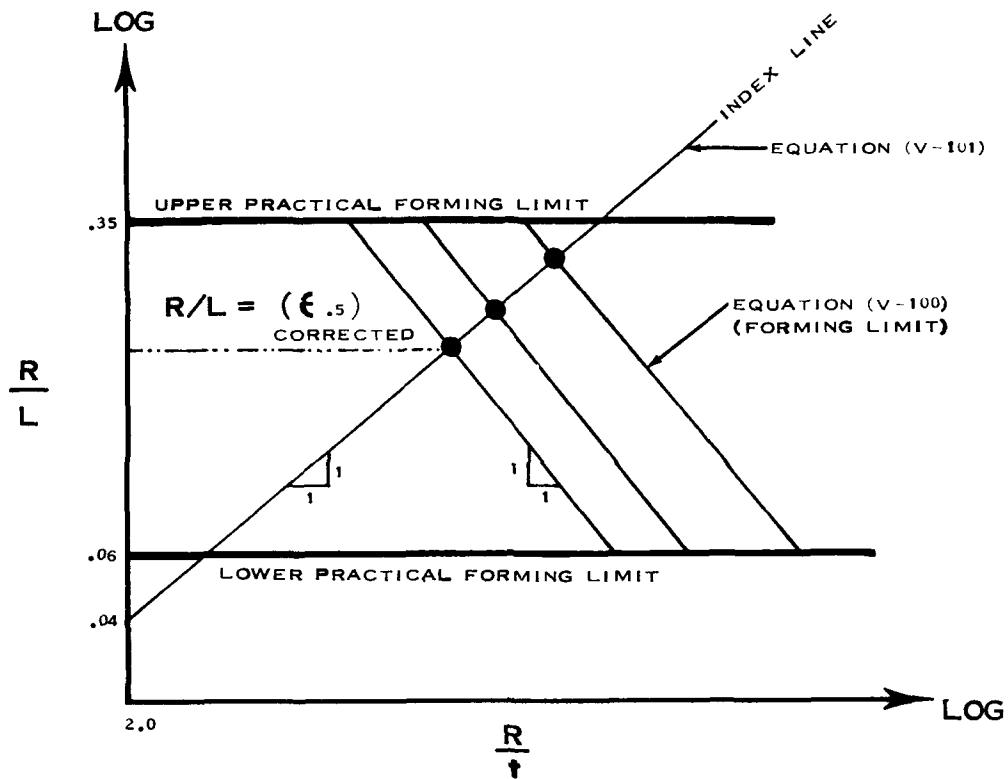


FIGURE V-77 COMPOSITE GRAPH FOR DROP HAMMER BEAD FORMING

The geometric parameters are defined by figure V-78.

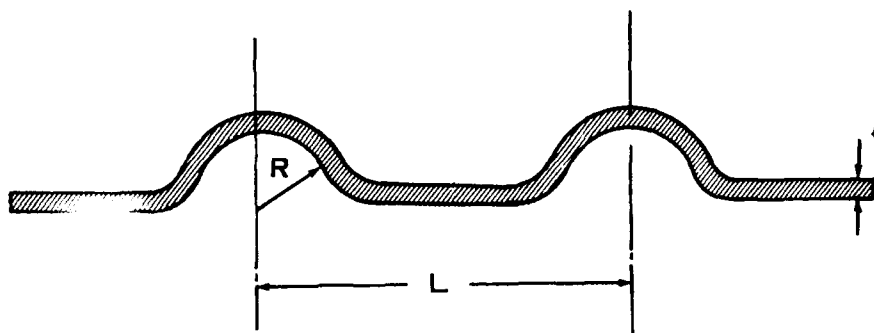


FIGURE V-78 GEOMETRIC PARAMETERS FOR DROP HAMMER BEAD FORMING

The upper and lower practical forming limits have been established at $R/L = 0.35$ and $R/L = .06$ respectively.

The basic equation for the splitting limit is:

$$\frac{R}{L} = \left[\epsilon_{.5} \right]_{\text{(CORRECTED)}} \left[B \right] \left[\frac{R}{t} \right]^{-1}$$

The equation for the formability index line is:

$$\frac{R}{t} = 50 \frac{R}{L}$$

At the intersection of equations (V-100) and (V-101):

$$(V-102) \quad \frac{R}{L} = \left[\epsilon_{.5} \right]_{\text{(CORRECTED)}}$$

Solving equation (V-100), (V-101) and (V-102) simultaneously for B and substituting back into equation (V-100):

$$\frac{R}{L} = \left[\epsilon_{.5} \right]_{\text{(CORRECTED)}}^2 50 \left[\frac{R}{t} \right]^{-1}$$

DESIGN TABLES

Design tables were developed for drop hammer bead forming in the same manner as in rubber bead forming.

CHAPTER VI
SURVEY OF INDUSTRY AND INSTITUTIONS

SURVEY OF INDUSTRY AND INSTITUTIONS

To assure maximum benefit from past work in theoretical formability, a survey was made of the industry and educational and research institutions. This survey was intended to insure a minimum duplication of effort.

Chance Vought Corporation has continually attempted to keep abreast of significant advances in analytical forming technology, even before this was made with the Air Force. The most important contributions were made during World War II and the years immediately following, generally by the universities. A number of contracts were let under government sponsorship, but they were related to formability of specific materials for a few forming processes. The materials studied were the most important of the time, the light aluminum and magnesium alloys.

The Boeing Airplane Company did some original work in analytical formability during the early part of the nineteen-fifties at the same time that the Chance Vought Corporation was originating work in the same field. Boeing developed information for the Air Force under contract 33(600)-23223 to predict bendability of materials based on true stress-true strain data of materials.

The survey for the current theoretical formability program was conducted in order to reaffirm that all existing information on analytical formability had been obtained. The following table indicates that this is true. Most of the companies responded to the inquiry, but little additional information regarding analytical formability was obtained beyond that which was received prior to the contract. It was determined through the initial survey by mail that further surveying by personal visit was

unnecessary because of the limited information available. Five of the companies, in addition to Chance Vought Corporation, indicated some previous attempt to develop an analytical approach to forming, however, the extent to which the information developed is currently being used could not be ascertained.

It has been found through correspondence and personal contacts that this type of a program for determining formability is greatly needed. All of the comments regarding the value of this approach to forming have been favorable.

FIGURE VI-1 FORMABILITY SURVEY RESULTS

Company or Institution	Answered Inquiry	Present Primary Method Used to obtain Formability		Previous Effort to Develop Analytical approach	Data Furnished on Previous Analytical Work	Comment Regarding Value of Predicting Formability
		Analytical	Experimental			
1. Aerojet General Corp. Sacramento, Cal.						
2. Buch Aircraft Corp. Wichita, Kan.	X					Very high interest
3. Bell Aircraft Corp. Buffalo, N. Y.						
4. Bell Helicopter Corp. Ft. Worth, Tex.						
5. Boeing Airplane Co. Seattle, Wash.	X			X	X	
6. Boeing Airplane Co. Wichita, Kan.						
7. Cessna Aircraft Co. Wichita, Kan.						
8. Cleveland Pneumatic Ind. Cleveland, Ohio	X					
9. Convair Ft. Worth, Tex.	X			X		
10. Convair * San Diego, Cal.	X					Urgently needed Program

FIGURE VI-1 FORMABILITY SURVEY RESULTS (CONTINUED)

Company or Institution	Answered Inquiry	Present Primary Method Used to obtain Formability		Previous Effort to Develop Analytical approach	Data Furnished on Previous Analytical Work	Comment Regarding Value of Predicting Formability
		Analytical	Experimental			
11. Douglas Aircraft Co. Santa Monica, Cal.	X		X	X		great value
12. Fairchild Engine and Airplane Corp., Hagerstown, Md.						
13. The Garrett Corp. Los Angeles, Cal.	X					interested
14. The Garrett Corp., Phoenix, Ariz.	X					
15. Goodyear Aircraft Corp. Akron, Ohio						
16. Grumman Aircraft Eng. Corp. Bethpage, N. Y.	X					excellent
17. Hughes Tool Co. Culver City, Cal.	X					
18. Jack and Heintz, Inc. Cleveland, Ohio						
19. Lockheed Aircraft Corp. Burbank, Cal.	X			X	X	Pleased

FIGURE VI-1 FORMABILITY SURVEY RESULTS (CONTINUED)

Company or Institution	Answered Inquiry	Present Primary Method Used to obtain Formability		Previous Effort to Develop Analytical approach	Data Furnished on Previous Analytical Work	Comment Regarding Value of Predicting Formability
		Analytical	Experimental			
20. Lockheed Aircraft Corp. Marietta, Georgia	X					
21. Lockheed Missile and Space Div. Sunnyvale, Cal.						
22. McDonnell Aircraft Corp. St. Louis, Mo.	X		X			
23. The Marquardt Corp. Van Nuys, Cal.						
24. The Martin Co. Baltimore, Md.	X		X	X		
25. The Martin Co. Denver, Colo.	X					Considerable Application
26. The Martin Co. Orlando, Fla.						
27. North American Aviation, Inc. Canoga Park, Cal.						

FIGURE VI-1 FORMABILITY SURVEY RESULTS (CONTINUED)

Company or Institution	Answered Inquiry	Present Primary Method Used to obtain Formability		Previous Effort to Develop Analytical approach	Data Furnished on Previous Analytical Work	Comment Regarding Value of Predicting Formability
		Analytical	Experimental			
28. North American Aviation, Inc. Columbus, Ohio	X		X			
29. North American Aviation, Inc. Los Angeles, Cal.						
30. Northrup Corp. Van Nuys, Cal.						
31. Republic Aviation Corp. Farmingdale, N. Y.	X					
32. Rohr Aircraft Corp. Chula Vista, Cal.						
33. Ryan Aeronautical Co. San Diego, Cal.	X	X				General interest to industry
34. Solar Aircraft Co. San Diego, Cal.						
35. Temco Aircraft Corp. Dallas, Texas						
36. Thompson Ramo Wooldridge, Inc. Cleveland, Ohio						

FIGURE VI-1 FORMABILITY SURVEY RESULTS (CONTINUED)

Company or Institution	Answered Inquiry	Present Primary Method Used to obtain Formability		Previous Effort to Develop Analytical approach	Data Furnished on Previous Analytical Work	Comment Regarding Value of Predicting Formability
		Analytical	Experimental			
37. New York University New York, N. Y.	X					
38. Armour Research Found. Chicago, Illinois	X					worthwhile
39. Syracuse University Syracuse, N. Y.	X					
40. Mass. Institute of Technology Cambridge, Mass.	X					most interesting
41. University of Cal. Los Angeles, Cal.						
42. Battelle Memorial Inst. ** Columbus, Ohio	X			X		excellent

* Information received by personal visit from Mr. S. Carpenter

** Information gained by personal visit to Battelle Memorial Institute

CHAPTER VII
SUMMARY OF PROGRAM AND
DISCUSSION OF PROBLEM AREAS

SUMMARY OF PROGRAM AND DISCUSSION
OF PROBLEM AREAS

As was brought out in the progress reports for this program, very good correlations were made for all forming processes with a minimum of scatter. Practically all of the scatter that occurred can be explained on the basis of variation in the materials, the process, and methods of measuring.

The curves for all of the processes were developed empirically. The shape of the graphs were determined theoretically, as shown in Chapter II, and the formability indices were developed from the same equations or by dimensional analysis as shown in Chapter III. Curves for all of the materials were positioned with the aid of the formability indices and experimental parts.

A total of approximately 21,000 parts were formed on the contract with the following distribution:

Process	Total Parts	Number of Different Materials Formed
Tension and Compression	1800	19
Brake Forming	4100	19
Joggling	1550	19
Dimpling	6800	19
Rubber Flanging	1250	16
Linear Contouring	1100	17
Linear Roll	1150	16
Sheet Stretch	120	15
Androform	70	6

FIGURE VII - 1 TABLE OF TOTAL PARTS FORMED ON CONTRACT

Figure VII-1 (Continued)

Process	Total Parts	Number of Different Materials Formed
Deep Drawing	1450	18
Spinning	500	19
Drop Hammer Beading	400	15
Rubber Beading	550	15
Total	20,840	

1800 of these were standard tension and compression specimens either with or without grids. These number of parts can be further distributed according to phases as shown below:

Phase	Number of Materials	Number of Parts Per Material
III	One	2600
IV	Five	1900
V	Thirteen	700

FIGURE VII - 2 TABLE OF NUMBER OF PARTS PER MATERIAL PER PHASE

Phase III comprised 2024 aluminum and was used for verification of the shape of the theoretical graphs. Phase IV consisted of five additional materials which were used for empirically positioning the curves with the aid of the formability indices. Phase V consisted of thirteen additional materials which were used for verification of both the shape and position of the curves. In this latter phase, formability predictions were made prior to forming of the parts.

The general usage of material by gage is shown in the table below.

Phase	Number of Materials	Eleven Forming Processes	Brake Forming	Tensile and Compr. Specimens
III	One	.020	.020	.020
		.040	.040	.040
		.063	.063	.063
			.100	.100
			.125	.125
			.187	.187
IV	Five	.020	.020	.020
		.040	.040	.040
		.063	.063	.063
			.100	.100
			.125	.125
			.187	.187
V	Thirteen	.020	.020	.020
		.063	.063	.063
			.100	.100
			.125	.125

FIGURE VII - 3 TABLE OF GAGES USED FOR TYPES OF PARTS AND SPECIMENS

All of the materials did not conform to these gages because of availability or otherwise; however, this list does illustrate the general gage distribution used on the contract.

The program objective was to develop an analytical method of predicting formability limits of sheet material using only the mechanical properties of the material. This objective has been accomplished for the twelve forming processes included in the contract. Equations have been defined for each type of failure for each process and methods analyzed for drawing limit graphs for any material, once the pertinent properties for the material are known.

Problems have been encountered in determining formability limits for nearly all of the processes. Most of these are explained on the basis of known answers; however, some of them are explained only by a theoretical analysis. The following pages of this chapter are devoted to a discussion of these problem areas by process:

Formability Tests

Formability tests included the half inch wide standard tensile specimen, the standard compression specimen, and a special 12 inch wide tensile specimen as brought out in Chapter IV. Some of these tensile specimens were gridded.

Gridding was a problem at room temperature on only 2 of the 19 materials. HM-21XA-T8 magnesium-thorium could not be gridded due to its radioactivity and Vascojet 1000 could not be gridded because of poor surface conditions. The latter material also rusted to such an extent that grid lines that did reproduce would almost be obliterated. Elevated temperature tensile specimens could not be gridded because they would burn off when subjected to the heat.

Another problem associated with the tensile tests was oblique fractures across the specimen rather than fractures perpendicular to the axis of the

tensile specimen. These oblique fractures occurred only for certain gage ranges for a few of the materials and were detrimental because they distorted the grids making it more difficult to read them accurately. Only two materials, 15 - 7 PH and, 17 - 7 PH stainless steels, exhibited oblique fractures for all gages.

In addition to the normal gridding problem; the 12 inch wide specimens presented problem of slipping in the jaws and notch sensitivity of some materials causing failure in the jaws. 6Al-4V titanium and J-1570 could not be pulled without slipping in the jaws and molybdenum, tungsten, beryllium, and columbium (10-10) could not be clamped in the jaws without breaking. By including the 2 materials that could not be gridded, this made 8 of the 19 total materials impossible from which to get strain data. Even though the 11 materials that produced tensile data correlated very well for some of the forming processes, these wide tensile specimens were abandoned in favor of the standard tensile specimen.

Bending

This type of forming operation includes both brake forming and joggling. Both processes produced good results; however, some of the problem areas need explaining, particularly for brake forming.

In the first place, HM - 21XA-T8magnesium-thorium and 6Al-4V titanium, the two hexagonal close packed alloys, did not correlate on the same curve with the other alloys, all of which were either body centered or face centered cubic. For this reason, it is expected that all H.C.P. metals will correlate on a single separate line due to the fact that the bending qualities for these

metals are not as good in comparison with simple tensile properties as are the B.C.C. and F.C.C. alloys. The reason for these relatively poor bending qualities for H.C.P. alloys is that the surface layers are not oriented for slip on the maximum shear stress planes as well as tensile specimens are.

Another deviation in the correlation curve for brake forming was found for 2024 aluminum which was caused by the punch imbedding into the soft material, particularly for the heavy gages. This is explained in more detail in Chapter I.

One gage each for each of the following materials exhibited different bending limits from the other 5 gages for the material:

Material	One Gage to Deviate From the Other Five
USS 12 MoV	.020
VASCOJET-1000	.063
HM-21XA-T8	.020
BETA TITANIUM	.125

FIGURE VII - 4 GAGE DEVIATION IN BRAKE FORMING

It is expected that the reason for this deviation in bendability of one gage from the other five is due to procurement of a material deviation within the gage. This was found true for USS 12 MoV where the .020 gage was found to have been cold rolled and the rest of the gages hot rolled.

Beta titanium and molybdenum (.5 titanium) had to be brake formed slow to correlate due to their strain rate sensitivity. The speed for forming these two materials had to be reduced to approximate the speed of tensile testing.

6Al-4V titanium was also included in this reduced speed testing but no increased formability resulted because of the rolling textures mentioned above for hexagonal close packed metals.

Magnesium-thorium HM21XA-T8, tungsten, and beryllium were formed at 750°F, 800°F, and 1200°F respectively because they could not be formed at room temperature. Elevated temperature seemed to be detrimental to molybdenum, columbium (10-10), USS-12-MoV, and Vascojet 1000. This can be explained by observing the following schematic:

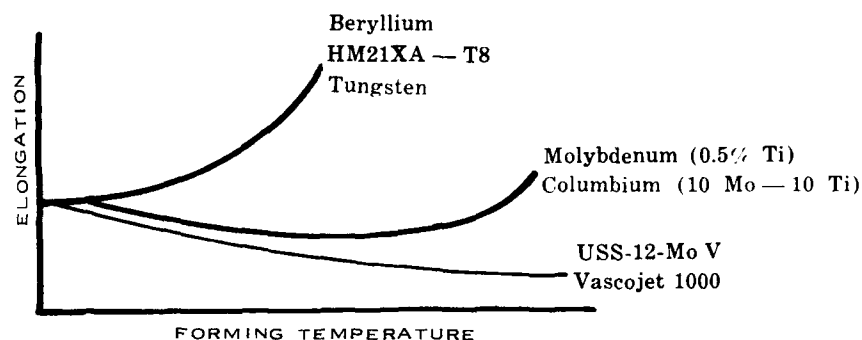


FIGURE VII - 5 ELONGATION VARIATION WITH TEMPERATURE

Beryllium, tungsten, and magnesium - thorium are shown to have elongation increasing with temperature whereas the other four materials are shown to decrease in elongation for the temperature tested.

Elevated temperature tests on tungsten resulted in extreme difference in bendability of the .020 and .040 gages above 400°F. The smallest radius to gage ratio, R/t , that could be obtained for the .020 gage was found to be 7.0 whereas the .040 resulted in .50.

Columbium (10 Mo - 10 Ti) produced very erratic results in brake forming. All gages except one resulted in severe delaminations during both tensile testing and brake forming, giving bend radius to gage ratios, R/t , of 1.0 to 4.5. The only sheet of this alloy to be absent of laminations was the .040 which produced the smallest values of R/t . No attempt has been made to correlate this material to the predictable limits established for the other eighteen materials due to the erratic behavior from sheet to sheet.

The major limitation found in joggling was the joggle bend radius r , discussed in Chapter I and shown below:

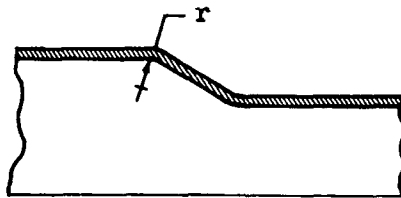


FIGURE VII - 6 JOGGLE BEND RADIUS

The standard bend radius of .032 was found to be too small for beryllium, tungsten, beta titanium, columbium (10-10), and vascojet 1000 for forming at room temperature. This radius was increased to .060 in order to form the last three materials at room temperature. 6Al-4V titanium could not be formed even at elevated temperature; however, heat increased the formability of HM-21XA-T8 considerably.

Flanging

The processes covered under flanging will be dimpling and rubber press stretch and shrink flanges. Very good correlations have been made for all three processes; however, small problems were encountered during the experimental work of each.

The principle problem area for dimpling was associated with a 900°F temperature limitation for the machine used. This limitation was noticeable chiefly on the high strength materials where poor definition resulted, even at maximum pressures, and the formability limits could not be reached on some of these materials. In addition, materials with poor bend ductility exhibited circumferential failures due, chiefly, to the 900°F temperature limitation thus increasing the difficulty of determining the radial splitting limits.

The 1925 psi pressure limit for the rubber press, on which the stretch and shrink flanges were formed, was the limiting factor for this type of forming. This pressure limitation made it difficult to determine formability limits for splitting heavy gages on dies with small curvature. In some materials, only the .020 gage was used to determine fracture limits due to this pressure limitation. In addition, the limited pressure of 1925 psi was not sufficient to remove normal secondary failures such as humping and shear buckling as

brought out in Chapter I.

In order to reach the expected splitting limits for HM-21XA-T8, the flange edge had to be polished similar to the tensile specimens.

Linear Contouring of Sections

Linear contouring of sections includes both linear stretch forming and linear roll forming. Very few problems were encountered in these types of forming so that correlations were readily made.

In linear stretch forming, the buckling line for molybdenum and columbium did not correlate as well as expected. A possible answer for this is that the forming on the stretch press was somewhat faster than the tensile specimens resulting in an increased yield strength. This makes buckling occur for smaller h/t values than predicted.

It was determined that tungsten, beryllium, and magnesium - thorium could not be formed due to the brittleness of these materials when placed in the stretch forming jaws. A solution was found for the magnesium alloy by heating the ends of the part immediately before inserting in the jaws.

The only difficulty encountered in linear roll forming was the inability to get splitting failures. The reason for this was found to be that buckling instabilities were so severe as to keep all stresses low enough so that splitting could not occur.

Plane Contouring of Sheet

Plane contouring of sheet includes sheet stretch forming and Androforming. Parts from both processes had to be evaluated on the basis of approaching formability limits rather than absolute limits with good and failed parts on either side of a limit line. Very good correlations were made with both processes using the appropriate indices developed in Chapter III.

Very little difficulty was encountered in sheet stretch forming and that was with hot forming. For HM-21XA-T8, magnesium - thorium, hot forming at 750 °F posed a necking stability problem in that extreme care had to be taken by the machine operator in regulating the jaw travel so as to prevent splitting the part at the die contact point. Provided this was observed, very good formability resulted for this material. In addition, the limits of beryllium and tungsten were not given due to the extreme brittleness and expected breakage during clamping in the jaws.

Some difficulty was encountered in tooling for both sheet stretch and Androforming. It was difficult to predict the severity to which some of the most ductile materials could be formed; as a result, it was found that only the more severe sheet stretch dies actually gave the forming limits. Additional tooling, considerably more severe than the conventional size, had to be made for the Androform process in order to reach the forming limits.

All Androforming was evaluated for the heat treated or highest strength condition. As brought out in Chapters I, II, and III, this is essential for this process. The splitting and buckling limits were both found on the special built dies with transverse radii of 50 and 20 inches respectively. However,

these two types of limits could not be placed on the same graph because the forming parameters were different. Androforming was the exceptional case for requiring a separate graph for each type of forming failure.

Deep Recessing

The two deep recessing methods evaluated for producing cylindrical cupping are deep drawing with mechanical dies and manual spinning. Both processes correlated very well with the formability indices developed in Chapter III; however, spinning gave some scatter due to the nature of the process.

The principle problem in deep drawing was related to the pressure for holding the pressure plate against the part. At low pressures, which were necessary for small ratios of blank radius to material gage, R_b/t , the hydraulic press was not sensitive enough to obtain maximum formability. In order to compensate for this machine deficiency, it was necessary to use shims for the two small dies with punch radii of 2.5 and 3.0 and the heavy material gage .063. These shims gave a constant clearance for the drawing flange resulting in formability comparable with the larger dies.

The second problem in deep drawing was associated with forming columbium (10-10), beta titanium, and 6Al-4V titanium at room temperature. The combined stresses in the bend radius formed by the punch radius was sufficient to cause premature failure in this bend radius rather than in the wall of the cup. This failure in all three materials started in the bend radius and propagated

across the bottom of the cup at 45° to the grain direction as shown below:

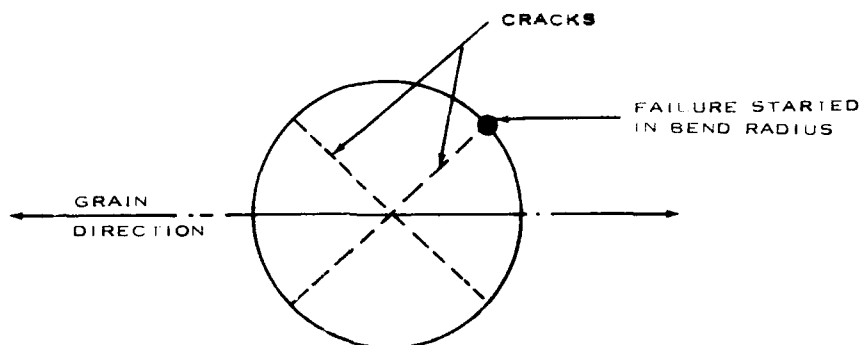


FIGURE VII - 7 VIEW OF BOTTOM OF CUP SHOWING CRACKING AT 45° TO GRAIN DIRECTION FOR DEEP DRAWING

These cracks are probably due to anisotropy because of their regularity in position with the grain direction. Although this premature failure prevented obtaining limits for columbium at room temperature, it was not of sufficient detriment to prevent obtaining the limits for the beta and 6Al-4V titaniums.

Problems in spinning were associated generally with the materials. Vascojet 1000 exhibited abnormal scatter which is presumably due to extreme variations in material properties, part of which has shown up in the tensile and compression testing. Some of the materials benefited with forming at elevated temperatures and some did not. Heating helped HM-21XA-T8 magnesium - thorium and USS-12MoV while it did no good to raise the temperature for Vascojet 1000 and columbium (10-10). Hot forming was essential for forming beryllium, tungsten, and molybdenum at the respective temperatures of 1200°F , 1700°F and 850°F . The high temperature for tungsten was found necessary after medium formability for the material was found at 1100°F .

Shallow Recessing

Shallow recessing consists of work accomplished in bead forming on the drop hammer and the rubber press. Good correlations were made for both of these forming processes, particularly after considering the nature of the variables.

A single problem existed for drop hammer beading and was associated with the poor bending qualities of HM-21XA-T8 magnesium - thorium, 6Al-4V titanium, and beta titanium. This difficulty was premature cracking at the small bend radius at the end of the male beads as shown below:

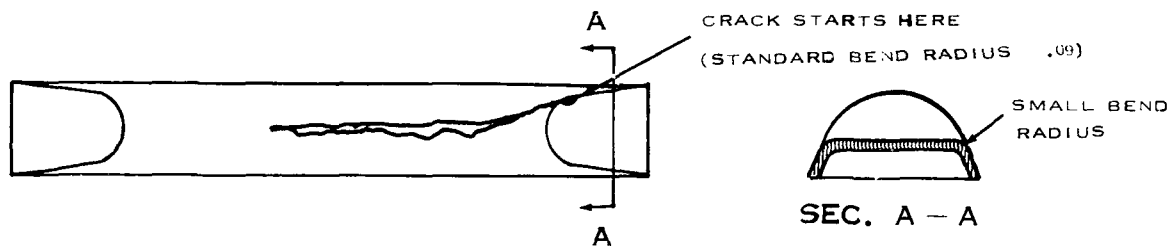


FIGURE VII - 8 PREMATURE FAILURE IN DROP HAMMER BEADING

These three materials could not be formed even for the least severe die at a ratio of bead radius to bead spacing, R/L of .06.

The principle problem associated with beading on the rubber press is the pressure limitation of the rubber press of 3000 psi resulting in large free forming radii. This limitation made it impossible to get fracture limits on all materials except 2024-O aluminum, Vascojet 1000, USS-12 MoV, A-286, and beta titanium. It was impossible to fracture these materials except for the

thinnest gage, .020. Aluminum was the exception for fractures occurred on all three gages. Predictability equations and graphs were made for the materials that did not fracture from the tensile and compression data. The resulting free forming radii were relatively large for these materials.

A minor problem associated with rubber press bead forming was the occurrence of plastic buckling perpendicular to the beads for the large beads with a large ratio of bead radius to length of bead, R/L . This buckling will not occur on practical ratios, however.

HM-21XA-T8 magnesium - thorium and 6Al-4V titanium fractured prematurely across the top of the bead for rubber press beading in a similar manner to drop hammer beading. Again this was due to the small bend radius at the end of the bead.

CHAPTER VIII
RECOMMENDATIONS FOR FUTURE WORK

RECOMMENDATIONS FOR FUTURE WORK

The results of this program have opened up new areas needing investigation in the sheet metal forming field. These needed developments may be classified into seven categories as shown below:

1. Additional Part Shapes
 - a. Rubber forming
 - b. Sheet stretch forming
 - c. Deep recessing
 - d. Linear stretch forming
 - e. Shallow recessing of irregular shapes
2. Extension of Forming Limits
 - a. Rubber forming pressures
 - b. Effect of segment angle
 - c. Elevated temperature creep forming
 - d. Multistage drawing
 - e. Compressive brake forming
 - f. Improved forming techniques
3. Results of Forming
 - a. Springback
 - b. Effect on material properties
 - c. Thinning during forming
 - d. New alloy development
4. Additional Conventional Forming Processes
 - a. Tube bending
 - b. Deep rubber bladder drawing

- c. Stretch - mechanical die forming
- d. Progressive forming
- 5. Advanced Forming Processes
 - a. High velocity forming
 - b. High temperature forming
- 6. Primary Forming Processes
 - a. Shear spinning
 - b. Forging
 - c. Extruding
 - d. Sheet rolling
- 7. Basic Mechanisms in Metal Forming
 - a. Plasticity
 - b. Buckling

Although all of these will be necessary to complete the quantitative aspects of sheet metal forming, some will be needed at a sooner date than others. Also, some of these recommendations need a more basic understanding before the theoretical formability concept can be applied.

ADDITIONAL PART SHAPES

Although the principal shapes have been considered on this initial program for the most basic forming processes, there are a number of part shapes that were not on the program.

Smoothly contoured flanges of the stretch and shrink types were considered on the current contract. Additional rubber formed parts that are

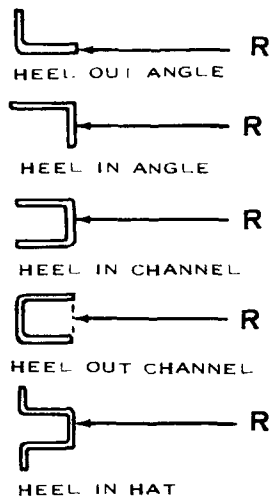
commonly used in design are: (1) straight flanging, (2) joggling, and (3) return flanges. Although there are other methods of producing these flanges and recesses, they are generally formed on the rubber press along with the curved flanges because of economic reasons.

Sheet stretch forming of symmetrical double curved skins was the basic part developed on the current contract; two additional types of parts needing investigation are: (1) nonsymmetrical double curved skins and (2) reversely curved skins. It is expected that correlations can be made on the current work and these new types of parts; however, some experimental work is needed to verify this.

Deep recessing was investigated on the initial program for both mechanical dies and manual spinning. However, this was performed only for the basic cylindrical cup. New types of parts needing development for the mechanical die method of deep drawing are: (1) box shapes, (2) dome ends, and (3) truncated cones. The last two also need development for manual spinning.

Linear stretch forming of the most basic sections was covered on the current program. There are a number of part shapes, however, that are needed to complete the formability study of this important method of section contouring. These parts are explained in the following sketch :

INCLUDED ON CURRENT CONTRACT



RECOMMENDED FOR FURTHER DEVELOPMENT

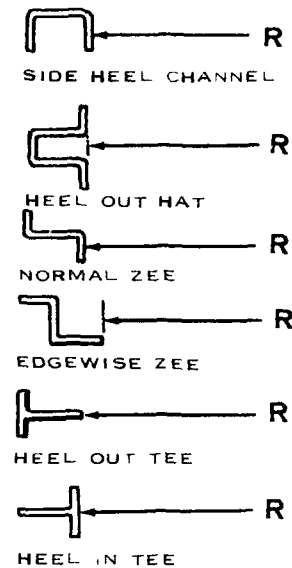


FIGURE VIII-1 LINEAR CONTOURED SECTION TYPES

It should be noted that these additional six sections will essentially complete the study of this type of forming.

Although shallow recessing was investigated on the current program for both drop hammer and rubber press forming, only the basic symmetrical beaded panel type of part was studied. Additional work should be included for irregular shapes such as shallow type panels stiffened with beads running in any direction.

EXTENSION OF FORMING LIMITS

The forming limits developed on the current program are generally based on standard equipment with ordinary pressures, techniques, forming speeds, lubrication, etc. With a few exceptions, most of the

forming limits can be extended for most of the processes in a number of ways.

First, the rubber forming pressures used on the contract were 1925 psi for flanging and 3000 psi for beading. These pressures greatly restricted the flanges and definition obtained, particularly on the shrink flanges and the beaded panels. An example of the manner in which formability can be increased in rubber press shrink flanging is shown in the limit graph below:

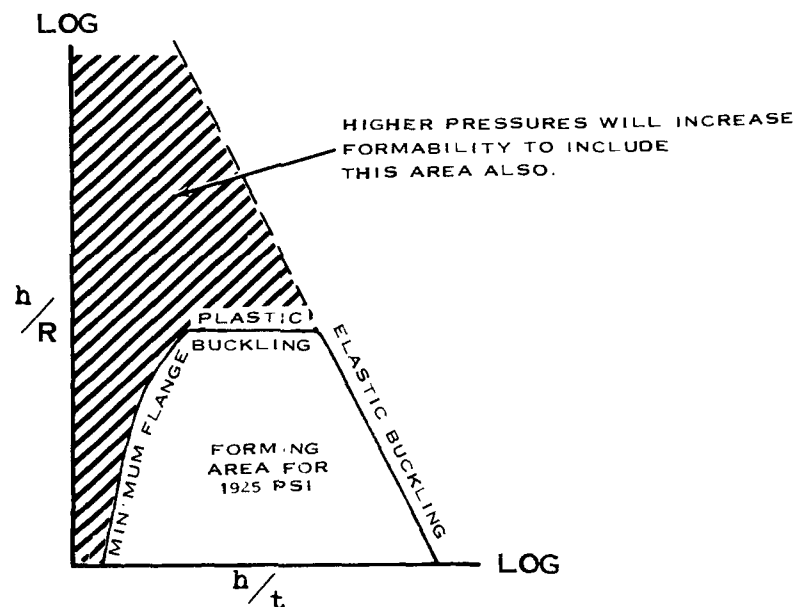


FIGURE VIII-2 INCREASED FORMABILITY WITH PRESSURE IN RUBBER PRESS SHRINK FLANGING

Although the elastic buckling limitation in shrink flanging for thin gages cannot be altered with pressure, the plastic buckling and minimum flange limitation for medium and heavy gages can be increased greatly. The free forming radius in rubber forming shallow recesses can be greatly

minimized with increased pressure as shown in the following sketch:

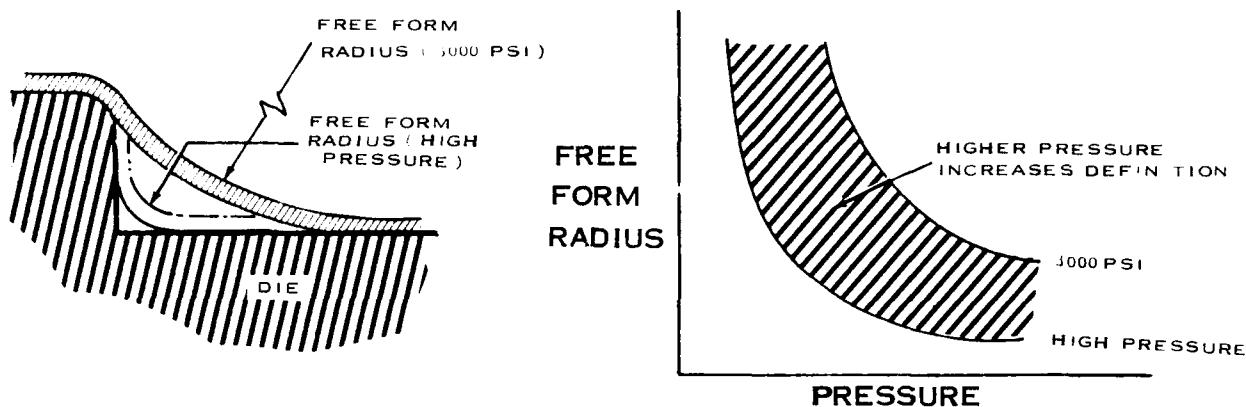


FIGURE VIII-3 INCREASED DEFINITION WITH PRESSURE IN RUBBER PRESS SHALLOW RECESSING

The segment angle in linear contouring and rubber press flanging was not considered a variable in the current contract. On the contrary, it was held approximately constant at a relatively high value so that it would not affect formability and would give conservative values. A decreasing segment angle, however, will greatly increase formability as shown schematically below for linear stretch forming:

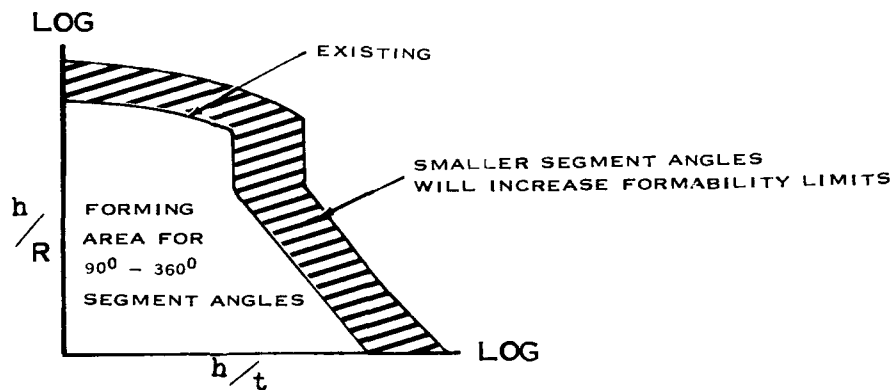


FIGURE VIII-4 INCREASED FORMABILITY FOR DECREASED SEGMENT ANGLE FOR LINEAR STRETCH FORMING

This same increase in formability can be made for rubber press flanging.

Elevated temperature creep forming will likewise increase formability limits by ironing out elastic buckling and other distortions resulting from springback in a part. Most metals are susceptible to this type of hot finish forming, the only limitation being a metallurgical consideration of maximum temperature based on recrystallization, precipitation, etc. This type of forming is generally a finish form operation so that parts are first preformed in another operation. Hot creep forming can greatly extend forming limits by finishing a part that was formed considerably outside its normal formability limits as shown schematically by the graph below:

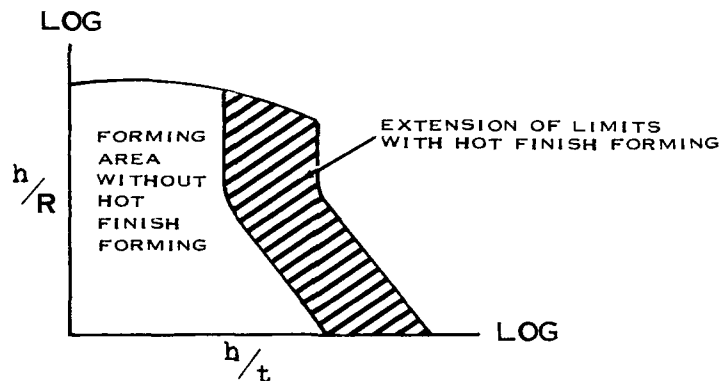


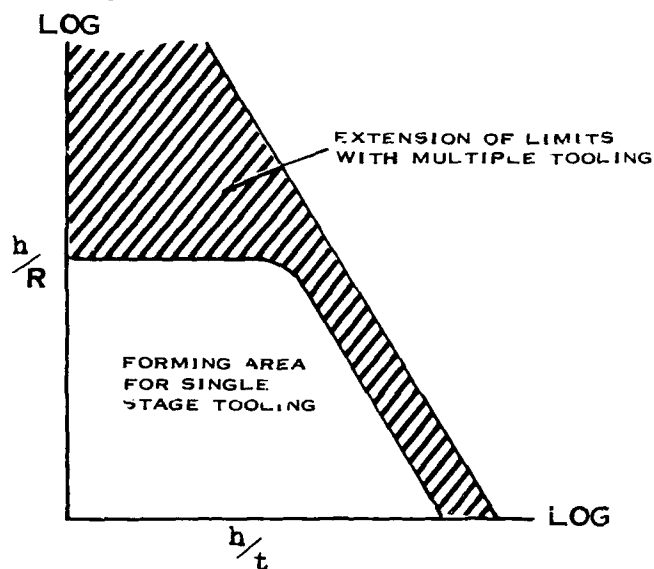
FIGURE VIII-5 INCREASED FORMABILITY WITH ELEVATED TEMPERATURE CREEP FORMING FOR LINEAR CONTOURING

This type of finish forming will essentially eliminate the need for any final handworking because such close tolerances can be maintained.

Multistage drawing with mechanical dies is another way of extending forming limits. This process is based on multiple tooling so that

several stages of drawing are necessary with a different geometry in each stage. This type of incremental forming can increase forming limits for deep recessing as shown schematically below:

FIGURE VIII-6
INCREASED FORMABILITY
IN DEEP RECESSING WITH
MULTISTAGE TOOLING



Multistage deep drawing can be seen to increase all formability areas over single stage including both the elastic and plastic regions of buckling.

Compressive brake forming is a method that can be used to increase brake forming limits as shown in the sketch below:

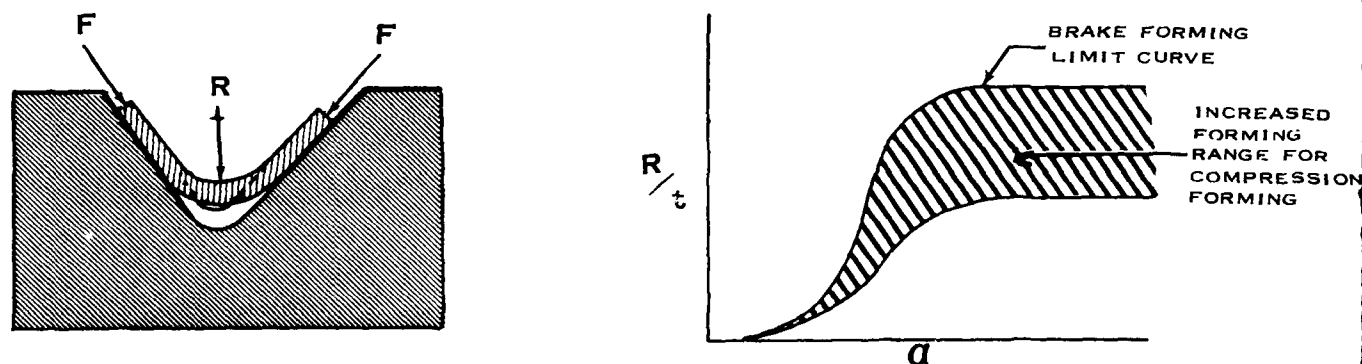
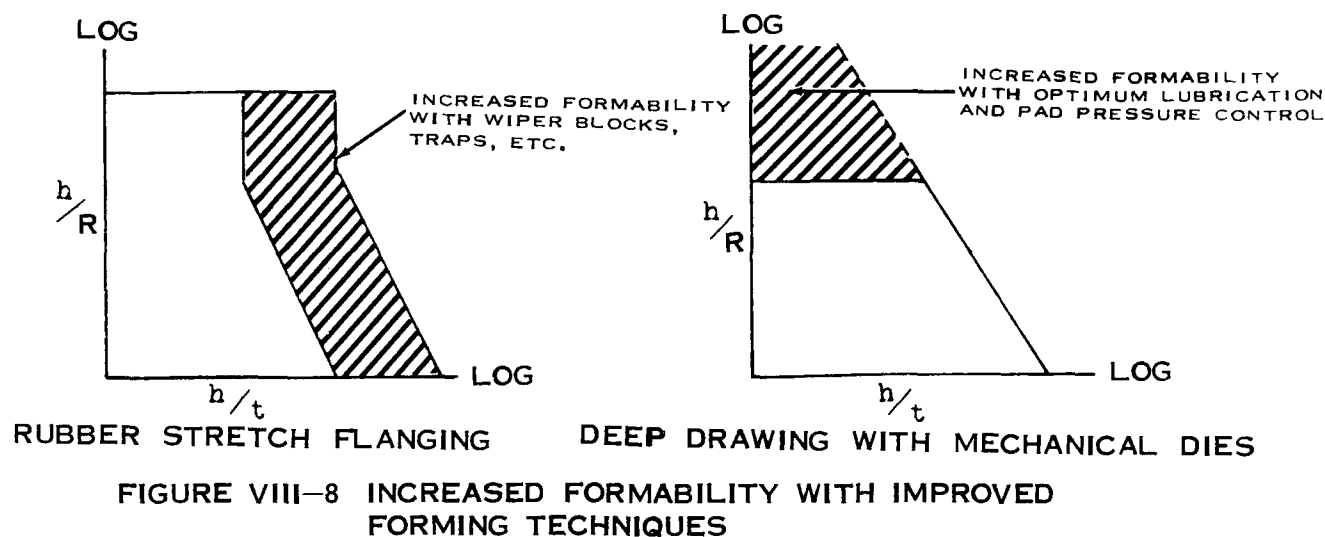


FIGURE VIII-7 **INCREASED LIMITS IN COMPRESSION**
BRAKE FORMING

By subjecting a part, that has been formed in the normal manner on a brake press to the material limit resulting in a bend radius of R , to compressive forces P as shown, the bend radius can be reduced considerably. This is due to the fact that the neutral axis is moved to near the convex surface resulting in small tensile stresses.

Improved forming techniques will also extend forming limits of most processes. For example, the use of wiping blocks, traps, and overlays in rubber press forming and the use of optimum lubrication and pad pressure control in mechanical die deep drawing will increase formability limits as shown below:



The elastic buckling line in rubber stretch flanging and the plastic buckling line in deep drawing can be extended considerably with the aid of these techniques.

RESULTS OF FORMING

There are a number of results from forming that are very important, both from the design and the fabrication viewpoint. Some of these have been studied in the past; however, a general program relative to a broad range of materials and processes has never been initiated.

Springback has been shown in the current theoretical formability program to be dependent on the same mechanical properties as buckling. This distortion can be predicted based on mechanical properties for straight flanging on the rubber press and brake press, curved flanging on the rubber press, and linear contouring on the stretch press. A knowledge of predictable springback will enable the manufacturing engineer to design springback into the forming tools. This will greatly decrease finish handworking, particularly for the high strength metals of the future.

The effect of forming on materials properties needs investigating from the standpoint of predicting changes in material properties based on fundamental shape change of the part. These resulting changes can be related to the elongation that the part has undergone during forming. The material properties to be included are the principal strength and elongation values such as yield strength, modulus of elasticity, ultimate strength, elongation, fatigue, and creep. This knowledge of property changes will enable the designer to more efficiently design structural parts.

Thinning of a part during forming is another consideration that should be predicted for efficient design. Thinning usually accompanies parts that have undergone stretching during forming while thickening

occurs on parts that have been compressed during forming. This change in thickness can be predicted for parts with specific geometries by the law of constant volume. Graphs and tables can be prepared for all shapes of parts to give the designer a ready reference for thickness changes in parts during forming. This information will be important both from a strength and weight standpoint.

The concept of theoretical formability can also be used in basic alloy development by having a good realization of the desired properties in a metal alloy for good formability. Alloying in the past has been made with the principal objective to achieve the utmost in strength properties. This has generally resulted in alloys of decreasing formability. With a knowledge of the properties needed for good formability, proper guidance can be made to the alloy developers to produce optimum formable materials.

ADDITIONAL CONVENTIONAL FORMING PROCESSES

There are a number of conventional forming processes not included on the initial contract such as tube bending, deep recessing with the rubber bladder press, stretch - mechanical die forming on the hydraulic press, and progressive forming. Although these are not as basic as the processes covered on the current program, they are of significant interest to include on future development programs.

Tube bending should be explored in the range of extruded tubing for the more important metal alloys. A typical formability graph that can be

developed is shown below:

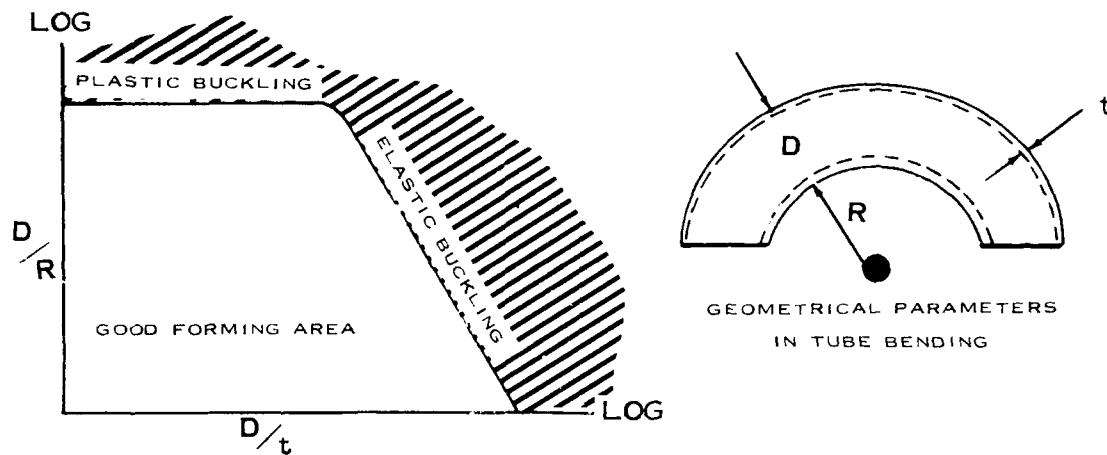


FIGURE VIII-9 EXPECTED FORMABILITY CURVE FOR TUBE BENDING

Buckling and wrinkling of the inner wall is expected to be the chief limitation in forming thin walled tubes. This type of buckling will be of the shell buckling rather than plate buckling; however, the same shape of curves should result.

Another method of deep recessing that was not investigated on the initial program is deep drawing with a rubber bladder as shown in the sketch below:

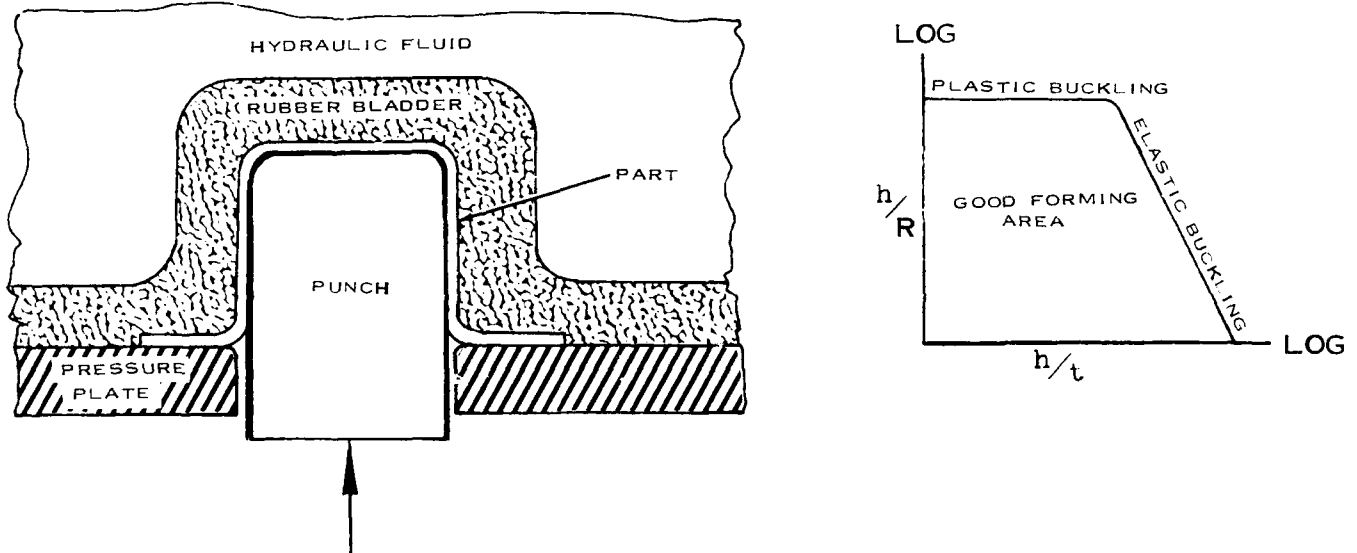


FIGURE VIII-10 DEEP DRAWING WITH A RUBBER BLADDER PRESS

This process has advantages over other methods of deep recessing in that tooling is less costly and, in some instances, better controls can be made on pressure giving better formability. The formability curves will probably be very similar in shape to the mechanical die method with buckling limiting forming in both areas of the graph.

A third additional forming process that requires development and was not included on the initial program is the stretch - mechanical die forming method used on the hydraulic press as shown schematically below:

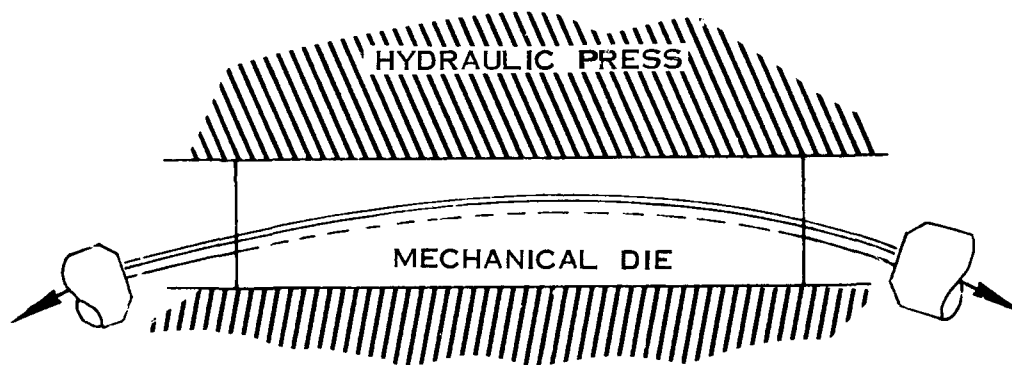


FIGURE VIII-11 STRETCH-MECHANICAL DIE FORMING

This type of tooling is generally used for forming relatively heavy extruded sections to contours with warped cross-section. When high strength materials are required, there is no other way of forming this type of part because of springback and other accompanying distortions. Formability limits can be obtained for these shapes of parts for different materials based on their mechanical properties.

Progressive forming is another process that would benefit from having a quantitative application of theoretical formability applied. This type of forming can generally be applied to corrugations, beaded panels, and double contoured skins. Taking the latter, as an example, the following sketch illustrates the process:

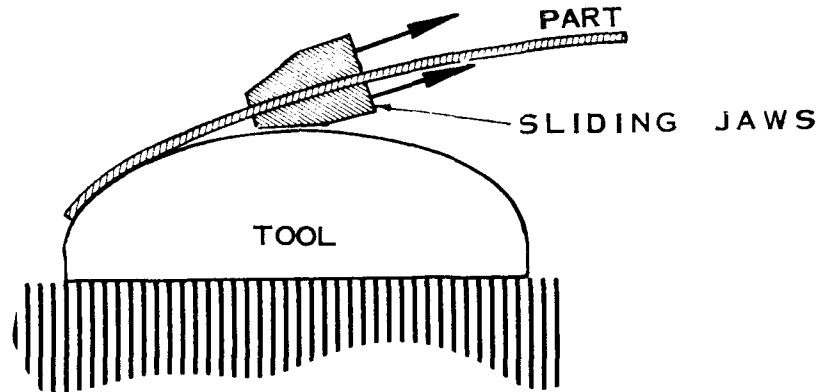


FIGURE VIII-12 PROGRESSIVE FORMING DOUBLE CONTOURED SKINS

This process can be seen to be based on incremental type forming with a frictional sliding jaw pulling the double curved skin around the stationary tool. The advantages of this process over the more conventional stretch presses can be seen to be increased formability due to a decreased friction between the part and the tool. Beaded panels and corrugations can benefit in the same manner.

ADVANCED FORMING PROCESSES

The so called high energy and high energy rate advanced forming processes have been under intense investigation for the past five years.

These are the high velocity and high temperature forming processes. The former includes such forming processes as: (1) explosive - water, (2) explosive - air, (3) electric discharge, (4) piston - gas, and (5) magnetic flux. The latter includes such advanced processes as: (1) integrally heated dies, (2) hot platen machines, (3) gas - expansion forming, and (4) hot fluid forming. Most of the work in these areas has been of a qualitative nature without real sincere regard to the applications and limitations of the process. This is due to the fact that most of these processes are still in their infancy and require more development.

The development of these high temperature and velocity processes is currently reaching the point where the quantitative aspects of forming can be applied. This means that material formability based on mechanical properties can be determined for most of these forming processes.

In the high velocity forming area, both the low and high explosive need investigation. Tables, graphs, and equations can be developed for both regimes of velocity for the following types of transfer mediums: (1) gas (air), (2) liquid (water), and (3) solid (sand or rubber). These quantitative data will give the limits of forming for the most applicable materials and the most applicable shapes of parts.

High temperature forming is currently being readily performed up to temperatures of 1200°F. This limitation is based on the current tooling material limitation around 1400°F due to oxidation. However, new tooling

materials and coatings are making it possible to achieve forming in the upper regimes of temperature. The methods of heating parts to these higher temperatures are principally by resistance and radiation heating. Material properties can be studied at these higher temperatures and correlated to formability for the most applicable materials. In this way, predictability information can be obtained for forming high strength materials at high temperature. Feasibility of this type of predictability has been established in the small amount of high temperature forming performed on the current program.

PRIMARY FORMING PROCESSES

The primary forming processes such as forging, extruding, sheet rolling, and shear spinning also need to be developed from a quantitative formability sense. These processes are based on large plastic deformation and, in most cases, elevated temperatures with or without intermediate anneals. The limitations of these processes are: (1) the shear deformation that the material can withstand, (2) friction forces along surfaces, (3) extremely large power requirements, and (4) distortions resulting from springback and residual stresses.

A quantitative analytical program is needed to determine the extent to which metal alloys, particularly the new higher strength ones, can be formed by these primary forming methods. The resistance that accompanies a metal being subjected to extreme plastic deformation can be related to

fundamental plastic properties of metals such as slip, twinning, and cleavage. The geometry, through which the parts are changing, can be expressed in graphical form representing the limits of forming for a given metal. Then metals can be correlated with their mechanical properties giving relative formability for all metals.

Forging, extruding, and sheet rolling each could be studied on the basis of fundamental shape changes associated with the process. Shear spinning could be evaluated for truncated cones, dome ends, and cylinders.

BASIC MECHANISMS IN METAL FORMING

The two fundamental mechanisms governing formability in sheet metal are plasticity and buckling. The former has been developed rather thoroughly in the past four decades, but has not been related directly to sheet metal forming except in rare cases. Until recently, buckling has been almost totally absent as related to thin gage metal forming. These two limiting factors in sheet metal forming need to be developed for a more complete understanding of the physics that a metal undergoes during forming.

The flow mechanisms of slip and twinning and the brittle and ductile types of metal separation need to be studied for various metals being subjected to plastic deformation at various temperatures and speeds of forming. Studies should be made, for example, on why the hexagonal close packed alloys 6Al-4V titanium and HM-21 magnesium thorium have such poor bendability relative to its tensile elongations, when compared with the

body centered cubic and the face centered cubic metals. Although theories have been expounded on some of these observances, no program has been initiated to systematically study plastic behavior for a broad range of materials.

Thin gage sheet metal buckling has been developed principally for design applications; however, even here only basic buckling has been developed based on simple edge and surface restraints. The effect that these restraints have in forming sheet metal need to be developed for a clearer understanding of the role of buckling in forming. In most forming operations, at least one surface of the sheet is restrained against a tool; otherwise formability would be severely restricted. In some types of sheet metal forming, such as deep drawing and linear contouring of sections, both surfaces of flanges being subjected to compression are restrained against the die. Studies should include the three basic types of parts failing by buckling: (1) flat sheet buckling, (2) shell buckling, and (3) twist buckling of sections.

Only through a thorough understanding of these two fundamental forming limitations will sheet metal forming be developed to the fullest.

CHAPTER IX
BIBLIOGRAPHY

CHAPTER IX
BIBLIOGRAPHY

BIBLIOGRAPHY

1. Nadai, A., Plasticity, McGraw-Hill Book Co., Inc., New York, N. Y., 1931.
2. Hoffman, Oscar, and Sachs, George, Theory of Plasticity, McGraw-Hill, 1953.
3. Shanley, F. R., "Elastic Theory in Sheet Metal Forming Problems," Journal of the Aeronautical Sciences, Vol. 9, No. 9, July 1942.
4. Schroeder, William, "Mechanics of Sheet Metal Bending," A.S.M.E. Trans., Vol. 65, 1943.
5. Lubahn, J. D. and Sachs, George, "Bending of an Ideal Plastic Metal," A.S.M.E. Trans., Vol. 72, 1950.
6. Timoshenko, S., Theory of Elastic Stability, McGraw-Hill Book Co., Inc., 1946.
7. Den Hartog, J. P., Advanced Strength of Materials, McGraw-Hill Book Co., Inc., 1952
8. Miklowitz, Julius, "The Influence of the Dimensional Factors on the Mode of Yielding and Fracture in Medium Carbon Steel - I, " Journal of Applies Mechanics, September 1948.
9. Brewer, G. A., "Measurement of Strain in the Plastic Range," Proceedings of the Socity for Experimental Stress Analysis, V.I N-2, 1944.
10. Miller, James A., "Improved Photogrid Techniques for Determination of Strain over Short Gage Lengths," National Bureau of Standards, Washington, D. C.

11. Senor, B. W., "Flange Wrinkling in Deep Drawing Operation," Journal of Mechanics and Physics of Solids, August 1956.
12. Low, J. R. and Prater, T. A., "Measurement of Ductility in Sheet Metals," ASTM Special Publication No. 87, June 22, 1948.
13. Sachs, George, Principals and Methods of Sheet Metal Fabricating, Reinhold Publishing Corp., 1950.
14. MacGregor, C. W., "The True Stress-Strain Tensile Test, and Its Role in Modern Materials Testing," Franklin Institute Journal, 1944.
15. Bridgman, P. W., "The Stress Distribution in the Neck of a Tension Specimen," Transactions of ASM, 1944.
16. Zener, C., and Hollomon, J. H. "Plastic Flow and Rupture of Metals," Transactions of ASM, 1944.
17. Sachs, G., and Lubahn, J. D., "Failure of Ductile Metals in Tension," Transactions of the ASME, May 1946.
18. Lubahn, J. D., "The Necking of Tensile-Test Specimens", Transactions of the ASME, May 1946.
19. "ASME Symposium on Flow and Fracture of Metals," Transactions of the ASME, 1948, (Journal of Applied Mechanics, June 1948).
20. Dorn, J. E., and Thomsen, "The Ductility of Metals Under General Conditions of Stress and Strain," Transactions of ASM, 1947.

21. Hill, R., (University of Bristol, England), The Mathematical Theory of Plasticity, Oxford University Press (London), 1950.
22. Fracturing of Metals, published by the American Society for Metals, 1948, 311 pages.
23. Gensamer, M., Saibel, Ransom, and Lowrie, The Fracture of Metals, published by the American Welding Society, 1947.
24. Marin, J., and Hu, L. W., "On the Validity of Assumptions Made in Theories of Plastic Flow of Metals," Transactions of the ASME, August 1953.

<p>CHANCE VOUGHT CORPORATION, Vought Aeronautics Division, Dallas, Texas. THEORETICAL FORMABILITY, Volume I, DEVELOPMENT, by W.W. Wood, R.E. Goforth, R.A. Ford, et al. 31 July 1961. [356]p. incl. illus. tables, 34 refs. (Project O(7-7381); Task 73811) (ASD TR61-191(I)) (Contract AF 33(616)-6951)</p> <p>Unclassified report</p> <p>The "cut-and-try" method of determining sheet metal formability has long been the standard practice in the aircraft industry. This report presents methods of determining formability analytically for the twelve most common processes of forming sheet metal. This method is based on utilization of a material's mechanical properties to predict formability.</p> <p>(over)</p>	<p>UNCLASSIFIED</p>
<p>Volume I (development) gives the procedure used to arrive at the objective of predicting formability. First, basic limit equations are developed relating geometry of the parts to the material properties. These equations are used to determine the shape of the limit graphs to give indices relating formability to the material. Then, experimental parts are formed to position the theoretically shaped curves with the aid of the formability indices.</p>	<p>UNCLASSIFIED</p>

<p>CHANCE VOUGHT CORPORATION, Vought Aeronautics Division, Dallas, Texas. THEORETICAL FORMABILITY, Volume I, DEVELOPMENT, by W.W. Wood, R.E. Goforth, R.A. Ford, et al. 31 July 1961. [356]p. incl. illus. tables, 34 refs. (Project O(7-7381); Task 73811) (ASD TR61-191(I)) (Contract AF 33(616)-6951)</p> <p>Unclassified report</p> <p>The "cut-and-try" method of determining sheet metal formability has long been the standard practice in the aircraft industry. This report presents methods of determining formability analytically for the twelve most common processes of forming sheet metal. This method is based on utilization of a material's mechanical properties to predict formability.</p> <p>(over)</p>	<p>UNCLASSIFIED</p>
--	---------------------